REPORT DOCUMENTATION PAGE

Form Approved
OMB No. 0704-0188

1. AGENCY USE ONLY (Leave blank)	2. REPORT DATE	3. REPORT TYPE AND DATES COVERED
		Final Report 01 April 1998 – 01 July 2001

4. TITLE AND SUBTITLE
Resource for Piezoelectric Single Crystals

5. FUNDING NUMBERS
DARPA/ONR Contract No.: N00014-98-1-0527

6. AUTHOR(S)
Thomas R. Shrout

7. PERFORMING ORGANIZATION NAME(S) AND ADDRESS(ES)
Materials Research Laboratory
The Pennsylvania State University
University Park, PA 16802

8. PERFORMING ORGANIZATION REPORTING NUMBER

9. SPONSORING/MONITORING AGENCY NAME(S) AND ADDRESS(ES)
DARPA
3701 North Fairfax Drive
Arlington, VA 2203-1714

Office of Naval Research
Ballston Centre Tower One
800 North Quincy Street
Arlington, VA 22217=5660

10. SPONSORING/MONITORING AGENCY REPORT NUMBER

11. SUPPLEMENTARY NOTES

12a. DISTRIBUTION/AVAILABILITY STATEMENT

Approved for public release; distribution is unlimited.

12b. DISTRIBUTION CODE

13. ABSTRACT (Maximum 200 words)

14. SUBJECT TERMS

15. NUMBER OF PAGES

16. PRICE CODE

17. SECURITY CLASSIFICATION OF REPORT	18. SECURITY CLASSIFICATION OF THIS PAGE	19. SECURITY CLASSIFICATION OF ABSTRACT	20. LIMITATION OF ABSTRACT

NSN 7540-01-280-5500

Standard Form 298 (rev. 2-89)
Prescribed by ANSI Std. 239-18
298-102

Resource for Piezoelectric Single Crystals

Period of Performance:

April 1, 1998 – July 1, 2001

Final Report

DARPA/ONR
Contract No. N00014-98-1-0527

Submitted by:

T.R. Shrout
Materials Research Laboratory
The Pennsylvania State University
University Park, PA 16802

December 2001

TABLE OF CONTENTS

PENNSTATE

Thomas R. Shrout
Professor of Materials
Senior Scientist
The Pennsylvania State University
150 Materials Research Laboratory
University Park, PA 16802

(814) 865-1645
(814) 865-2326 (Fax)
TShrout@psu.edu
www.mri.psu.edu

December 14, 2001

Defense Technical Information Center
8725 John J. Kingman Road
STE 0944
Ft. Belvoir, VA 22060-6218

To Whomever It Concerns:

Enclosed please find a copy of the final report, "Resource for Piezoelectric Single Crystals," Contract No. N00014-98-1-0527.

Sincerely,

Thomas R. Shrout
Professor of Materials
Senior Scientist

TRS:jea

Enclosure

MRI

Abstract

This report documents work performed over the period of April 1, 1998–July 1, 2001 under the ONR/DARPA program titled "Resource for Piezoelectric Single Crystals," contract no. N00014-98-1-0527. The program encompasses novel piezoelectric materials, characterization, and domain studies, innovative growth technique and device engineering, the latter including MEMS and electro-optics. Research on this program is represented in the technical appendices.

The program was on domain/crystallographic engineering of Relaxor-PT single crystals, e.g. $Pb(Zn_{1/3}Nb_{2/3})O_3$–$PbTiO_3$ and $Pb(Mg_{1/3}Nb_{2/3})O_3$–$PbTiO_3$. From this program, it was confirmed that in single crystal form, Relaxor-PT materials offer significant piezoelectric performance with coupling coefficients greater than 90% and strains exceeding 1%.

In *Characterization*, the complete set of dielectric, piezoelectric, and elastic coefficients were determined for <100> domain engineering rhombohedral PZN–4.5%PT, PZN–8%PT, and PMN–33%PT crystals. For all the systems characterized, coupling coefficients ($k_{33} > 90\%$) with piezoelectric strain coefficients ($d_{33} > 2000$ pC/N) were found. The concept of cryogenic poling was utilized to reduce property variation among crystals relatively close to the morphotropic phase boundary, due to rhombohedral–tetragonal transformations. Domain studies revealed the complexity of the crystals in terms of the macrosymmetry being orthorhombic mm2 or lower than the assumed 4mm. The possibility of a monoclinic phase was suggested to aid in the understanding of the complex domain configuration of underlying high piezoelectric activity.

In addition to high temperature flux and Bridgman growth technique, Laser Heating Pedestal Growth crystal of non-lead Zr modified $BaTiO_3$ and PMN-PT were successfully grown with rates > 0.3 mm/min. The concept of domain engineering was demonstrated on non-PbO ferroelectrics with enhanced levels of piezoelectric activity confirmed.

Thin film fabrication of PMN-PT and $Pb(Yb_{1/2}Nb_{1/2})O_3$–$PbTiO_3$ (PYN-PT) systems using pulsed laser deposition and sol-gel processing resulted in <100> oriented films with piezoelectric coefficients d_{31} as high as –80 pC/N, significantly higher than that achieved for PZT films. PYN-PT films offer the additional merit of a high transition temperature ~ 300°C versus 150°C, with remanent polarization values > 60μC/cm^2.

Fatigue studies of both bulk and thin film crystals revealed a crystallographic origin. Samples oriented on the <001> had little to no polarization fatigue up to 10^{11} cycles, with <111>

films exhibiting rapid fatigue. The low fatigue rate, coupled with high values of remanent polarization, suggest these films to be interesting for ferroelectric memories.

The large ferroelectric activity in Relaxor-PT crystals, particularly near the morphotropic phase boundary translated into high electro-optic (E-O) and acousto-optic (A-O) activity. Electro-optic coefficient $d_{33} \geq 180$ pm/V and near zero r_{13} were found for tetragonal PZN-PT. The r_{33} values are six times higher than that for $LiNbO_3$. The A-O response was higher than TeO_2, the most widely used materials.

Introduction

This report overviews the research performed for the period of April 1, 1998 to July 1, 2001, ONR/DARPA Program Contract No. N00014-98-1-0527, titled "Resource for Piezoelectric Single Crystals". The program established a resource for the growth, characterization, and evaluation of piezoelectrics for high impact defense applications.

The program exploits recent research results from the Pennsylvania State University, demonstrating that single crystal relaxor piezoelectrics exhibit a quantum enhancement in performance: electromechanical coupling factors greater than 90% with strain levels exceeding 1%, in contrast to ~ 75% and 0.1% levels in polycrystalline PZT ceramics, respectively.

The program brought together activities in the Materials Research Laboratory (MRL) in the areas of innovative growth techniques, novel materials, characterization, and domain engineering, while establishing new application opportunities in the area of MEMs and electro-optics.

In the program, there were four primary thrusts, as schematically presented in Figure 1: (1) Novel Materials, (2) Characterization, (3) Innovative Growth Techniques, and (4) Device Engineering, by a team of faculty and support group crossing a spectrum of academic disciplines.

- Novel materials development explored $Pb(B,B)O_3$-PT relaxor systems, their commonality, and underlying E-field strain coupling. Demonstrated crystallographic and/or domain engineering in single crystal piezoelectric for enhanced performance, including non-PbO materials.
- Innovative growth techniques included Laser Heated Pedestal Growth and Epitaxial Thin Film Deposition as unconventional growth methods, allowing the synthesis of metastable compositions, solid solutions, etc.
- Critical to the understanding and selection of novel high performance piezoelectric crystals was their characterization, including elastic and domain investigations. Studies of the change of material properties under high E-field and pressure were deemed essential for various device applications.
- New device concepts, beyond electro-mechanical actuators, included electro-optic and elasto-optic applications, whereby the high piezoelectric activity could markedly improve the sensitivity of optical hydrophones for underwater acoustics and for high sensitivity optical modulator, shutters, photorefractive devices, etc.

This report will draw upon published results in the form of appendices, which will be introduced by a brief narrative and summary to highlight achievements and issues. For convenience, the appendices are organized in the focused areas as follows:

1.0 Modeling and Characterization

2.0 Crystal Growth and New Systems

3.0 Thin Film Studies

4.0 Electro-optics

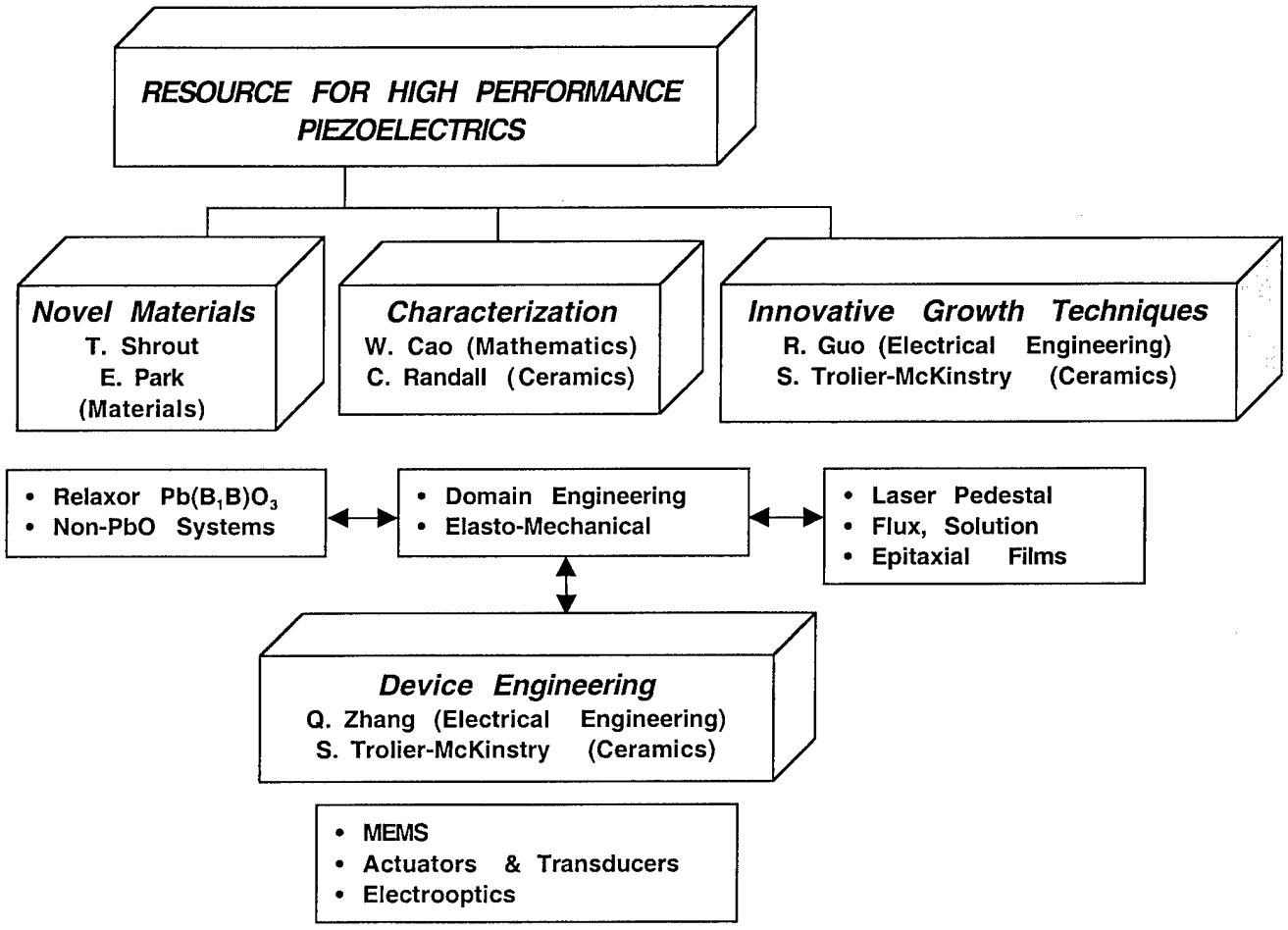

Figure 1. Resource for High Performance Piezoelectrics Program Structure

1.0 Modeling and Characterization

1.1 Electromechanical Properties

Various aspects of electromechanical properties and characterization of Relaxor-PT crystals may be found in nearly every appendix. Specifically, they can be grouped into low field (< 100 V/cm) and high field (>> 1 kV/cm) measurements and as a function of temperature, including issues of domain (in)stability, domain configuration, and macrosymmetry and subsequent role on properties.

In Appendix (1), the full set of elastic, piezoelectric, and dielectric properties were determined for $0.955Pb(Zn_{1/3}Nb_{2/3})O_3–0.045PbTiO_3$ (PZN-4.5%PT) multi-domain single crystals poled along the [100] pseudo-cubic axes. A macrosymmetry of tetragonal 4mm was assumed. The full set of parameters is essential for finite element modeling of device performance. To reduce error, a combined ultrasonic and resonance technique was used. Relatively small samples reduced the influence of chemical inhomogeneity.

The properties for the composition PZN-8%PT is given in Table I. The data presented has yet to be published owing to the variability of properties associated with compositions close to the morphotropic phase boundary.

Following the work on the flux grown PZN-PT crystals above, the full set of properties for $0.67(Pb(Mg_{1/3}Nb_{2/3})O_3–0.33PbTiO_3$ (PMN-33%PT) crystals grown using the Bridgman technique are given in Appendix 2.

For all the systems characterized, large coupling coefficients (k_{33} > 90%) with piezoelectric strain coefficients (d_{33} > 2000 pC/N) were found.

The directional dependence of the electromechanical properties was also reported. It was found that the lateral coupling k_{31} was highest in the [110] direction suggesting that the macrosymmetry was orthorhombic mm2 or lower. It was concluded that the macrosymmetry may be the consequence of the sample geometry and scale relative to the size of the domain.

Table I. Material Properties of PZN-8%PT Single Crystals

Elastic Constants: $c(10^{10}N/m^2)$, $s(10^{-12}m^2/N)$

	c_{12}^E	c_{13}^E	c_{33}^E	c_{44}^E	c_{66}^E
11.1	10.2	9.97	10.2	6.1	6.56
c_{11}^D	c_{12}^D	c_{13}^D	c_{33}^D	c_{44}^D	c_{66}^D
12.6	11.7	7.93	13.0	6.45	6.56
s_{11}^E	s_{12}^E	s_{13}^E	s_{33}^E	s_{44}^E	s_{66}^E
82.0	-29.1	-51.5	110	16.41	5.2
s_{11}^D	s_{12}^D	s_{13}^D	s_{33}^D	s_{441}^D	s_{66}^D
59.0	-52.1	-4.17	12.8	15.5	15.2

Dielectric Constants: $\varepsilon(\varepsilon_0)$, $\beta(10^{-4}/\varepsilon_0)$

ε_{11}^S	ε_{33}^S	ε_{11}^T	ε_{33}^T
2848	579	3012	5689
β_{11}^S	β_{33}^D	β_{11}^T	β_{33}^T
3.51	17.3	3.32	1.76

Piezoelectric Constants: $e(C/m^2)$, $d(10^{-12}$ C/N) $g10^{-3}m^2/C)$ and h $(10^8N/C)$

e_{15}	e_{31}	e_{33}	d_{15}	d_{31}	d_{33}
9.39	-8.84	11.8	154	-1080	2231
g_{15}	g_{31}	g_{33}	h_{15}	h_{31}	h_{33}
5.78	-21.4	43.9	3.73	-17.2	23.1

Density: $\rho = 8.315$ g/cm^3

Electromechanical Coupling Constants:

k_{15}	k_{31}	k_{33}
0.23	0.53	0.94

1.1.1 Cryogenic Poling

Variations in properties reported in crystals that lie in proximity to the morphotropic phase boundary may also be a result of temperature and/or E-field induced phases. As shown in Figure 2, the MPB for PZN-PT is strongly curved with temperature. For rhombohedral compositions, for example, PZN-8%PT, a transformation to tetragonal phase occurs at ~ 80°C. With the application of an E-field, this transformation occurs at relatively low E-fields (< 10 kV/cm), the field required decreasing with increasing temperature. As a result of this instability, conventional poling at elevated temperatures and E-fields resulted in varying levels of induced tetragonality, consequently leading to large levels of hysteresis, as shown in Figure 3. The result is large variation in properties. Consequently, poling at cryogenic temperatures was developed where the crystals are poled at reduced temperature (< –50°C), effectively stabilizing the rhombohedral phase in relation to the MPB and possibility of phase transformation. As shown in Figure 3b, the strain E-field behavior for a cryogenically poled PZN-8%PT crystal

exhibits minimal hysteresis and good linearity, and subsequently little variation in properties between crystals.

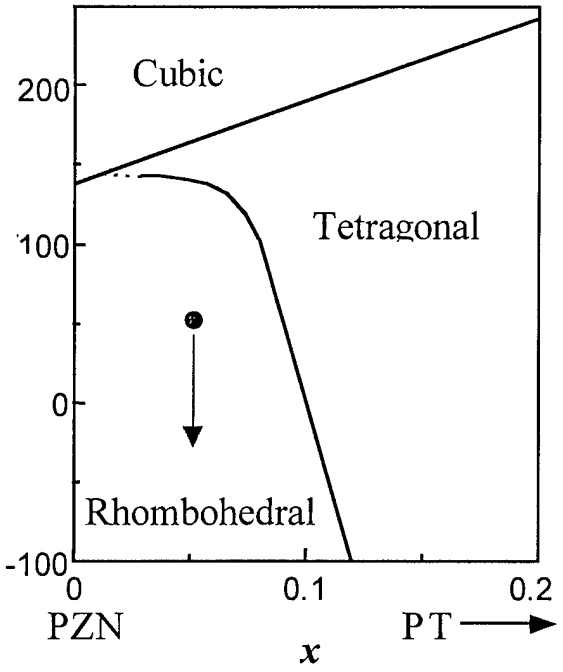

Figure 2. Phase diagram of PZN-PT. Note the strong curvation of the MPB.

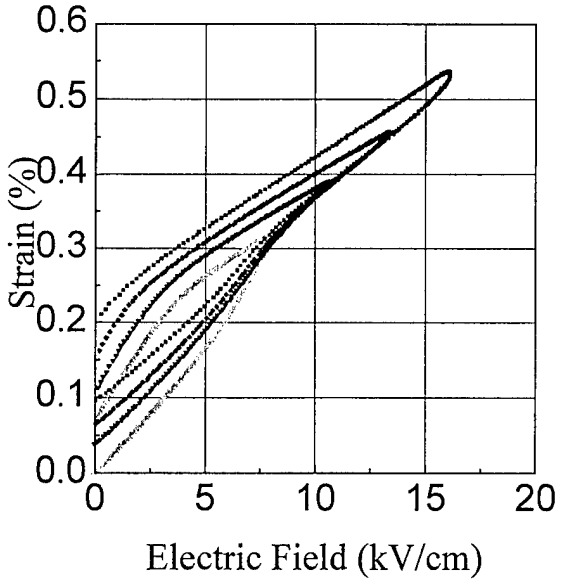

Figure 3a. Room temperature poling of a PZN-8%PT crystal at varying E-field. Note the varying level of hysteresis associated with induced tetragonal phase during poling.

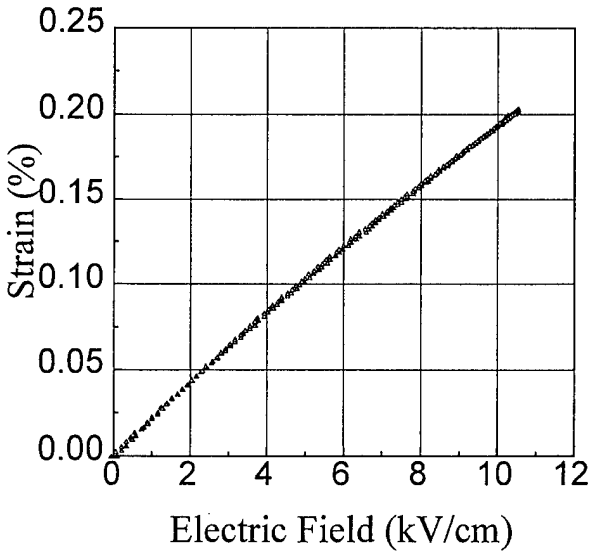

Figure 3b. Cryogenic poling of PZN-8%PT at 70°C. Note the minimal hysteresis and good linearity.

1.1.2 Pulse Poling

In addition to cryogenic poling, the application of various E-field pulses was reported in Appendix 3 to affect the domain structure and subsequent electromechanical properties. The piezoelectric properties were found to increase with increased number of pulses owing to an increase in the density of domain nuclei.

1.2 Domain Studies

Both theoretical and experimental studies carried out to investigate the influence of domains and domain patterns on the crystal properties and given in Appendices 4–8. Strictly speaking, for these domain-engineered crystals, the effective symmetry does not reflect the crystals symmetry but rather the arrangement of domains. While the domain pattern can be easily changed by the boundary conditions, the associated material properties will also change. For example, when sample geometry changes, it implies that the boundary conditions have been changed, which will cause the change of stable domain patterns and eventually cause the effective properties to change. It was also found that the engineered domains can be fairly large in size in many samples and the effective symmetry, i.e., the symmetry of the domain pattern may vary, ranging from monoclinic, orthorhombic to tetragonal, although the underlying crystal structure is rhombohedral. Because of this reason, the resonance technique cannot produce a self-consistent data set because different geometry samples are needed for the measurements and the geometrical difference will cause large uncertainties.

Focusing on the influence of domains, optical observations were analyzed for the possible combinations of domains in a rhombohedral system. A theoretical model was proposed, which takes into account domain interactions in a twin system. It was observed that many different types of domain patterns, including "T"-shaped and "L"-shaped domain walls that connect charged and uncharged domain walls may exist. These types of domain patterns are unique to these single crystal systems. The complex domain patterns also demonstrate that the effective symmetry of the system can be much lower than 4mm, an assumed symmetry in most publications.

1.3 Modeling

Investigations on the origin of the ultrahigh piezoelectricity in the Relaxor-PT crystals along the [001] direction was presented in Appendix 9. Using high energy x-rays, the E-field induced phase transformation in PZN-8%PT was investigated and modeled. Also reported in Appendix 10 is the evidence of a monoclinic phase, as recently found in the PZT system. Though controversial, the existence of a monoclinic phase may be the consequence of strained rhombohedral regions within tetragonal regions.

Further phase transformation studies are given in Appendices 11 and 12, where it was found that PMN-32%PT crystals poled in the <011> direction resulted in a stable orthorhombic phase with interesting piezoelectric properties.

2.0 Crystal Growth and New Systems

2.1 Bridgman Growth

The high temperature flux growth was primarily used for the growth of PZN-PT crystals. Owing to its potential for large crystal growth, the Bridgman technique was investigated for the growth of PMN-PT.

As expected from the high temperature phase diagram PMN-PT, there was a compositional gradient along the length of grain boundaries of PMN-PT, as presented in Figure 4 and tabulated in Table II. Though there was a compositional gradient of ~ 4 mole% $PbTiO_3$, the properties were found to be excellent, as summarized below.

Orientation	k_{33}	S_{33}^E (10^{-12} m^2/N)	d_{33} (pC/N)	K	Freq. Const.
<001>	0.881	41.5	2200	5600	1716

2.2 Laser Heated Pedestal Growth (LHPG)

Single crystals of Zr modified $BaTiO_3$ and PMN-PT were successfully grown by LHPG and reported in Appendices 13 and 14, respectively. The PMN-PT fiber crystals were pyrochlore free with good compositional uniformity, i.e. minimal PbO loss from the surface. Growth rates of greater than 0.3 mm/min were achieved.

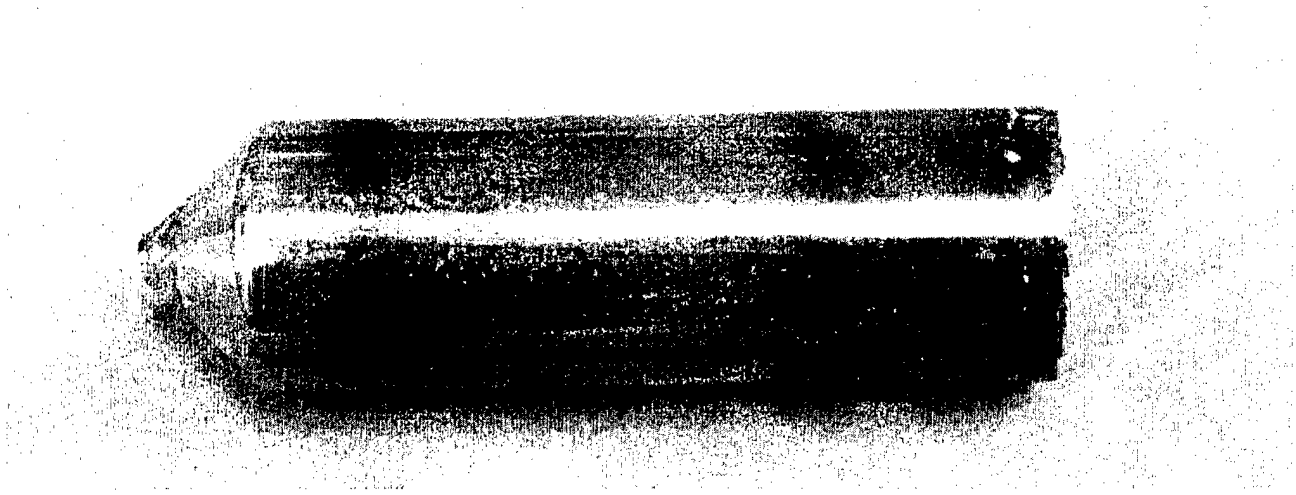

Figure 4. Bridgman grown PMN-PT crystal (3 inches in length). Compositional analysis revealed a 4 mole% $PbTiO_3$ gradient from top to bottom, as reported in Table II.

Table II. Compositional analysis of Bridgman grown PMN-PT.

Location	Color	Mg	Nb	Pb	Ti	O	Mg/Nb	A/B
bottom	dark	4.06	8.40	18.82	6.75	61.97	0.484	0.980
bottom	light	3.93	8.41	18.70	6.26	62.70	0.468	1.006
top	dark	4.17	9.12	20.93	10.46	55.33	0.457	0.881
top	light	3.93	8.89	20.40	8.97	57.80	0.442	0.936

3.0 Thin Film Studies

3.1 Thin Film Synthesis and Characterization

This portion of the work revolved around the growth and properties of relaxor ferroelectric – $PbTiO_3$ perovskites as oriented and epitaxial thin films. In particular, $Pb(Mg_{1/3}Nb_{2/3})O_3$ – 30% $PbTiO_3$ and $Pb(Yb_{1/2}Nb_{1/2})O_3$ – $PbTiO_3$ [PYbN-PT) (60/40) and (50/50) films were prepared by either pulsed laser deposition (PLD) or by sol-gel processing, as presented in Appendices 15 and 16, respectively. Epitaxial PYbN-PT and PMN-PT films were grown on (100) $LaAlO_3$, (100) $SrTiO_3$, and (111) $SrTiO_3$ single crystal substrates by pulsed laser deposition. $SrRuO_3$ was used as an epitaxial bottom electrode. High quality PYbN-PT films

could be grown from PbO-excess targets in the 600-600°C temperature range, with a dynamic O_3/O_2 pressure of 300 mTorr at high growth rates. Most of the films showed room temperature dielectric constants greater than 900 associated with low dielectric losses (~0.03–0.05) and exhibit saturated hysteresis loops with remanent polarizations up to P_r = 40 $\mu C/cm^2$. Fiber textured PMN-PT films were grown on either $Pt/Ti/SiO_2/Si$ or $LaNiO_3/SiO_2/Si$ substrates using sol-gel deposition. Typically, the films showed significant levels of {001} orientation, with rocking curve widths on the order of 3 – 5°. Again, the permittivitites were ~ 1500 at room temperature, and tanδ was ~ 3%. Such films showed broad maxima in the permittivity vs. temperature curves, with T_{max} ~ 120°C. As was the case for epitaxial films of the same composition, the fiber textured films show more dielectric dispersion below T_{max} than is typical for bulk single crystals.

The electromechanical properties, as well as their switching behavior of the resulting films were also studied. In both cases, compositions on the rhombohedral side of the morphotropic phase boundary were chosen in order to investigate the importance of the engineered domain state in thin films.

It was found that for the same thickness, {100} oriented PMN-PT films showed larger piezoelectric coefficients than {111} oriented films. For 1.5 μm thick, {100} oriented films on Si, d_{31} reached values as high as –70 to –80 pC/N, despite the low value for the remanent polarization (PR ~ 10 – 12 $\mu C/cm^2$). It is expected that lowering the residual tensile stress in the film will enable a significant increase in P_R, as well as the piezoelectric response available. Epitaxial films on $LaAlO_3$ perform significantly better, with piezoelectric coefficients approximately twice as high as those for films on Si. By appropriately adjusting the PLD deposition conditions to produce large levels of imprint, the aging rate of the piezoelectric properties could also be adjusted to near zero. Epitaxial PYbN-PT films showed d_{31} * Young's modulus values of ~ –10 to –12 C/m^2, which is the highest reported piezoelectric response in the ferroelectric film literature.

3.2 Fatigue Studies

A particularly significant result in this program was the fatigue behavior in oriented Relaxor-PT films, as reported in Appendices 17–20. In studying the switching behavior of epitaxial $PT/Pb(Yb_{1/2}Nb_{1/2})O_3–PbTiO_3/SrRuO_3/(001)LaAlO_3$ and $Pt/Pb(Yb_{1/2}Nb_{1/2})O_3 – PbTiO_3/$

$SrRuO_3$/ $SrRuO_3$/(111) Sr TiO_3 film stacks, it was found that $\{001\}_p$c rhombohedral thin films showed a much smaller tendency to ferroelectric fatigue on repeated switching than did $\{111\}_{pc}$ films (pc refers to the pseudocubic cell). Little to no decrease in the switchable polarization was noted for $\{001\}_{pc}$ films out to 10^{11} switching cycles. In contrast, $\{111\}_{pc}$ films fatigued normally. It was also seen that the amount of fatigue observed in partially oriented films was proportional to the percentage of non- <001> material. These results are consistent with observations on the orientation dependence of fatigue in bulk single crystals of $Pb(Zn_{1/3}Nb_{2/3})O_3$–$PbTiO_3$. The low fatigue rate, coupled with the high values for the remanent polarization (PR ~ 40 $\mu C/cm^2$), the modest deposition temperatures, and the low imprint rate, suggest that such films may be interesting for application in ferroelectric memories.

4.0 Electro-Optics

The large ferroelectric and ferroelastic responses of the Relaxor-PT crystals, particularly near the morphotropic phase boundary, make these systems potential candidates for a variety of electro-optic (E-O) and acoustic-optic (A-O) devices.

To characterize the crystals, automated scanning laser interferometer, capable of measuring E-O and A-O properties of single crystals over a broad temperature and stress range, was developed with results reported in Appendices 21–24. It was demonstrated that both PZN-PT and PMN-PT single crystals possess very high E-O and A-O responses. For E-O response, r_{33}=180 pm/V and near zero r_{13} were found for PZN-10PT (tetragonal composition) and more importantly, both coefficients are constant over a broad temperature range. r_{33} is about 6 times higher than that in $LiNbO_3$. The A-O response of PZN-PT is the same or even better than those in TeO_2, one of the best A-O crystals current available and most widely used.

5.0 Graduate Students in the Program

Student	Advisor	Student	Advisor
Jianyi Cui	R. Guo	Hanxing Yu	C. Randall
Yu Lu	Q. Zhang	Richard Eitel	T. Shrout/C. Randall
Haifeng Wang	W. Cao	Zhanshan Zhang	S. Trolier-McKinstry
Shumao Xie	W. Cao	Jeong Hwan Park	S. Trolier-McKinstry

6.0 Honors and Awards

- Q. M. Zhang, Outstanding Research Award, College of Engineering, Penn State University, 1999
- S. Trolier-McKinstry
  - Wilson Teaching Award, College of Earth and Mineral Sciences, 2000
  - Faculty Achievement Award – Materials Research Laboratory – 2000
  - Robert Cole Award – American Ceramic Society – 2000
- W. Cao, Best paper award in the category of theory and modeling, ISFD-6, Nanjing, China, May 29–June 2, 2000.

7.0 Papers Published in Refereed Journals

V. Bornand and S. Trolier-McKinstry, "Phase Development in Pulsed Laser Deposited $Pb[Yb_{1/2}Nb_{1/2}]O_3$–$PbTiO_3$ Thin Films," Thin Solid Films, **370** [1-2] 70–77 (2000).

V. Bornand, S. Trolier-McKinstry, K. Takemura, and C.A. Randall, "Orientation Dependence of Fatigue Behavior in Relaxor Ferroelectric – $PbTiO_3$ Thin Films," J. Appl. Phys. **87**(8) 3965–3972 (2000).

V. Bornand, S. Trolier-McKinstry, Structural and Electrical Characterization of Heteroepitaxial $Pb[Yb_{1/2}Nb_{1/2}]O_3$–$PbTiO_3$ Thin Films," J. Appl. Phys. **87**(8) 3958–3964 (2000).

K. Takemura, M. Ozgul, V. Bornand, S. Trolier-McKinstry, and C.A. Randall, "Fatigue Anistropy in Single Crystal $Pb(Zn_{1/3}Nb_{2/3})O_3$–$PbTiO_3$," J. Appl. Phys. **88** (12) 7272–7277 (2000).

M. Ozgul, K. Takemura, S. Trolier-McKinstry, and C.A. Randall, "Polarization Fatigue in PZN-PT Ferroelectric Single Crystals," J. Appl. Phys. **89**(9) 5100–5106 (2001).

V. Ya Shur, E.L. Rumyantsev, E.V. Nikolaeva, E.I. Shishkin, I.S. Baturin, M. Ozgul, and C.A. Randall, "Kinetics of Fatigue Effect," Integrated Ferroelectrics **33** (1-4): 117–132 (2001).

B. Noheda, D. E. Cox, G. Shirane, S.-E. Park, L. E. Cross, and Z. Zhong, "Polarization rotation via a monoclinic phase in the piezoelectric $92\%PbZn_{1/3}Nb_{2/3}O_3$- $8\%PbTiO_3$," Phys. Rev. Lett. **86** [17], 3891 -3894 (2001).

K. Ohwada, K. Hirota, P. Rehrig, P. Gehring, B. Noheda, Y. Fujii, S.–E. Park, and G. Shirane, "Neutron Diffraction Study of the Irreversible R-MA-Mc Phase Transition in Single Crystal Pb[($Zn_{1/3}Nb_{2/3}$)1-xTi_x]O_3," J. of Phys. Soc. Japan **70**[9] (2001).

M. K. Durbin, E. W. Jacobs, J. C. Hicks, S.-E. Park, and T.R. Shrout, "X-Ray Diffraction and Phenomenological Studies of Symmetries in Solid Solutions with Lead Zinc Niobate and Lead Titanate," J. of Appl. Phys. **87** [11], 8159-8164 (2000).

Y. Barad, Yu Lu, Z.-Y. Cheng, S.-E. Park, and Q. M. Zhang, "Composition, temperature, and crystal orientation dependence of the linear electro-optic properties of $Pb(Zn_{1/3}Nb_{2/3})O_3$-$PbTiO_3$ single crystals," Appl. Phys. Lett. **77** [9], 1247-1249 (2000).

P. M. Gehring, S.-E. Park, G. Shirane, "Soft Phonon Anomalies in the Relaxor Ferroelectric Pb[($Zn_{1/3}Nb_{2/3}$)0.92Ti0.08]O_3," Physical Review Letter **84** [22], 5216–5219 (2000).

T. Ritter, K. K. Shung, X. Geng, P. D. Lopath, S.-E. Park and T. R. Shrout, "Single crystal PZN/PT-polymer composite for ultrasound transducer applications," IEEE Trans. on Ultrasonics, Ferroelectric and Frequency Control Special Issue on Ultrasonic Transducers **47** [4], 792-800 (2000).

P. W. Rehrig, S. Trolier-McKinstry, S.-E. Park, and G. L. Messing, "Dielectric and Electromechanical Properties of Barium Titanate Single Crystals Grown by Templated Grain Growth," IEEE Trans. on Ultrasonics, Ferroelectric and Frequency Control Special Issue on Ultrasonic Transducers **47** [4], 895-901 (2000)

S.-E. Park, S. Wada, L. E. Cross, and T. R. Shrout, "Crystallographically engineered $BaTiO_3$ crystals for high performance piezoelectrics," J. of Appl. Phys., **86** [5], 2746-2750 (1999).

S. Wada, S. Suzuki, T. Noma, T. Suzuki, M. Osada, M. Kakihana, S.-E. Park, L. E. Cross, T. R. Shrout, "Enhanced Piezoelectric Property of Barium Titanate Single Crystals with Engineered Domain Configurations," Jap. J. Appl. Phys. **38**, 5505-5511 (1999).

S. Wada, S.–E. Park, L.E. Cross, and T.R. Shrout, "Engineered Domain Configuration in Rhombohedral PZN-PT Crystals and Their Ferroelectric Related Properties," Ferroelectrics **221**: (1-4) 147–155 (1999).

Y. Barad, Yu Lu, Z.Y. Cheng, S.–E. Park, and Q.M. Zhang, "Composition, Temperature, and Crystal Orientation Dependence of Linear Electro-optic Properties of PZN-PT Single Crystals," Appl. Phys. Lett. **77**, 1247–1249 (2000).

Yu Lu, Z.-Y. Cheng, S.-E. Park, S.-F. Liu, and Q. M. Zhang, "Linear Electro-optic Effect of $0.88Pb(Zn_{1/3}Nb_{2/3})O_3$-$0.12PbTiO_3$ single Crystal," Jap. J. Appl. Phy., **39** 141 –145 (2000).

Shizuo Yin, Q.M. Zhang, K .–W. Chung, R. Yang, Z.Y. Cheng, and Yu Lu, "Investigation of the Electro-optic Properties of Electron-irradiated P(VDF-TrFE) Copolymer," Opt. Eng. **39** 670–672 (2000).

Yu Lu, D.–Y. Jeong, Z.Y. Cheng, Q.M. Zhang, H. Luo, Z. Yin, and D. Viehland," Phase Transitional Behavior and Piezoelectric Properties of the Orthorhombic Phase of PMN-PT Single Crystals," Appl. Phys. Lett. **78** 3109 (2001).

Y. Lu, Z.–Y. Cheng, Y. Barad, and Q.M. Zhang, "Photoelastic Effects in the Tetragonal PZN-PT Single Crystals Near the Morphotropic Phase Boundary," J. Appl. Phys. **89** 5075 (2001).

Y. Lu, Z.–Y. Cheng, D.–J. Jeong, T. Shrout, and Q.M. Zhang, "Phase Stability of "Morphotropic" Phases in PZN-PT Single Crystals," submitted to Appl. Phys. Lett. (2001).

M. K. Durbin, E. W. Jacobs, J. C. Hicks, and S.-E. Park, "In-situ X-Ray Diffraction Study of High Strain Single Crystal Relaxor Ferroelectric Materials," Applied Physics Letter, **74** [19], 2848-2850 (1999).

D.-S. Paik, S.-E. Park, S. Wada, S.-F. Liu, and T. R. Shrout, "E-field Induced Phase Transition of <001> Oriented Rhombohedral $0.92Pb(Zn_{1/3}Nb_{2/3})O_3$-$0.08PbTiO_3$ Crystals," Journal of Applied Physics, **85** [2], 1080-1083 (1999).

S. Wada, S.-E. Park, L. E. Cross, and T. R. Shrout, "Defect-Induced Domain Configuration in Relaxor PZn Single Crystal and its Origin," Transactions of the Materials Research Society of Japan, **24** [1], 19-22 (1999).

S.–E. Park, T.R. Shrout, P. Bridenbaugh, J. Rottenberg, and G. Loiacono, "Electric-field Induced Anisotropy in Electrostrictive $Pb(Mg_{1/3}Nb_{2/3})O_3$–$PbTiO_3$ Crystals," Ferroelectrics **207** 519–526 (1998).

Jirí Erhart and W. Cao, "Effective Material Properties in Twinned Ferroelectric Crystals", J. Appl. Phys., vol. **86**, pp. 1073- 1081 (1999).

J.H. Yin, B. Jiang and W. Cao, "Elastic, Piezoelectric and Dielectric Properties of $0.955Pb(Zn_{1/3}Nb_{2/3})\ O_3$-$0.045PbTiO_3$ Single Crystal with Designed Multi-domains", IEEE Transactions UFFC. vol. **47**, pp. 285-291 (2000).

J.H. Yin, and W. Cao, "Domain Configurations in Domain-Engineered 0.955Pb($Zn_{1/3}Nb_{2/3}$)O_3-0.045$PbTiO_3$ Single Crystals", J. Appl. Phys, vol. **87**, pp. 7438-7441 (2000).

J. Erhart and W. Cao, "Effective Symmetry and Physical Properties of Twinned Perovskite Ferroelectric Single Crystals", J. Mater. Res. vol. **16**, pp.570-577 (2001).

J.H. Yin, and W. Cao, " Observation and Analysis of Domain Configuration Domain Engineered PZN-PT Single Crystals", Ferroelectrics, Vol. **251**, (No 1-4) pp93-100 (2001).

R. Ahluwalia and W. Cao, "Effect of Defect Induced Nucleation and Growth on Switching Behavior in Ferroelectrics", Vol. **251** pp191-198 (2001).

Rajeev Ahluwalia and Wenwu Cao, "Size Dependence of Domain Patterns in a Ferroelectric system with a surface dead layer". J. Appl. Phys., vol. **89**, 8105-8110 (2001).

Rui Zhang, Bei Jiang and Wenwu Cao, "Elastic, piezoelectric and dielectric properties of multi-domain 0.67Pb($Mg_{1/3}Nb_{2/3}$)O_3-0.33$PbTiO_3$ single crystal", J. Appl. Phys., vol. **90**, pp3471-3475 (2001).

Yu Zhi, R. Guo, A.S. Bhalla, Ba($Ti_{1-x}Zr_x$)O_3 (x=0.15 and 0.20) Single Crystals Grown by LHPG Technique, Ceramic Transactions, ed. K.M. Nair, ACerS, Westerville, OH, **106,** 185-192 (2000).

Yu Zhi, R. Guo, A.S. Bhalla, Dielectric Behavior of Ba($Ti_{1-x}Zr_x$)O_3 Single Crystals, J. Appl. Phys. **88**(1), 410-415, (2000).

Yu Zhi, R. Guo, A.S. Bhalla, Ferroelectric and Piezoelectric Properties of Ba($Ti_{1-x}Zr_x$)O_3 Single Crystals, Ferroelectrics (accepted 2000).

Yu Zhi, Ruyan Guo, A.S. Bhalla, Growth of Ba($Ti_{1-x}Zr_x$)O_3 Single Crystal Fibers by Laser Heated Pedestal Growth Technique, Ferroelectric Letters **27**(5/6), 113-123, (2000).

Yu Zhi, Ruyan Guo, A.S. Bhalla, Orientation Dependence of the Ferroelectric and Piezoelectric Behavior of Ba(Ti1-xZrx)O3 Single Crystals, Appl. Phys. Lett. **77**(10), 1535-1537, (2000).

Yu Zhi, Ruyan Guo, A.S. Bhalla, Growth of Ba($Ti_{1-x}Zr_x$)O_3 Single Crystals by Laser Heated Pedestal Growth Technique, J. Crystal Growth, (in printing, 2001)

Jianyi Cui, "Growth and Characterization of Lead-Containing Perovskite Single Crystal Fibers by Laser Heated Pedestal Growth Technique," pp. 104, M.S. Thesis, Penn State University, Dec. 2000.

Jianyi Cui, Ruyan Guo and Amar Bhalla, "Growth and Characterization of Lead Magnesium Niobate – Lead Titanate by the Laser Heated Pedestal Growth Technique", J. Crystal Growth (submitted, 2001).

Y.H. Bing, Jianyi Cui, Ruyan Guo and Amar Bhalla, "PMN-PT single crystals grown by a traveling flux LHPG method" (in preparation, 2001).

Y.H. Bing, R. Guo and A.S. Bhalla, "Optical Properties of Relaxor Ferroelectric Crystal: $Pb(Zn_{1/3}Nb_{2/3})O_3$-4.5%$PbTiO_3$," Ferroelectrics **242**(1-4), 1-11, (2000).

Yonghong Bing, R. Guo, A.S. Bhalla, "Optical Indices and Polarization Properties of Relaxor Ferroelectric $Pb(Zn_{1/3}Nb_{2/3})O_3$-$PbTiO_3$ Single Crystal of Near MPB Composition," Ferroelectrics (Asia Meetings on Ferroelectrics AMF-III) (in printing 2001).

Ruyan Guo, Effect of electric boundary conditions on thermal strain behavior of PZN-PT single crystals, Ceramic Transactions, ACerS, Westerville, OH (accepted 2000).

S. Gupta, R.S. Katiyar, R. Guo, A. Bhalla, Study of Structural Phase Transitions in Solid-Solution (1-x)PZN-xPT Relaxor Ferroelectric Using Raman Scattering, J. Raman Spectrosc. **31**(10), 921-924 (2000).

S. Gupta, R.S. Katiyar, R. Guo, and A.S. Bhalla, Polarized Raman Spectroscopy Study of Phase Transitions in 0.915$Pb(Zn_{1/3}Nb_{2/3})O_3$-0.085$PbTiO_3$ Relaxor Ferroelectric Single Crystals, Ferroelectrics Letters **27**(1-2), 39-48 (2000).

S. Gupta, R.S. Katiyar, R. Guo, A. Bhalla, Micro-Raman Study of Self-Assembled Nanostrctures: (1-x)PZN:xPT Solid Solution, Materials Research Society Symp. Proc., 581(Nanophase and Nanocomposite Materials III), 529-534 (2000).

P.S. Dobal, A. Dixit, R.S. Katiyar, Z. Yu, R. Guo, A.S. Bhalla, Phase Transition Behavior of $BaZr_xTi_{1-x}O_3$ Ceramics, J. Raman Spectrosc. **32**(1), 69-71 (2001).

P.S. Dobal, A. Dixit, Z. Yu, R. Guo, A.S. Bhalla, R. S. Katiyar, Micro-Raman Scattering and Dielectric Investigations of Phase Transition Behavior in $BaTiO_3$-$BaZrO_3$ System, J. Appl. Phys. (submitted 2001).

R. Guo, L.E. Cross, S-E. Park, B. Noheda, D.E. Cox, G. Shirane, Origin of the high piezoelectric response in $PbZr_{1-x}Ti_xO_3$, Phys. Rev. Letters, **84(23),** 5423-5426 (2000).

B. Noheda, J.A. Gonzalo, L.E. Cross, R. Guo, S-E. Park, D.E. Cox, G. Shirane, Tetragonal-to-Monoclinic Phase Transition in a Ferroelectric Perovskite: the Structure of $PbZr_{0.52}Ti_{0.48}O_3$, Phys. Rev. B, **61(13),** 8687-8689 (2000).

B. Noheda, J.A. Gonzalo, R.Guo, S.-E. Park, L.E. Cross, D.E. Cox, G. Shirane, The Monoclinic Phase in PZT: new light on morphotropic phase boundaries, AIP Conf. Proc. (Fundamental Physics of Ferroelectrics 2000), 535, 304-313, (2000).

B. Noheda, D.E. Cox, G. Shirane, R. Guo, B. Jones, L.E. Cross, Stability of the monoclinic phase in the ferroelectric perovskite $PbZr_{1-x}Ti_xO_3$, Los Alamos Natl. Lab., Prepr. Arch., Condens. Matter, arXiv:cond-mat/0006152, 1-8, (2000).

B. Noheda, J.A. Gonzalo, R.Guo, S.-E. Park, L.E. Cross, D.E. Cox, G. Shirane, The monoclinic phase in PZT: new light on morphotropic boundaries, Los Alamos Natl. Lab., Prepr. Arch., Condens. Matter, arXiv:cond-mat/0002409, 1-5 (2000).

B. Noheda, D.E. Cox, G. Shirane, R. Guo, B. Jones, L.E. Cross, Stability of the monoclinic phase in the ferroelectric perovskite $PbZr(1-x)Ti_xO_3$, Phys. Rev. B: Condens. Matter Mater. Phys. **63**(1), 014103/1-014103/9, (2001).

Ceramic Transactions: Electronic Ceramic Materials and Devices, Editors, K.M. Nair, Amar Bhalla, American Ceramic Society, Westerville, OH,106, pp.554 (2000).

A. S. Bhalla, R. Guo, Rustum Roy, "The Perovskite Structure - A Review of Its Role in Ceramic Science and Technology," Mat. Res. Innovat. **4**(1), 3-26, (2000).

Perovskite oxides for electronic, energy conversion, and energy efficiency applications, Editors, Winnie Wong-Ng, T. Holesinger, G. Riley, Ruyan Guo, Ceram. Trans., Publisher: (American Ceramic Soc, Westerville, Ohio), 104, pp.284, (2000).

Rustum Roy, R. Guo and A.S. Bhalla, Perovskite - Lessons from its History and Its Crystal Chemistry, (Review) Ceramic Transactions, ACerS, Westerville, OH, 104, 3-39, (2000).

Optoelectronic Materials and Technology in the Information Age, Editors Ruyan Guo et. al, Ceramic Transactions, ACerS, Westerville, OH (in printing, 2001).

Edward Alberta, R. Guo and A.S. Bhalla, Structure-Property Diagrams of Ferroic Solid Solutions. Part I: Perovskite Relaxor Ferroelectrics with Morphotropic Phase Boundaries, (Review/Monograph) Ferroelectric Review, V.4 (1-4) (in printing 2001).

8.0 Patents

Q.M. Zhang, Yaniv Barad, Yu Lu, and A.Y. Cheng, "PZN-PT and PMN-PT Single Crystal Electro-optic Devices," filed (2000).

9.0 Commercialization and Technology Transfer

There has been interest from Geospace Corporation and Northrop Grumman Corporation in utilizing the relaxor ferroelectric – $PbTiO_3$ films for fast rf MEMS switches. An SBIR phase II program on PZT films for these applications is currently in negotiation. If it comes through, then Northrop Grumman is planning on committing internal money to prototype a faster switch with PYbN-PT.

There is some interest from Wilcoxen Research Corporation on using PYbN-PT or PMN-PT films in MEMS accelerometers to improve the sensitivity.

Appendix 1

Jinhua Yin, Bei Jiang, and Wenwu Cao, "Elastic, Piezoelectric, and Dielectric Properties of $0.955Pb(Zn_{1/3}Nb_{2/3})O_3$–$0.045PbTiO_3$ Single Crystal with Designed Multidomains," IEEE Trans. on Ultrasonics, Ferroelectrics, and Frequency Control, , Vol. 47, No. 1, 285–291 (January 2000).

Elastic, Piezoelectric, and Dielectric Properties of $0.955Pb(Zn_{1/3}Nb_{2/3})O_3$-$0.045PbTiO_3$ Single Crystal with Designed Multidomains

Jianhua Yin, Bei Jiang, and Wenwu Cao

Abstract—**The elastic, piezoelectric, and dielectric properties of a $0.955Pb(Zn_{1/3}Nb_{2/3})O_3$-$0.045PbTiO_3$ (PZN-4.5%PT) multi-domain single crystal, poled along [001] of the original cubic direction, have been determined experimentally using combined resonance and ultrasonic methods. At room temperature, the PZN-4.5%PT single crystal has rhombohedral symmetry. After being poled along [001], four degenerate states still remain. Statistically, such a domain-engineered crystal may be treated as having an average tetragonal symmetry, and its material constants were determined based on 4 mm symmetry. It was confirmed that the electromechanical coupling coefficient k_{33} for the domain-engineered samples is >90%, and the piezoelectric constant d_{33} is >2000 pC/N. A soft shear mode with a velocity of 700 m/s was found in the [110] direction. From the measured experimental data, the orientational dependence of phase velocities and electromechanical coupling coefficients was calculated. The results showed that the transverse and longitudinal coupling coefficients, k_{31} and k_{33}, reach their maximum along [110] and [001], respectively.**

I. Introduction

ALTHOUGH early work on $Pb(Zn_{1/3}Nb_{2/3})O_3$-$PbTiO_3$ (PZN-PT) solid solution system can be dated back to the 1960s [1], [2], it was not until very recently that this relaxor-based ferroelectric single crystal system has generated a great deal of attention. It was found that the single crystal system exhibits an extraordinary large electromechanical coupling coefficient k_{33} (>90%) and piezoelectric coefficient d_{33} (>2000 pC/N) at room temperature after being poled in [001], which is off the polarization direction of <111> [3]–[5]. Considering that the best piezoelectric materials used today, the modified $Pb(Zr_xTi_{1-x})O_3$(PZT), only has k_{33} of 75% and d_{33} of 700 pC/N, the new system shows a promising potential to produce higher sensitivity ultrasonic transducers with superior broadband characteristics [6], large strain actuators, and other electromechanical devices.

The physical mechanism of this multidomain system is still unclear at the moment. The lack of complete physical property data is the main hindrance for theoretical studies.

Manuscript received August 13, 1999; accepted October 7, 1999. This research was sponsored by the Office of Naval Research under Grant #N00014-98-1-0527 and the National Institutes of Health under Grant #P41 RR11795-01A1.

The authors are with the Material Research Laboratory, The Pennsylvania State University, University Park, PA 16802 (e-mail: cao@math.psu.edu).

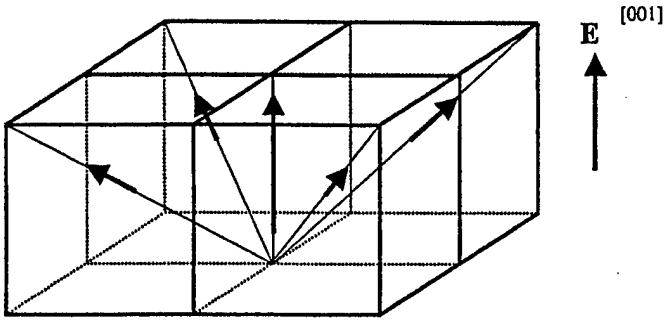

Fig. 1. Possible domain configuration and associated polarization orientation in a PZN-4.5%PT single crystal after being poled in [001] direction.

Practically, it is also very important to have a complete set of elastic, piezoelectric, and dielectric constants available. At present, only one electromechanical coupling coefficient k_{33} and one piezoelectric coefficient d_{33} have been reported [3]–[5]. The aim of this paper is to provide a complete set of such data for the PZN-4.5%PT domain-engineered single crystal. These data were obtained by using a combined method involving both pulse-echo and impedance resonance techniques.

Above 150°C, the crystal PZN-4.5%PT has a cubic perovskite structure with symmetry $m\bar{3}m$ but becomes a rhombohedral ferroelectric phase with 3m symmetry below the phase transition temperature [5]. When an electric poling field along [001] of the original cubic axis is applied to the crystal, a multidomain configuration can be produced (as shown in Fig. 1) consisting of four degenerate states and charged domain walls [5]. For convenience, the coordinate systems used for the orientations in this paper are all based on the high temperature cubic phase. Statistically, the poled system should have a pseudo-tetragonal 4 mm macroscopic symmetry, although the microscopic symmetry of the system is 3m [5]. Our measured material properties presented in this paper are based on this 4 mm symmetry. There are total of 11 independent physical constants describing the elasto-piezo-dielectric matrices for the 4 mm symmetry [7].

The dielectric constants ε_{11}^T and ε_{33}^T were calculated from the low frequency capacitance using the parallel capacitor approximation. Two of the elastic compliances, s_{11}^E and s_{33}^D, and the two electromechanical coupling coefficients, k_{33} and k_{31}, were calculated from the resonance and antiresonance frequencies of the length-extensional modes

of long vibration bars. Another five elastic constants (c_{11}^E, c_{12}^E, c_{44}^E, c_{66}^E, and c_{44}^D) were determined from the measurements of phase velocities of ultrasonic waves propagating along certain orientations. Using this measurement scheme, the only samples needed are those with the orientations of [001]/[010]/[100] and [001]/[110]/[1$\bar{1}$0]. Thus, fewer samples are required when using this combined measurement technique [8].

For each given wave propagation direction, the relationship between the phase velocity and associated material constants can be obtained by solving the Christoffel wave equations [9], and these velocities can be measured using the pulse-echo technique [7].

II. Experimental Procedure

The impedance resonance method and ultrasonic pulse-echo technique, described in the IEEE standards on piezoelectricity [7], are often used to characterize material properties for piezoelectric materials [10], [11]. Theoretically, all independent elastic, piezoelectric, and dielectric constants for any crystal symmetry can be determined either by the resonance method or by the ultrasonic method, provided there are sufficient numbers of differently oriented samples. In reality, however, for materials of lower symmetry, some geometries for resonance measurements are difficult to prepare, especially when the available crystal is too small to make large aspect ratio resonators. On the other hand, because the ultrasonic technique can only measure certain elastic constants through the measurement of phase velocities, large errors can be introduced for derived material constants that are not related to pure modes. High acoustic attenuation of certain modes may also damp the propagation of ultrasonic waves in certain directions so that a complete set of material constants for low symmetry systems is also difficult to obtain using the ultrasonic method alone. In this work, we have selected only those simple pure modes in each method and combine the measured data to minimize errors in the results.

In the ferroelectric phase, the dipole in each unit cell of the PZN-4.5%PT crystal is along one of the eight <111> directions. It has been shown experimentally that the crystal can hold a macroscopic polarization only when the electric field is applied along one of the six <100> directions[3], [4]. After the application of a poling electric field along [001], there are still four remaining degenerate dipole orientations. Such a poling field creates a multidomain structure with strong elastic interaction among the existing domains. Statistically, the four remaining domains have an equal possibility to form so that the global macroscopic symmetry has been assumed as 4 mm in all previous studies [5].

The as-grown crystals were first orientated using the Laue method with an accuracy of $\pm 0.5°$. Then, each sample was cut and polished into a rectangular parallelepiped shape with three pairs of parallel surfaces. Gold electrodes were sputtered on to the [001] and [00$\bar{1}$] faces of each sample, and an external electric field of 1.0 to 1.5 MV/m was applied at room temperature to pole the sample. The final dimensions of the samples used for the ultrasonic measurements were about $3 \times 3 \times 1$ mm^3. For the length-extensional resonance measurements, the aspect ratio of the sample exceeded 5:1 to yield nearly pure resonance modes [7]. Several sets of samples were prepared for a consistency check. For the bar samples used in the resonance measurements, different aspect ratios were fabricated to ensure purity of the modes. In addition to samples with [001]/[010]/[100] and [001]/[110]/[1$\bar{1}$0] orientations, a resonance bar with its long dimension in [110] and thickness in [001] was also made to verify the anisotropy calculations.

A 15-MHz longitudinal wave transducer (Ultran Laboratories, Inc., Boalsburg, PA) and a 20-MHz shear wave transducer (Panametrics, Waltham, MA) were used for the pulse-echo measurements. The electric pulses used to excite the transducer were generated by a Panametrics 200-MHz pulser/receiver, and the time of flight between echoes was measured by using a Tektronix 460A digital oscilloscope.

For the length-extensional resonance measurements, a HP 4194A impedance/gain-phase analyzer was employed. The resonance and antiresonance frequencies corresponding to the minimum and maximum values of the impedance-frequency spectrum were obtained and used to calculate the corresponding electromechanical coupling coefficients and elastic compliance.

The dielectric measurements were carried out at 1 kHz using a Stanford Research System SR715 LCR Meter.

III. Results and Analyses

Table I lists the measured phase velocities of the longitudinal and shear waves propagating along different crystal orientations in the domain engineered PZN-4.5%PT single crystals. The measured longitudinal electromechanical coupling coefficient k_{33}, the transverse coupling coefficient k_{31} in [110] and [100] directions, and the frequency constants $2lf_r$ and $2lf_a$ for the resonance bars are given in Table II. Here l is the length of the resonance bar, and f_r and f_a are the resonance and antiresonance frequencies, respectively, obtained from the electrical impedance spectrum. The lateral coupling coefficient k_{31} is different when the long dimension is along [001] or [110] for this system because of the anisotropy of the crystal. For comparison, the coupling coefficients and the frequency constants of PZT-5H, $BaTiO_3$ ceramic, and $BaTiO_3$ crystal are also listed in Table II. The coupling coefficients, k_{33} and k_{31}, of PZT-5H and of $BaTiO_3$ were directly taken from [12], but the other constants of these three materials were calculated using the data from the same source. The relationship between the measured phase velocities and related elastic constants were derived from the Christoffel wave equations and listed in Table III. Using the four sets of piezoelectric constitutive equations [7], a complete set of elastic, piezoelectric, and dielectric constants of a PZN-

TABLE I

MEASURED PHASE VELOCITIES (M/S) OF ULTRASONIC WAVES IN A PZN-4.5%PT CRYSTAL POLED IN [001].

$v_l^{[001]}$	$v_s^{[001]}$	$v_l^{[100]}$	$v_{s\perp}^{[100]}$	$v_{s\parallel}^{[100]}$	$v_l^{[110]}$	$v_{s\perp}^{[110]}$	$v_{s\parallel}^{[110]}$
4110	2777	3656	2755	2853	4618	668	2855

TABLE II

MEASURED ELECTROMECHANICAL COUPLING COEFFICIENTS AND FREQUENCY CONSTANTS FOR PZN-4.5%PT CRYSTAL POLED IN [001] COMPARED WITH PZT-5H AND $BaTiO_3$.[1]

	$k_{31}^{[110]}$	$2lf_r$	$k_{31}^{[100]}$	$2lf_r$	k_{33}	$2lf_a$	k_t	$2lf_a$
PZN-%4.5PT	0.80	2300	0.50	1210	0.90	2414	0.50	4102
$BaTiO_3$,crystal[2]	0.40	5729	0.32	4542	0.56	3926	0.29	5452
$BaTiO_3$,ceramic[2]	0.21	4391	0.21	4391	0.50	4971	0.43	5477
PZT-5H[2]	0.39	2843	0.39	2843	0.75	3851	0.60	4575

[1] Unit for frequency constant = Hertz · meter.
[2] k_{31} [001] and k_{33} are from [12]. Others are calculated from the material constants in [12].

TABLE III

THE RELATIONSHIPS BETWEEN PHASE VELOCITIES AND ELASTIC CONSTANTS.

	$v_l^{[001]}$	$v_s^{[001]}$	$v_l^{[100]}$	$v_{s\perp}^{[100]}$	$v_{s\parallel}^{[100]}$	$v_l^{[110]}$	$v_{s\perp}^{[110]}$	$v_{s\parallel}^{[110]}$
$\rho v^2 =$	c_{33}^D	c_{44}^E	c_{11}^E	c_{66}^E	c_{44}^D	$\frac{1}{2}\left(c_{11}^E + c_{12}^E + 2c_{66}^E\right)$	$\frac{1}{2}\left(c_{11}^E - c_{12}^E\right)$	c_{44}^D

TABLE IV

MEASURED AND DERIVED MATERIAL PROPERTIES OF PZN-4.5%PT SINGLE CRYSTAL POLED ALONG [001].[1]

Elastic constants: c_{ij} (10^{10}N/m^2)

c_{11}^{E*}	c_{12}^E	c_{13}^E	c_{33}^E	c_{44}^{E*}	c_{66}^{E*}	c_{11}^D	c_{12}^D	c_{13}^D	c_{33}^{D*}	c_{44}^{D*}	c_{66}^D
11.1	10.2	10.1	10.5	6.4	6.3	11.3	10.4	9.5	13.5	6.7	6.3
±0.15	±0.16	±0.15	±0.3	±0.05	±0.05	±0.15	±0.15	±0.35	±0.5	±0.05	±0.05

Elastic constants: s_{ij} (10^{-12}m^2/N)

s_{11}^{E*}	s_{12}^E	s_{13}^E	s_{33}^E	s_{44}^E	s_{66}^E	s_{11}^D	s_{12}^D	s_{13}^D	s_{33}^{D*}	s_{44}^D	s_{66}^D
82.0	−28.5	−51.0	108	15.6	15.9	61.5	−49.0	−9.0	20.6	14.9	15.9
±3.2	±0.9	±0.8	±0.5	±0.12	±0.18	±0.8	±0.1	±0.5	±0.8	±0.1	±0.18

Piezoelectric constants: e (C/m^2), d (10^{-12}C/N), g (10^{-3} Vm/N), h (10^8V/m)

e_{15}	e_{31}	e_{33}	d_{15}	d_{31}	d_{33}	g_{15}	g_{31}	g_{33}	h_{15}	h_{31}	h_{33}
8.9	−3.7	15.0	140	−970	2000	5.0	−21.0	44	3.4	−4.3	17
±0.9	±1.6	±1.6	±16	±19	±75	±0.58	±0.4	±0.8	±0.4	±2.0	±1.7

Dielectric constants: ε (ε_0), β ($10^{-4}/\varepsilon_0$) Coupling constants

ε_{11}^S	ε_{33}^S	ε_{11}^{T*}	ε_{33}^{T*}	β_{11}^S	β_{33}^S	β_{11}^T	β_{33}^T	k_{15}	k_{31}^*	k_{33}^*	k_t^*
3000	1000	3100	5200	3.4	10.0	3.2	1.9	0.23	0.50	0.91	0.50
±110	±45	±120	±200	±0.1	±0.5	±0.1	±0.05	±0.02	±0.01	±0.01	±0.01

[1] Density: $\rho = 8310$ kg/m^3.

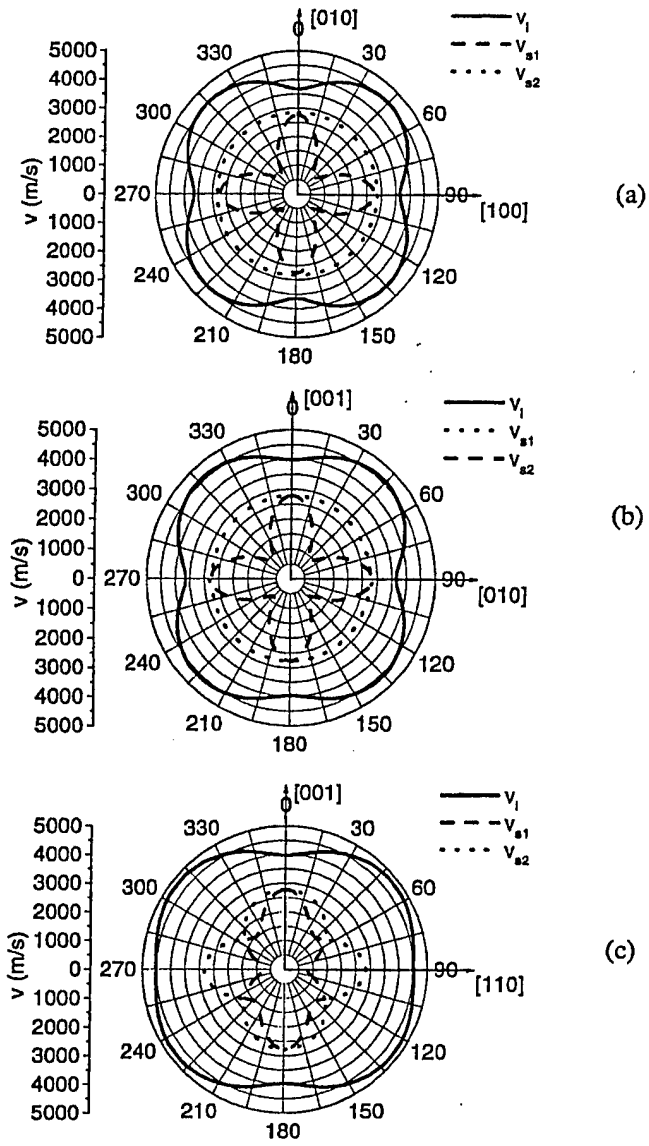

Fig. 2. Directional dependence of the longitudinal velocity, v_l, and the two shear velocities, v_{s1} and v_{s2} in a) the [100] and [010] plane, b) the [010] and [001] plane, and c) the [110] and [001] plane.

4.5%PT crystal based on the 4 mm symmetry has been derived and is given in Table IV. The independent material constants marked with a star (*) in Table IV were measured directly; the other constants in Table IV were derived using the constitutive relations.

Our experimental results confirmed the extraordinarily large room temperature electromechanical coupling coefficient, $k_{33} > 90\%$, and piezoelectric constant, $d_{33} > 2000$ pC/N, reported earlier [3]. More importantly, we have provided a complete set of material constants for this PZN-4.5%PT domain-engineered single crystal, which can be used to perform theoretical analysis and device designs. A very slow shear wave with a sound velocity of only 700 m/s propagating in [110] and polarized in $[1\bar{1}0]$ was observed, which implies that a "soft transverse acoustic mode" exists in this domain-engineered single crystal system.

IV. Error Analysis

The errors in these measured material constants come from the following sources: 1) the use of parallel plate capacitor approximation for dielectric measurements, 2) errors in measuring the time of flight between ultrasonic echoes, 3) errors in the measurements of resonance and antiresonance frequencies and sample thickness, 4) misorientation and imperfect parallelness of sample surfaces, 5) inconsistency between different samples, and 6) numerical errors for calculating those derived constants. We have analyzed each error source to provide an estimate for the measurement errors.

Using a 15-MHz longitudinal transducer, we have quantified the error for measuring the sound velocity to be <1% for sample with thickness >2 mm. The error in the capacitance measurement is about 4%. Error from misorientation is <1% if the misorientation is <2° as analyzed subsequently. The largest error comes from the inconsistency of different samples because the properties of each sample depend strongly on the domain pattern; the domain pattern is controlled by the geometry of the sample and the poling process. This error was minimized through an oversampling scheme in the measurements.

Table V shows the velocities from several measurements in differently orientated samples. One can see that the difference among the measured velocities is <1%. However, because the measured coupling coefficients vary from 1 to 3%, the error of the calculated coefficient $s_{33}^E = s_{33}^D/(1-k_{33}^2)$ [7] can be very large. This can be seen from the relative error of s_{33}^E caused by the error of k_{33}:

$$\left|\frac{\delta s_{33}^E}{s_{33}^E}\right| = \left|\frac{2k_{33}\delta k_{33}}{(1-k_{33}^2)}\right|. \quad (1)$$

When k_{33} reaches > 90%, the relative error of s_{33}^E calculated from this formula will be an order of magnitude larger than that of k_{33}. For instance, if k_{33} is 0.90 with a relative error of 1%, the relative error for s_{33}^E calculated from (1) will be >10%.

Table VI gives the changes of some constants caused by a 1% change in the coupling coefficient k_{33}. Table VII lists the measured results of the length-extension modes from samples of different aspect ratios. For this system, the aspect ratio (length/width) effects come not only from the influence of mode pureness as stated in [13], but also from the change of the domain patterns. It was found that the coupling coefficient decreases if the aspect ratio decreases, but the frequency constant increases for smaller aspect ratios.

V. Anisotropy Study

Unlike $Pb(Zr,Ti)O_3$ ceramic samples, domain-engineered PZN-4.5%PT single crystals are anisotropic in the plane perpendicular to the poling direction. Therefore, an analysis of the directional dependence of phase velocities and

TABLE V

MEASURED PHASE VELOCITIES (M/S) OF ULTRASOUND WAVES IN A POLED PZN-4.5%PT CRYSTAL POLED ALONG [001]. THE LEFT COLUMN REPRESENTS THE NUMBER OF MEASUREMENTS. (NOTE: DATA IN THE SAME ROW DOES NOT NECESSARILY MEAN THEY ARE FROM THE SAME SAMPLE.)

Measurements (no.)	$v_l^{[001]}$	$v_s^{[001]}$	$v_l^{[100]}$	$v_{s\perp}^{[100]}$	$v_{s\parallel}^{[100]}$	$v_l^{[110]}$	$v_{s\perp}^{[110]}$	$v_{s\parallel}^{[110]}$
1	4098	2794	3611	2773	2865	4612	649	2864
2	4127	2783	3681	2737	2841	4602	667	2851
3	4122	2766	3639			4612	669	2855
4	4112	2766	3696			4648	688	2842
5	4121		3672					2870
6	4080		3640					2854
7	4123							2860
8								2847
Average	4110	2777	3656	2755	2853	4618	668	2855
Relative error (%)	0.3	0.4	0.7	0.6	0.4	0.3	1.5	0.2

TABLE VI

COMPARISON OF DERIVED CONSTANTS FOR THE TWO CASES OF $k_{33} = 0.90$ AND $k_{33} = 0.91$.

	k_{33}	c_{13}^E	c_{33}^E	c_{13}^D	c_{33}^D	s_{11}^E	s_{33}^E	ε_{33}^S	e_{31}	e_{33}	d_{33}	g_{33}	h_{31}	h_{33}
	0.91	9.6	9.5	9.3	13.0	54.1	120	890	−1.5	16.5	2100	46.4	−1.9	20.9
	0.90	10.1	10.5	9.45	13.1	51.4	108	970	−3.7	15.5	2000	43.7	−4.3	17.4
δ^1 (%)	1.1	5.1	10	1.6	0.8	5.1	11	8.6	85	6.3	4.9	6.0	77	18

[1] δ is relative error.

TABLE VII

EXPERIMENTAL RESULTS OBTAINED FROM THE LENGTH EXTENSIONAL RESONANCE USING SAMPLES WITH DIFFERENT ASPECT RATIOS.

l (mm)	l/w	f_r (kHz)	f_a (kHz)	k_{33}	$2lf_a$(Hz·m)
4.05	9.0	143.9	298.0	0.90	2414
2.90	6.3	222.5	427.5	0.88	2480
3.10	4.5	217.5	408.8	0.87	2534
3.62	3.9	202.4	372.3	0.86	2695

TABLE VIII

RELATIVE ERRORS (IN PERCENTAGES) INTRODUCED IN VELOCITIES WITH A MISORIENTATION OF 2°.

	$v_l^{[001]}$	$v_s^{[001]}$	$v_l^{[100]}$	$v_{s\perp}^{[100]}$	$v_{s\parallel}^{[100]}$	$v_l^{[110]}$	$v_{s\perp}^{[110]}$	$v_{s\parallel}^{[110]}$
Relative error (%)	0.2	0.4	0.3	0.5	0.5	0.06	2.0	0.2

electromechanical coupling coefficients will be very helpful to understand the nature of PZN-PT crystals. The anisotropy analysis was performed by using the measured data given in Table IV. Fig. 2 provides the directional dependence of phase velocities for sound wave propagating in the a) X-Y, b) Y-Z, and c) [110]-Z planes. The calculated results reveal that the velocities of the longitudinal waves do not change with orientation as much as that of the shear waves. As shown in Fig. 2(a), the shear wave propagating in the X-Y plane and polarized in the same plane has the strongest orientational dependence. It has a maximum in [100] and a minimum in [110], respectively. Fig. 2(b) shows that the phase velocity of the shear wave propagating and polarizing in the Y-Z plane also changes drastically with the propagation direction. Its maximum and minimum are in [001] and [011], respectively. Therefore, the error in phase velocity measurements caused by misorientation is larger for the shear wave propagating in [110] than in other orientations. Table VIII lists the errors of the velocities for an assumed misorientation of 2° in the propagation directions. The maximum error from this error source is 2%.

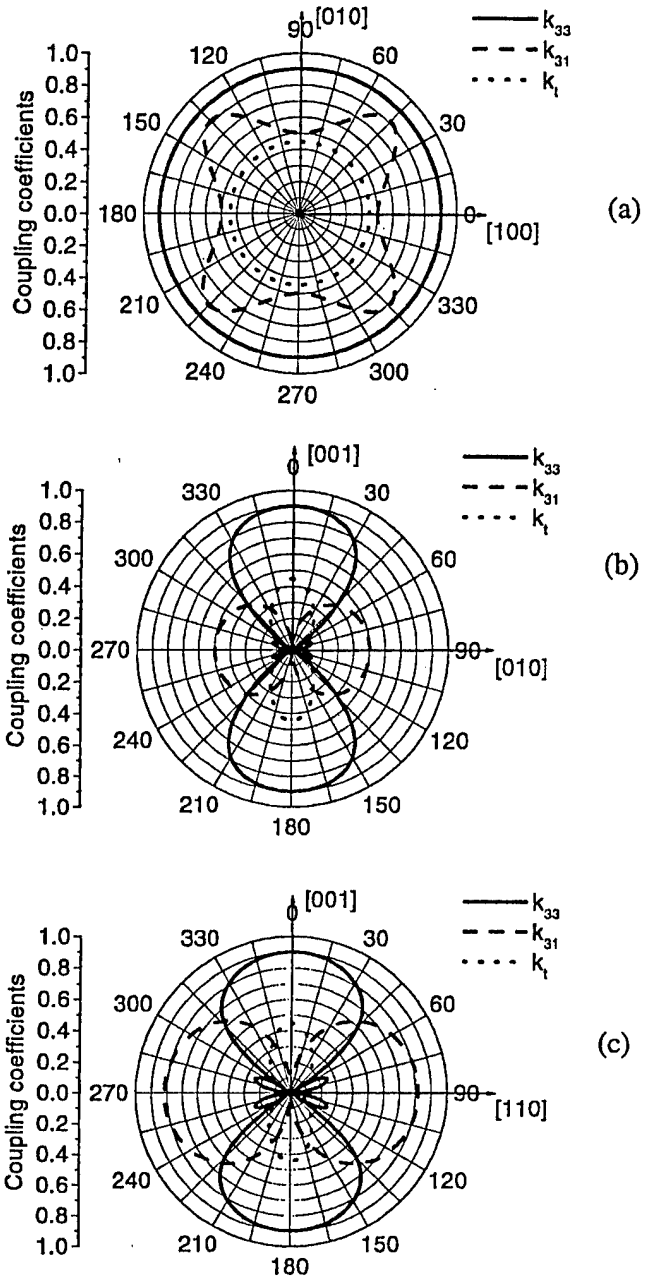

Fig. 3. Directional dependence of the coupling coefficients k_{33}, k_{31}, and k_t, respectively, in a) the [100] and [010] plane, b) the [010] and [001] plane, and c) the [110] and [001] plane.

Fig. 3 shows the directional dependence of the electromechanical coupling coefficients k_{33} and k_{31}. The poling direction is parallel to the length direction for the k_{33} bar and perpendicular to the length direction for the k_{31} bar. The coupling coefficient k_{33} has a maximum value when the length is in [001] [Fig. 3(b)]; the coupling coefficient of k_{31} reaches the maximum when the length is in [110] direction [Fig. 3(c)]. This calculated anisotropy of the lateral coupling coefficient was verified by the direct measurement given in Table II. Fig. 3 also gives the directional dependence of k_t, the coupling coefficient of the thickness mode for a flat plate. It has a maximum in the [001] direction.

Because the 1-D formula for calculating the coupling coefficient and elastic compliance from the length-extensional mode is derived based on the assumption of a long thin bar without lateral constraints, a large aspect ratio is needed to produce such decoupled modes [7]. Otherwise, the measured coupling coefficient from the resonance method will be between the value of k_t and k_{33}. In other words, the longitudinal velocity would be higher for smaller aspect ratios. These results were verified also by the experimental results given in Table VII. It is worth mentioning that some of the modes were not pure even with a very large aspect ratio for this multidomain system; therefore, it is not possible to obtain the complete set of the material properties by using the resonance technique alone.

VI. Summary and Conclusions

The material properties of a PZN-4.5%PT single crystal poled in the [001] direction of the original cubic axes were measured using a combined method of ultrasonic and resonance techniques. The crystal symmetry of the ferroelectric state is 3m at room temperature, but the macroscopic average symmetry of the domain pattern is pseudo-tetragonal for the [001] poled samples. Rectangular parallelepiped samples with [001]/[010]/[100] and [001]/[110]/[1$\bar{1}$0] orientations were made for our measurements. A complete set of elastic, piezoelectric, and dielectric constants for the PZN-4.5%PT single crystals were determined from the measured resonance frequencies, sound velocities, and low frequency capacitance values. The directional dependence of the phase velocities of the ultrasonic waves propagating in the X-Y, Y-Z, and [110]-Z planes were calculated based on the measured data. The calculated results showed that the phase velocities are strongly anisotropic for shear waves but directional dependence is relatively weaker for the longitudinal waves. A slow shear wave, about 700 m/s, was found in the [110] direction polarized in [1$\bar{1}$0]. The directional dependence of the electromechanical coupling coefficients was also calculated based on the measured materials properties. It was showed that the maximum value of k_{33} is in [001], and the maximum of effective lateral coupling coefficient k_{3i} is in [110]. These calculated results agree well with our experimental verifications. Detailed error analysis was performed for each measured coefficient, and it was concluded that the errors are small for directly measured quantities but relatively larger for the derived coefficients.

Acknowledgments

The crystals used for this study were provided by Drs. S. E. Park and T. R. Shrout through the Piezocrystal Resource Center of the Pennsylvania State University.

REFERENCES

[1] S. Nomura, T. Takahashi, and Y. Yokomizo, "Ferroelectric properties in the system Pb $(Zn_{1/3}Nb_{2/3}O_3-$ $PbTiO_3$," *J. Phys. Soc. Jpn.*, vol. 27, no. 1, p. 262, 1969.

[2] J. Kuwata, K. Uchino, and S. Nomura, "Dielectric and piezoelectric properties of 0.91PZN-0.09PT single crystals," *Jpn. J. Appl. Phys.*, vol. 21, no. 9, pp. 1298–1302, 1982.

[3] S. E. Park, and T. R. Shrout, "Ultrahigh strain and piezoelectric behavior in relaxor based ferroelectric single crystals," *J. Appl. Phys.*, vol. 82, no. 4, pp. 1804–1811, 1997.

[4] ——, "Characteristics of relaxor-based piezoelectric single crystals for ultrasonic transducers," *IEEE Trans. Ultrason., Ferroelect., Freq. Contr.*, vol. 44, no. 5, pp. 1140–1147, 1997.

[5] S. F. Liu, S. E. Park, T. R. Shrout, and L. E. Cross, "Electric field dependence of piezoelectric properties for rhombohedral $0.955Pb(Zn_{1/3}Nb_{2/3})O_3$-$0.045PbTiO_3$ single crystal," *J. Appl. Phys.*, vol. 85, no. 5, pp. 2810–2814, 1999.

[6] S. Saitoh, T. Takeuchi, T. Kobayashi, K. Harada, S. Shimanuki, and Y.Yamashita, "A 3.7 MHz phase array probe using $0.91Pb(Zn_{1/3}Nb_{2/3})O_3$-$0.09PbTiO_3$ single crystal," *IEEE Trans. Ultrason., Ferroelect., Freq. Contr.*, vol. 46, no. 2, pp. 414–421, 1999.

[7] *IEEE Standard on Piezoelectricity*, ANSI/IEEE STD. 176-1987, 1987.

[8] S. Zhu, B. Jiang, and W. Cao, "Characterization of piezoelectric materials using ultrasonic and resonant techniques," in *Proc. SPIE, Med. Imag. 1998*, no. 3341, San Diego, CA, pp. 154–162.

[9] B. A. Auld, *Acoustic Fields and Waves in Solids*. New York: Wiley, 1973.

[10] A. W. Warner, M. Onoe, and G. A. Coquin, "Determination of elastic and piezoelectric constants for crystals in class(3m)," *J. Acoust. Soc. Amer.*, vol. 42, no. 6, pp. 1223–1231, 1967.

[11] J. Kushibiki and I. Takanaga, "Elastic properties of single- and multi-domain crystals of $LiTaO_3$," *J. Appl. Phys.*, vol. 81, no. 10, pp. 6906–6910, 1997.

[12] K.-H.Hellwege, *Landolt-Bornstein Numerical Data and Functional Relationships in Science and Technology, Group III, Band 1*, Vol. 1. New York: Springer-Verlag.

[13] W. Cao, S. N. Zhu, and B. Jiang, "Analysis of shear modes in a piezoelectric vibrator," *J. Appl. Phys.*, vol. 83, no. 8, pp. 4415–4420, 1998.

Jianhua Yin received his B.Sc., M.Sc., and Ph.D. degrees from Nanjing University, P.R. China in 1994, 1997, and 1990, respectively. He joined the Institute of Acoustics and the Department of Electronic Science and Engineering at Nanjing University in 1990. He became an Associate Professor there in 1992.

His research interests are in the field of surface acoustic wave device and its application in communication system, ultrasonic transducer, ultrasonic nondestructive evaluation, and acoustic signal processing.

Dr. Yin is a member of the Acoustic Society of China. He was a visiting researcher in Tokai University, Japan, from 1992 to 1993, and a visiting scholar in the University of Kansas from 1997 to 1998. He has been a visiting Research Associate in Material Research Laboratory at Pennsylvania State University since 1998. He is now working on the characterization of ferroelectric single crystal.

Bei Jiang received her B.A. in English from Northeast Normal University, P.R. China, in 1983 and M.Ed. from The Pennsylvania State University in 1989. She has been working in the Material Research Laboratory of Penn State as a research assistant from 1988 to 1989 and from 1996 to now. Her research interests are piezoelectric crystals and ultrasonic characterization.

Wenwu Cao received his B.S. degree in physics from Jilin University, Changchun, China, in 1982 and the Ph.D. degree in condensed matter physics from The Pennsylvania State University in 1987.

He is currently holding a joint appointment between the Department of Mathematics and the Materials Research Laboratory of The Pennsylvania State University as Associate Professor of Mathematics and Materials Science. He has conducted both theoretical and experimental research in the area of condensed matter physics and materials, including theories on proper- and improper-ferroelastic phase transitions and static and dynamic properties of domains and domain walls in ferroelectric and ferroelastic materials. He has also performed measurements on second- and third-order elastic constants, linear and nonlinear dielectric constants, and piezoelectric constants in single crytals and ceramics. His current interests also include the static and dynamic behavior of piezoelectric ceramic-polymer composites, simulation design of piezoelectric sensors, transducers and actuators for underwater acoustics, and medical ultrasonic imaging as well as ultrasonic NDE and signal processing.

Dr. Cao is a member of the Society for Industrial and Applied Mathematics and the American Physical Society.

Appendix 2

Rui Zhang, Bei Jiang, and Wenwu Cao, "Elastic, piezoelectric, and dielectric properties of multidomain $0.67Pb(Mg_{1/3}Nb_{2/3})O_3$–$0.33PbTiO_3$ single crystals," Journal of Applied Physics, 90 [7], 3471–3475 (October 2001).

Elastic, piezoelectric, and dielectric properties of multidomain $0.67Pb(Mg_{1/3}Nb_{2/3})O_3-0.33PbTiO_3$ single crystals

Rui Zhang, Bei Jiang, and Wenwu Cao[a)]
Materials Research Laboratory, The Pennsylvania State University, University Park, Pennsylvania 16802

(Received 18 April 2001; accepted for publication 11 June 2001)

The elastic, piezoelectric, and dielectric constants of $0.67Pb(Mg_{1/3}Nb_{2/3})O_3-0.33PbTiO_3$ domain engineered single crystal were determined experimentally by using ultrasonic and resonance methods. It was confirmed that the single crystal system has large electromechanical coupling coefficient k_{33} (~94%) and piezoelectric constant d_{33} (~2800 pC/N) if the poling is done along the [001] of pseudocubic directions. A soft shear mode with a velocity of 880 m/s was observed in the [110] direction with displacement in $[\bar{1}10]$. Using the measured data, the orientation dependence of phase velocities and electromechanical coupling coefficients were calculated. The origin of experimental errors and their influence on measured results are also examined. © *2001 American Institute of Physics.* [DOI: 10.1063/1.1390494]

I. INTRODUCTION

Relaxor based ferroelectric single crystal systems, $Pb(Zn_{1/3}Nb_{2/3})O_3-PbTiO_3$ (PZN–PT) and $Pb(Mg_{1/3}Nb_{2/3})O_3-PbTiO_3$ (PMN–PT) exhibit extraordinary large electromechanical coupling coefficient k_{33} (>90%) and piezoelectric coefficient d_{33} (>2000 pC/N) at room temperature after being poled in [001] of the cubic coordinates.[1–5] Such high electromechanical coupling coefficient and piezoelectric coefficient values make the domain engineered single crystal systems very useful for producing higher sensitivity ultrasonic transducers with superior broadband characteristics, large strain actuators, and many other electromechanical devices.[6–7] For these systems, because the dipoles in each unit cell are formed along ⟨111⟩ of the cubic parent phase, the poling along [001] produces a multidomain structure, which is macroscopically pseudotetragonal.

The mechanism that causes the domain engineered single crystal systems to have such large electromechanical properties is still not well understood. The lack of complete physical property data is the main hindrance for further theoretical studies. It is also very important for device designers to have a complete set of elastic, piezoelectric, and dielectric constants since many simulation packages require the complete data set as input. Previously, we have published a complete set of elastic, piezoelectric, and dielectric constants for domain engineered single crystal PZN–4.5%PT.[8] However, it was found that the PMN–PT system can have a larger electromechanical coupling coefficient k_{33} and is mechanically more stable than the PZN–PT system. In addition, larger size PMN–PT single crystals are now readily available from many crystal growers. In this article we report one complete set of elastic, piezoelectric, and dielectric constants for the 0.67PMN–0.33PT domain engineered single crystal, which has the best properties among all the crystal compositions of this system.

The foremost concern to device designers is the reported high electromechanical properties. Our experimental results indeed confirmed that the 0.67PMN–0.33PT single crystal system has an electromechanical coupling coefficient k_{33} of 94% and piezoelectric constant d_{33} of 2800 pC/N. Similar to the PZN–4.5%PT system reported earlier, a soft shear mode with a velocity of 880 m/s was observed in the [110] direction with the displacement polarized in $[\bar{1}10]$.

Quite different from characterizing single domain single crystals, we found that the properties of these multidomain samples depend strongly on the domain patterns that are generated in the poling process, or the effective symmetry associated with the domain patterns of the system. This domain pattern dependence often creates inconsistencies when more than one sample is used for characterization, particularly when these samples have different geometry, such as those used in the resonance measurements. In this article, we will also analyze the origins of experimental errors and point out the error influence on particular measured constants.

II. EXPERIMENTAL PROCEDURE

The experimental setup and procedure are similar to that used in Ref. 8, except for some small modifications that were made in the averaging method to improve measurement accuracy. Several batches of samples have been used to ensure the self-consistency of the final results.

At room temperature, the 0.67PMN–0.33PT single crystals are in the ferroelectric phase with rhombohedral ($3m$) symmetry. From the phase diagram of PMN–PT, 0.67PMN–0.33PT is near the morphotropic boundary (~35% PT). It has been shown experimentally that the crystal can hold the highest level of stable macroscopic polarization only when the poling field is applied along one of the six ⟨100⟩ directions of the cubic axes.[6,7] Such a poling field direction will create a multidomain structure since there are still four remaining degenerate polarization orientations, [111], $[\bar{1}11]$, $[1\bar{1}1]$, and $[\bar{1}\bar{1}1]$, remaining in the crystal after poling. If the number of domains is large enough, statistically speaking, the global macroscopic symmetry can be treated as a

a)Author to whom correspondence should be addressed; electronic mail: cao@math.psu.edu

TABLE I. The relationships between phase velocities and elastic constants for $4mm$ symmetry and the measured values of phase velocities in PMN–33%PT multidomain single crystals poled in [001] of cubic axes.

Phase velocities	$v_l^{[001]}$	$v_s^{[001]}$	$v_l^{[100]}$	$v_{s\perp}^{[100]}$	$v_{s\parallel}^{[100]}$	$v_l^{[110]}$	$v_{s\perp}^{[110]}$	$v_{s\parallel}^{[110]}$
Related elastic constants	c_{33}^D	c_{44}^E	c_{11}^E	c_{66}^E	c_{44}^D	$\frac{1}{2}(c_{11}^E+c_{12}^E+2c_{66}^E)$	$\frac{1}{2}(c_{11}^E-c_{12}^E)$	c_{44}^D
Value of measured velocity (m/s)	4610	2930	3792	2882	3099	4727	880	3090

pseudotetragonal $4mm$ as discussed in Ref. 7. For the tetragonal symmetry, there are a total of 11 independent electro–elastic constants: six elastic, three piezoelectric, and two dielectric constants to be determined.

In principle, all independent elastic, piezoelectric, and dielectric constants for crystals with any symmetry can be determined either by the resonance method or by the ultrasonic method alone, so long as sufficient numbers of differently oriented samples are available.[9] In reality, however, for materials of lower symmetry, some geometries for resonance measurements are difficult to obtain, especially when the available crystal is too small to make large aspect ratio free resonators. On the other hand, since the ultrasonic technique can only directly measure certain constants through the measurements of pure mode phase velocities, large errors may be introduced for those material derived constants that are not related to pure modes.[10] High acoustic attenuation of certain modes may also damp the propagation of ultrasonic waves of certain modes so that a complete set of material constants for the low symmetry system is also difficult to obtain by using the ultrasonic method alone. Over the past few years, we have developed a hybrid method by combining the ultrasonic and resonant technique, so that the least number of samples are needed to resolve the problem of property variation from sample to sample and also to eliminate some of the unreliable geometries in the resonance method.[11]

The PMN–PT crystal samples were made in the Piezocrystal Resource at the Pennsylvania State University. The as grown crystals are orientated using the Laue method with an orientation accuracy of ±0.5°. Then, samples were cut into different geometries and dimensions based on the requirements of different types of measurements. The final dimensions of the samples used for the ultrasonic measurements were 4×4×2 mm^3. For the length extensional and the thickness resonance measurements, the aspect ratio of the sample exceeded 5:1 in order to yield nearly pure resonance modes.[9] Gold electrodes were sputtered onto the parallel surface of samples for poling. An external electric field of 1.0–1.5 MV/m was applied at room temperature along the [001] direction of cubic axes to pole these samples into pseudotetragonal structure.

A 15 MHz longitudinal wave transducer (Ultran Laboratories, Inc.) and a 20 MHz shear wave transducer (Panametrics) were used for the pulse–echo measurements. The electric pulses used to excite the transducer were generated by a Panametrics 200 MHz pulser/receiver, and the time-of-flight between echoes was measured by a Tektronix 460 A digital oscilloscope. For a crystal with tetragonal $4mm$ symmetry, sound velocities can be directly measured for eight independent pure modes. From each measurement, either one elastic constant or a linear combination of several elastic constants can be obtained as shown in Table I. It is seen that c_{44}^D and c_{12}^E can be determined by more than one measurements, which provides a control check.

In resonant measurements, two length-extension resonators and one thickness resonator are used. A HP 4194 A impedance/gain-phase analyzer was employed to measure the resonance and antiresonance frequencies of these resonators. From the resonance and antiresonance frequencies, three electromechanical coupling coefficients k_{31}, k_{33}, k_t and three elastic compliance s_{11}^E, s_{33}^E, s_{33}^D can be determined.

The dielectric constants are determined by measuring capacitances of [100] and [001] orientated parallel plates. The capacitance were measured at 1 kHz using a Stanford Research System SR715 *LCR* meter. From the capacitance measurements, dielectric permittivities ϵ_{11}^T and ϵ_{33}^T were determined.

III. RESULTS AND DISCUSSION

The measured sound velocities for the eight pure modes are listed in Table I. Since none of these eight pure modes involves the elastic constants c_{13}^E or c_{33}^E, these two elastic constants must be derived from other quantities. Usually, the c_{33}^E is derived from the electromechanical coupling coefficient k_t and the elastic constant c_{33}^D by

$$c_{33}^E=c_{33}^D(1-k_t^2), \tag{1}$$

and c_{13}^E is calculated by

$$c_{13}^E=-\frac{s_{13}^E}{s}, \tag{2}$$

where

$$s_{13}^E=-\left[s_{33}^E\left(\frac{s_{11}^E c_{12}^E+s_{12}^E c_{11}^E}{c_{11}^E+c_{12}^E}\right)\right]^{1/2},$$
$$s=s_{33}^E(s_{11}^E+s_{12}^E)-2(s_{13}^E)^2, \quad s_{12}^E=s_{11}^E-\frac{1}{c_{11}^E-c_{12}^E}. \tag{3}$$

Since it is much harder to make a resonator with the appropriate aspect ratio to measure the shear coupling coefficient k_{15}, its value is usually calculated by

$$k_{15}^2=1-\frac{c_{44}^E}{c_{44}^D}. \tag{4}$$

TABLE II. Measured and derived material properties of PMN–33%PT multidomain single crystal poled in [001] (Density: $\rho=8060\ \mathrm{kg/m^3}$).

Elastic stiffness constants: c_{ij} (10^{10} N/m^2)											
$c_{11}^{E\,a}$	c_{12}^{E}	c_{13}^{E}	c_{33}^{E}	$c_{44}^{E\,a}$	$c_{66}^{E\,a}$	c_{11}^{D}	c_{12}^{D}	c_{13}^{D}	$c_{33}^{D\,a}$	$c_{44}^{D\,a}$	c_{66}^{D}
11.5 ±0.15	10.3 ±0.16	10.2 ±0.15	10.3 ±0.3	6.9 ±0.05	6.6 ±0.05	11.7 ±0.15	10.5 ±0.15	9.0 ±0.35	17.4 ±0.5	7.7 ±0.05	6.6 ±0.05
Elastic compliance constants: s_{ij} (10^{-12} m^2/N)											
$s_{11}^{E\,a}$	s_{12}^{E}	s_{13}^{E}	s_{33}^{E}	s_{44}^{E}	s_{66}^{E}	s_{11}^{D}	s_{12}^{D}	s_{13}^{D}	$s_{33}^{D\,a}$	s_{44}^{D}	s_{66}^{D}
69.0 ±2.0	−11.1 ±1.2	−55.7 ±1.2	119.6 ±4.0	14.5 ±0.1	15.2 ±0.2	44 ±1.0	−34 ±1.0	−4.1 ±1.0	11.1 ±0.8	13.0 ±0.1	15.2 ±0.18
Piezoelectric constants: e(C/m^2)			d(10^{-12} C/N)			g(10^{-3} V m/N)			h(10^8 V/m)		
e_{15}	e_{31}	e_{33}	d_{15}	d_{31}^{a}	d_{33}^{a}	g_{15}	g_{31}	g_{33}	h_{15}	h_{31}	h_{33}
10.1 ±0.9	−3.9 ±1.6	20.3 ±1.6	146 ±16	−1330 ±19	2820 ±75	10.3 ±0.6	−18.4 ±0.4	38.8 ±0.8	7.9 ±0.4	−5.9 ±2.0	33.7 ±1.7
Dielectric constants: $\epsilon(\epsilon_0)$				$\beta(10^{-4}/\epsilon_0)$			Electromechanical coupling constants				
ϵ_{11}^{S}	ϵ_{33}^{S}	$\epsilon_{11}^{T\,a}$	$\epsilon_{33}^{T\,a}$	β_{11}^{S}	β_{33}^{S}	β_{11}^{T}	β_{33}^{T}	k_{15}	k_{31}^{a}	k_{33}^{a}	k_1^{a}	k_p
1434 ±110	680 ±45	1600 ±120	8200 ±200	7.0 ±0.1	14.7 ±0.5	6.30 ±0.1	1.2 ±0.1	0.32 ±0.02	0.59 ±0.01	0.94 ±0.01	0.64 ±0.01	0.77 ±0.04

[a]Measure properties.

Then, the piezoelectric strain constant d_{15} is determined by

$$d_{15}=k_{15}\sqrt{\epsilon_{11}^{T}s_{44}^{E}}. \tag{5}$$

After all the elastic stiffness constants c_{ij}^{E}, piezoelectric strain constant d_{ij}, and free dielectric permittivity ϵ_{ij}^{T} are obtained, other constants can be derived from constitutive equations. Finally, the whole set of elastic, piezoelectric, and dielectric constants of PMN–33%PT single crystal are obtained. The complete set of these material constants are shown in Table II. The errors were obtained from the average of properties measured using three batches of crystals with the same chemical composition. It is seen that the measured PMN–33%PT single crystal has larger d_{33} and k_{33} compared to PZN–4.5%PT.[8]

Based on the measured constants, the orientation dependence of sound velocity has been calculated by finding the eigenvalues and eigenvectors of Christoffel's tensor for given wave propagation directions. The calculated results for sound wave propagating in: (a) $X-Y$, (b) $Y-Z$ and (c) [110]-Z planes are shown Figs. 1(a)–1(c), where the length of a vector from the origin to any points on the curves gives sound velocity in that propagation direction. It is seen from Fig. 1 that the velocities of the longitudinal waves do not change as much as shear waves do for different propagation directions. The shear wave propagating in the $X-Y$ plane with its particle displacement also in the same plane, has the strongest orientation dependence as shown in Fig. 1(a). This shear wave velocity v_{s1} has a maximum (2882 m/s) in [100] and a minimum (about 880 m/s) in [$\bar{1}$10], respectively, which implies that a "soft shear acoustic mode" also exists in this domain-engineered single crystal system, similar to the PZN–4.5%PT case reported earlier.[8] Figure 1(b) shows that the phase velocity of the shear wave propagating and polarizing in the $Y-Z$ plane also changes drastically with the propagation direction. It has a maximum in [010] and a minimum in [011].

In order to further investigate the anisotropy of the multidomain PMN–PT single crystal system, some constant ratios are calculated. The calculated results are listed in Table III. Since there are no data available for the single domain single crystal PMN–PT system at the moment, the corresponding ratios for single crystal $BaTiO_3$ are listed in Table III for comparison. It is seen that the measured anisotropy of PMN–33%PT single crystal is comparable to the PZN–4.5%PT single crystal reported in Ref. 8 and it is generally less than that of single domain $BaTiO_3$. In particular, the dielectric anisotropy of measured PMN–33%PT is much smaller than that of $BaTiO_3$. This may be caused by the averaging effect of the multidomain structure of PMN–PT single crystals. On the other hand, the anisotropy for shear waves that propagate in the $X-Y$ plane with the displacement also in the same plane is larger for PMN–PT than for $BaTiO_3$. The "soft shear wave mode" along [110] is related to domain wall motion, since the dynamics of domain wall motions will contribute to the effective elastic compliance. The phase velocity of the shear wave that propagates along [110] and polarizes in [$\bar{1}$10] is related to elastic compliance by

$$v=1/\sqrt{2\rho(s_{11}^{E}-s_{12}^{E})}. \tag{6}$$

Experimental results imply that the domain wall motion results in a very large effective $(s_{11}^{E}-s_{12}^{E})$, therefore, a slower sound velocity.

In order to obtain a complete set of self-consistent material properties from the measured data, proper analysis of measurement errors is very important. There are four equivalent kinds of piezoelectric constitutive equations for a piezoelectric system, which provide us with several control checks to minimize errors in those derived quantities. For each expression of derived quantities, errors will be introduced so that the same constant may be assigned different values

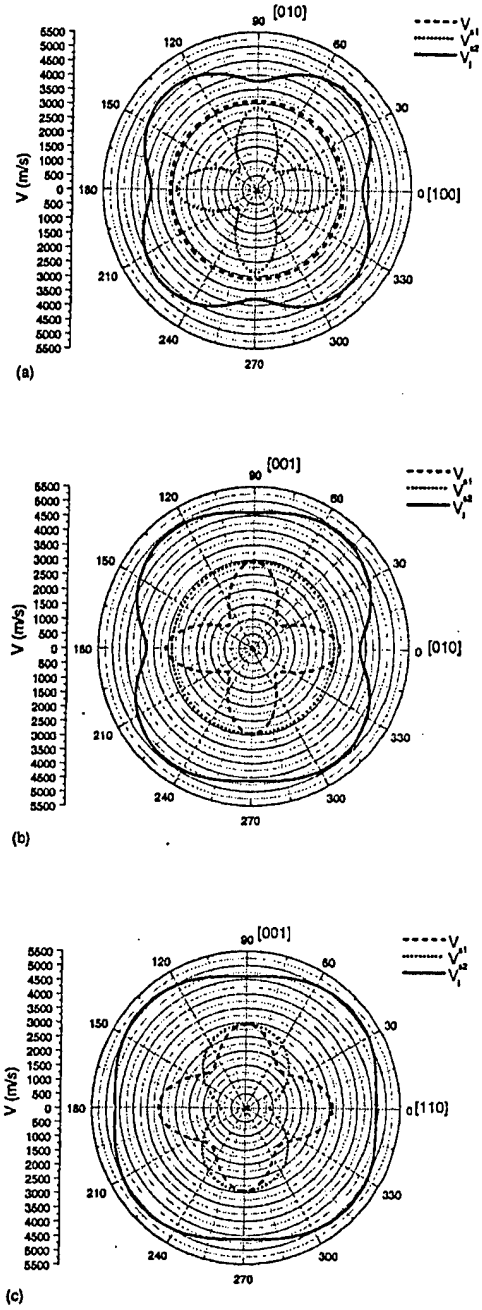

FIG. 1. Orientation dependence of the longitudinal velocity v_l and the shear velocities, v_{s1} and v_{s2}, respectively: (a) $X-Y$ plane, (b) $Y-Z$ plane, and (c) [110]-Z plane.

based on different formulas. For example, the c_{33}^E may be determined by Eq. (1), or by the following relation:

$$c_{33}^E=\frac{s_{11}^E+s_{12}^E}{s}. \tag{7}$$

When the measurement errors are large, the result obtained using Eq. (1) could be much different from the one obtained using Eq. (7). In sound velocity measurements, the resolutions of time of flight and sample thickness are 1 ns and 0.01 mm, respectively. For samples with 4 mm thickness, the relative error is about 0.1%. But nonperfect parallelness and misorientation limit the accuracy of sound velocity measurements to about 1%. The calculated orientation dependence of sound velocities can be used to estimate errors from misorientation. We found that the misorientation errors are very small for the longitudinal waves when the crystal orientations are done by the Laue method (within $\pm 0.5°$). But the orientation error can be serious for shear waves, especially for the shear wave propagating along the [110] with displacement in $[\bar{1}10]$. We also found that the value of the derived e_{31} is very sensitive to the uncertainty of c_{12}^E. A variation of 0.1% in c_{12}^E will cause substantial change in the value of e_{31}, sometimes, even change its sign. On the other hand, as analyzed above, it is very difficult to determine c_{12}^E, a derived quantity, with error less than 0.1% due to the limitation of the ultrasonic method. For this reason, resonance measurement is made using an edge excited thickness-vibration resonator. The thickness direction of the resonator is along [001] and the applied electric field is in the [100] direction. From the measured resonance and antiresonance frequencies, e_{31} can be derived with much higher accuracy. The result can be used to check the value of c_{12}^E and also to ensure the self-consistency of data listed in Table II.

In the measurements it is observed that the values of some elastic constants such as c_{33}^D are strongly dependent on the poling process. If the sample is not properly poled, the values of some elastic constants can change substantially since the constant D elastic constant values include large contribution from the piezoelectric effect. In order to check the poling status, d_{33} was also measured independently by the quasistatic method. Partial polarization reversal will cause the domain pattern to change and hence influence the macroscopic effective properties of the domain engineered single crystals. Therefore, ensuring a full polarization in the system is very important to obtain good electromechanical properties in the PMN–PT system.

TABLE III. Anisotropy of measured material properties of PMN–33%PT multidomain single crystal poled in [001].

Compound	$\epsilon_{11}^T/\epsilon_{33}^T$	$\epsilon_{11}^S/\epsilon_{33}^S$	s_{33}^E/s_{11}^E	s_{33}^D/s_{11}^D	s_{44}^E/s_{66}^E	s_{44}^D/s_{66}^E	s_{13}^E/s_{12}^E	s_{13}^D/s_{12}^D
PMN–PT	0.195	2.1	1.73	0.25	0.95	0.86	5.01	0.12
PZN–PT	0.596	3	1.32	0.33	0.98	0.94	1.79	0.18
$BaTiO_3$[a]	17.4	18.1	1.95	1.49	2.08	1.40	2.32	1.03

[a]See Ref. 12.

IV. SUMMARY AND CONCLUSIONS

0.67PMN–0.33PT single crystals poled along the [001] direction of the cubic axes were characterized by using both ultrasonic and resonance methods. A complete set of elastic, piezoelectric, and dielectric constants for the domain engineered single crystal PMN–33%PT system have been obtained. It was confirmed that the PMN–33%PT system has very large d_{33} and k_{33} coefficients. Based on the measured data, orientation dependence of the phase velocities of ultrasonic waves propagating in the $X-Y$, $Y-Z$, and [110]-Z planes has been calculated, and the anisotropy of material properties has been analyzed. We found that the anisotropy of phase velocities is very strong for shear waves, whereas it is relatively weak for the longitudinal waves. Similar to the case of PZN–4.5%PT reported in Ref. 8, a very slow shear wave with velocity of 880 m/s was found in the [110] direction with the displacement in $[\bar{1}10]$. The soft shear wave mode is associated with domain wall motions. This complete set of material property data not only will provide the necessary input for device design using these crystals, it will also provide bases for further theoretical studies on the principles of the domain engineering process.

ACKNOWLEDGMENTS

This research was sponsored by the ONR/DARPA under Grant No. N00014-98-1-0527. Crystals used for this study were provided by Dr. T. R. Shrout, Dr. P. Rehrig, and Dr. S. Zhang through the Piezocrystal Resource Center of the Pennsylvania State University. The authors would also like to thank Professor Wenhua Jiang for helpful discussions on the characterization techniques.

[1] S. E. Park and T. R. Shrout, J. Appl. Phys. **82**, 1804 (1997).
[2] H. Luo, G. Xu, P. Wang, and Z. Yin, Ferroelectrics **231**, 97 (1999).
[3] Z. Yin, H. Luo, P. Wang, and G. Xu, Ferroelectrics **229**, 207 (1999).
[4] M. Dong and Z. G. Ye, J. Cryst. Growth **209**, 81 (2000).
[5] S. Nomura and Uchino, Ferroelectrics **50**, 107 (1983).
[6] S. Park, P. Lopath, K. Shung, and T. Shrout, Proc. SPIE **3037**, 140 (1997).
[7] S. E. Park and T. R. Shrout, IEEE Trans. Ultrason. Ferroelectr. Freq. Control **44**, 1140 (1997).
[8] J. Yin, B. Jiang, and W. Cao, IEEE Trans. Ultrason. Ferroelectr. Freq. Control **47**, 285 (2000).
[9] ANSI/IEEE STD. 176-1987, *IEEE Standard on Piezoelectricity* (IEEE, New York, 1987).
[10] A. W. Warner, M. Onoe, and G. A. Coquin, J. Acoust. Soc. Am. **42**, 1223 (1967).
[11] S. Zhu, B. Jiang, and W. Cao, Proc. SPIE **3341**, 154 (1998).
[12] D. A Berlincourt, D. R. Curran, and H. Jaffe, in *Physical Acoustics*, edited by W. P. Mason, Vol. 1A, p. 218.

Appendix 3

Hanxing Yu, Venkat Gopalan, Jürgen Sindel, and Clive A. Randall, "Domain switching and electromechanical properties of pulse poled $Pb(Zn_{1/3}Nb_{2/3})O_3$–$PbTiO_3$ crystals," Journal of Applied Physics, 89[1], 561–567 (January 2001).

Domain switching and electromechanical properties of pulse poled $Pb(Zn_{1/3}Nb_{2/3})O_3-PbTiO_3$ crystals

Hanxing Yu, Venkat Gopalan, Jürgen Sindel, and Clive A. Randall[a)]
Materials Research Laboratory, The Pennsylvania State University, University Park, Pennsylvania 16802

(Received 1 February 2000; accepted for publication 23 June 2000)

Domain switching behavior is studied under pulse field conditions in $(1-x)Pb(Zn_{1/3}Nb_{2/3})O_3-xPbTiO_3$ single crystals oriented at various crystallographic directions. The activation energy, critical field, and domain wall mobilities are determined from simple methods earlier employed to ferroelectric single crystals by Merz [Phys. Rev. **95**, 690 (1954)]. Domain structures were observed by atomic force microscopy of etched surfaces and shown to have a dendritic morphology under pulse conditions. The size and density of these dendritic domains are compared for various pulse conditions and discussed in terms of nucleation and domain growth behavior. The pulsed electric fields were also utilized to pole the crystals in the $[001]_C$ directions, and the corresponding piezoelectric strains were determined. © *2001 American Institute of Physics.* [DOI: 10.1063/1.1289221]

I. INTRODUCTION

A ferroelectric phase can be the result of a phase transition from a high temperature paraelectric phase. The order parameters of the transition is spontaneous polarization which is electrostrictively coupled to spontaneous strain in the ferroelectrics.[1] The elastic and electric field energies are typically minimized by the formation of domains. A single domain within the crystal has largely a spatially uniform distribution of spontaneous polarization and is separated from other domains by thin domain walls. The number of different domains (variants) formed under equilibrium conditions are linked to the order of the point group symmetries between the paraelectric and ferroelectric phases, respectively.[2] The domain sizes under equilibrium conditions relate to conditions of a total minimized energy, considering the wall energy, electrostatic, and depolarization energy contributions. The domain walls often coincide with crystallographic habit planes, that are in turn associated with the loss of symmetry operations in the phase transition and strain compatibility conditions.[3,4] When an electric field is applied to a ferroelectric material, there is a driving force to rearrange the domain configuration to minimize the energy configuration. This is accomplished by the motion of existing domain walls to increase the volume of domains with polarization aligned in the direction of the electric field. Alternatively, new domains are grown from nuclei that are possessing the same polarization direction. The alignment of domains produces a change in the macrosymmetry and the crystal develops anisotropic properties, with regard to linear electro-optic effects, pyroelectricity, and piezoelectricity with the development of a net polarization.[5] This process of developing a new macroscopic symmetry by aligning or growing domains is referred to as poling a ferroelectric.

The single crystals of $Pb(B_1B_2)O_3-PbTiO_3$ are of major interest owing to the high piezoelectric coefficient and electromechanical coupling, specifically in the [001] directions of $(1-x)Pb(Zn_{1/3}Nb_{2/3})O_3-xPbTiO_3$ (PZN-PT) crystals. High piezoelectric properties ($d_{33}\sim 2500$ pC/N) in combination with large electric fields induce strains of ~1.7% in $(1-x)$PZN:xPT ($x=0-0.09$) crystals oriented along $[001]_C$.[6,7] The magnitudes of the piezoelectric coefficient depends on composition, orientation, temperature, and electric field strength. The excellent piezoelectric properties result from the field dependence of the polarization orientation, the polarization in the pseudo-rhombohedral ferroelectric phase being aligned into four equivalent orientations, $[111]_C$, $[1\bar{1}1]_C$, $[\bar{1}11]_C$, and $[\bar{1}\bar{1}1]_C$, about the $[001]_C$ poling direction.

The objective of this article is to further investigate the nucleation and growth of metastable dendritic domain structures in PZN:PT crystals, and to determine the associated electromechanical properties present after applying various pulse poling conditions.

II. EXPERIMENT PROCEDURES

Crystals of PZN and their solid solutions with PT were grown using a high temperature flux technique described elsewhere.[8] Typical crystal sizes used in this study ranged from 5 to 20 mm. As-grown crystals were oriented along one of the ⟨001⟩ directions using a back reflection Laue camera before they were cut into square plates. The final crystal dimensions were 5 mm×5 mm with a thickness of 200–300 μm.

To study the dynamic behavior of domains in an electric field, electric transient currents were measured by pulsing experiments. Square pulses were applied through liquid mercury electrodes to a crystal in series with a resistor. We applied 1–100 pulses of 10 μs in length with a rise time of about 100 ns (IRCO C12K-20). The resulting switching currents were monitored by an oscilloscope (Tektronix TDS 340). The system setup is illustrated in Fig. 1, whereas Fig. 2 shows the profile of the applied electric fields.

a)Electronic mail: car4@psu.edu

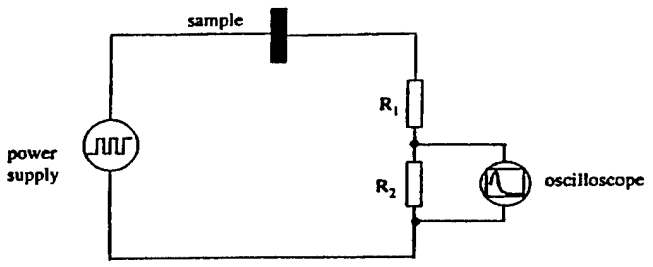

FIG. 1. Schematic system setup of switching current measurement.

Following the pulsing experiments, the samples were chemically etched at room temperature using a solution made of HNO_3 and HF. The etched surfaces were investigated with an optical reflection microscope and additionally probed by an atomic force microscope, which was operated in contact mode (Multi Mode, Digital Instruments Inc., Santa Barbara, CA).

Electric field measurements carried out on the poled crystals allowed simultaneous recording of the polarization and strain hysteresis curves using a computer-controlled modified Sawyer–Tower system and a linear variable displacement transducer (LVDT) sensor driven by a lock-in amplifier (Stanford Research Systems, Model SR830). The voltage was supplied using either a Trek 609C-6 high voltage dc amplifier and/or a Kepco BOP 1000M amplifier. The same system was used to measure unipolar strain curves on poled crystals with $[001]_C$ direction crystals. The values of the longitudinal piezoelectric coefficients, d_{33}, were estimated from the slope of the unipolar strain versus electric field curve at low fields.

III. RESULTS AND DISCUSSIONS

A. Switching behavior studies

The characteristic properties of the polarization reversal transients of PZN-PT crystals are found to be basically analogous to many other ferroelectric materials, such as $BaTiO_3$ with superposition contributions from polarization reversal and capacitance.[9–11] In Figs. 3 and 4, a plot of the measured peak current density J_{max} and $1/t_s$ versus the applied electric field for three different PZN:PT compositions and two directions for each composition is given. First, for low applied electric fields ($E<4$ kV/cm) at a fixed temperature the peak of the switching current (or current density), J_{max}, is proportional to $\exp(-\alpha/E)$; second, at higher fields, a linear relation between J_{max} and E develops (Fig. 3). The

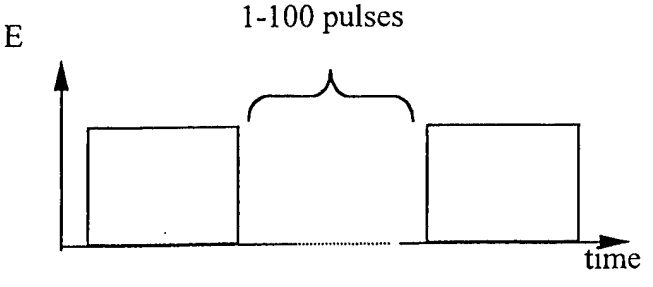

FIG. 2. Electric field profiles of poling modulation.

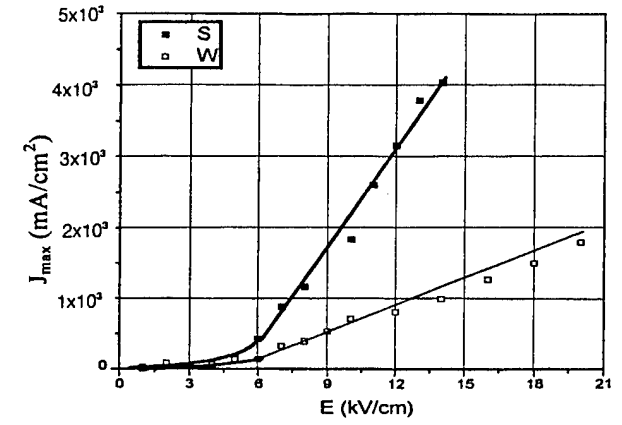

(a)

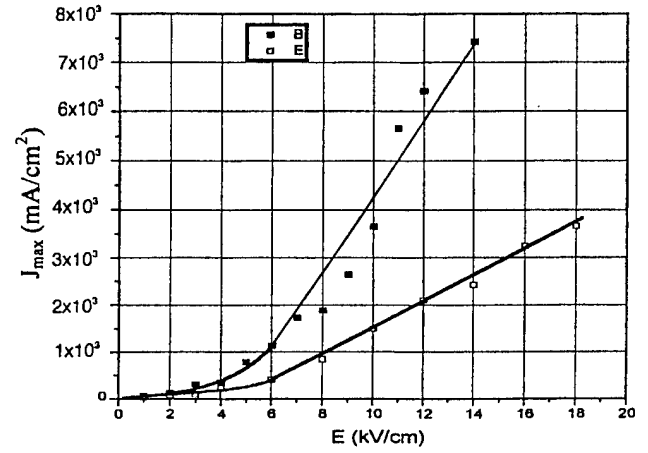

(b)

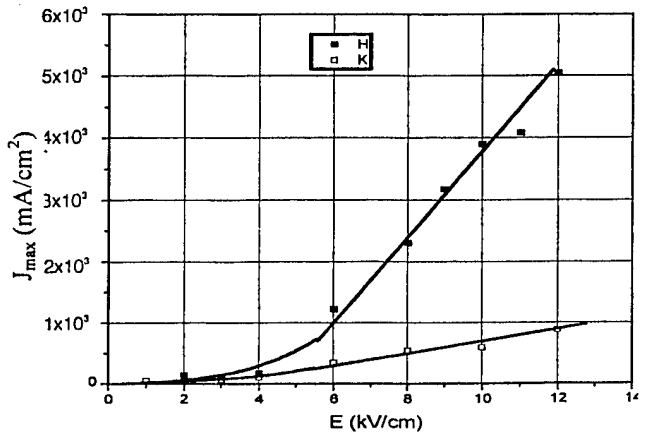

(c)

FIG. 3. Switching current peak density J_{max} vs electric field E on (a) PZN, (b) PZN 4.5%PT, and (c) PZN-8%PT for ⟨001⟩ and ⟨111⟩, respectively (note solid squares ⟨001⟩).

switching time, t_s, in which the transient current reaches an arbitrarily defined polarization reversal time (90% in our case) is inversely proportional to the applied fields at high E fields (Fig. 4). For low fields, the reciprocal switching time is proportional to $\exp(-\alpha/E)$ (where α is the activation energy). An empirical expression which provides the proper field dependence at a fixed temperature over both the linear and exponential regions of J_{max} vs E is given in

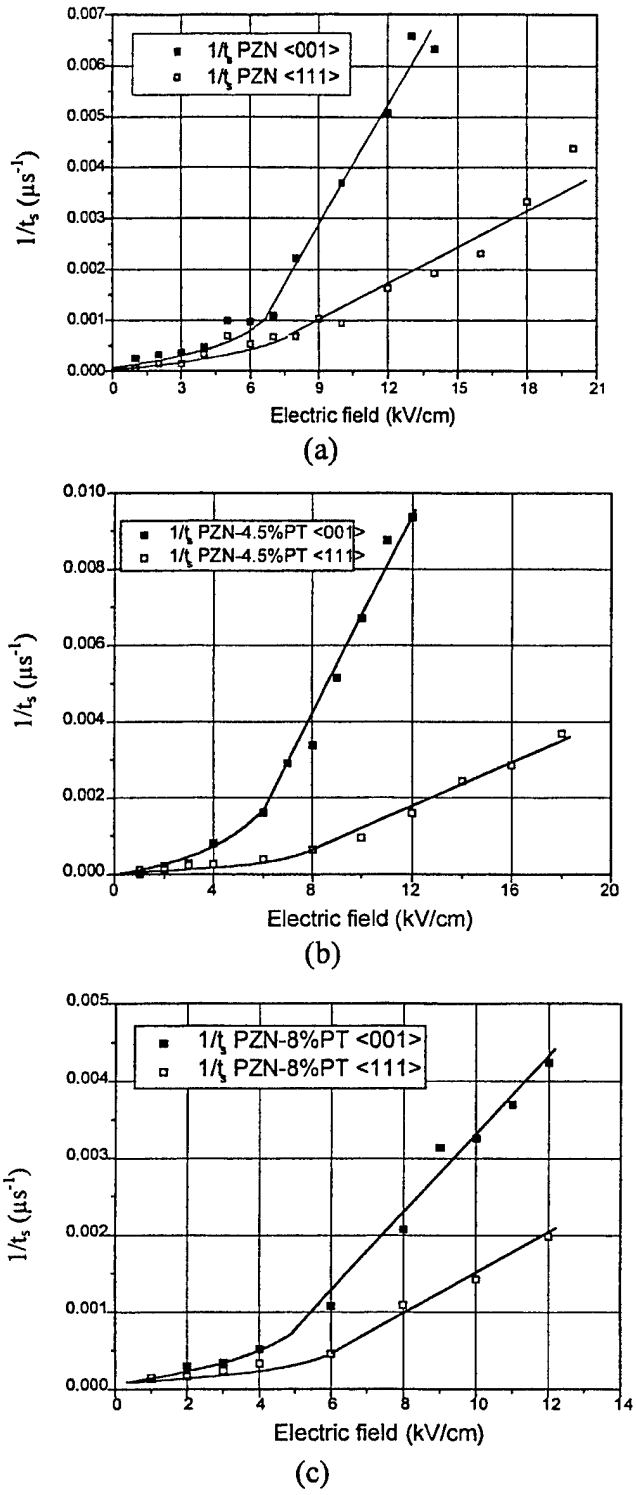

FIG. 4. Reciprocal switching time vs electric field E on (a) PZN, (b) PZN-4.5%PT, and (c) PZN-8%PT.

TABLE I. α, E', and μ as functions of composition and orientation.

	α (kV/cm)	μ ($cm^2 s^{-1} kV^{-1}$)	E' (kV/cm)
PZN ⟨001⟩	23.3	14.2	5.35
PZN ⟨111⟩	15.7	4.89	4.25
PZN-4.5%PT ⟨001⟩	8.90	23.7	5.10
PZN-4.5%PT ⟨111⟩	6.71	9.98	4.28
PZN-8%PT ⟨001⟩	2.74	9.57	4.09
PZN-8%PT ⟨111⟩	2.27	5.11	3.97

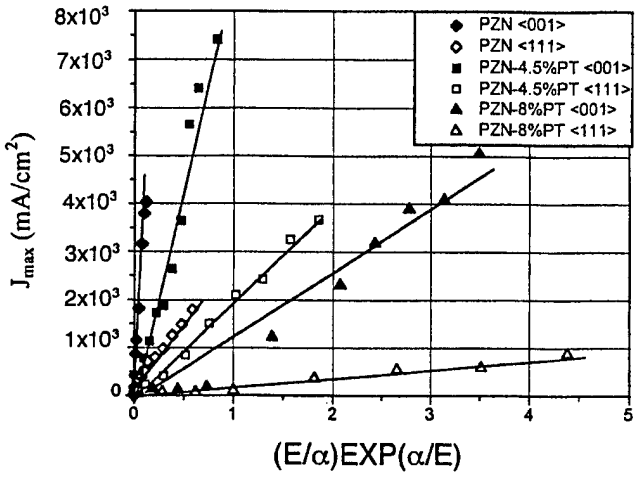

FIG. 5. Linearity expressed in Eq. (1) between J_{max} and $(E/\alpha) \times \exp(-\alpha/E)$ is shown for different compositions and orientations.

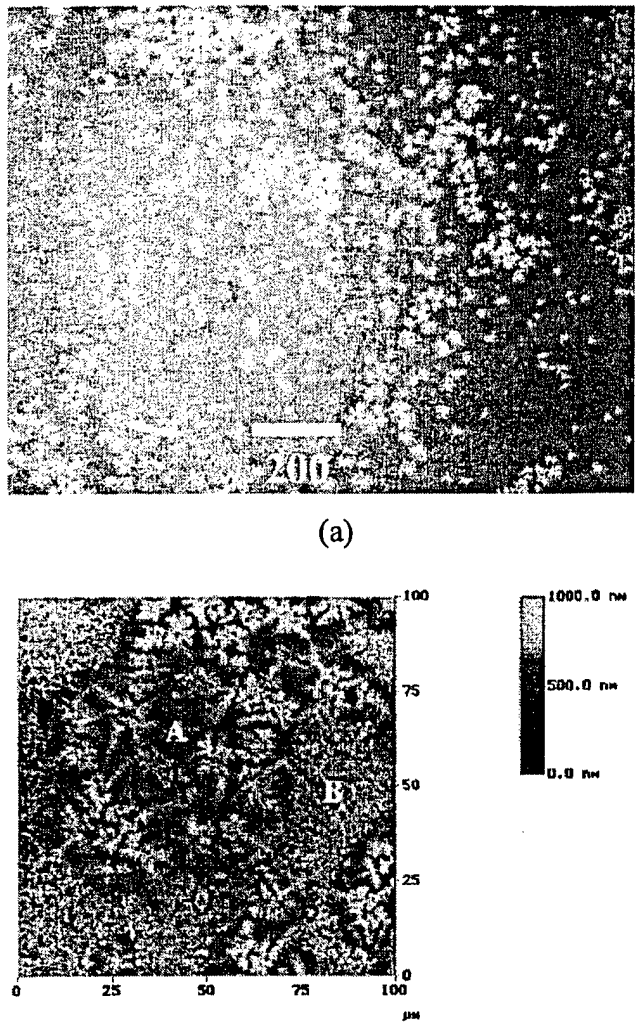

FIG. 6. Domain nucleation on PZN-4.5PT ⟨001⟩ crystal after 10 μs at 3 kV/cm (a) optical (b) AFM observation, finer scale nuclei associated with backswitching is observed in AFM image.

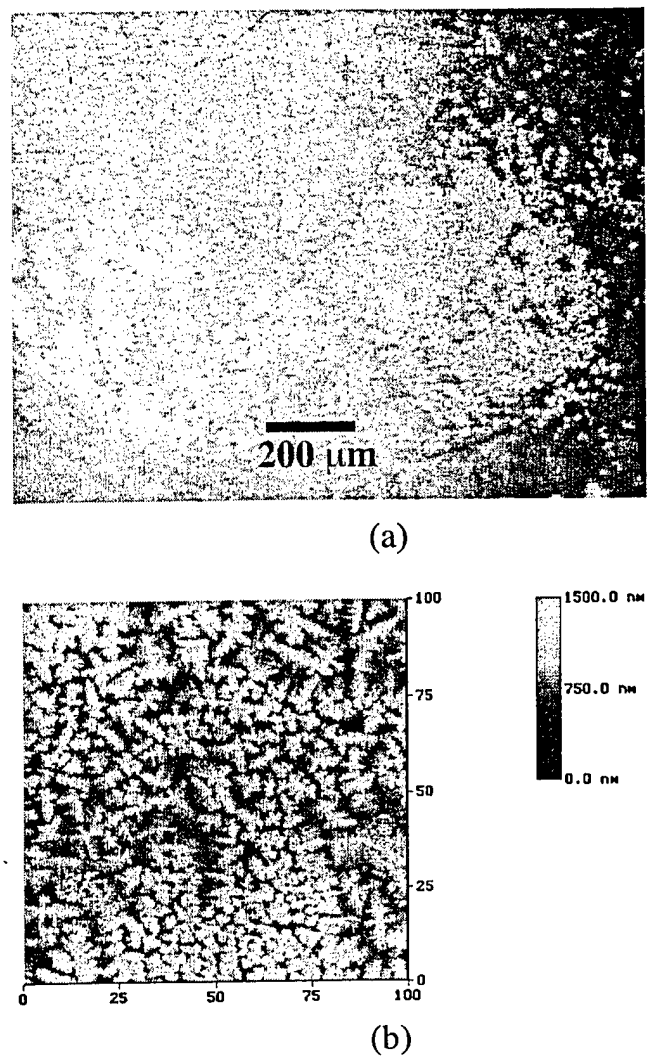

FIG. 7. Domain nucleation on PZN-4.5PT ⟨001⟩ crystal after 10 μs pulses at 3 kV/cm (a) optical (b) AFM observation with less backswitching observed and a better defined dendritre structure.

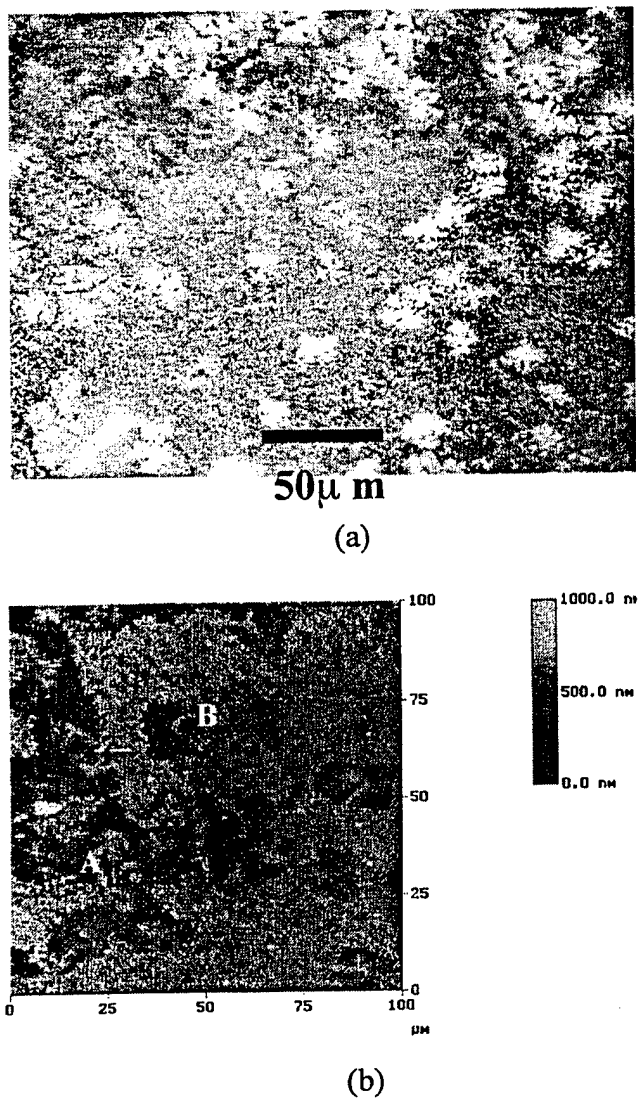

FIG. 8. Domain growth on PZN-4.5PT ⟨001⟩ crystal at $E=10$ kV/cm for a single 10 μs (a) optical and (b) AFM observations. Large areas of backswitched are observed in Region B.

$$J_{\max}=\left(\frac{E}{\alpha}\right)\exp\left(-\frac{\alpha}{E}\right). \tag{1}$$

Plots of this relation for all the PZN-PT compositions in both polarization directions are illustrated in Fig. 5 in an electric field range between 1 and 18 kV/cm.

In general, the higher the applied electric field, the faster the domains switch and thus the larger the peak current density, $J_{\max}$. The total switching time is approximately given by

$$t_s \approx t_n + t_d, \tag{2}$$

where t_n is the time necessary to form (or activate) all nuclei, and t_d is the time necessary for one domain to grow through the sample. Thus, if the two quantities t_n and t_d are not of the same order of magnitude, the total switching time, t_s, is determined principally by the slower of the two processes.

At lower field strengths, the switching time is primarily determined by the number of domains which are nucleated (or activated) per unit time. This nucleation process has an exponential relation with the electrical field. Therefore, the observed exponential behavior between switching current or reciprocal switching time and applied field was expected. The linear part of the curves shown in Fig. 4 can be rationalized by the fact that the nucleation (or activation) of new domains at high field strengths is so fast that the switching time t_s is primarily determined by the time it takes to move domain walls. We can, therefore, use the reciprocal of the switching time $(1/t_s)$ to estimate the velocity v of the domain walls, using the linear approximation

$$(1/t_s)\sim v=\mu(E-E'), \tag{3}$$

where μ is the mobility of the domain walls and E' is a limiting field.[10]

Table I shows the constants α, E', and μ, which were determined for a number of PZN:PT compositions and crystalline directions. In general, $[001]_C$ oriented crystals have a larger value of α, μ, and E' than the $[111]_C$ oriented crystals of the same chemical composition. However, we observed that the $J_{\max}$ for $[001]_C$ oriented crystals is also greater than that for $[111]_C$ oriented crystals. The larger $J_{\max}$, involving

(a)

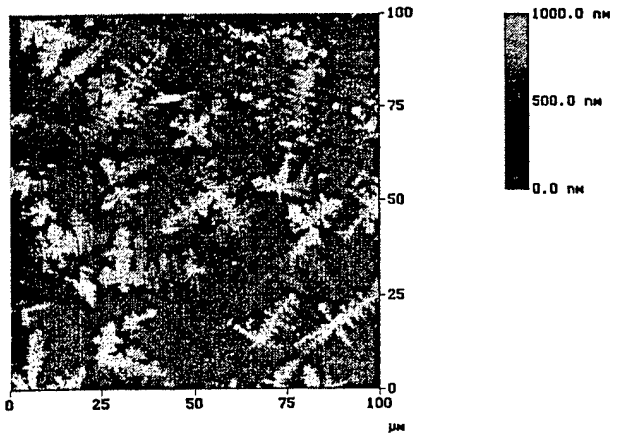

(b)

FIG. 9. Domain growth on PZN-4.5PT ⟨001⟩ crystal at $E=10$ kV/cm for 10 μs×100 (a) optical and (b) AFM observations.

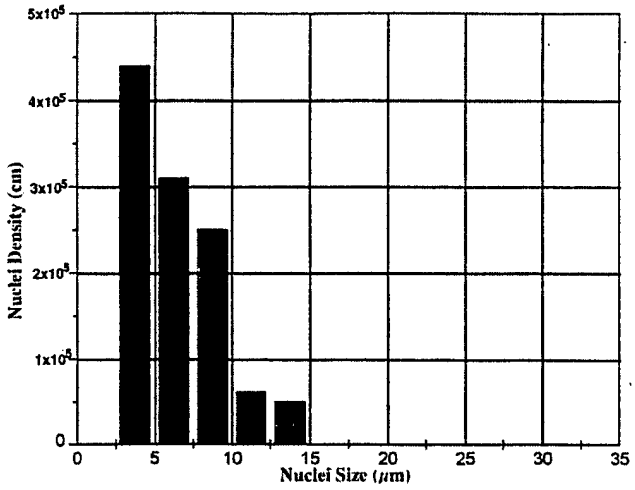

(a)

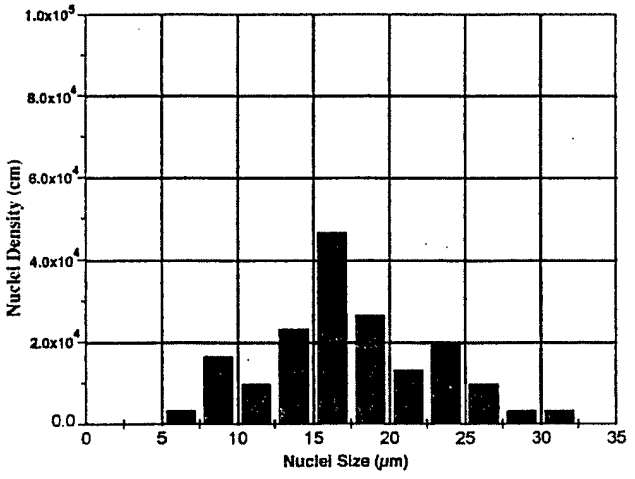

(b)

FIG. 10. Dendritic nuclei size distribution after (a) 3 kV/cm for 10 μs×100 and (b) 10 kV/cm for 10 μs×100.

larger associated activation fields α, are believed to indicate that the engineered domain state along $[001]_C$ direction is more stable than that in the $[111]_C$ direction. Consequently, a larger activation field is needed for $[001]_C$ oriented crystals. However, once the energy well is overcome during switching process, domains move faster in $[001]_C$ direction, leading to a larger current peak (the shape of switching currents along both direction are basically the same).

B. *Ex situ* domain nucleation and growth study

From the switching current studies discussed above, the switching process is predominantly composed of two parts. One is domain nucleation which is found to dominate the switching process at low fields (curved part in $J_{\max}$, $1/t_s$ vs. E behavior). The other is domain growth which is believed to be the most important process at high fields (linear part in $J_{\max}$, $1/t_s$ vs. E behavior). In the *ex situ* domain study, two different field strengths were investigated: one is 3 kV/cm (nucleation); the other is 10 kV/cm (domain wall mobility), as shown in Fig. 3.

The dendritic domain structures of the regions which were in contact with the liquid electrodes in the $[001]_C$ oriented crystals were investigated with both optical microscopy and scanning electron microscopy.[12] The higher resolution of the AFM reveals nuclei or domain structures on a submicrometer scale, as shown in Fig. 6(b). Region A shows domains with the dendritic domain structures that are resolved in the optical micrograph of Fig. 6. Region B shows a higher density nuclei surrounding these larger dendrite domains. Similar results are shown for both 3 kV/cm (Fig. 6) and 10 kV/cm (Fig. 8) for a 10 μs duration single pulse. When samples are exposed to either longer electrical pulses or multiple pulses (Figs. 7 and 9), the nanoscale domain structures are no longer present, and there is a coarsening of the larger dendritic structures. Owing to the relative size of the dendritic domain structures, we anticipate the nanosized domains under the single pulse condition to be related to a spontaneous backswitching, or pinned nanopolar regions, associated with the relaxor characteristics observed in the permittivity.

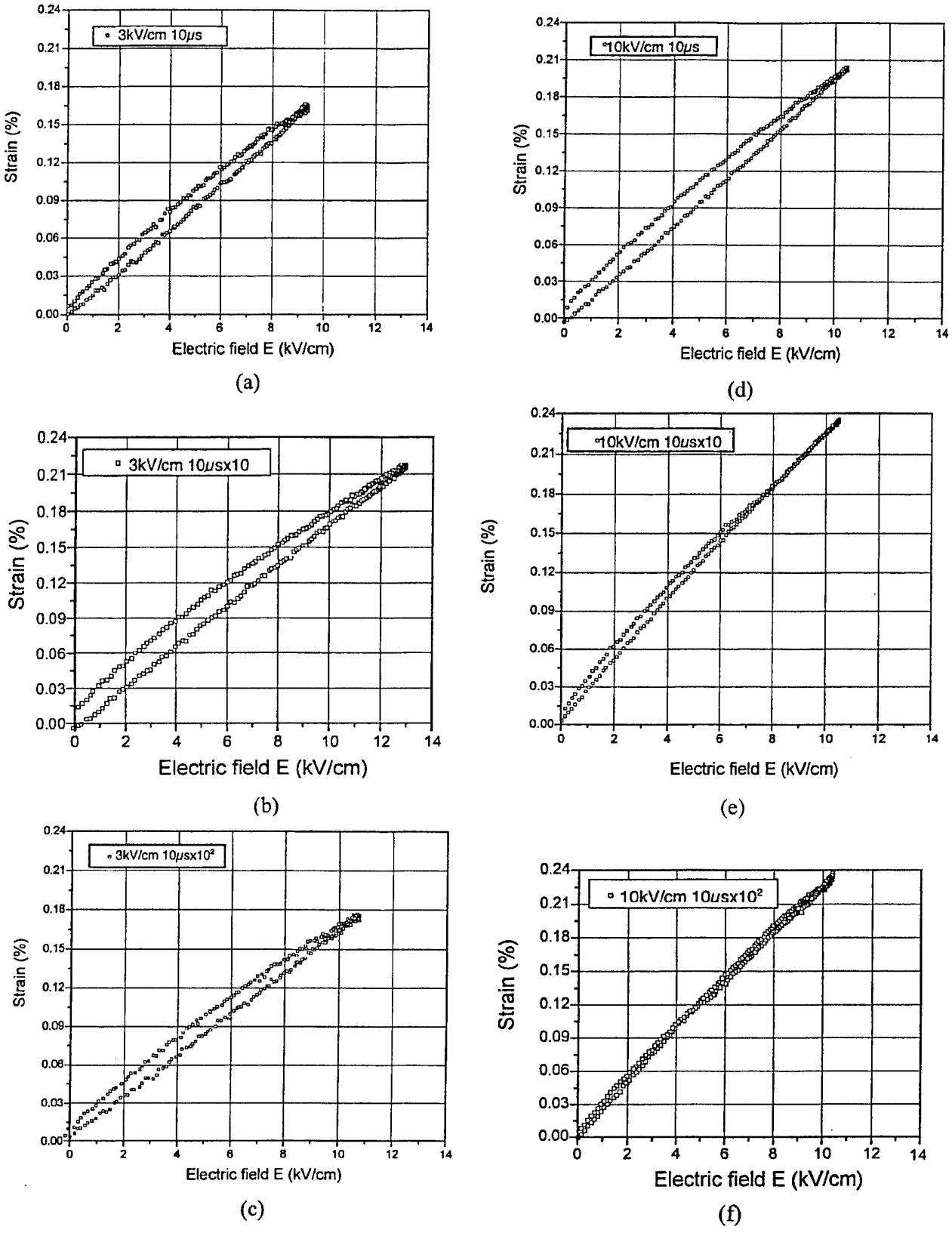

FIG. 11. Strain vs electric field measurement under different poling conditions 3 kV/cm for 10 μs, (b) 3 kV/cm for 10 μs$\times$10, (c) 3 kV/cm for 10 μs$\times$100, (d) 10 kV/cm for 10 μs, (e) 10 kV/cm for 10 μs$\times$10, and (f) 10 kV/cm for 10 μs$\times$100.

Contrasting Figs. 6 and 7 demonstrates the dendritic domain structures of PZN-4.5%PT $[001]_C$ crystal after an electric field exposure of 3 kV/cm for the two different durations, 10 and 1000 μs, respectively. Increasing the field exposure from 10 to 1000 μs increased the dendrite density enormously.However, the sizes of the dendrites in both regions are basically identical. Recalling the switching current studies, we know that the switching process at this field strength ($\cong$3

TABLE II. d_{33} values as functions of poling strength and time length.

Poling condition	3 kV/cm 10 μs	3 kV/cm 100 μs	3 kV/cm 1000 μs	10 kV/cm 10 μs	10 kV/cm 100 μs	10 kV/cm 1000 μs
d_{33} (pC/N)	~1300	~1800	~2100	~1850	~2000	~2600

kV/cm) is mainly a nucleation process, where the domain growth is negligible. The similar domain sizes are consistent with this effect. On the other hand, when an E field of 10 kV/cm is applied to the crystal for 10 and 1000-μs, domain growth can be clearly observed (Figs. 8 and 9). The distribution of domain nuclei sizes under both low field and high field conditions is plotted in Fig. 10. Under low field condition (3 kV/cm), the dendritic domain density is almost increased by an order of magnitude when multiple pulses are applied to the crystal, while the domain sizes basically have the same distribution (<10 μm). However, this observation is significantly different under high field conditions (10 kV/cm). Large domains (>15 μm) are observed after a multiple pulses treatment. Furthermore, the density of the domain nuclei sites is lower than the conditions at 3 kV/cm (ignoring the nanoscale backswitching). The growth and size distributions of the dendritic domains is consistent with the results of switching current studies in which the switching process is predominantly a domain growth process at 10 kV/cm and a domain nucleation process at 3 kV/cm.

C. Piezoelectric properties from pulse poling single crystals

Pulse poling conditions were also studied on PZN:PT single crystals as functions of field strength and pulse length. Traditionally, PZN-4.5%PT $[001]_C$ crystals are poled at 10–20 kV/cm with a linear increase of the applied field and then held at peak for 5 s, to produce d_{33} values usually ~2000 pC/N. Two pulsing field strengths are considered, i.e., 3 and 10 kV/cm, and three different number of pulse sequences, i.e., 10 μs, 10 μs$\times$10, and 10 μs$\times$100, were applied to crystals with gold electrodes. Strain versus E-field behavior under unipolar conditions was measured and plotted in Fig. 11. The d_{33} values were estimated from the slope of the strain versus E behavior at low fields (Table II). In general, the longer the total time of a given field level, and the higher the electric field strength, the higher the value of d_{33}, and the smaller the hysteresis in the strain-field curves.

IV. CONCLUSIONS

Building upon our recent discovery of metastable dendritic domain structures in pulsed $(1-x)$PZN-PT single crystals, we have investigated the systematic changes in switching current in $[001]_C$ and $[111]_C$ directions for a variety of field strengths. It was found that the switching behavior is analogous to much earlier work on single crystal $BaTiO_3$ by Drougard *et al.*[13] The activation energy for polarization switching in the $[111]_C$ direction is smaller than in the $[001]_C$ direction, but the domain wall mobility is higher in $[001]_C$. The switching curve data were used to investigate domain structures (size and morphologies) at fields within the nucleation controlled regime (3 kV/cm) and the domain growth regime (10 kV/cm).

An atomic force microscope (AFM) was used to characterize chemically etched domain structures that were formed under the pulse fields under metal liquid electrodes. The AFM images are consistent with the earlier studies by optical and scanning electron microscopy that revealed unique dendritic domain structures. However, AFM studies reveal that in a short single pulse ~10 μs duration that many submicron domains are observed and associated with backswitching. A repeated pulsing showed that the submicron domains are not as prevalent. Stereological analysis of the dendritic domain structures demonstrates that a higher nuclei density exists after 3 kV/cm pulses. Against that, a low density of larger dendrites developed with 10 kV/cm pulses is consistent with a classical description of nucleation and growth.

Pulses are also applied to determine the associated piezoelectric properties in the $[001]_C$ direction. For both 3 and 10 kV/cm pulsing, the piezoelectric coefficient increases and hysteresis decreases with the increased number of pulses. 10 kV/cm pulses totaling a direction of 1000 μs gives $d_{33} \approx 2600$ pC/N.

ACKNOWLEDGMENTS

This research has been supported by the Office of Navy Research funded by Grant No. DARPA MURI 7160 and Single Crystal Resource 704 T. The authors would like to thank Dr. L. E. Cross, Dr. J. Fousek, Dr. V. Shur, and Dr. S. E. Park for their helpful and informative suggestions. They also thank Hua Lei and Shifang Liu for their help with crystal growth.

[1] A. F. Devonshire, Philos. Mag. B 1040 (1989).
[2] V. K. Wadhawan, Phase Transit. **3**, 3 (1982).
[3] J. Fousek and V. Janovec, J. Appl. Phys. **40**, 135 (1969).
[4] J. Sapriel, Phys. Rev. B **12**, 5128 (1975).
[5] S.-E. Park and T. R. Shrout, J. Appl. Phys. **82**, 1804 (1997).
[6] J. Kuwata, K. Uchino, and S. Nomura, Jpn. J. Appl. Phys., Part 1 **21**, 1298 (1982).
[7] Y. Yamashita, Jpn. J. Appl. Phys., Part 1 **33**, 5328 (1994).
[8] S. F. Liu, S. E. Park, T. R. Shrout, and L. E. Cross, J. Appl. Phys. **85**, 2810 (1999).
[9] W. J. Merz, Phys. Rev. **95**, 690 (1954).
[10] R. C. Miller and A. Savage, Phys. Rev. **112**, 755 (1958).
[11] H. H. Wieder, J. Appl. Phys. **31**, 180 (1960).
[12] H. Yu and C. A. Randall, J. Appl. Phys. **86**, 5733 (1999).
[13] M. E. Drougard and D. R. Young, Phys. Rev. **94**, 1561 (1954).

Appendix 4

Jinhua Yin and Wenwu Cao, "Observation and Analysis of Domain Configurations in Domain Engineered PZN-PT Single Crystals," Ferroelectrics, 251, 93–100 (2001).

Ferroelectrics, 2001, Vol. 251, pp. 93-100
Reprints available directly from the publisher
Photocopying permitted by license only

Observation and Analysis of Domain Configurations in Domain Engineered PZN-PT Single Crystals

JIANHUA YIN and WENWU CAO

Materials Research Laboratory, The Pennsylvania State University, University Park, Pennsylvania 16802, USA

(Received June 2, 2000)

The effective macroscopic symmetry of the PZN-PT single crystal systems is a key issue for the characterization of domain engineered single crystals. We report an optical microscopy study on the domain structures of $0.955Pb(Zn_{1/3}Nb_{2/3})O_3$-$0.045PbTiO_3$(PZN-PT) rhombohedral phase single crystals poled along [001] of the cubic coordinates. Both charged and uncharged domain walls are observed in domain engineered samples and they could join together to form "L" and "T" shaped domain walls. The observed domains are between 10–100 μm in size, which are too big for statistical treatment. Most of the poled samples have only two of the four possible degenerate domain states, making the macroscopic symmetry to be either orthorhombic *mm*2 or monoclinic m, or even triclinic 1 rather than tetragonal 4 *mm* previously assumed. Physical property measurements also support the conclusion or lower symmetry.

Keywords: PZN-PT; ferroelectric material; domain; domain wall; domain engineering

INTRODUCTION

Rhombohedral relaxor based ferroelectric $(1-x)Pb(Zn_{1/3}Nb_{2/3})O_3$-$xPbTiO_3$ (PZN-PT) single crystal system can have very high coupling constant ($k_{33} > 90\%$) and piezoelectric constant ($d_{33} > 2000pC/N$) if it

is poled along the [001] of the parent cubic coordinates.[1-3] It has triggered a new wave of material research recently to improve material properties using domain engineering, i.e., using different poling scheme to manipulate domain structures. It also raised many interesting scientific questions, such as the origin of these superior properties and the role of domains in general. The extremely high electromechanical coupling coefficient and piezoelectric coefficient of this system produced by domain engineering method makes the PZN-PT another promising candidate for transducer materials other than the $PbZrO_3$-$PbTiO_3$ (PZT) solid solution system, which was used for the past 40 years. The PZN-PT single crystal solid solution system has been made in the late 1960s [4] and it was found that the electromechanical coupling coefficient k_{33} could be even more than 90% in some samples.[5,6] However, the composition studied before was at the morphotropic boundary composition between the rhombohedral and the tetragonal phases, therefore, properties were not reproducible. The more recent effort using domain-engineering concept makes it possible to stabilize the polarization of the rhombohedral phase by poling the crystals in [001] rather than the polarization direction of [111] (all refer to the cubic coordinates). [1-3]

Naturally, the key issue is the domain structures produced in the system since the off-polarization direction poling will create multi-domains. This paper reports an experimental study on the domain structures as well as the property measurement in a $0.955Pb(Zn_{1/3}Nb_{2/3})O_3$-$0.045PbTiO_3$ (PZN-4.5%PT) system. Based on the experimental results, a macroscopic mm2 symmetry is more plausible than the 4mm symmetry as all previous studies had assumed.

POSSIBLE DOMAINS

Because the dipoles of the PZN-4.5%PT form along the body diagonal of the parent cubic perovskite structure at the ferroelectric phase transition, the crystal has microscopic rhombohedral symmetry with the symmetry group 3m in the ferroelectric state.[4,5] Poling was done by applying an electric field along [001] of the cubic coordinates so that only four of the eight possible polarization orientations with positive projections in [001] could remain, i.e. [111], $[\bar{1}11]$, $[1\bar{1}1]$ and $[\bar{1}\,\bar{1}1]$ as shown in Figure 1.

Statistically, such a system would have a macroscopic pseudo-tetragonal symmetry, considering the degeneracy of these four domain states. All previous studies on this system were based on this 4*mm* symmetry assumption. [1-3,7]

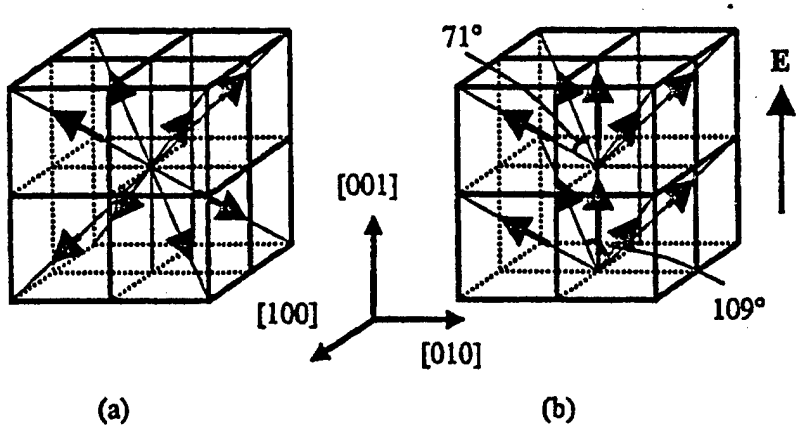

FIGURE 1 Illustration of the assumed domain structure with cross intersecting charged domain walls for the PZN-4.5%PT. (a) Eight possible orientations before poling. (b) Four orientations remain after poling.

The macroscopic symmetry referred here is what reflected in the macroscopic material properties, which do not change with the overall shape of the sample but only with the domain configurations. The 4mm macroscopic tetragonal symmetry assumption implicitly assumed the following two conditions: (1) the domain size is very small compared to sample dimensions so that large amount of domains exist to allow the use of statistical principle; (2) the domain walls are all charged and are parallel to the effective polarization direction (i.e., the wall normal is perpendicular to the applied poling field) as shown in Figure 1.

In a $m\bar{3}m \rightarrow 3m$ ferroelectric phase transition, such as what occurred in the PZN-4.5%PT system, the permissible domain walls formed in the ferroelectric phase are orientated in <100> and <110> family.[8,9] The angle between polarization vectors on the two sides of a domain wall can be either 109° or 71°. All the permissible domain walls between different pairing schemes among the four remaining domains after poling are listed in Table I. Both charged and uncharged walls are possible.

TABLE I Permissible orientations of domain walls in [001] poled PZN-4.5%PT crystals of rhombohedral phase. The polarization directions of $\mathbf{P}_s$ and $\mathbf{P}_s'$ in a twin structure are given in the first row.

$\mathbf{P}_s/\mathbf{P}_s'$	[111]/[$\bar{1}$11]	[111]/[1$\bar{1}$1]	[111]/[$\bar{1}\bar{1}$1]	[$\bar{1}$11]/[1$\bar{1}$1]	[$\bar{1}$11]/[$\bar{1}\bar{1}$1]	[1$\bar{1}$1]/[$\bar{1}\bar{1}$1]
charged	[100]	[010]	[110]	[1$\bar{1}$0]	[010]	[100]
uncharged	[011]	[101]	[001]	[001]	[$\bar{1}$01]	[0$\bar{1}$1]

DOMAIN OBSERVATIONS AND CONFIGURATIONS

For the domain observations, we prepared the samples with three pairs of mutually perpendicular surfaces. These samples have two types of orientations referring to the cubic coordinates: [001]/[010]/[100] and [001]/[110]/[1$\bar{1}$0]. The sample shapes are cubes, plates, or bars with the typical dimension of 1-5 mm. Observations were performed on the surfaces of the following three

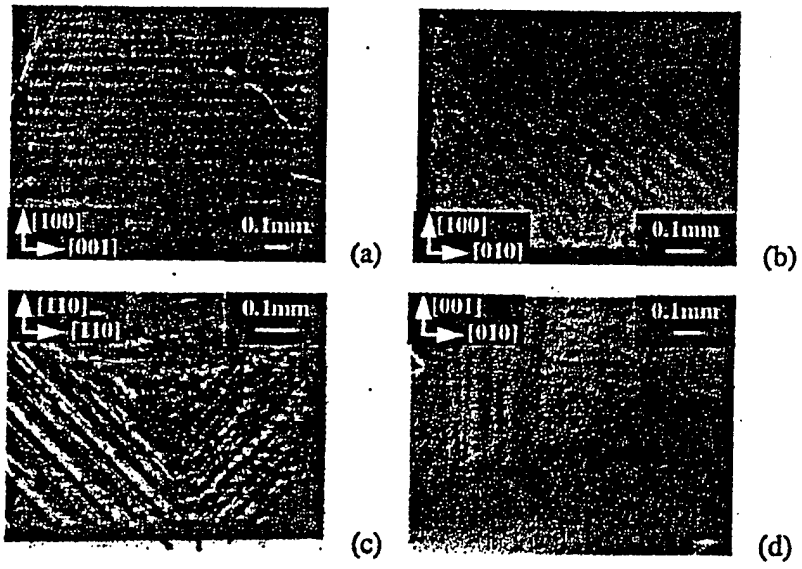

FIGURE 2 Domain patterns observed on different sample surfaces. A set of twins with fairly large domain size are shown in (a) and (b). A charged and an uncharged domain walls join together to form "L" or "T" shaped domain walls shown in (c) and (d).

orientations: [001], [110] and [100], with the samples being poled along [001] in all cases. Because the crystal is translucent, domains could be observed by polarizing optical microscopy in either reflection mode or transmission mode. Figure 2 shows a few of the domain patterns obtained in the domain engineered PZN-4.5%PT single crystal system. Figure 3 shows the domain structures correspond to the patterns in Figure 2. One can see that the intersection lines of domain

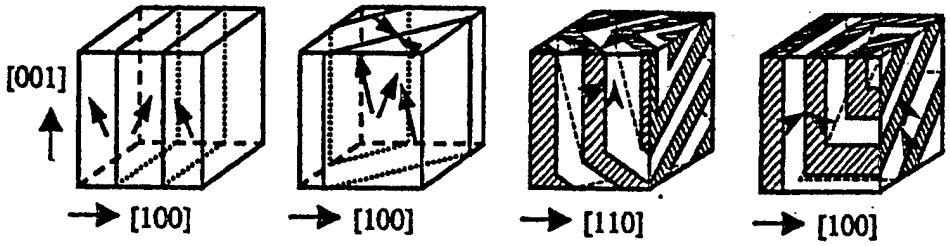

FIGURE 3 Illustration of possible domain structures that form the patterns in Figure 2. (a) front view. (b) top view. (c) top view. (d) front view.

walls with sample surfaces are either parallel or form a 45° angle with one of the edges of the sample. More importantly, contrary to the conventional reported ferroelectric twins of head to tail charge neutral configurations, the twin patterns in Figure 3(a) contain charged walls with the polarizations form either head to head or tail to tail configurations between the two domain states $\mathbf{Ps}\|[111]$ and $\mathbf{Ps}\|[1\bar{1}1]$. The polarization vectors of the two domains in the twins form a 71° angle in this case. In Figure 3(b), the domain walls between the two domain states $\mathbf{Ps}\|[111]$ and $\mathbf{Ps}\|[\bar{1}\bar{1}1]$ are also charged with the polarization vectors form a 109° angle. The most interesting phenomena observed was the co-existence of charged and uncharged domain walls, which has never been reported in the literature. Figure 2(c) and 2(d) show two complex domain patterns of such co-existence of charged and uncharged domain walls, which join each other to form "L" and "T" shaped patterns. One can see that the macroscopic symmetry of such systems is very low.

MACROSCOPIC SYMMETRY

From Figure 2 and Figure 3, one can see that the two implicit assumptions in treating the multi-domain systems to be macroscopic tetragonal are generally not satisfied. First of all, the domain size is fairly large compared to the sample size, ranging from 10 to 100μm, so that there will be only 20-100 domains across the sample. Second, the domains are coupled strongly to each other in the form of elastic twins. These two facts invalidate the use of statistical description, which requires a large ensemble of independent elements. In fact, we found that only two of the four possible domains exist in most of the samples. This effectively reduced the macroscopic symmetry of this multi-domain crystal from 4*mm* to *mm*2 or even lower. In addition, both charged and neutral domain walls are present in the system, while the 4*mm* macroscopic symmetry requires all the walls to be charged. Theoretical study [9] predicted that the highest macroscopic symmetry of a two-domain system is orthorhombic *mm*2. The symmetry could be monoclinic *m* if the volume ratios of the two domains in the twin are different.[10]

The physical properties have been measured to corroborate the domain study on the macroscopic symmetry. Both ultrasonic and resonance methods [7] have been used for the measurements. Some of the measured properties of PZN-4.5%PT single crystal are listed in Table II, where ρ is the density, v is the ultrasonic velocity and d is the piezoelectric constant. The subscripts l and s represent the longitudinal and shear waves, respectively. For the shear waves, the first superscript direction [*lmn*] is for the propagating direction and the second superscript direction [*lmn*] is the displacement polarization direction.

TABLE II Measured properties of PZN-4.5%PT single crystal

$\rho(v_l^{[110]})^2$ 10^{10} N/m^2	$\rho(v_l^{[1\bar{1}0]})^2$ 10^{10} N/m^2	$\rho(v_s^{[001],[100]})^2$ 10^{10} N/m^2	$\rho(v_s^{[001],[010]})^2$ 10^{10} N/m^2	d_{31} 10^{-12}C/N	$d_{31}^{[110]}$ 10^{-12}C/N
17.7	14.9	6.8	6.7	970	1154

The relations between measured values and physical property constants are given by

$$\rho(v_l^{[110]})^2 = \rho(v_l^{[1\bar{1}0]})^2 = \frac{1}{4}(c_{11}^E + c_{22}^E + 2c_{12}^E + 4c_{66}^E) \quad (1)$$

$$\rho(v_s^{[001],[100]})^2 = c_{55}^E \qquad \rho(v_s^{[001],[010]})^2 = c_{44}^E$$

$$d_{31}^{[110]} = \frac{1}{2}(d_{31} + d_{32})$$

For the microscopic symmetry of *4mm*,

$$c_{44}^E = c_{55}^E \quad \text{or} \quad \rho(v_s^{[001],[100]})^2 = \rho(v_s^{[001],[010]})^2 \quad (2)$$

$$d_{31} = d_{32} \quad \text{or} \quad d_{31} = d_{31}^{[110]} \quad (3)$$

Obviously, equations (1)-(3) cannot be met by the measured values in Table II. Therefore, the macroscopic symmetry of the domain engineered PZN-4.5%PT single crystal is better represented by the orthorhombic symmetry *mm*2 or even lower rather than the tetragonal *4mm*.

SUMMARY

Our optical microscopy studies showed that the domain patterns in the domain engineered PZN-4.5%PT single crystals are predominantly twins containing only two of the four possible domains after being poled in [001]. The size of the domains is relatively large, ranging from 10-100 μm, therefore, one may conclude that the previously assumed macroscopic *4mm* symmetry for the [001] poled rhombohedral phase crystal might not be always appropriate. This conclusion is supported by the ultrasonic measurements. As theoretically predicted [9] the highest macroscopic symmetry of a two-domain system is orthorhombic *mm*2. The symmetry could be even lower if the volume ratios of the two domains in the twin are different.[10] The most intriguing phenomenon observed was the co-existence of charged and uncharged domain walls joining together to form either "L" or "T" shaped domain walls. Based on energy

consideration, in order for the charged walls to exist, charged dopants or charged defects must be distributed near the wall region to reduce the electrostatic energy. On the other hand, the existence of these intersected domain walls could introduce high elastic strain energy, making the domain structures less stable, which could be one of the main reasons for the multi-domain structure to produce high value of dielectric and piezoelectric coefficients.

ACKNOWLEDGEMENTS

This research was sponsored the Office of Naval Research under Grant # N00014-98-1-0527 and the National Institute of Health under Grant #P41 RR11795-01A1. Crystals used for this study were provided by Drs. S. E. Park and T. R. Shrout and we are also indebted to the technical assistance of Ms. Bei Jiang in sample preparation.

References

[1] S. E. Park and T. R. Shrout, *IEEE Trans. UFFC*, **44**, 1140 (1997).
[2] S. E. Park and T. R. Shrout, *J. Appl. Phys.*, **82**, 1804 (1997).
[3] S. F. Liu, S. E. Park, T. R. Shrout, and L. E. Cross, *J. Appl. Phys.*, **85**, 2810 (1999).
[4] S. Nomura, T. Takahashi and Y.Yokomizo, *J. Phys. Soc. Jpn.*, **27**, 262 (1969).
[5] J. Kuwata, K. Uchino and S. Noemura, *Ferroelectrics*, **37**, 579 (1981).
[6] J. Kuwata, K. Uchino and S. Noemura, *Jpn. J. Appl. Phys.*, **21**, 1298 (1982).
[7] J. Yin, B. Jiang and W. Cao, *IEEE Trans. UFFC*, **47**, 285 (2000).
[8] J. Fousek and V. Janovec, J. Appl. Phys., **40**, 135 (1969).
[9] J. Yin and W. Cao, J. Appl. Phys., **87**, 7438 (2000).
[10] J. Erhart and W. Cao, *J. Appl. Phys.*, **86**, 1073 (1999).
[11] J. Erhart and W. Cao, *J. Mat. Res.*, in press, (2000).

Appendix 5

Jianhua Yin and Wenwu Cao, "Domain configurations in domain engineered 0.955Pb(Zn1/3Nb2/3)O3–0.045PbTiO3 single crystals," Journal of A pplied Physics, 87 [10], 7438–7441 (May 2000).

Domain configurations in domain engineered $0.955Pb(Zn_{1/3}Nb_{2/3})O_3-0.045PbTiO_3$ single crystals

Jianhua Yin and Wenwu Cao[a)]
Materials Research Laboratory, The Pennsylvania State University, University Park, Pennsylvania 16802

(Received 21 September 1999; accepted for publication 3 February 2000)

We report an optical microscopy study on the domain structures of $0.955Pb(Zn_{1/3}Nb_{2/3})O_3-0.045PbTiO_3$ rhombohedral phase single crystals poled along [001] of the cubic coordinates. Both charged and uncharged domain walls are observed in domain engineered samples and they could join together to form "L" and "T" shaped domain walls, which are very unique. The observed domains are between 10 and 100 μm in size, which are much bigger than expected. Most of the samples have only two of the four possible degenerate domain states, making the macroscopic symmetry to be *mm2* or lower rather than *4mm* previously assumed. © *2000 American Institute of Physics.* [S0021-8979(00)02710-9]

Single crystal $(1-x)Pb(Zn_{1/3}Nb_{2/3})O_3-xPbTiO_3$ (PZN–PT) system of the rhombohedral ferroelectric phase can have very high coupling constant and piezoelectric constant after being poled along [001].[1–3] It has triggered a new wave of material research recently to improve material properties using domain engineering, i.e., using a different poling scheme to manipulate domain structures. It also raised many interesting scientific questions, such as the origin of these superior properties and the role of domains in general. The very high electromechanical coupling coefficient (k_{33} >90%) and piezoelectric coefficient (d_{33}>2000 pC/N) produced by domain engineering method make the PZN–PT a much better candidate for transducer materials than the $PbZrO_3$–$PbTiO_3$(PZT) solid solution system used for the past 40 years. The PZN–PT single crystal solid solution system has been made in the late 1960s[4] and it was found that the electromechanical coupling coefficient k_{33} could be more than 90% in some samples.[5,6] However, the composition studied was at the boundary composition of the tetragonal phase, therefore, properties were not as high and not as consistent. The newly established domain engineering method makes it possible to stabilize the polarization of the rhombohedral phase by poling the crystals in [001] rather than the polarization direction of [111].[1–3]

Understanding the physical mechanism of this property enhancement is very important for extending this domain engineering idea to other materials. Naturally, the key issue is the domain structures since the off-polarization direction poling will create a multidomain single crystal system. This article reports an experimental study on the domain structures in a $0.955Pb(Zn_{1/3}Nb_{2/3})O_3-0.045PbTiO_3$ [PZN–4.5%PT] system, which has a microscopic symmetry of *3m*.

Because the dipoles of the PZN–4.5%PT form along the body diagonals of the parent cubic perovskite structure at the ferroelectric phase transition, the crystal has rhombohedral symmetry with the symmetry group *3m* in the ferroelectric state.[4,5] Poling was done by applying an electric field along [001] of the cubic coordinates so that only four of the eight possible polarization orientations remain, i.e., [111], [$\bar{1}$11], [1$\bar{1}$1], and [$\bar{1}\bar{1}$1]. Statistically, such a system would have a pseudomacroscopic tetragonal symmetry considering the degeneracy of these four domain states. All previous studies on this system were based on this *4mm* symmetry assumption.[1–3,7,8]

However, it was found experimentally that the material properties of the domain engineered PZN–4.5%PT could

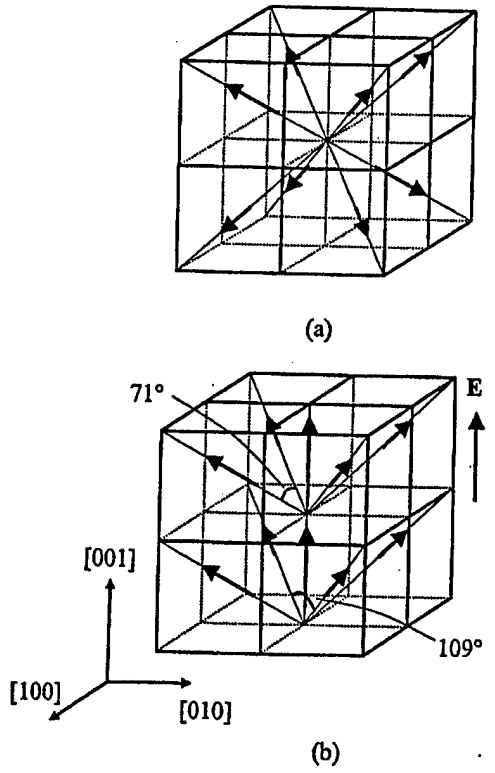

FIG. 1. Illustration of the assumed domain structure with cross intersecting charged domain walls for the PZN–4.5%PT. (a) There are eight possible orientations of dipoles before poling. (b) Four orientations remain after poling for the polarization. The structure is macroscopically tetragonal.

a)Electronic mail: cao@math.psu.edu

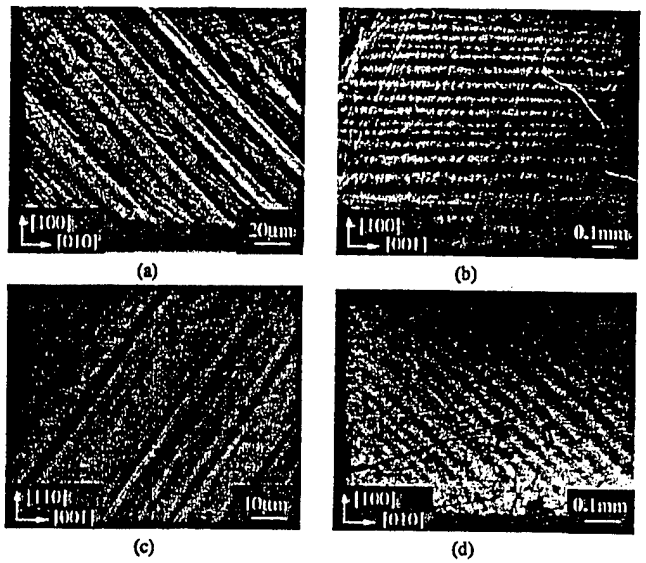

FIG. 2. Domain patterns observed on different sample surfaces. In each sample, there is only one set of twins with fairly large domain size. (a) On (001) surface; (b) on (010) surface; (c) on ($1\bar{1}0$) surface; and (d) same as (a) but in different sample and different scale.

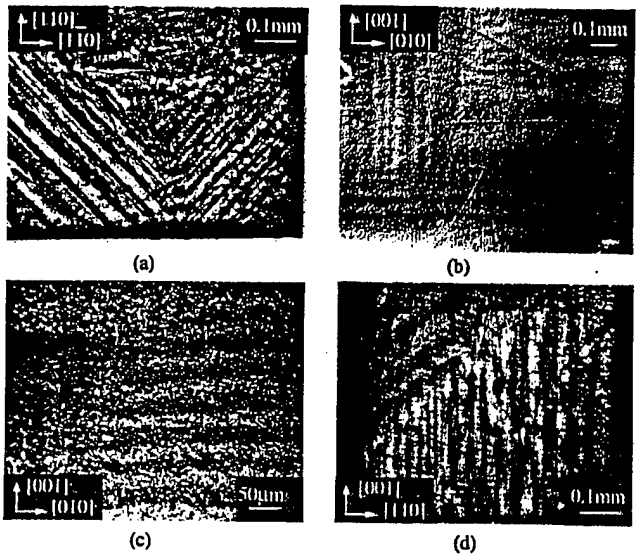

FIG. 3. A charged and an uncharged domain walls join together to form L or T shaped domain walls. (a) on (001) surface; (b) and (c) on (001) surface; and (d) on ($1\bar{1}0$) surface.

change substantially from sample to sample, particularly sensitive to the sample geometry.[7,8] There are also indications from our ultrasonic measurements that the elastic properties deviate from the *4mm* symmetry in many of the samples. In order to understand this issue, we used optical microscopy to exam the domain patterns in the [001] poled PZN–4.5%PT multidomain single crystals and performed some simple analyses to interpret these observed domain structures. The most interesting phenomena observed was the coexistence of charged and uncharged domain walls, which has never been reported in the literature.

The macroscopic symmetry defined in this article is what reflected in the macroscopic material properties, which do not change with the overall shape of the sample but only with the domain configurations. The *4mm* macroscopic tetragonal symmetry assumption implicitly assumed the following two conditions: (1) the domain size is very small compared to sample dimensions so that large amount of domains exist to allow the use of statistical principle; and (2) the domain walls are all charged and are parallel to the effective polarization direction (i.e., the wall normal is perpendicular to the applied poling field) as shown in Fig. 1.

For the domain observations, we prepared many samples with three pairs of mutually perpendicular surfaces. These samples have two types of orientations: [001]/[010]/[100] and [001]/[110]/[$1\bar{1}0$]. The sample shapes are cubes, plates, or bars with the typical dimension of *1–5mm*. Observations were performed on the surfaces of the following three orientations: [001], [110], and [100], with the samples being poled along [001] in all cases. Because the crystal is translucent, domains could be observed by polarizing optical microscopy in either reflection mode or transmission mode.

Figures 2 and 3 show a few of the domain patterns obtained in the domain engineered PZN–4.5%PT system. One can see that the two implicit assumptions in treating the system to be macroscopic tetragonal are not satisfied. First of all, the domain size is fairly large compared to the sample size, ranging from 10 to 100 μm, so that there will be only 20–100 domains across the sample. Second, the domains are coupled strongly to each other in the form of elastic twins. These two facts invalidate the use of statistical description, which requires a large ensemble of independent elements. In fact, we found that only two of the four possible domains exist in most of the samples. This effectively reduced the macroscopic symmetry of this multidomain crystal from *4mm* to *mm 2* or even lower. In addition, both charged and neutral domain walls are present in the system, while the *4mm* macroscopic symmetry requires all the walls to be charged.

In a $m\bar{3}m \rightarrow 3m$ ferroelectric phase transition, such as occurred in the PZN–4.5%PT system, the permissible domain walls formed in the ferroelectric phase are orientated in ⟨100⟩ and ⟨110⟩ family. The angle between polarization vectors on the two sides of a domain wall can be either 109° or 71°. We listed in Table I, all the permissible domain walls

TABLE I. Permissible orientations of domain walls in [001] poled PZN–4.5%PT crystals of rhombohedral phase. The polarization directions of $\mathbf{P}_s$ and $\mathbf{P}_s'$ in a twin structure are given in the first row.

$\mathbf{P}_s/\mathbf{P}_s'$	[111]/[$\bar{1}$11]	[111]/[1$\bar{1}$1]	[111]/[11$\bar{1}$]	[$\bar{1}$11]/[1$\bar{1}$1]	[$\bar{1}$11]/[11$\bar{1}$]	[1$\bar{1}$1]/([11$\bar{1}$]
Charged	[100]	[010]	[110]	[1$\bar{1}$0]	[010]	[100]
Uncharged	[011]	[101]	[001]	[001]	[$\bar{1}$01]	[0$\bar{1}$1]

TABLE II. Illustration of possible twin patterns in [001]/[010]/[100] and [001]/[110]/[1$\bar{1}$0] oriented rhombohedral PZN–4.5%PT single crystals poled along [001].

wall orientation	{001}	{110}	{010}	{101}
[001] [010] [100]	(a)	(b) 45°	(c)	(d) 45°
[001] [110] [1$\bar{1}$0]	(e)	(f)	(g) 45°	(h) 45° 55°

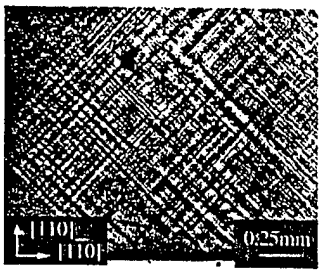

FIG. 4. Two sets of twins intersecting each other to form a network of four different domain states. This is the top view from [001].

between different pairing schemes among the four remaining domains after poling. It can be shown that the intersection lines of the domain walls on the sample surface may form 0°, 45°, and 55° angles with respect to the edges of the samples as shown in Table II.

Figure 2 shows the domain patterns of types (b), (c), (f), and (g), respectively, listed in Table II. One can see that the intersection lines of domain walls with sample surfaces are either parallel or form a 45° angle with one of the edges of the sample. More importantly, contrary to the conventional reported ferroelectric twins of head to tail charge neutral configurations, the twin patterns type (b) and type (f) in Table II contain charged walls with the polarizations form either head to head or tail to tail configurations between the two domain states $\mathbf{P}_s\|[111]$ and $\mathbf{P}_s\|[\bar{1}\bar{1}1]$. The polarization vectors of the two domains in the twins form a 109° angle in this case. Types (c) and (g) in Table II are the twin patterns between $\mathbf{P}_s\|[111]$ and $\mathbf{P}_s\|[1\bar{1}1]$. The domain walls are also charged with the polarization vectors form a 71° angle. Uncharged walls, such as type (h) in Table II between $\mathbf{P}_s\|[111]$ and $\mathbf{P}_s\|[1\bar{1}1]$, were also observed in some of the samples. The intersection lines between the charge neutral walls and the sample surfaces form either a 45° or 55° angle with respect to the sample edges as indicated in Table II.

Figure 3 shows several observed complex domain patterns. They are both charged and uncharged domain walls and it is very interesting to see that the charged and uncharged walls could join each other to form "L" and "T" shaped patterns. In part of one sample with the orientations of [100]/[010]/[001] and the corresponding dimensions of *2.4mm/2.27mm/0.43mm*, respectively, all four possible domains were found to coexist after poling in [001] as shown in Fig. 4.

In order to better understand these observed patterns, we have made simple analysis based on the crystal structure and illustrated in Fig. 5 some possible complex patterns made of two and four domain states. The observed patterns in Figs. 3 and 4 could be matched to those patterns of Fig. 5 as the following:

Fig. 3(a)→the top view of Fig. 5(e);

Fig. 3(b)→front view of the configuration Figs. 5(b) or 5(c);

Fig. 3(c)→front view of Fig. 5 (a);

Fig. 3(d)→front view of Fig. 5 (d) (upside down), and

Fig. 4→front view of Fig. 5(f).

Figure 4 is a pattern showing the coexistence of all four possible domains, $\mathbf{P}_s\|[111]$, $\mathbf{P}_s\|[1\bar{1}1]$, $\mathbf{P}_s\|[\bar{1}11]$, and $\mathbf{P}_s\|[\bar{1}\bar{1}1]$. Statistically speaking, this configuration should be the most probable structure after poling in [001], since the four ferroelectric variants are energetic degenerate. However, because the wall intersection causes energy, we only have seen such domain patterns in a small potion of one of the samples.

In summary, our optical microscopy studies showed that the domain patterns in the domain engineered PZN–4.5%PT single crystals are predominantly twins containing only two

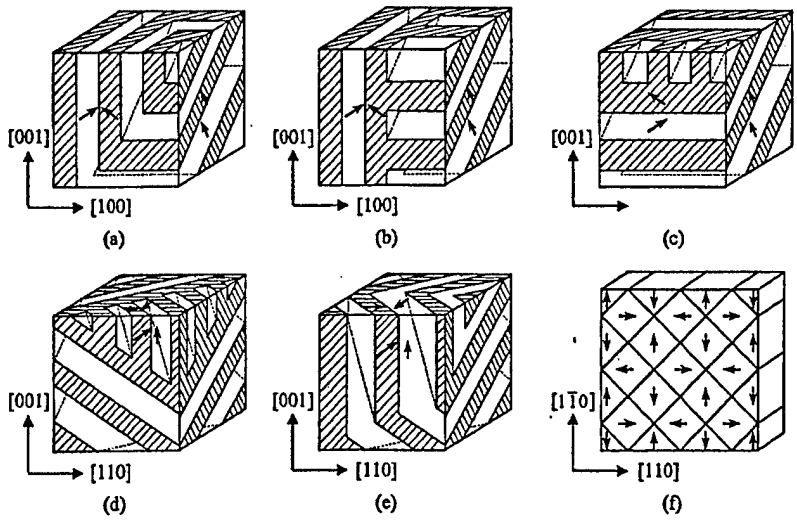

FIG. 5. Illustration of domain patterns that can be formed by the combination of charged and uncharged domain walls. (a)–(e) are patterns of twinning by two domains. One can see that L and T shaped domain walls are formed by joining a charged and an uncharged wall. (f) is the domain pattern for the coexistence of all four possible domains.

of the four possible domains after being poled in [001]. The size of the domains is relatively large, ranging from 10 to 100 μm, therefore, one may conclude that the previously assumed macroscopic *4mm* symmetry for the [001] poled rhombohedral phase crystal might not be always appropriate. As theoretically predicted[9] the highest macroscopic symmetry of a two-domain system is orthorhombic *mm2*. The symmetry could be even lower if the volume ratios of the two domains in the twin are different.[10] The most intriguing phenomenon observed was the coexistence of charged and uncharged domain walls joining together in a poled PZN–4.5%PT system, and these joined walls could form either L or T shaped domain walls. Based on energy consideration, in order for the charged walls to exist, charged dopants or defects must be distributed near the wall region to reduce the electrostatic energy. On the other hand, the existence of these intersected domain walls could introduce high elastic strain energy, making the domain structures less stable, which could be one of the main reasons for the multidomain structure to be more responsive to external drive, producing high value of dielectric and piezoelectric coefficients.

This research was sponsored the Office of Naval Research under Grant No. N00014-98-1-0527 and the National Institute of Health under Grant No. P41 RR11795-01A 1. Crystals used for this study were provided by Dr. S. E. Park and Dr. T. R. Shrout and we are also indebted to the technical assistance of Bei Jiang in sample preparation.

[1] S. E. Park and T. R. Shrout, IEEE Trans. Ultrason. Ferroelectr. Freq. Control **44**, 1140 (1997).
[2] S. E. Park and T. R. Shrout, J. Appl. Phys. **82**, 1804 (1997).
[3] S. F. Liu, S. E. Park, T. R. Shrout, and L. E. Cross, J. Appl. Phys. **85**, 2810 (1999).
[4] S. Nomura, T. Takahashi, and Y. Yokomizo, J. Phys. Soc. Jpn. **27**, 262 (1969).
[5] J. Kuwata, K. Uchino, and S. Noemura, Ferroelectrics **37**, 579 (1981).
[6] J. Kuwata, K. Uchino, and S. Noemura, Jpn. J. Appl. Phys., Part 1 **21**, 1298 (1982).
[7] J. Yin, B. Jiang, and W. Cao, Proc. SPIE, Medical Imaging, San Diego, CA (1999).
[8] J. Yin, B. Jiang and W. Cao, IEEE Trans. Ultranson. Ferroelectr. Freq. Control **43**, 285 (2000).
[9] J. Erhart and W. Cao, J. Appl. Phys. **86**, 1073 (1999).
[10] J. Erhart and W. Cao (unpublished).

Appendix 6

Jirí Erhart and Wenwu Cao, "Effective material properties in twinned ferroelectric crystals," Journal of Applied Physics, 86[2] 1073–1081 (July1999).

Effective material properties in twinned ferroelectric crystals

Jiří Erhart[a] and Wenwu Cao[b]
Materials Research Laboratory, Pennsylvania State University, University Park, Pennsylvania 16802

(Received 25 January 1999; accepted for publication 7 April 1999)

Without external fields, ferroelectric materials will have multidomain configuration in the ferroelectric state. Detailed analysis found that twinning may not be treated as random since the number of orientations for the domain walls are limited in a given symmetry change during a ferroelectric phase transition. In each finite region of a large crystal or in small crystallites, a particular set of twins is favored under certain boundary conditions, which consists of only two of the low temperature variants. Statistic models of random distribution of domains do not apply for calculating the physical properties of such twin structures. However, one could derive the two domain twin properties by using the constitutive equations and appropriate mechanical boundary considerations. This paper presents a theoretical analysis on such a two-domain twin system, including its global symmetry and effective material properties resulting from different twinning configurations. Numerical results are derived for $LiNbO_3$ and $BaTiO_3$. © *1999 American Institute of Physics.* [S0021-8979(99)01214-1]

I. INTRODUCTION

The macroscopic material properties of a multidomain ferroelectric system are the collective average of individual domains. Traditionally, people took statistic average of the properties of all the low temperature variants and used the volume ratio as the weighting factor. However, in reality, different physical properties may follow different averaging rules depending on the geometric configuration. For many properties the contribution of each domain do not always coincide with their volume ratio. For example, the elastic constant of a fiber reinforced composite is much larger in the fiber length direction than in its radial direction, although the volume ratio can be the same. Similarly, in a multidomain system the contribution of each domain not only depends on the volume ratio but also on the relative geometric configuration and on the orientation of the applied external fields. Experimental evidence showed that the domains often appear in a twin band with only two variants in the set.[1,2] Even for a ceramic system, domains observed in each given grain are mostly twin pair sets rather than all the available variants. Such a limited variant twinning pattern is more pronounced in a single crystal system since all orientations must be coherently joined together. Each twin band often occupies a sizable volume in a large single crystal. Generally speaking, two-variant twinning is the basis of all multidomain systems in ferroelectrics.

Recent development in domain engineering of relaxor based single crystal systems (e.g., for single crystals PZN-PT, PMN-PT) produced much enhanced piezoelectric and dielectric properties.[3] Experimental observation showed that many engineered crystal systems have only two variants.[4] Even those nonpoled samples are composed of large regions of two-variant twin band structures. Experimental observation of these relaxor based single crystals revealed that the twinning mostly consists of two variant twins[5,6] (for PZN and for $BaTiO_3$). It is also found that the orientation of the two-domain system and the selection of the variants can significantly influence the effective material properties of multidomain systems. This means that the statistical model or models, based only on the volume ratio, will not give proper prediction of the physical properties in these domain engineered crystals. Roughly speaking, the volume ratio average scheme assumed isotropic distribution of domain walls and ignored the cross coupling between different quantities of the associated domains.

If we utilize the fact that the basic domain structure only consists of two variants and they have a certain orientation relation in domain engineered crystal systems, it is possible to accurately derive the apparent macroscopic property by directly applying external loads to the system. Such a two-variant domain set can then serve as the building block for calculating properties of systems with more complex domain patterns.

The importance of calculating the effective properties of two domains lies in the fact that the macroscopic properties observed experimentally, whether from an ultrasonic method or from a resonance technique, are actually a collective contribution of the *existing* domains, not all *possible* domains. In a given domain engineered single crystal, only some of the low temperature variants can appear.

Because of the importance of predicting the effective material properties, there is vast literature on property averaging of multicomponent systems. For example, the equivalent elastic constants were previously calculated for two layer elastic system[7] by using the volume ratio as the weighting factor for both the stress and strain. This approach allows the calculation of elastic properties in two layer system for materials of any symmetry and any orientation between the two layers. This method was later extended to piezoelectric materials.[8] The dynamic approach for calculating the effec-

[a]On leave from the Department of Physics, Technical University of Liberec, Liberec, Czech Republic.
[b]Electronic mail: cao@math.psu.edu

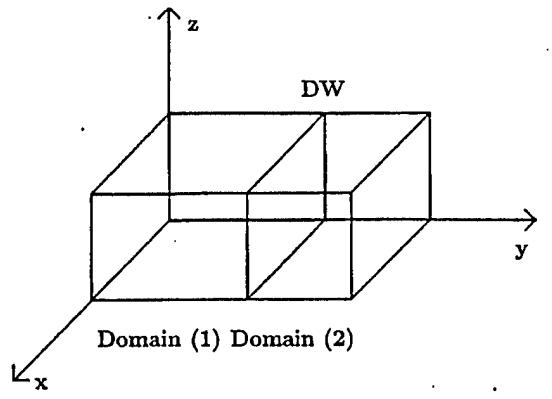

FIG. 1. The two domain system with coordinate systems chosen with the y axis perpendicular to the domain wall (DW).

tive material properties of piezoelectric layered material of arbitrary orientation[9] was based on the nature of acoustic wave propagation in layered material in the long-wavelength limit. It allowed explicit calculation of a complete set of all material properties. Another method for effective material property calculations is the method of effective medium which was applied to calculate the properties of polycrystalline ceramics[10–12] and piezoelectric composites.[13,14] The mechanical stress and electric field were assumed uniform in the matrix and in the inclusion (grains). The average was calculated under a number of assumptions about the space distribution and the shape of inclusions (spherical and elliptical shape). Effective material properties for 1–3 composites were calculated for $6mm$ symmetry as a function of volume fraction.[13] While all of these techniques have advantages and disadvantages in certain aspects, they have provided guidance for many particular applications and for the proper characterization of multicomponent systems of interest to a certain accuracy.

However, it is not appropriate to use the volume ratio average if there are only a limited number of domains in a system. In this paper we will try to eliminate some of those less convincing assumptions used in previous averaging methods and to develop a systematic procedure particularly applicable to a two-domain twin system. We will use different weighting factors for different physical properties based on the relative orientation to the external stress and electric field. Some quantities in each domain can be the same as in the combined twin system rather than all quantities being the weighted average. We will also give the macroscopic symmetry associated with twinning of different pairs of the low temperature variants resulting from cubic to rhombohedral and cubic to tetragonal ferroelectric phase transitions.

II. AVERAGING OF TENSOR PROPERTIES IN A TWIN CRYSTAL

For the twinned structure under study, we assume that the two variants have a volume ratio of $v^{(1)}$ and $v^{(2)}$ and the domain wall (DW) is perpendicular to the y axis. Considering the unit cell of a twin structure as shown in Fig. 1, we can apply static stress and electric field to the system and use the response to derive the effective average property of this twin crystal. For generality, we allow the crystallographic symmetry of both materials to be arbitrary, however the material properties of both domains must be expressed in the same coordinate system before performing the average. For a ferroelectric system, the material properties are represented by the elastic compliance tensor $\mathbf{s}^{(i)}$, piezoelectric constant tensor $\mathbf{d}^{(i)}$ and dielectric constant tensor $\boldsymbol{\epsilon}^{(i)}$, which satisfy the constitutive relations

$$\begin{pmatrix} \boldsymbol{\eta}^{(i)} \\ \mathbf{D}^{(i)} \end{pmatrix} = \begin{pmatrix} \mathbf{s}^{(i)} & \mathbf{d}^{(i)T} \\ \mathbf{d}^{(i)} & \boldsymbol{\epsilon}^{(i)} \end{pmatrix} \begin{pmatrix} \mathbf{T}^{(i)} \\ \mathbf{E}^{(i)} \end{pmatrix} \quad (i=1,2), \tag{1}$$

where the superscripts (1) and (2) represent the quantity for domain 1 and domain 2, respectively. $\boldsymbol{\eta}^{(i)}$ and $\mathbf{D}^{(i)}$ are the elastic strain tensor and the electric displacement vector, $\mathbf{T}^{(i)}$ and $\mathbf{E}^{(i)}$ are the stress and electric field, respectively. The two domains can be of different thickness, which is represented by volume ratios $v^{(1)}$ and $v^{(2)}$ with $v^{(1)}+v^{(2)}=1$. Components of elastic strain $\boldsymbol{\eta}$ are assumed to be symmetric, while the components of elastic stress do not have this symmetry due to the cross domain coupling. The simplified notation is related to the true tensor notation in the following form:

$$T_\lambda = \begin{cases} T_{ij} & i=j \\ T_{ij}+T_{ji} & i\neq j \end{cases} \quad (i,j=1,2,3; \quad \lambda=1,\ldots,6). \tag{2}$$

Since the material properties are similar in magnitude for the two domains, unlike the case of polymer–ceramic composite,[15,16] it is reasonable to assume that the mechanical stress, strain, electric field and electric displacement in both domains are homogeneous in the equilibrium state. At equilibrium, the effective stress and strain of the twin system is symmetric and the two domains are required to form a coherent nonseparating boundary (DW) under external applied stresses. For convenience, we will use the shortened notation for all the tensor components of material properties defined by[17]

$$s_{\lambda\nu} = \begin{cases} s_{ijkl} & i=j,k=l \\ 2s_{ijkl} & i\neq j,k=l \\ 2s_{ijkl} & i=j,k\neq l \\ 4s_{ijkl} & i\neq j,k\neq l \end{cases} \quad (i,j,k,l=1,2,3; \quad \lambda,\nu=1,\ldots,6), \tag{3a}$$

$$d_{i\mu} = \begin{cases} d_{ijk} & j=k \\ 2d_{ijk} & j\neq k \end{cases} \quad (j,k=1,2,3;\mu=1,\ldots,6). \tag{3b}$$

The constitutive relations for each of the domains are

$$\eta_{ij}^{(n)} = d_{kij}^{(n)} E_k^{(n)} + s_{ijkl}^{(n)} T_{kl}^{(n)}, \tag{4a}$$

$$D_i^{(n)} = \epsilon_{ij}^{(n)} E_j^{(n)} + d_{ijk}^{(n)} T_{jk}^{(n)} \quad (i,j,k,l=1,2,3;n=1,2), \tag{4b}$$

where $T_{ij}^{(n)}$ and $E_k^{(n)}$ are the components of the elastic stress tensor and electric field vector, respectively.

Volume ratio averaging conditions can be expressed as[8]

$$\eta_{ij}^{\text{eff}} = v^{(1)}\eta_{ij}^{(1)} + v^{(2)}\eta_{ij}^{(2)}, \tag{5a}$$

$$T_{ij}^{\text{eff}} = v^{(1)}T_{ij}^{(1)} + v^{(2)}T_{ij}^{(2)} \quad (i,j=1,2,3). \tag{5b}$$

These relations cannot hold true simultaneously for both the strain and stress as one can see from the twin structure in Fig. 1. We need to redefine the conditions for such a system for which the orientation and configuration are known. Mechanical equilibrium and nonseparable boundary conditions, i.e., the continuity of the three components of stress: $T_{22}^{(i)}, T_{23}^{(i)}$ and $T_{21}^{(i)}$, six components of strain: $\eta_{11}^{(i)}, \eta_{33}^{(i)}, \eta_{32}^{(i)}, \eta_{13}^{(i)}, \eta_{31}^{(i)}$ and $\eta_{12}^{(i)}$, two components of electric field, $E_1^{(i)}$ and $E_3^{(i)}$, and the electric displacement $D_2^{(i)}$, $(i=1,2)$, lead directly to the following conditions across the domain wall:

$$\eta_{11}^{(1)} = \eta_{11}^{(2)}, \tag{6a}$$

$$\eta_{33}^{(1)} = \eta_{33}^{(2)}, \tag{6b}$$

$$\eta_{32}^{(1)} = \eta_{32}^{(2)}, \tag{6c}$$

$$\eta_{13}^{(1)} = \eta_{13}^{(2)}, \tag{6d}$$

$$\eta_{31}^{(1)} = \eta_{31}^{(2)}, \tag{6e}$$

$$\eta_{12}^{(1)} = \eta_{12}^{(2)}, \tag{6f}$$

$$D_2^{(1)} = D_2^{(2)}, \tag{6g}$$

$$T_{22}^{(1)} = T_{22}^{(2)}, \tag{6h}$$

$$T_{23}^{(1)} = T_{23}^{(2)}, \tag{6i}$$

$$T_{21}^{(1)} = T_{21}^{(2)}, \tag{6j}$$

$$E_1^{(1)} = E_1^{(2)}, \tag{6k}$$

$$E_3^{(1)} = E_3^{(2)}. \tag{6l}$$

These conditions provided different averaging rules for some components of elastic stress, strain, electric field and electric displacement.

Equations (6a)–(6l) give the relations between the elastic stress and electric field in domain 2 and domain 1. For a prescribed stress or electric field to the twinned system, one can first represent the stress and field in domains 1 and 2 using the global quantities. Then, these tensor components can be substituted into Eqs. (5a)–(5b) to find the effective material properties. The linear system of equations, Eqs. (6a)–(6l) can be solved in matrix form

$$\mathbf{b}^{(1)}\boldsymbol{\tau}^{(1)} = \mathbf{b}^{(2)}\boldsymbol{\tau}^{(2)}, \tag{7}$$

where

$$\mathbf{b}^{(i)} = \begin{pmatrix}
s_{11}^{(i)} & s_{12}^{(i)} & s_{13}^{(i)} & s_{14}^{(i)} & s_{14}^{(i)} & s_{15}^{(i)} & s_{16}^{(i)} & s_{16}^{(i)} & d_{11}^{(i)} & d_{21}^{(i)} & d_{31}^{(i)} \\
0 & 1 & 0 & 0 & 0 & 0 & 0 & 0 & 0 & 0 & 0 \\
s_{13}^{(i)} & s_{23}^{(i)} & s_{33}^{(i)} & s_{34}^{(i)} & s_{34}^{(i)} & s_{35}^{(i)} & s_{36}^{(i)} & s_{36}^{(i)} & d_{13}^{(i)} & d_{23}^{(i)} & d_{33}^{(i)} \\
0 & 0 & 0 & 1 & 0 & 0 & 0 & 0 & 0 & 0 & 0 \\
s_{14}^{(i)} & s_{24}^{(i)} & s_{34}^{(i)} & s_{44}^{(i)} & s_{44}^{(i)} & s_{45}^{(i)} & s_{46}^{(i)} & s_{46}^{(i)} & d_{14}^{(i)} & d_{24}^{(i)} & d_{34}^{(i)} \\
s_{15}^{(i)} & s_{25}^{(i)} & s_{35}^{(i)} & s_{45}^{(i)} & s_{45}^{(i)} & s_{55}^{(i)} & s_{56}^{(i)} & s_{56}^{(i)} & d_{15}^{(i)} & d_{25}^{(i)} & d_{35}^{(i)} \\
s_{16}^{(i)} & s_{26}^{(i)} & s_{36}^{(i)} & s_{46}^{(i)} & s_{46}^{(i)} & s_{56}^{(i)} & s_{66}^{(i)} & s_{66}^{(i)} & d_{16}^{(i)} & d_{26}^{(i)} & d_{36}^{(i)} \\
0 & 0 & 0 & 0 & 0 & 0 & 0 & 1 & 0 & 0 & 0 \\
0 & 0 & 0 & 0 & 0 & 0 & 0 & 0 & 1 & 0 & 0 \\
d_{21}^{(i)} & d_{22}^{(i)} & d_{23}^{(i)} & d_{24}^{(i)} & d_{24}^{(i)} & d_{25}^{(i)} & d_{26}^{(i)} & d_{26}^{(i)} & \epsilon_{12}^{(i)} & \epsilon_{22}^{(i)} & \epsilon_{23}^{(i)} \\
0 & 0 & 0 & 0 & 0 & 0 & 0 & 0 & 0 & 0 & 1
\end{pmatrix} \quad (i=1,2) \tag{8}$$

and transposed vector $\boldsymbol{\tau}^{(i)}$ is given by

$$\boldsymbol{\tau}^{(i)T} = (T_{11}^{(i)}, T_{22}^{(i)}, T_{33}^{(i)}, \tfrac{1}{2}T_{23}^{(i)}, \tfrac{1}{2}T_{32}^{(i)}, \tfrac{1}{2}(T_{13}^{(i)}+T_{31}^{(i)}), \tfrac{1}{2}T_{12}^{(i)}, \tfrac{1}{2}T_{21}^{(i)}, E_1^{(i)}, E_2^{(i)}, E_3^{(i)}). \tag{9}$$

To find out the effective material properties of the two-domain system, we can use matrix calculations. In the examples, however, we will solve them in steps for convenience.

Nine simple loads for the two-domain system were applied to help us derive the independent effective constants. In each case, only one or two components of the load are nonzero.

longitudinal stress

1. $T_{11}^{\text{eff}} \neq 0$
2. $T_{22}^{\text{eff}} \neq 0$
3. $T_{33}^{\text{eff}} \neq 0$

} all other T_{ij}^{eff} are zero and $E_i^{\text{eff}} = 0$;

shear stress

4. $T_{23}^{\text{eff}}\neq 0, T_{32}^{\text{eff}}\neq 0$
5. $T_{13}^{\text{eff}}\neq 0, T_{31}^{\text{eff}}\neq 0$
6. $T_{12}^{\text{eff}}\neq 0, T_{21}^{\text{eff}}\neq 0$

} all other T_{ij}^{eff} are zero and $E_i^{\text{eff}}=0$;

electric field

7. $E_1^{\text{eff}}\neq 0$
8. $E_2^{\text{eff}}\neq 0$
9. $E_3^{\text{eff}}\neq 0$

} all other E_i^{eff} are zero and $T_{ij}^{\text{eff}}=0$.

The constitutive relations become relatively simple for these nine independent loads for calculating the effective material properties. Usually only one kind of material constants for the effective material is involved in each equation.

Putting each of these nine independent loads into Eqs. (6a)–(6l) and using the averaging rules, Eqs. (5a)–(5b) we obtain the linear system of equations

$$\mathbf{A}\mathbf{x}_i=\mathbf{y}_i, \tag{10a}$$

$$\mathbf{A}=\mathbf{A}^{(1)}+\frac{v^{(1)}}{v^{(2)}}\mathbf{A}^{(2)}, \tag{10b}$$

$$\mathbf{A}^{(i)}=\begin{pmatrix} s_{11}^{(i)} & s_{13}^{(i)} & s_{14}^{(i)} & s_{15}^{(i)} & s_{16}^{(i)} & d_{21}^{(i)} \\ s_{13}^{(i)} & s_{33}^{(i)} & s_{34}^{(i)} & s_{35}^{(i)} & s_{36}^{(i)} & d_{23}^{(i)} \\ s_{14}^{(i)} & s_{34}^{(i)} & s_{44}^{(i)} & s_{45}^{(i)} & s_{46}^{(i)} & d_{24}^{(i)} \\ s_{15}^{(i)} & s_{35}^{(i)} & s_{45}^{(i)} & s_{55}^{(i)} & s_{56}^{(i)} & d_{25}^{(i)} \\ s_{16}^{(i)} & s_{36}^{(i)} & s_{46}^{(i)} & s_{56}^{(i)} & s_{66}^{(i)} & d_{26}^{(i)} \\ d_{21}^{(i)} & d_{23}^{(i)} & d_{24}^{(i)} & d_{25}^{(i)} & d_{26}^{(i)} & \epsilon_{22}^{(i)} \end{pmatrix} \quad (i=1,2), \tag{10c}$$

$$\mathbf{x}_i=\begin{pmatrix} T_{11}^{(1)} \\ T_{33}^{(1)} \\ \frac{1}{2}T_{32}^{(1)} \\ \frac{1}{2}(T_{13}^{(1)}+T_{31}^{(1)}) \\ \frac{1}{2}T_{12}^{(1)} \\ E_2^{(1)} \end{pmatrix} \quad (i=1,2,\ldots,9), \tag{10d}$$

$$\mathbf{y}_1=\frac{1}{v^{(2)}}T_{11}^{\text{eff}}\begin{pmatrix} s_{11}^{(2)} \\ s_{13}^{(2)} \\ s_{14}^{(2)} \\ s_{15}^{(2)} \\ s_{16}^{(2)} \\ d_{21}^{(2)} \end{pmatrix} \qquad \mathbf{y}_2=T_{22}^{\text{eff}}\begin{pmatrix} s_{12}^{(2)}-s_{12}^{(1)} \\ s_{23}^{(2)}-s_{23}^{(1)} \\ s_{24}^{(2)}-s_{24}^{(1)} \\ s_{25}^{(2)}-s_{25}^{(1)} \\ s_{26}^{(2)}-s_{26}^{(1)} \\ d_{22}^{(2)}-d_{22}^{(1)} \end{pmatrix}, \tag{10e}$$

$$\mathbf{y}_3=\frac{1}{v^{(2)}}T_{33}^{\text{eff}}\begin{pmatrix} s_{13}^{(2)} \\ s_{33}^{(2)} \\ s_{34}^{(2)} \\ s_{35}^{(2)} \\ s_{36}^{(2)} \\ d_{23}^{(2)} \end{pmatrix}$$

$$\mathbf{y}_4=\tfrac{1}{2}T_{23}^{\text{eff}}\begin{pmatrix} \left(1+\frac{1}{v^{(2)}}\right)s_{14}^{(2)}-s_{14}^{(1)} \\ \left(1+\frac{1}{v^{(2)}}\right)s_{34}^{(2)}-s_{34}^{(1)} \\ \left(1+\frac{1}{v^{(2)}}\right)s_{44}^{(2)}-s_{44}^{(1)} \\ \left(1+\frac{1}{v^{(2)}}\right)s_{45}^{(2)}-s_{45}^{(1)} \\ \left(1+\frac{1}{v^{(2)}}\right)s_{46}^{(2)}-s_{46}^{(1)} \\ \left(1+\frac{1}{v^{(2)}}\right)d_{24}^{(2)}-d_{24}^{(1)} \end{pmatrix}, \tag{10f}$$

$$\mathbf{y}_5=\frac{1}{v^{(2)}}T_{13}^{\text{eff}}\begin{pmatrix} s_{15}^{(2)} \\ s_{35}^{(2)} \\ s_{45}^{(2)} \\ s_{55}^{(2)} \\ s_{56}^{(2)} \\ d_{25}^{(2)} \end{pmatrix}$$

$$\mathbf{y}_6=\tfrac{1}{2}T_{12}^{\text{eff}}\begin{pmatrix} \left(1+\frac{1}{v^{(2)}}\right)s_{16}^{(2)}-s_{16}^{(1)} \\ \left(1+\frac{1}{v^{(2)}}\right)s_{36}^{(2)}-s_{36}^{(1)} \\ \left(1+\frac{1}{v^{(2)}}\right)s_{46}^{(2)}-s_{46}^{(1)} \\ \left(1+\frac{1}{v^{(2)}}\right)s_{56}^{(2)}-s_{56}^{(1)} \\ \left(1+\frac{1}{v^{(2)}}\right)s_{66}^{(2)}-s_{66}^{(1)} \\ \left(1+\frac{1}{v^{(2)}}\right)d_{26}^{(2)}-d_{26}^{(1)} \end{pmatrix}, \tag{10g}$$

$$\mathbf{y}_7 = E_1^{\text{eff}} \begin{pmatrix} d_{11}^{(2)} - d_{11}^{(1)} \\ d_{13}^{(2)} - d_{13}^{(1)} \\ d_{14}^{(2)} - d_{14}^{(1)} \\ d_{15}^{(2)} - d_{15}^{(1)} \\ d_{16}^{(2)} - d_{16}^{(1)} \\ \epsilon_{12}^{(2)} - \epsilon_{12}^{(1)} \end{pmatrix} \quad \mathbf{y}_8 = \frac{1}{v^{(2)}} E_2^{\text{eff}} \begin{pmatrix} d_{21}^{(2)} \\ d_{23}^{(2)} \\ d_{24}^{(2)} \\ d_{25}^{(2)} \\ d_{26}^{(2)} \\ \epsilon_{22}^{(2)} \end{pmatrix}, \tag{10h}$$

$$\mathbf{y}_9 = E_3^{\text{eff}} \begin{pmatrix} d_{31}^{(2)} - d_{31}^{(1)} \\ d_{33}^{(2)} - d_{33}^{(1)} \\ d_{34}^{(2)} - d_{34}^{(1)} \\ d_{35}^{(2)} - d_{35}^{(1)} \\ d_{36}^{(2)} - d_{36}^{(1)} \\ \epsilon_{23}^{(2)} - \epsilon_{23}^{(1)} \end{pmatrix}. \tag{10i}$$

The mechanical stresses $T_{ij}^{(1)}$ and electric field $E_2^{(1)}$ are different in general for these simple loads. Values of mechanical stress and electric field in domain 2 can be expressed from Eqs. (6a)–(6l) using values of corresponding components in domain 1. We can solve Eq. (10a) and substitute the results into Eqs. (5a)–(5b) to find the effective material properties for the two-domain system. Detailed procedure is illustrated in the example below.

III. EXAMPLES OF TENSOR PROPERTY AVERAGING FOR A TWIN CRYSTAL WITH THE SAME VOLUME RATIOS OF THE TWO DOMAINS

As an example, we calculate the effective material properties of a $3m$ symmetry class single crystal, such as the PZN-PT single crystal, with a set of twins containing equal volume ratios of the two domains. First of all, we need to rotate all tensor components of material properties for both domains from their own material coordinates to the same global coordinate system (material coordinate for the parent cubic structure). Components of material properties for domains 1 and 2 are rotated to the common coordinate system using matrices

$$\mathbf{R}^{(1)} = \begin{pmatrix} \frac{1}{\sqrt{2}} & \frac{1}{\sqrt{6}} & \frac{1}{\sqrt{3}} \\ -\frac{1}{\sqrt{2}} & \frac{1}{\sqrt{6}} & \frac{1}{\sqrt{3}} \\ 0 & -\frac{2}{\sqrt{6}} & \frac{1}{\sqrt{3}} \end{pmatrix}$$

and

$$\mathbf{R}^{(2)} = \begin{pmatrix} -\frac{1}{\sqrt{2}} & \frac{1}{\sqrt{6}} & \frac{1}{\sqrt{3}} \\ -\frac{1}{\sqrt{2}} & -\frac{1}{\sqrt{6}} & -\frac{1}{\sqrt{3}} \\ 0 & -\frac{2}{\sqrt{6}} & \frac{1}{\sqrt{3}} \end{pmatrix}. \tag{11}$$

Because the prototype symmetry of the paraelectric phase is cubic, the possible DW orientations[18] for the two domains with polarization $P_S[111]$ and $P_S[1\bar{1}1]$ are [010] and [101]. We calculate the effective material properties for the case with DW oriented in [010]. Domains are often observed as periodic twin bands in most ferroelectric materials, therefore it is reasonable to assume the same volume ratios for the two domains, i.e., $v^{(1)} = v^{(2)} = \frac{1}{2}$, the expected symmetry of such a twin structure and its effective material properties is $mm2$.

Independent material properties for the $3m$ symmetry class in its own crystallographic coordinate system with the mirror symmetry plane perpendicular to the x axis can be found in published tables.[17]

Material properties for domain 1 in the chosen coordinate system (as plotted in Fig. 1) are

$$\mathbf{s}'^{(1)} = \begin{pmatrix} s'_{11} & s'_{12} & s'_{12} & s'_{14} & s'_{15} & s'_{15} \\ s'_{12} & s'_{11} & s'_{12} & s'_{15} & s'_{14} & s'_{15} \\ s'_{12} & s'_{12} & s'_{11} & s'_{15} & s'_{15} & s'_{14} \\ s'_{14} & s'_{15} & s'_{15} & s'_{44} & s'_{45} & s'_{45} \\ s'_{15} & s'_{14} & s'_{15} & s'_{45} & s'_{44} & s'_{45} \\ s'_{15} & s'_{15} & s'_{14} & s'_{45} & s'_{45} & s'_{44} \end{pmatrix}, \tag{12a}$$

$$\boldsymbol{\epsilon}'^{(1)} = \begin{pmatrix} \epsilon'_{11} & \epsilon'_{12} & \epsilon'_{12} \\ \epsilon'_{12} & \epsilon'_{11} & \epsilon'_{12} \\ \epsilon'_{12} & \epsilon'_{12} & \epsilon'_{11} \end{pmatrix}, \tag{12b}$$

$$\mathbf{d}'^{(1)} = \begin{pmatrix} d'_{11} & d'_{12} & d'_{12} & d'_{14} & d'_{15} & d'_{15} \\ d'_{12} & d'_{11} & d'_{12} & d'_{15} & d'_{14} & d'_{15} \\ d'_{12} & d'_{12} & d'_{11} & d'_{15} & d'_{15} & d'_{14} \end{pmatrix}, \tag{12c}$$

while material properties for the second domain in the same coordinate system can be derived as

$$\mathbf{s}'^{(2)} = \begin{pmatrix} s'_{11} & s'_{12} & s'_{12} & -s'_{14} & s'_{15} & -s'_{15} \\ s'_{12} & s'_{11} & s'_{12} & -s'_{15} & s'_{14} & -s'_{15} \\ s'_{12} & s'_{12} & s'_{11} & -s'_{15} & s'_{15} & -s'_{14} \\ -s'_{14} & -s'_{15} & -s'_{15} & s'_{44} & -s'_{45} & s'_{45} \\ s'_{15} & s'_{14} & s'_{15} & -s'_{45} & s'_{44} & -s'_{45} \\ -s'_{15} & -s'_{15} & -s'_{14} & s'_{45} & -s'_{45} & s'_{44} \end{pmatrix}, \tag{13a}$$

$$\boldsymbol{\epsilon}'^{(2)} = \begin{pmatrix} \epsilon'_{11} & -\epsilon'_{12} & \epsilon'_{12} \\ -\epsilon'_{12} & \epsilon'_{11} & -\epsilon'_{12} \\ \epsilon'_{12} & -\epsilon'_{12} & \epsilon'_{11} \end{pmatrix}, \tag{13b}$$

$$\mathbf{d}'^{(2)} = \begin{pmatrix} d'_{11} & d'_{12} & d'_{12} & -d'_{14} & d'_{15} & -d'_{15} \\ -d'_{12} & -d'_{11} & -d'_{12} & d'_{15} & -d'_{14} & d'_{15} \\ d'_{12} & d'_{12} & d'_{11} & -d'_{15} & d'_{15} & -d'_{14} \end{pmatrix}, \tag{13c}$$

where

$$s'_{11}=\tfrac{1}{9}(4s_{11}+4s_{13}+4\sqrt{2}s_{14}+s_{33}+2s_{44}), \tag{14a}$$

$$s'_{12}=\tfrac{1}{9}(s_{11}+3s_{12}+4s_{13}-2\sqrt{2}s_{14}+s_{33}-s_{44}), \tag{14b}$$

$$s'_{14}=\tfrac{2}{9}(s_{11}-3s_{12}+s_{13}+\sqrt{2}s_{14}+s_{33}-s_{44}), \tag{14c}$$

$$s'_{15}=\tfrac{1}{9}(-4s_{11}+2s_{13}-\sqrt{2}s_{14}+2s_{33}+s_{44}), \tag{14d}$$

$$s'_{44}=\tfrac{2}{9}(5s_{11}-3s_{12}-4s_{13}-4\sqrt{2}s_{14}+2s_{33}+s_{44}), \tag{14e}$$

$$s'_{45}=\tfrac{1}{9}(-2s_{11}+6s_{12}-8s_{13}+4\sqrt{2}s_{14}+4s_{33}-s_{44}), \tag{14f}$$

$$d'_{11}=\frac{1}{3\sqrt{3}}(2d_{15}-2\sqrt{2}d_{22}+2d_{31}+d_{33}), \tag{14g}$$

$$d'_{12}=\frac{1}{3\sqrt{3}}(-d_{15}+\sqrt{2}d_{22}+2d_{31}+d_{33}), \tag{14h}$$

$$d'_{14}=-\frac{2}{3\sqrt{3}}(d_{15}+2\sqrt{2}d_{22}+d_{31}-d_{33}), \tag{14i}$$

$$d'_{15}=\frac{1}{3\sqrt{3}}(d_{15}+2\sqrt{2}d_{22}-2d_{31}+2d_{33}), \tag{14j}$$

$$\epsilon'_{11}=\tfrac{1}{3}(2\epsilon_{11}+\epsilon_{33}), \tag{14k}$$

$$\epsilon'_{12}=\tfrac{1}{3}(-\epsilon_{11}+\epsilon_{33}). \tag{14l}$$

As an example, let us apply load 1, i.e., $T_{11}^{\text{eff}}\neq 0$, other are all zero (the other loads 2–9 can be solved similarly). The corresponding matrices for the linear system are

$$\mathbf{A}=\begin{pmatrix} 2s'_{11} & 2s'_{12} & s'_{15} & 0 & 0 & 0 \\ 2s'_{12} & 2s'_{11} & s'_{15} & 0 & 0 & 0 \\ 2s'_{15} & 2s'_{15} & s'_{44} & 0 & 0 & 0 \\ 0 & 0 & 0 & s'_{44} & s'_{45} & 2d'_{15} \\ 0 & 0 & 0 & s'_{45} & s'_{44} & 2d'_{15} \\ 0 & 0 & 0 & d'_{15} & d'_{15} & 2\epsilon'_{11} \end{pmatrix}, \tag{15a}$$

$$\mathbf{x}_1=\begin{pmatrix} T_{11}^{(1)} \\ T_{33}^{(1)} \\ T_{12}^{(1)} \\ T_{32}^{(1)} \\ T_{13}^{(1)}+T_{31}^{(1)} \\ E_2^{(1)} \end{pmatrix}, \tag{15b}$$

$$\mathbf{y}_1=(2T_{11}^{\text{eff}})\begin{pmatrix} s'_{11} \\ s'_{12} \\ s'_{15} \\ -s'_{14} \\ -s'_{15} \\ -d'_{12} \end{pmatrix}, \tag{15c}$$

where we reshaped matrix $\mathbf{A}$ and vectors $\mathbf{x}_1,\mathbf{y}_1$ for convenience. The solution of Eq. (10a) for our particular case is given by

$$T_{11}^{(1)}=T_{11}^{\text{eff}},\quad T_{33}^{(1)}=0,\quad T_{13}^{(1)}+T_{31}^{(1)}=0, \tag{16}$$

$$T_{32}^{(1)}=(-2T_{11}^{\text{eff}})\frac{\det\mathbf{B}_1}{\det\mathbf{B}},\quad T_{12}^{(1)}=(-2T_{11}^{\text{eff}})\frac{\det\mathbf{B}_2}{\det\mathbf{B}},$$

$$E_2^{(1)}=(-T_{11}^{\text{eff}})\frac{\det\mathbf{B}_3}{\det\mathbf{B}}, \tag{17}$$

where

$$\mathbf{B}=\begin{pmatrix} s'_{44} & s'_{45} & d'_{15} \\ s'_{45} & s'_{44} & d'_{15} \\ d'_{15} & d'_{15} & \epsilon'_{11} \end{pmatrix}\quad \mathbf{B}_1=\begin{pmatrix} s'_{14} & s'_{45} & d'_{15} \\ s'_{15} & s'_{44} & d'_{15} \\ d'_{12} & d'_{15} & \epsilon'_{11} \end{pmatrix}, \tag{18}$$

$$\mathbf{B}_2=\begin{pmatrix} s'_{44} & s'_{14} & d'_{15} \\ s'_{45} & s'_{15} & d'_{15} \\ d'_{15} & d'_{12} & \epsilon'_{11} \end{pmatrix}\quad \mathbf{B}_3=\begin{pmatrix} s'_{44} & s'_{45} & s'_{14} \\ s'_{45} & s'_{44} & s'_{15} \\ d'_{15} & d'_{15} & d'_{12} \end{pmatrix}. \tag{19}$$

Mechanical stresses in domain 2 are expressed as

$$T_{11}^{(2)}=T_{11}^{\text{eff}},\quad T_{33}^{(2)}=0,\quad T_{32}^{(2)}=-T_{32}^{(1)}, \tag{20}$$

$$T_{13}^{(2)}+T_{31}^{(2)}=0,\quad T_{12}^{(2)}=-T_{12}^{(1)},\quad E_2^{(2)}=-E_2^{(1)}. \tag{21}$$

Now we can substitute these expressions into the averaging conditions Eqs. (6a)–(6l) and obtain some of the effective material properties for the two-domain system. The same procedure can be applied to the other loads 2–9 and a complete set of effective material properties for the twin structure will be obtained and they are explicitly given below:

$$\mathbf{s}^{\text{eff}}=\begin{pmatrix} s_{11}^{\text{eff}} & s_{12}^{\text{eff}} & s_{13}^{\text{eff}} & 0 & s_{15}^{\text{eff}} & 0 \\ s_{12}^{\text{eff}} & s_{22}^{\text{eff}} & s_{12}^{\text{eff}} & 0 & s_{25}^{\text{eff}} & 0 \\ s_{13}^{\text{eff}} & s_{12}^{\text{eff}} & s_{11}^{\text{eff}} & 0 & s_{15}^{\text{eff}} & 0 \\ 0 & 0 & 0 & s_{44}^{\text{eff}} & 0 & s_{46}^{\text{eff}} \\ s_{15}^{\text{eff}} & s_{25}^{\text{eff}} & s_{15}^{\text{eff}} & 0 & s_{55}^{\text{eff}} & 0 \\ 0 & 0 & 0 & s_{46}^{\text{eff}} & 0 & s_{44}^{\text{eff}} \end{pmatrix}, \tag{22a}$$

$$\boldsymbol{\epsilon}^{\text{eff}}=\begin{pmatrix} \epsilon_{11}^{\text{eff}} & 0 & \epsilon_{13}^{\text{eff}} \\ 0 & \epsilon_{22}^{\text{eff}} & 0 \\ \epsilon_{13}^{\text{eff}} & 0 & \epsilon_{11}^{\text{eff}} \end{pmatrix}, \tag{22b}$$

$$\mathbf{d}^{\text{eff}}=\begin{pmatrix} d_{11}^{\text{eff}} & d_{12}^{\text{eff}} & d_{13}^{\text{eff}} & 0 & d_{15}^{\text{eff}} & 0 \\ 0 & 0 & 0 & d_{24}^{\text{eff}} & 0 & d_{24}^{\text{eff}} \\ d_{13}^{\text{eff}} & d_{12}^{\text{eff}} & d_{11}^{\text{eff}} & 0 & d_{15}^{\text{eff}} & 0 \end{pmatrix}, \tag{22c}$$

where

$$s_{11}^{\text{eff}}=s'_{11}-(s'_{14}\det\mathbf{B}_1+s'_{15}\det\mathbf{B}_2+d'_{12}\det\mathbf{B}_3)/\det\mathbf{B}, \tag{23a}$$

$$s_{12}^{\text{eff}}=s'_{12}-(s'_{15}\det\mathbf{B}_1+s'_{15}\det\mathbf{B}_2+d'_{11}\det\mathbf{B}_3)/\det\mathbf{B}, \tag{23b}$$

$$s_{13}^{\text{eff}}=s'_{12}-(s'_{15}\det\mathbf{B}_1+s'_{14}\det\mathbf{B}_2+d'_{12}\det\mathbf{B}_3)/\det\mathbf{B}, \tag{23c}$$

$$s_{15}^{\text{eff}}=s'_{15}-(s'_{45}\det\mathbf{B}_1+s'_{45}\det\mathbf{B}_2+d'_{14}\det\mathbf{B}_3)/\det\mathbf{B}, \tag{23d}$$

$$s_{22}^{\text{eff}}=s'_{11}-(s'_{15}\det\mathbf{B}_4+s'_{15}\det\mathbf{B}_5+d'_{11}\det\mathbf{B}_6)/\det\mathbf{B}, \tag{23e}$$

$$s_{25}^{\text{eff}}=s'_{14}-(s'_{45}\det\mathbf{B}_4+s'_{45}\det\mathbf{B}_5+d'_{14}\det\mathbf{B}_6)/\det\mathbf{B}, \quad (23f)$$

$$s_{44}^{\text{eff}}=s'_{44}-(s'_{14}\det\mathbf{B}_7+s'_{15}\det\mathbf{B}_8+s'_{45}\det\mathbf{B}_9)/\det\mathbf{B}^*, \quad (23g)$$

$$s_{46}^{\text{eff}}=s'_{45}-(s'_{15}\det\mathbf{B}_7+s'_{14}\det\mathbf{B}_8+s'_{45}\det\mathbf{B}_9)/\det\mathbf{B}^*, \quad (23h)$$

$$s_{55}^{\text{eff}}=s'_{44}-(s'_{45}\det\mathbf{B}_{10}+s'_{45}\det\mathbf{B}_{11}+d'_{14}\det\mathbf{B}_{12})/\det\mathbf{B}, \quad (23i)$$

$$\epsilon_{11}^{\text{eff}}=\epsilon'_{11}-(d'_{14}\det\mathbf{B}_{13}+d'_{15}\det\mathbf{B}_{14}+\epsilon'_{12}\det\mathbf{B}_{15})/\det\mathbf{B}, \quad (23j)$$

$$\epsilon_{13}^{\text{eff}}=\epsilon'_{12}-(d'_{15}\det\mathbf{B}_{13}+d'_{14}\det\mathbf{B}_{14}+\epsilon'_{12}\det\mathbf{B}_{15})/\det\mathbf{B}, \quad (23k)$$

$$\epsilon_{22}^{\text{eff}}=\epsilon'_{11}-(d'_{12}\det\mathbf{B}_{16}+d'_{12}\det\mathbf{B}_{17}+d'_{14}\det\mathbf{B}_{18})/\det\mathbf{B}^*, \quad (23l)$$

$$d_{11}^{\text{eff}}=d'_{11}-(s'_{14}\det\mathbf{B}_{13}+s'_{15}\det\mathbf{B}_{14}+d'_{12}\det\mathbf{B}_{15})/\det\mathbf{B}, \quad (23m)$$

$$d_{12}^{\text{eff}}=d'_{12}-(s'_{15}\det\mathbf{B}_{13}+s'_{15}\det\mathbf{B}_{14}+d'_{11}\det\mathbf{B}_{15})/\det\mathbf{B}, \quad (23n)$$

$$d_{13}^{\text{eff}}=d'_{12}-(s'_{15}\det\mathbf{B}_{13}+s'_{14}\det\mathbf{B}_{14}+d'_{12}\det\mathbf{B}_{15})/\det\mathbf{B}, \quad (23o)$$

$$d_{15}^{\text{eff}}=d'_{15}-(s'_{45}\det\mathbf{B}_{13}+s'_{45}\det\mathbf{B}_{14}+d'_{14}\det\mathbf{B}_{15})/\det\mathbf{B}, \quad (23p)$$

$$d_{24}^{\text{eff}}=d'_{15}-(s'_{14}\det\mathbf{B}_{16}+s'_{15}\det\mathbf{B}_{17}+s'_{45}\det\mathbf{B}_{18})/\det\mathbf{B}^*, \quad (23q)$$

where

$$\mathbf{B}^*=\begin{pmatrix} s'_{11} & s'_{12} & s'_{15} \\ s'_{12} & s'_{11} & s'_{15} \\ s'_{15} & s'_{15} & s'_{44} \end{pmatrix} \quad \mathbf{B}_4=\begin{pmatrix} s'_{15} & s'_{45} & d'_{15} \\ s'_{14} & s'_{44} & d'_{15} \\ d'_{11} & d'_{15} & \epsilon'_{11} \end{pmatrix}, \quad (24a)$$

$$\mathbf{B}_5=\begin{pmatrix} s'_{44} & s'_{15} & d'_{15} \\ s'_{45} & s'_{15} & d'_{15} \\ d'_{15} & d'_{11} & \epsilon'_{11} \end{pmatrix} \quad \mathbf{B}_6=\begin{pmatrix} s'_{44} & s'_{45} & s'_{15} \\ s'_{45} & s'_{44} & s'_{15} \\ d'_{15} & d'_{15} & d'_{11} \end{pmatrix}, \quad (24b)$$

$$\mathbf{B}_7=\begin{pmatrix} s'_{14} & s'_{12} & s'_{15} \\ s'_{15} & s'_{11} & s'_{15} \\ s'_{45} & s'_{15} & s'_{44} \end{pmatrix} \quad \mathbf{B}_8=\begin{pmatrix} s'_{11} & s'_{14} & s'_{15} \\ s'_{12} & s'_{15} & s'_{15} \\ s'_{15} & s'_{45} & s'_{44} \end{pmatrix}, \quad (24c)$$

$$\mathbf{B}_9=\begin{pmatrix} s'_{11} & s'_{12} & s'_{14} \\ s'_{12} & s'_{11} & s'_{15} \\ s'_{15} & s'_{15} & s'_{45} \end{pmatrix} \quad \mathbf{B}_{10}=\begin{pmatrix} s'_{45} & s'_{45} & d'_{15} \\ s'_{45} & s'_{44} & d'_{15} \\ d'_{14} & d'_{15} & \epsilon'_{11} \end{pmatrix}, \quad (24d)$$

$$\mathbf{B}_{11}=\begin{pmatrix} s'_{44} & s'_{45} & d'_{15} \\ s'_{45} & s'_{45} & d'_{15} \\ d'_{15} & d'_{14} & \epsilon'_{11} \end{pmatrix} \quad \mathbf{B}_{12}=\begin{pmatrix} s'_{44} & s'_{45} & s'_{45} \\ s'_{45} & s'_{44} & s'_{45} \\ d'_{15} & d'_{15} & d'_{14} \end{pmatrix}, \quad (24e)$$

$$\mathbf{B}_{13}=\begin{pmatrix} d'_{14} & s'_{45} & d'_{15} \\ d'_{15} & s'_{44} & d'_{15} \\ \epsilon'_{12} & d'_{15} & \epsilon'_{11} \end{pmatrix} \quad \mathbf{B}_{14}=\begin{pmatrix} s'_{44} & d'_{14} & d'_{15} \\ s'_{45} & d'_{15} & d'_{15} \\ d'_{15} & \epsilon'_{12} & \epsilon'_{11} \end{pmatrix}, \quad (24f)$$

$$\mathbf{B}_{15}=\begin{pmatrix} s'_{44} & s'_{45} & d'_{14} \\ s'_{45} & s'_{44} & d'_{15} \\ d'_{15} & d'_{15} & \epsilon'_{12} \end{pmatrix} \quad \mathbf{B}_{16}=\begin{pmatrix} d'_{12} & s'_{12} & s'_{15} \\ d'_{12} & s'_{11} & s'_{15} \\ d'_{14} & s'_{15} & s'_{44} \end{pmatrix}, \quad (24g)$$

$$\mathbf{B}_{17}=\begin{pmatrix} s'_{11} & d'_{12} & s'_{15} \\ s'_{12} & d'_{12} & s'_{15} \\ s'_{15} & d'_{14} & s'_{44} \end{pmatrix} \quad \mathbf{B}_{18}=\begin{pmatrix} s'_{11} & s'_{12} & d'_{12} \\ s'_{12} & s'_{11} & d'_{12} \\ s'_{15} & s'_{15} & d'_{14} \end{pmatrix}. \quad (24h)$$

The symmetry of these effective material properties is at least $mm2$. Some may show degeneracy in certain components.

Similar calculations can be carried out for any arbitrary material symmetry and arbitrary orientation of domains and DW.

IV. NUMERICAL EXAMPLES FOR $m3m \rightarrow 3m$ AND $m3m \rightarrow 4mm$ FERROELECTRIC SPECIES

In order to make some comparison between our method and the volume ratio weighted average, we have performed a numerical computation for two systems that have experimental data available in the single domain single crystal state. Unfortunately, the lack of experimental results prevented us from direct comparison to measured data for a two-domain twin band system. The two systems calculated represent domains formed at the ferroelectric phase transitions of $m3m \rightarrow 3m$ and $m3m \rightarrow 4mm$. ($BaTiO_3$) was chosen as an example for the $m3m \rightarrow 4mm$ transition. There are unfortunately no complete data sets available for the $m3m \rightarrow 3m$ transition. Therefore we used the numerical data of $LiNbO_3$ in the $3m$ phase and assumed that the domain structures could be engineered to the configurations resulting from a $m3m \rightarrow 3m$ transition (the true phase transition of $LiNbO_3$ is $\bar{3}m \rightarrow 3m$ and there are only 180° domains in its natural $3m$ phase).

If the effective material properties could be calculated based on volume ratio weighted average,[8] the effective material properties can have a very compact form. In vector notation, the effective material properties of a two-domain system are given by a 9×9 matrix

$$\mathbf{M}=\begin{pmatrix} \mathbf{s} & \mathbf{d}^T \\ \mathbf{d} & \boldsymbol{\epsilon} \end{pmatrix}, \quad (25)$$

where $\mathbf{s}$ is a 6×6 matrix of the elastic compliances, $\mathbf{d}$ is a 6×3 matrix of piezoelectric constants and $\boldsymbol{\epsilon}$ is a 3×3 matrix of the dielectric constant. Because the volume ratio weighting method eliminated the cross coupling between domain 1 and domain 2 and ignored the orientation effect, the effective material properties can be simply expressed as

$$\mathbf{M}=\left(\mathbf{M}^{(1)}(\mathbf{m}^{(1)})^{-1}\mathbf{m}^{(2)}+\frac{v^{(2)}}{v^{(1)}}\mathbf{M}^{(2)}\right) \times\left((\mathbf{m}^{(1)})^{-1}\mathbf{m}^{(2)}+\frac{v^{(2)}}{v^{(1)}}\mathbf{I}\right)^{-1}, \quad (26)$$

where $\mathbf{M}^{(1)}$ and $\mathbf{M}^{(2)}$ are matrices of material properties of both domains and $\mathbf{I}$ is a 9×9 unit matrix. The matrices $\mathbf{m}^{(1)}$ and $\mathbf{m}^{(2)}$ are given by

TABLE I. Effective material properties for two variant twin structure of $LiNbO_3$ and $BaTiO_3$. The coordinate system is chosen in the way that the y-axis is perpendicular to the DW. Zero values of tensor components are listed by dots.

Material property		$LiNbO_3$ DW(010)				$BaTiO_3$ DW(110)			
		$P_S[111]$	$P_S[1\bar{1}1]$	This work	Ref. 8	$P_S[100]$	$P_S[010]$	This work	Ref. 8
$S_{\alpha\beta}$	11	5.60	5.60	5.42	5.50	7.92	7.92	7.49	7.92
$[10^{-12}\,m^2\,N^{-1}]$	12	−1.36	−1.36	−1.10	−1.08	−1.28	−1.28	−1.71	−1.28
	13	−1.36	−1.36	−1.38	−1.46	−3.80	−3.80	−3.47	−3.79
	14	−1.35	1.35	...	...	...	...	...	...
	15	0.26	0.26	−0.49	−0.53	...	...	...	...
	16	0.26	−0.26	...	...	3.83	−3.83	...	...
	22	5.60	5.60	4.65	4.84	7.92	7.92	7.49	7.92
	23	−1.36	−1.36	−1.10	−1.08	−3.80	−3.80	−3.47	−3.79
	24	0.26	−0.26	...	...	...	...	...	...
	25	−1.35	−1.35	1.36	0.87	...	...	...	...
	26	0.26	−0.26	...	...	3.83	−3.83	...	...
	33	5.60	5.60	5.42	5.50	8.05	8.05	7.81	8.05
	34	0.26	−0.26	...	...	...	...	...	...
	35	0.26	0.26	−0.49	−0.53	...	...	...	...
	36	−1.35	1.35	...	...	−2.89	2.89	...	...
	44	15.65	15.65	15.27	15.27	13.62	13.62	11.94	11.94
	45	−0.98	0.98	...	...	4.78	−4.78	...	...
	46	−0.98	−0.98	−0.99	−0.99	...	...	...	...
	55	15.65	15.65	7.92	9.22	13.62	13.62	11.94	13.62
	56	−0.98	0.98	...	...	...	...	...	...
	66	15.65	15.65	15.27	15.27	34.23	34.23	30.63	30.63
$d_{l\alpha}$	11	16.28	16.28	11.84	15.53	−157	157	...	...
$[10^{-12}CN^{-1}]$	12	−5.83	−5.83	−5.03	−3.74	121	−121	...	...
	13	−5.83	−5.83	−3.14	−6.58	24	−24	...	...
	14	−47.11	47.11	...	...	...	...	...	...
	15	26.44	26.44	23.84	20.40	...	...	...	...
	16	26.44	−26.44	...	...	−85	−85	−127	−127
	21	−5.83	5.83	...	...	121	121	130	121
	22	16.28	−16.28	...	...	−157	−157	−147	−157
	23	−5.83	5.83	...	...	24	24	17	24
	24	26.44	26.44	22.23	22.23	...	...	...	...
	25	−47.11	47.11	...	...	...	...	...	...
	26	26.44	26.44	22.23	22.23	−85	85	...	...
	31	−5.83	−5.83	−3.14	−6.58	...	...	...	...
	32	−5.83	−5.83	−5.03	−3.74	...	...	...	...
	33	16.28	16.28	11.84	15.53	...	...	...	...
	34	26.44	−26.44	...	...	−277	−277	−179	−180
	35	26.44	26.44	23.84	20.40	−277	277	...	...
	36	−47.11	47.11	...	...	...	...	...	...
ϵ_{ij}	11	3.45	3.45	1.68	3.40	135	135	24.1	24.1
$[10^{-10}Fm^{-1}]$	12	−0.44	0.44	...	...	−121	121	...	...
	13	−0.44	−0.44	1.04	−0.50	...	...	...	...
	22	3.45	3.45	1.91	1.92	135	135	133.3	135.5
	23	−0.44	0.44	...	...	...	...	...	...
	33	3.45	3.45	1.68	3.40	256	256	199.6	199.6

$$\mathbf{m}^{(i)}=\begin{pmatrix} s_{11}^{(i)} & s_{12}^{(i)} & s_{13}^{(i)} & s_{14}^{(i)} & s_{15}^{(i)} & s_{16}^{(i)} & d_{11}^{(i)} & d_{21}^{(i)} & d_{31}^{(i)} \\ 0 & 1 & 0 & 0 & 0 & 0 & 0 & 0 & 0 \\ s_{13}^{(i)} & s_{23}^{(i)} & s_{33}^{(i)} & s_{34}^{(i)} & s_{35}^{(i)} & s_{36}^{(i)} & d_{13}^{(i)} & d_{23}^{(i)} & d_{33}^{(i)} \\ 0 & 0 & 0 & 1 & 0 & 0 & 0 & 0 & 0 \\ s_{15}^{(i)} & s_{25}^{(i)} & s_{35}^{(i)} & s_{45}^{(i)} & s_{55}^{(i)} & s_{56}^{(i)} & d_{15}^{(i)} & d_{25}^{(i)} & d_{35}^{(i)} \\ 0 & 0 & 0 & 0 & 0 & 1 & 0 & 0 & 0 \\ 0 & 0 & 0 & 0 & 0 & 0 & 1 & 0 & 0 \\ d_{21}^{(i)} & d_{22}^{(i)} & d_{23}^{(i)} & d_{24}^{(i)} & d_{25}^{(i)} & d_{26}^{(i)} & \epsilon_{12}^{(i)} & \epsilon_{22}^{(i)} & \epsilon_{23}^{(i)} \\ 0 & 0 & 0 & 0 & 0 & 0 & 0 & 0 & 1 \end{pmatrix} \quad (i=1,2). \tag{27}$$

Numerical values for a two-domain system of engineered $LiNbO_3$ and $BaTiO_3$ calculated using this approach[8] are listed in Table I to compare with the numerical values obtained by using the method given in this paper (also listed in Table I).

It is important to point out that the global symmetry of the twin structure is maintained whether or not the intercoupling between the two domains has been considered. For the case of $LiNbO_3$, the symmetry belongs to the $mm2$ class. For $BaTiO_3$ the symmetry of the system is also $mm2$, but there is additional degeneracy for some material properties. They are: $s_{44}^{\text{eff}}=s_{55}^{\text{eff}}$. Using the method of volume ratio average,[8] only two of the degenerate relations $s_{11}^{\text{eff}}=s_{22}^{\text{eff}}, s_{13}^{\text{eff}}=s_{23}^{\text{eff}}$ hold for the elastic compliance tensor.

From Table I, the difference in elastic properties calculated using these two methods is small. This is because the elastic properties of the two variants are very similar, the intercoupling effect is not significant. The difference is much larger in the piezoelectric and dielectric constants for lower symmetry systems. For $LiNbO_3$, the calculated piezoelectric coefficient d_{13} using these two methods differ by more than 100% and the dielectric coefficient ϵ_{13} even have different signs. It appears that the difference becomes smaller for higher symmetry systems. For the $4mm$ symmetry $BaTiO_3$, the difference is within a few percent for most of the quantities. Therefore, the volume ratio averaging method could give good predictions on the effective properties for higher symmetry systems but may run into problems for lower symmetry systems.

V. DISCUSSION AND CONCLUSIONS

In summary, we have reported in this paper a general procedure to calculate the effective material properties of a two-variant twin structure. The method has taken into account specifically all the boundary conditions and used more realistic relations for each individual tensor component, rather than using a unified volume ratio averaging scheme. This procedure requires to solve two sets of linear systems of equations and could be easily implemented using a computer. The equations are all linear and can be solved without much difficulty.

In order to compare our method to the volume averaging scheme, we have calculated two systems with polar symmetries of $3m$ and $4mm$ using both methods. It was found that the new method gives similar results for a $4mm$ system but predicts quite different piezoelectric and dielectric coefficients for $3m$ systems. In some components, the difference can exceed 100%. The elastic properties, however, differ very little for both symmetries because the two types of domains are very similar in elastic properties, therefore the coupling of the two domains does not make a significant difference while performing the property average.

Two variant twins are the basis of all twin structures as revealed by all microscopy works. Properly calculated, the effective property of the two-variant twins will pave the way to calculating more precisely more complicated multidomain single crystal ferroelectric systems.

ACKNOWLEDGMENTS

This work was supported by the National Science Foundation under Grant No. DNS 9704714 and by the Office of Naval Research under Grant Nos. N00014-98-1-0527 and N00014-96-1-1173. One of the authors (J.E.) is also grateful for partial support from the Ministry of Education of the Czech Republic (Code No. VS 96006, 1996).

[1] R. C. DeVries and J. E. Burke, J. Am. Ceram. Soc. **40**, 200 (1957).
[2] G. Arlt and P. Sasko, J. Appl. Phys. **51**, 4956 (1980).
[3] S. E. Park and T. Shrout, J. Appl. Phys. **82**, 1804 (1997).
[4] J. Yin and W. Cao (to be published).
[5] M. L. Mulvihill, L. E. Cross, W. Cao, and K. Uchino, J. Am. Ceram. Soc. **80**, 1462 (1997).
[6] M. L. Mulvihill, K. Uchino, Z. Li, and W. Cao, Philos. Mag. B **74**, 25 (1996).
[7] M. Grimsditch and F. Nizzolli, Phys. Rev. B **33**, 5891 (1986).
[8] E. Aksakaya and G. W. Farnell, J. Appl. Phys. **64**, 4469 (1988).
[9] E. Aksakaya, G. W. Farnell, and E. L. Adler, J. Appl. Phys. **68**, 1009 (1990).
[10] C.-W. Nan and D. R. Clarke, J. Am. Ceram. Soc. **79**, 2563 (1996).
[11] T. Olson and M. Avellaneda, J. Appl. Phys. **71**, 4455 (1992).
[12] N. A. Pertsev, A. G. Zembilgotov, and R. Waser, J. Appl. Phys. **84**, 1524 (1998).
[13] C.-W. Nan, J. Appl. Phys. **76**, 1155 (1994).
[14] M. L. Dunn and M. Taya, Int. J. Solids Struct. **30**, 161 (1993).
[15] W. Cao, Q. M. Zhang, and L. E. Cross, IEEE Trans. Ultrason. Ferroelectr. Freq. Control **40**, 103 (1993).
[16] W. A. Smith, A. Shaulov, and B. A. Auld, Proceedings IEEE Ultrasonic Symposium 1985, 642–647.
[17] J. F. Nye, *Physical Properties of Crystals* (Clarendon, Oxford, 1957).
[18] J. Fousek and V. Janovec, J. Appl. Phys. **40**, 135 (1969).

Appendix 7

Jirí Erhart and Wenwu Cao, "Effective symmetry and phyical properties of twinned perovskite ferroelectric single crystals," Journal of Materials Research, 16[2], 570–577 (February 2001).

Effective symmetry and physical properties of twinned perovskite ferroelectric single crystals

Jiří Erhart[a] and Wenwu Cao
Materials Research Laboratory, Pennsylvania State University, University Park, Pennsylvania 16802

(Received 21 July 1999; accepted 15 November 2000)

The effective symmetry and material properties of twinned ferroelectric crystals with perovskite structure were analyzed. The twins or twinbands studied here were formed during ferroelectric phase transitions, which resulted in one of the following symmetry changes: $m\bar{3}m \rightarrow 3m$, $m\bar{3}m \rightarrow 4mm$, and $m\bar{3}m \rightarrow mm2$. It was found that the volume ratios of the two domains in a twin structure were not always equal due to the existence of defect pinning to the domain walls. This unequal partition changed the effective symmetry; hence, the effective macroscopic physical properties of the twin system. Using the data of $LiNbO_3$, $BaTiO_3$, and $KNbO_3$, a detailed analysis has been carried out on macroscopic material property changes caused by the deviation from equal domain volume partition for crystals having $3m$, $4mm$, and $mm2$ symmetries.

I. INTRODUCTION

The macroscopic properties of a multidomain ferroelectric system are the collective contribution of many differently oriented domains. The macroscopic symmetry is in general different from the microscopic symmetry of the crystal when it is not in a single domain state. The recently developed relaxor-based ferroelectric single crystals $(1-x)Pb(Zn_{1/3}Nb_{2/3})O_3 - xPbTiO_3$ (PZN–PT) and $(1-x)Pb(Mg_{1/3}Nb_{2/3})O_3 - xPbTiO_3$ (PMN–PT) with intentionally created multidomain configurations are practical examples of such systems.[1] For these crystals, the microscopic crystal symmetry belongs to the rhombohedral $3m$ with dipoles formed in $\langle 111 \rangle$ family of the parent cubic perovskite structure. When a single ferroelectric crystal is poled along [001] of the cubic coordinates, four domain states, [111], $[\bar{1}11]$, $[1\bar{1}1]$, and $[\bar{1}\bar{1}1]$, are energetically equivalent to exist. Statistically, the effective macroscopic symmetry of the multidomain system has been assumed to have tetragonal $4mm$ symmetry. However, experimental measurements of the physical properties showed that the symmetry of many multidomain PZN–PT samples could be lower than $4mm$.[2,3] Further study of the domain patterns in these samples using optical microscopy revealed that most of the poled samples consist of only two of the four symmetry-allowed low-temperature domains.[4] For a two-domain system, the proper symmetry for the effective macroscopic properties should be $mm2$ or lower.[5]

Experimental evidence showed that the domains often form a twinband in which only two variants exist.[4] Even for a ceramic system, domains observed in each grain are mostly twin pairs rather than involving all the low-temperature variants. Such limited variant twinning patterns are more pronounced in a single-crystal system because all orientations must be coherently joined together. Generally speaking, two-variant twinning is the basis of all multidomain systems in ferroelectrics.

Understanding the symmetry of a multidomain system is very important for proper characterization of the macroscopic properties. It has been shown in Ref. 5 that a simple statistical model[6] would not provide accurate macroscopic properties because the interactions between the domains must be taken into account while responding to external fields. For this purpose, a new average scheme has been developed,[5] which takes into account the coherent interaction between the two domains across the domain wall in a twin structure.

Energetically, equal size domains are expected in a twinband because the domain wall energy is positive and the interactions between the walls are repulsive.[7,8] This may not be true in practical situations because the domain size adjustment is through domain wall (DW) movement while the wall movement is usually pinned by defects, preventing the equal domain size state to be reached. The pinning of surfaces and other elastic and electric boundary constraints to the domain movements could also cause the unequal partition of domains. This unequal volume partition has been observed experimentally in the twinband structures of lead titanate,[9] doped barium titanate,[10,11] and PZT,[12] and, practically speaking, in all other systems to a certain degree.

[a]On leave from the Department of Physics, Technical University of Liberec, Liberec, Czech Republic.

In this article, we generalize the method described in Ref. 5, in which only equal domain systems were studied, to analyze the symmetries of a twinned single crystal and calculate the corresponding changes of the macroscopic physical properties due to the change of domain ratio for three ferroelectric species: $m\bar{3}m \rightarrow 3m$, $m\bar{3}m \rightarrow 4mm$, and $m\bar{3}m \rightarrow mm2$. The objective is to provide the definition of effective macroscopic physical properties and the associated macroscopic symmetry for realistic twin structures, and more importantly, to quantify the variation of these properties caused by the change of domain volume ratio.

II. MICROSCOPIC AND MACROSCOPIC SYMMETRIES

In a $m\bar{3}m \rightarrow 3m$ ferroelectric phase transition, the possible directions for dipole formation are along the cube diagonals; i.e., the $\langle 111 \rangle$ family in the cubic coordinate system. The so-called domain enegineering of the PZN–PT and PMN–PT single crystals is to apply a poling field along the [001] direction rather than along the dipolar directions of $\langle 111 \rangle$ family. Four domain states, [111], $[\bar{1}11]$, $[1\bar{1}1]$, and $[\bar{1}\,\bar{1}1]$, remain energetically equivalent after poling with all dipoles at a 54.7° angle to the field direction of [001].[4] Permissible DWs[13] among these four ferroelectric states are listed in Table I. N/A means that DW does not exist. Two perpendicular DWs always exist between any two given domains states; one is charged and the other is neutral. The DW orientations are illustrated in Fig. 1 in the cubic coordinates.

For a charged DW between $\boldsymbol{P}^I$ and $\boldsymbol{P}^{II}$ oriented in [010] and a neutral DW between $\boldsymbol{P}^I$ and $\boldsymbol{P}^{III}$ oriented in [001], the effective macroscopic symmetry of the twin structure is monoclinic m [Figs. 1(a) and 1(b)]. The symmetry can be raised to orthorhombic $mm2$ when the two domains have identical size [Fig. 1(c)]. The twofold axis, which is also the direction of the effective polarization, is oriented in [101] as shown in Fig. 1(c).

For a $m\bar{3}m \rightarrow 4mm$ ferroelectric phase transition (such as $BaTiO_3$), the possible spontaneous polarization directions are in $\langle 100 \rangle$ family (in the cubic coordinate system). If the poling field is applied in [111] rather than one of the polarization directions, three domain states remain energetically equivalent to exist after poling with the dipoles in each of the unit cells also at a 54.7° angle to the poling field direction. Permissible DWs[13] among these three remaining ferro-

TABLE I. Permissible DW orientations[13] in ferroelectrics resulting from a $m\bar{3}m \rightarrow 3m$ phase transition and poled in [001] direction.

Domain state	$\mathbf{P}^I = \frac{P_S}{\sqrt{3}}[111]$	$\mathbf{P}^{II} = \frac{P_S}{\sqrt{3}}[1\bar{1}1]$	$\mathbf{P}^{III} = \frac{P_S}{\sqrt{3}}[\bar{1}\,\bar{1}\,1]$	$\mathbf{P}^{IV} = \frac{P_S}{\sqrt{3}}[\bar{1}11]$
$\mathbf{P}^I = \frac{P_S}{\sqrt{3}}[111]$	N/A	[010]	[001]	[100]
		[101]	[110]	[011]
$\mathbf{P}^{II} = \frac{P_S}{\sqrt{3}}[1\bar{1}1]$		N/A	[100]	[001]
			$[0\bar{1}1]$	$[\bar{1}10]$
$\mathbf{P}^{III} = \frac{P_S}{\sqrt{3}}[\bar{1}\,\bar{1}\,1]$			N/A	[010]
				$[\bar{1}01]$

The four domain states are energetically equivalent and P_S is the spontaneous polarization in a single domain state.

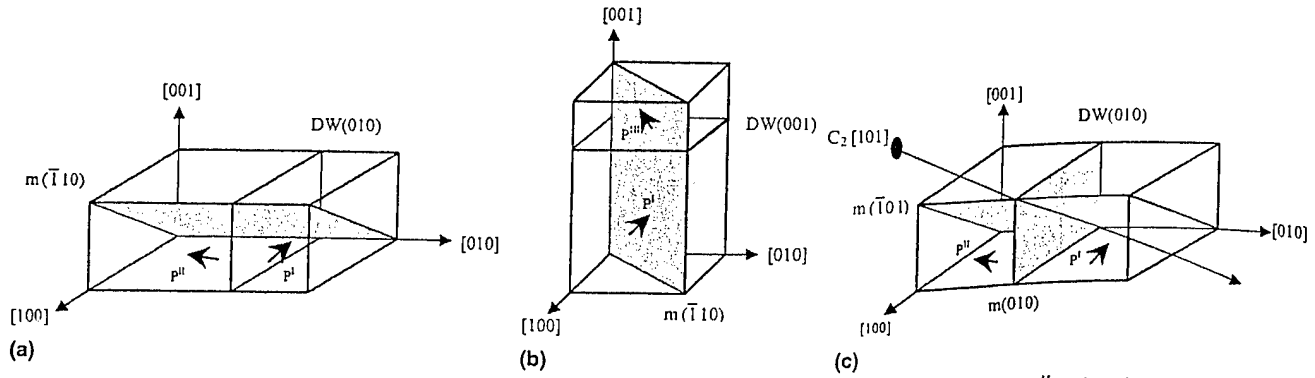

FIG. 1. Twin systems and their symmetry in a $m\bar{3}m \rightarrow 3m$ ferroelectrics. (a) Unequally partitioned twin of $\boldsymbol{P}^I$ and $\boldsymbol{P}^{II}$ with a charged DW oriented in [010]. The shaded plane is the mirror plane. (b) Unequally portioned twin of $\boldsymbol{P}^I$ and $\boldsymbol{P}^{III}$ with a neutral wall oriented in [001]. Both (a) and (b) have monoclinic m symmetry. (c) The same as (a) but with equal partition of the two domains. The symmetry is now orthorhombic $mm2$ because the DW becomes another mirror symmetry plane. The structures shown in (a) and (c) are used to make the calculations of Table IV and $v^{(1)}$ is the volume ratio of $\mathbf{P}^I = P_S/\sqrt{3}\,[111]$.

TABLE II. Permissible DW orientations[13] in ferroelectrics resulting from a $m\bar{3}m \rightarrow 4mm$ phase transition and poled in [111] direction.

Domain	$\mathbf{P}^{I} = P_S[100]$	$\mathbf{P}^{II} = P_S[010]$	$\mathbf{P}^{III} = P_S[001]$
$\mathbf{P}^{I} = P_S[100]$	N/A	[110]	[101]
		$[1\bar{1}0]$	$[10\bar{1}]$
$\mathbf{P}^{II} = P_S[010]$		N/A	[011]
			$[01\bar{1}]$

Three domain states are energetically equivalent and the value P_S is the spontaneous polarization.

electric states are listed in Table II. Similarly, two perpendicular DWs between any two given domains are permitted: One is charged and the other is neutral. The DW orientations for this case are illustrated in Fig. 2.

Again, twins containing neutral DWs and charged DWs have monoclinic m symmetry unless the domains are identical in size (for neutral DW the macroscopic symmetry cannot be higher than monoclinic m). Figs. 2(a) and 2(b) illustrate a twin of $\boldsymbol{P}^{I}$ and $\boldsymbol{P}^{III}$ with DW oriented in [101], and a twin of $\boldsymbol{P}^{I}$ and $\boldsymbol{P}^{III}$ with the DW oriented in $[\bar{1}01]$, respectively. For the special case of equal domain size twins, the symmetry becomes orthorhombic $mm2$ with a twofold axis oriented in [101] direction as shown in Fig. 2(c). The twofold axis is also the direction of the effective polarization of the system.

For a $m\bar{3}m \rightarrow mm2$ ferroelectric phase transition (e.g., $KNbO_3$), the possible spontaneous polarization directions are the face diagonals $\langle 110 \rangle$ (in the cubic coordinate system). Assuming we apply a poling field in [001] of the cubic coordinates, four domain states will remain energetically equivalent with permissible domain walls among them[13] listed in Table III. The dipoles are at a 45° angle to the poling field. A new feature for this $m\bar{3}m \rightarrow mm2$ system is the presence of S walls[13,14] (or W′ walls), which do not lie on lattice planes. Instead, their orientations depend on the values of the elastic distortion in the two domains involved, and, therefore, change with temperature. There are four types of S-wall orientations determined by the following relationships[13]

$$S_1: \quad ds_1 + ds_2 + Kds_3 = 0 \qquad \text{(II.1)}$$

$$S_2: \quad ds_1 - ds_2 + Kds_3 = 0 \qquad \text{(II.2)}$$

$$S_3: \quad ds_1 - ds_2 - Kds_3 = 0 \qquad \text{(II.3)}$$

$$S_4: \quad ds_1 + ds_2 - Kds_3 = 0 \qquad \text{(II.4)}$$

$$K = \frac{Q_{44}}{Q_{11} - Q_{12}} \qquad \text{(II.5)}$$

where $Q_{\alpha\beta}$ are the electrostrictive coefficients in the cubic $m\bar{3}m$ phase.

DW orientations in the $mm2$ system are illustrated in Fig. 3. For a charged DW, such as a wall between $\boldsymbol{P}^{I}$ and $\boldsymbol{P}^{III}$ oriented in $[\bar{1}10]$, the effective symmetry of this twin

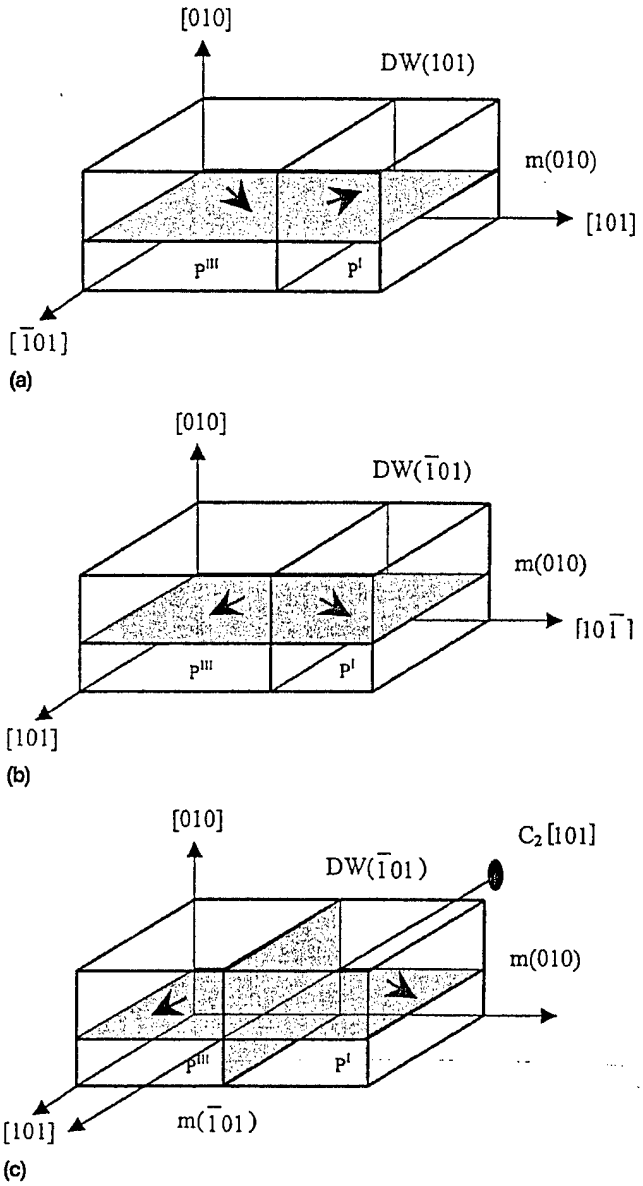

FIG. 2. Twin systems and their symmetry in a $m\bar{3}m \rightarrow 4mm$ ferroelectrics. (a) Unequally partitioned twin of $\boldsymbol{P}^{I}$ and $\boldsymbol{P}^{III}$ with a neutral DW oriented in [101] and the shaded plane (010) is the mirror plane of the structure. (b) Unequally partitioned twin of $\boldsymbol{P}^{I}$ and $\boldsymbol{P}^{III}$ with a charged DW oriented in $[10\bar{1}]$. Both (a) and (b) have monoclinic m symmetry. (c) The same structure as (b) but with equal partition of the two domains. The symmetry is orthorhombic $mm2$ in this case because the DW becomes another mirror symmetry plane.

structure is triclinic with symmetry group *1* [Fig. 3(a)]. If the two domains have equal volume ratio, the symmetry is monoclinic m [Fig. 3(b)]. For a twin between $\boldsymbol{P}^{III}$ and $\boldsymbol{P}^{IV}$ with a charged DW oriented in [010], the effective symmetry is monoclinic m [Fig. 3(c)] for unequal volume ratio, and orthorhombic $mm2$ when the sizes of the two domains become equal. The twofold axis is oriented in [001], which is also the direction of the total effective polarization [Fig. 3(d)].

The twin state between P^{III} and P^{IV} has a neutral DW oriented in [001], which again has a monoclinic symmetry m [Fig. 3(e)]. The S walls are charge neutral in all cases as listed in Table III, and the macroscopic symmetry of a twin crystal with an S wall is always triclinic *1*.

III. EFFECTIVE MATERIAL PROPERTIES OF TWINNED SINGLE CRYSTALS CONTAINING ONLY ONE SET OF TWINS

All of the effective material properties of a twin system can be determined from nine simple loads and enforcement of the usual electric and elastic continuity at the DW for certain twin configurations.[5] It was showed that the consideration of nine simple loads permits the determination of all the effective properties of the twin structure.[5] Here, instead of using the complex procedure described in Ref. 5, we combine the components of the elastic stress and the electric field to form a vector (note: the $T_4^{(i)}$ and $T_6^{(i)}$ components must be used twice):

$$\tau^{(i)} = [T_1^{(i)}, T_2^{(i)}, T_3^{(i)}, T_4^{(i)}, T_4^{(i)}, T_5^{(i)}, T_6^{(i)}, T_6^{(i)}, E_1^{(i)}, E_2^{(i)}, E_3^{(i)}], \quad (i = 1, 2) \quad . \tag{III.1}$$

The averaging conditions can now be expressed as

$$\tau^{eff} = \nu^{(1)}\tau^{(1)} + \nu^{(2)}\tau^{(2)} \quad , \tag{III.2}$$

and

$$\mathbf{M}^{eff}\tau^{eff} = \nu^{(1)}\mathbf{M}^{(1)}\tau^{(1)} + \nu^{(2)}\mathbf{M}^{(2)}\tau^{(2)} \quad . \tag{III.3}$$

TABLE III. Permissible DW orientations[13] in ferroelectrics resulting from a $m\bar{3}m \rightarrow mm2$ phase transition and poled in [001] direction.

Domain	$\mathbf{P}^{I} = \frac{P_S}{\sqrt{2}}[101]$	$\mathbf{P}^{II} = \frac{P_S}{\sqrt{2}}[\bar{1}01]$	$\mathbf{P}^{III} = \frac{P_S}{\sqrt{2}}[011]$	$\mathbf{P}^{IV} = \frac{P_S}{\sqrt{2}}[0\bar{1}1]$
$\mathbf{P}^{I} = \frac{P_S}{\sqrt{2}}[101]$	N/A	[100]	[1$\bar{1}$0]	[110]
		[001]	S_1	S_2
$\mathbf{P}^{II} = \frac{P_S}{\sqrt{2}}[\bar{1}01]$		N/A	[110]	[1$\bar{1}$0]
			S_3	S_4
$\mathbf{P}^{III} = \frac{P_S}{\sqrt{2}}[011]$			N/A	[010]
				[001]

Four domain states are energetically equivalent and the value P_S is the spontaneous polarization.

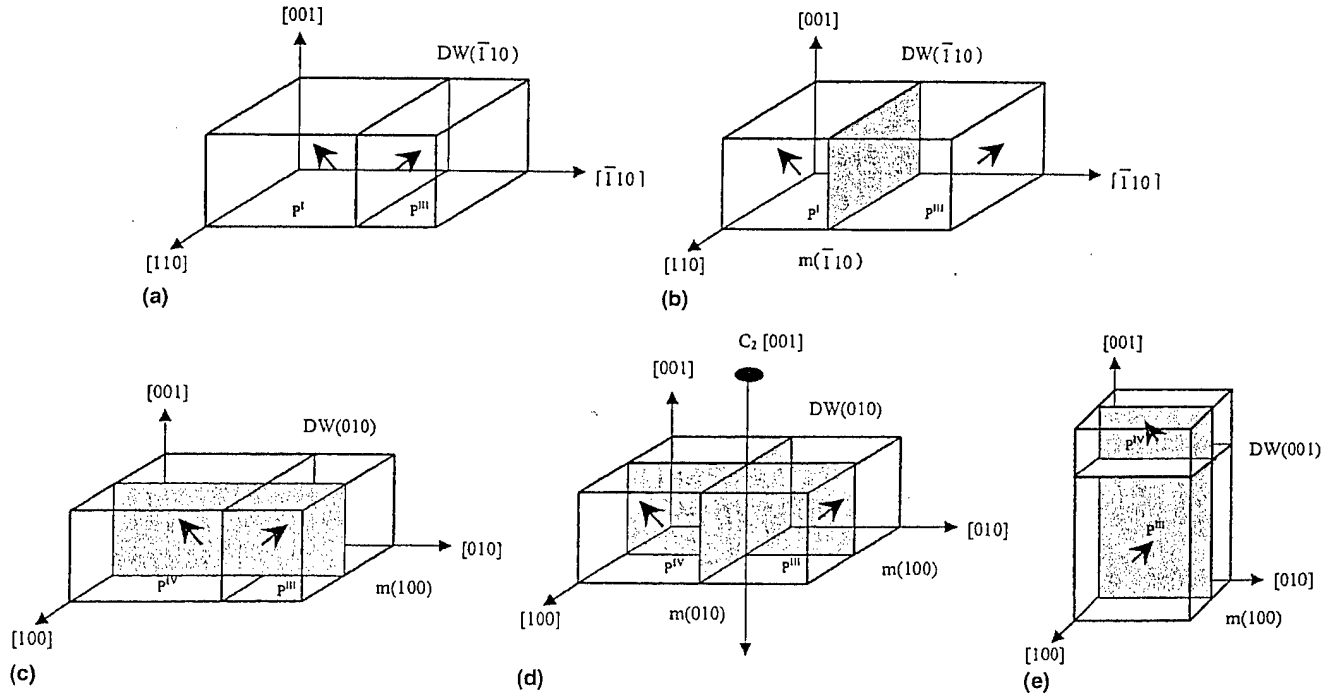

FIG. 3. Twin systems and their symmetry in a $m\bar{3}m \rightarrow mm2$ ferroelectrics. (a) Unequally portioned twin of P^I and P^{III} of Table III with a charged DW oriented in [$\bar{1}$10]. The symmetry is triclinic *1*. (b) The same as (a) but equal partition of the two domains. The symmetry is increased to monoclinic m with the DW as the mirror plane. (c) Unequally partitioned twin of P^{III} and P^{IV} with a charged DW oriented in [010]. The symmetry is monoclinic m with (100) plane as the mirror plane. (d) The same as (c) but equally partitioned domains. The symmetry is orthorhombic $mm2$.

Boundary conditions at the interfaces now can be described by the compact matrix equation

$$\mathbf{b}^{(1)}\tau^{(1)} = \mathbf{b}^{(2)}\tau^{(2)} \quad . \tag{III.4}$$

Combining Eqs. (*III*.1)–(*III*.4), the following matrix equation can be found for the effective material properties of a twin structure:

$$\mathbf{M}^{eff} = \{\nu^{(1)}\mathbf{M}^{(1)}[\mathbf{b}^{(1)}]^{-1} + \nu^{(2)}\mathbf{M}^{(2)}[\mathbf{b}^{(2)}]^{-1}\}\{\nu^{(1)}[\mathbf{b}^{(1)}]^{-1} + \nu^{(2)}[\mathbf{b}^{(2)}]^{-1}\}^{-1} \quad , \tag{III.5}$$

where $\nu^{(1)}$ and $\nu^{(2)}$ are the volume ratios of the two domains with $\nu^{(1)} + \nu^{(2)} = 1$, and the matrices $\mathbf{M}^{(i)}$ and $\mathbf{b}^{(i)}$ are defined by ($i = 1,2$):

$$\mathbf{M}^{(i)} = \begin{bmatrix} s_{11}^{(i)} & s_{12}^{(i)} & s_{13}^{(i)} & s_{14}^{(i)} & s_{14}^{(i)} & s_{15}^{(i)} & s_{16}^{(i)} & s_{16}^{(i)} & d_{11}^{(i)} & d_{21}^{(i)} & d_{31}^{(i)} \\ s_{12}^{(i)} & s_{22}^{(i)} & s_{23}^{(i)} & s_{24}^{(i)} & s_{24}^{(i)} & s_{25}^{(i)} & s_{26}^{(i)} & s_{26}^{(i)} & d_{12}^{(i)} & d_{22}^{(i)} & d_{32}^{(i)} \\ s_{13}^{(i)} & s_{23}^{(i)} & s_{33}^{(i)} & s_{34}^{(i)} & s_{34}^{(i)} & s_{35}^{(i)} & s_{36}^{(i)} & s_{36}^{(i)} & d_{13}^{(i)} & d_{23}^{(i)} & d_{33}^{(i)} \\ s_{14}^{(i)} & s_{24}^{(i)} & s_{34}^{(i)} & s_{44}^{(i)} & s_{44}^{(i)} & s_{45}^{(i)} & s_{46}^{(i)} & s_{46}^{(i)} & d_{14}^{(i)} & d_{24}^{(i)} & d_{34}^{(i)} \\ s_{14}^{(i)} & s_{24}^{(i)} & s_{34}^{(i)} & s_{44}^{(i)} & s_{44}^{(i)} & s_{45}^{(i)} & s_{46}^{(i)} & s_{46}^{(i)} & d_{14}^{(i)} & d_{24}^{(i)} & d_{34}^{(i)} \\ s_{15}^{(i)} & s_{25}^{(i)} & s_{35}^{(i)} & s_{45}^{(i)} & s_{45}^{(i)} & s_{55}^{(i)} & s_{56}^{(i)} & s_{56}^{(i)} & d_{15}^{(i)} & d_{25}^{(i)} & d_{35}^{(i)} \\ s_{16}^{(i)} & s_{26}^{(i)} & s_{36}^{(i)} & s_{46}^{(i)} & s_{46}^{(i)} & s_{56}^{(i)} & s_{66}^{(i)} & s_{66}^{(i)} & d_{16}^{(i)} & d_{26}^{(i)} & d_{36}^{(i)} \\ s_{16}^{(i)} & s_{26}^{(i)} & s_{36}^{(i)} & s_{46}^{(i)} & s_{46}^{(i)} & s_{56}^{(i)} & s_{66}^{(i)} & s_{66}^{(i)} & d_{16}^{(i)} & d_{26}^{(i)} & d_{36}^{(i)} \\ d_{11}^{(i)} & d_{12}^{(i)} & d_{13}^{(i)} & d_{14}^{(i)} & d_{14}^{(i)} & d_{15}^{(i)} & d_{16}^{(i)} & d_{16}^{(i)} & \epsilon_{11}^{(i)} & \epsilon_{12}^{(i)} & \epsilon_{13}^{(i)} \\ d_{21}^{(i)} & d_{22}^{(i)} & d_{23}^{(i)} & d_{24}^{(i)} & d_{24}^{(i)} & d_{25}^{(i)} & d_{26}^{(i)} & d_{26}^{(i)} & \epsilon_{12}^{(i)} & \epsilon_{22}^{(i)} & \epsilon_{23}^{(i)} \\ d_{31}^{(i)} & d_{32}^{(i)} & d_{33}^{(i)} & d_{34}^{(i)} & d_{34}^{(i)} & d_{35}^{(i)} & d_{36}^{(i)} & d_{36}^{(i)} & \epsilon_{13}^{(i)} & \epsilon_{23}^{(i)} & \epsilon_{33}^{(i)} \end{bmatrix} \tag{III.6}$$

$$\mathbf{b}^{(i)} = \begin{bmatrix} s_{11}^{(i)} & s_{12}^{(i)} & s_{13}^{(i)} & s_{14}^{(i)} & s_{14}^{(i)} & s_{15}^{(i)} & s_{16}^{(i)} & s_{16}^{(i)} & d_{11}^{(i)} & d_{21}^{(i)} & d_{31}^{(i)} \\ 0 & 1 & 0 & 0 & 0 & 0 & 0 & 0 & 0 & 0 & 0 \\ s_{13}^{(i)} & s_{23}^{(i)} & s_{33}^{(i)} & s_{34}^{(i)} & s_{34}^{(i)} & s_{35}^{(i)} & s_{36}^{(i)} & s_{36}^{(i)} & d_{13}^{(i)} & d_{23}^{(i)} & d_{33}^{(i)} \\ 0 & 0 & 0 & 1 & 0 & 0 & 0 & 0 & 0 & 0 & 0 \\ s_{14}^{(i)} & s_{24}^{(i)} & s_{34}^{(i)} & s_{44}^{(i)} & s_{44}^{(i)} & s_{45}^{(i)} & s_{46}^{(i)} & s_{46}^{(i)} & d_{14}^{(i)} & d_{24}^{(i)} & d_{34}^{(i)} \\ s_{15}^{(i)} & s_{25}^{(i)} & s_{35}^{(i)} & s_{45}^{(i)} & s_{45}^{(i)} & s_{55}^{(i)} & s_{56}^{(i)} & s_{56}^{(i)} & d_{15}^{(i)} & d_{25}^{(i)} & d_{35}^{(i)} \\ s_{16}^{(i)} & s_{26}^{(i)} & s_{36}^{(i)} & s_{46}^{(i)} & s_{46}^{(i)} & s_{56}^{(i)} & s_{66}^{(i)} & s_{66}^{(i)} & d_{16}^{(i)} & d_{26}^{(i)} & d_{36}^{(i)} \\ 0 & 0 & 0 & 0 & 0 & 0 & 0 & 1 & 0 & 0 & 0 \\ 0 & 0 & 0 & 0 & 0 & 0 & 0 & 0 & 1 & 0 & 0 \\ d_{21}^{(i)} & d_{22}^{(i)} & d_{23}^{(i)} & d_{24}^{(i)} & d_{24}^{(i)} & d_{25}^{(i)} & d_{26}^{(i)} & d_{26}^{(i)} & \epsilon_{12}^{(i)} & \epsilon_{22}^{(i)} & \epsilon_{23}^{(i)} \\ 0 & 0 & 0 & 0 & 0 & 0 & 0 & 0 & 0 & 0 & 1 \end{bmatrix} \tag{III.7}$$

The material properties in $M^{(i)}$ and $\mathbf{b}^{(i)}$ refer to the same cubic coordinate system as indicated in Fig. 1. The $\mathbf{b}^{(i)}$ matrix results directly from the electric and elastic continuity conditions.[5] The superscript *eff*, (1), and (2) describe the physical properties of effective, domain 1, and domain 2, respectively. The *y* axis is perpendicular to the DW as shown in Fig. 1. The formula in Eq. (*III*.5) is another form of the ones given in Ref. 5, which is different from the statistical average formula of Ref. 6. (The dimension here is 11×11, whereas in Ref. 6 the dimension is 9×9.)

Effective material properties of ferroelectrics resulting from a $m\bar{3}m \rightarrow 3m$ phase transition were calculated for a twin of $\boldsymbol{P}^{I}$ and $\boldsymbol{P}^{II}$ with a DW in [010] as shown in Fig. 1(a). Both cases $\nu^{(1)} \neq \nu^{(2)}$ and $\nu^{(1)} = \nu^{(2)}$ were studied.

Because there were no complete single-crystal data for ferroelectrics with a $m\bar{3}m \rightarrow 3m$ phase transition in the current literature, we borrowed the material data of $LiNbO_3$,[15] but used the domain structures of $m\bar{3}m \rightarrow 3m$ phase transition to demonstrate the method. ($LiNbO_3$ has a $\bar{3}m \rightarrow 3m$ transition and only has 180° coherent twins).

A. $\nu^{(1)} \neq \nu^{(2)}$

To perform the effective material property evaluation, the tensor components of elastic constants, piezoelectric coefficients, and dielectric constants were first transformed to a common coordinate system (i.e., the cubic coordinates), and then these transformed properties were put into Eqs. (*III*.6) and (*III*.7). Finally, the effective properties were calculated using Eq. (*III*.5) for different volume ratios. Numerical solutions show that the following relations are fulfilled within the relative errors of less than 10^{-12}.

$$s_{15}^{eff} = s_{35}^{eff}, s_{12}^{eff} = s_{23}^{eff}, s_{11}^{eff} = s_{33}^{eff}, s_{24}^{eff} = s_{26}^{eff}, s_{34}^{eff} = s_{16}^{eff}, s_{36}^{eff} = s_{14}^{eff}, s_{56}^{eff} = s_{45}^{eff}, s_{66}^{eff} = s_{44}^{eff} \tag{III.8}$$

$$d_{23}^{eff} = d_{21}^{eff}, d_{26}^{eff} = d_{24}^{eff}, d_{31}^{eff} = d_{13}^{eff}, d_{32}^{eff} = d_{12}^{eff}, d_{33}^{eff} = d_{11}^{eff}, d_{34}^{eff} = d_{16}^{eff}, d_{35}^{eff} = d_{15}^{eff}, d_{36}^{eff} = d_{14}^{eff} \tag{III.9}$$

$$\epsilon_{11}^{eff} = \epsilon_{33}^{eff}, \epsilon_{23}^{eff} = \epsilon_{12}^{eff} \quad . \tag{III.10}$$

Numerical data verified that the symmetry of this twin structure is monoclinic *m* with a mirror symmetry plane perpendicular to $[\bar{1}01]$.

B. $\nu^{(1)} = \nu^{(2)}$

For this case, in addition to the relationships (*III*.8)–(*III*.10), the following components become zero[5]

$$s_{15}^{eff} = s_{35}^{eff} = s_{24}^{eff} = s_{26}^{eff} = s_{34}^{eff} = s_{16}^{eff} = s_{36}^{eff} = s_{14}^{eff} = s_{56}^{eff} = s_{45}^{eff} = 0 \quad , \tag{III.11}$$

$$d_{23}^{eff} = d_{21}^{eff} = d_{34}^{eff} = d_{16}^{eff} = d_{36}^{eff} = d_{14}^{eff} = d_{22}^{eff} = d_{25}^{eff} = 0 \quad , \tag{III.12}$$

$$\epsilon_{23}^{eff} = \epsilon_{12}^{eff} = 0 \quad . \tag{III.13}$$

For twins with a charged DW, if the volume ratios of the two domains are the same, the effective symmetry could be raised to orthohombic *mm*2, whereas for twins with a neutral DW, the effective symmetry cannot be higher than monoclinic *m*.

TABLE IV. Calculated effective material constants of a twinned crystal of rhombohedral $3m$ symmetry by using the single domain data of $LiNbO_3$ [Units: $s_{\alpha\beta}$ (10^{-12} m^2N^{-1}), $d_{i\alpha}$ (10^{-12} CN^{-1}), ϵ_{ij} (ϵ_0)].

$\nu^{(1)}$	1.00	0.00	0.50	0.55	0.60	0.65	0.70
Elastic properties							
S_{11}	5.60	5.60	5.42	5.43	5.43	5.44	5.45
S_{12}	−1.36	−1.36	−1.10	−1.10	−1.11	−1.11	−1.12
S_{13}	−1.36	−1.36	−1.38	−1.38	−1.38	−1.38	−1.38
S_{14}	−1.35	1.35	...	−0.13	−0.25	−0.38	−0.51
S_{15}	0.26	0.26	−0.49	−0.48	−0.47	−0.45	−0.42
S_{16}	0.26	−0.26	...	0.03	0.06	0.09	0.12
S_{22}	5.60	5.60	4.65	4.66	4.67	4.70	4.73
S_{23}	−1.36	−1.36	−1.10	−1.10	−1.11	−1.11	−1.12
S_{24}	0.26	−0.26	...	0.00	0.00	0.01	0.02
S_{25}	−1.35	−1.35	1.36	1.35	1.30	1.23	1.13
S_{26}	0.26	−0.26	...	0.00	0.00	0.01	0.02
S_{33}	5.60	5.60	5.42	5.43	5.43	5.44	5.45
S_{34}	0.26	−0.26	...	0.03	0.06	0.09	0.12
S_{35}	0.26	0.26	−0.49	−0.48	−0.47	−0.45	−0.42
S_{36}	−1.35	1.35	...	−0.13	−0.25	−0.38	−0.51
S_{44}	15.65	15.65	15.27	15.27	15.28	15.30	15.32
S_{45}	−0.98	0.98	...	−0.03	−0.07	−0.11	−0.16
S_{46}	−0.98	−0.98	−0.99	−0.99	−0.99	−0.99	−0.99
S_{55}	15.65	15.65	7.92	7.96	8.08	8.27	8.57
S_{56}	−0.98	0.98	...	−0.03	−0.07	−0.11	−0.16
S_{66}	15.65	15.65	15.27	15.27	15.28	15.30	15.32
Piezoelectric properties							
d_{11}	16.28	16.28	11.84	11.88	12.01	12.22	12.52
d_{12}	−5.83	−5.83	−5.03	−5.04	−5.04	−5.06	−5.08
d_{13}	−5.83	−5.83	−3.14	−3.17	−3.25	−3.39	−3.59
d_{14}	−47.11	47.11	...	−4.59	−9.19	−13.80	−18.43
d_{15}	26.44	26.44	23.84	23.85	23.88	23.94	24.03
d_{16}	26.44	−26.44	...	2.60	5.20	7.81	10.43
d_{21}	−5.83	5.83	...	−0.34	−0.68	−1.05	−1.43
d_{22}	16.28	−16.28	...	0.77	1.56	2.41	3.34
d_{23}	−5.83	5.83	...	−0.34	−0.68	−1.05	−1.43
d_{24}	26.44	26.44	22.23	22.26	22.32	22.44	22.61
d_{25}	−47.11	47.11	...	−2.25	−4.57	−7.05	−9.78
d_{26}	26.44	26.44	22.23	22.26	22.32	22.44	22.61
d_{31}	−5.83	−5.83	−3.14	−3.17	−3.25	−3.39	−3.59
d_{32}	−5.83	−5.83	−5.03	−5.04	−5.04	−5.06	−5.08
d_{33}	16.28	16.28	11.84	11.88	12.01	12.21	12.52
d_{34}	26.44	−26.44	...	2.60	5.20	7.81	10.43
d_{35}	26.44	26.44	23.84	23.85	23.88	23.94	24.03
d_{36}	−47.11	47.11	...	−4.59	−9.19	−13.80	−18.43
Dielectric properties							
ϵ_{11}	38.97	38.97	18.97	19.20	19.77	20.78	22.14
ϵ_{12}	−4.97	4.97	...	−0.34	−0.79	−1.13	−1.58
ϵ_{13}	−4.97	−4.97	11.63	11.52	11.07	10.28	9.04
ϵ_{22}	38.97	38.97	21.57	21.69	22.02	22.48	23.04
ϵ_{23}	−4.97	4.97	...	−0.34	−0.79	−1.13	−1.58
ϵ_{33}	38.97	38.97	18.97	19.20	19.77	20.78	22.14

The two domains are $\mathbf{P}^I = P_S/\sqrt{3}\,[111]$ and $\mathbf{P}^{II} = P_S/\sqrt{3}\,[1\bar{1}1]$ from Table I and the twin stucture is illustrated in Fig. 1(a). Data blanks represent that the corresponding component is zero and the column of $\nu^{(1)} = 0.5$ are the values from Ref. 5. Domain wall orientation is [010].

One must remember that the macroscopic and microscopic symmetries are different in multidomain systems. The former refers to symmetry relations between different components of macroscopic physical properties whereas the latter refers to the crystal lattice structure. The lower symmetry of the twinned crystal increases the difficulty to fully characterize the physical properties because the number of nonzero components grows rapidly with the decrease of symmetry.[16]

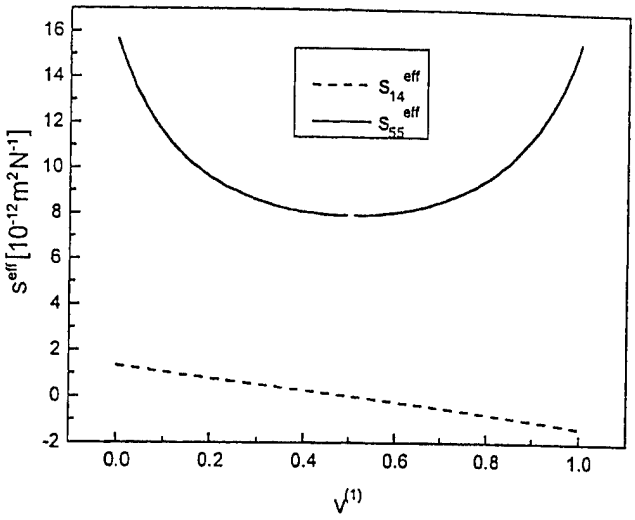

FIG. 4. Calculated effective elastic constants, s_{14}^{eff} and s_{55}^{eff}, of different volume ratios for a twinned crystal resulting from a $m\bar{3}m \rightarrow 3m$ phase transition. The components of material properties are either symmetric (e.g. s_{55}^{eff}) or antisymmetric (e.g. s_{14}^{eff}) with respect to $\nu^{(1)} = 0.50$.

As analyzed above, the effective symmetry of a twin becomes lower if the domain volume ratio deviates from 50:50. Experience tells us that this deviation is usually within a few percent for most of twinned crystals. The question is: Which quantities are influenced the most by this volume-ratio-induced symmetry breaking? We used a few numerical examples to gain quantitative understanding on this issue and to give the reader some understanding of the degree of property changes.

Listed in Table IV are some numerical results calculated by using the single-crystal data of $LiNbO_3$ for the twin structure of rhombohedral $3m$ system. One can see that if a component is nonzero for the case of $\nu^{(1)} = 0.5$, the relative change caused by small deviation from equal volume ratio is not significant for most of the quantities, particularly the elastic properties (see Fig. 4). The symmetry breaking is, however, important for those components that change from zero to nonzero when the volume ratio deviates from equal partition. The relative changes are very large. Twins with a charge-neutral DW cannot reach orthorhombic $mm2$ symmetry for any volume ratio; therefore, they must be treated as monoclinic m symmetry at all times.

We have also calculated two other materials resulting from $m\bar{3}m \rightarrow 4mm$ ($BaTiO_3$)[6] and from $m\bar{3}m \rightarrow mm2$ ($KNbO_3$)[17] ferroelectric phase transitions.

For $BaTiO_3$, the effective material properties shown in Table V were calculated for a twin of $\boldsymbol{P}^I$ and $\boldsymbol{P}^{II}$ in Table II with a DW oriented in [110]. Using the same

TABLE V. Calculated effective material constants of twinned $BaTiO_3$ crystal with a neutral DW[110] (units are the same as in Table IV).

$\nu^{(1)}$	1.00	0.00	0.50	0.55	0.60	0.65	0.70
Elastic properties							
S_{11}	7.92	7.92	7.49	7.49	7.51	7.52	7.55
S_{12}	−1.28	−1.28	−1.71	−1.71	−1.69	−1.68	−1.65
S_{13}	−3.80	−3.80	−3.47	−3.47	−3.48	−3.50	−3.52
S_{14}	...	...	...	...	...	...	...
S_{15}	...	...	...	...	...	...	...
S_{16}	3.83	−3.83	...	0.34	0.69	1.04	1.39
S_{22}	7.92	7.92	7.49	7.49	7.51	7.52	7.55
S_{23}	−3.80	−3.80	−3.47	−3.47	−3.48	−3.50	−3.52
S_{24}	...	...	...	...	...	...	...
S_{25}	...	...	...	...	...	...	...
S_{26}	3.83	−3.83	...	0.34	0.69	1.04	1.39
S_{33}	8.05	8.05	7.81	7.81	7.81	7.83	7.84
S_{34}	...	...	...	...	...	...	...
S_{35}	...	...	...	...	...	...	...
S_{36}	−2.89	2.89	...	−0.26	−0.52	−0.78	−1.05
S_{44}	13.62	13.62	11.94	11.96	12.00	12.08	12.18
S_{45}	4.78	−4.78	...	0.42	0.84	1.27	1.71
S_{46}	...	...	...	...	...	...	...
S_{55}	13.62	13.62	11.94	11.96	12.00	12.08	12.18
S_{56}	...	...	...	...	...	...	...
S_{66}	34.23	34.23	30.63	30.66	30.76	30.92	31.16
Piezoelectric properties							
d_{11}	−156.66	156.66	...	−16.14	−32.24	−48.30	−64.28
d_{12}	120.53	−120.53	...	11.58	23.19	34.85	46.59
d_{13}	24.40	−24.40	...	2.79	5.57	8.30	10.98
d_{14}	...	...	...	...	...	...	...
d_{15}	...	...	...	...	...	...	...
d_{16}	−84.92	−84.92	−127.29	−126.92	−125.77	−123.85	−121.12
d_{21}	120.53	120.53	130.02	129.93	129.68	129.44	128.63
d_{22}	−156.66	−156.66	−147.17	−147.26	−147.51	−147.94	−148.55
d_{23}	24.40	24.40	17.23	17.29	17.48	17.81	18.27
d_{24}	...	...	...	...	...	...	...
d_{25}	...	...	...	...	...	...	...
d_{26}	−84.92	84.92	...	−7.61	−15.26	−23.02	−30.92
d_{31}	...	...	...	...	...	...	...
d_{32}	...	...	...	...	...	...	...
d_{33}	...	...	...	...	...	...	...
d_{34}	−277.19	−277.19	−179.91	−180.76	−183.33	−187.67	−193.83
d_{35}	−277.19	277.19	...	−24.33	−48.85	−73.73	−99.17
d_{36}	...	...	...	...	...	...	...
Dielectric properties							
ϵ_{11}	1530	1530	272	285	322	385	472
ϵ_{12}	−1362	1362	...	−135	−270	−405	−541
ϵ_{13}	...	...	...	...	...	...	...
ϵ_{22}	1530	1530	1506	1506	1507	1508	1509
ϵ_{23}	...	...	...	...	...	...	...
ϵ_{33}	2891	2891	2254	2260	2277	2305	2345

The two domains are $\mathbf{P}^{I} = P_S$ [100] and $\mathbf{P}^{II} = P_S$ [010] of Table II. Data blanks represent that the corresponding component is zero and the column of $\nu^{(1)} = 0.5$ are the values from Ref. 5.

TABLE VI. Calculated effective material constants of twinned $KNbO_3$ crystal (units are the same as in Table IV).

$\nu^{(1)}$	1.00	0.00	0.50	0.55	0.60	0.65	0.70
Elastic properties							
S_{11}	5.41	5.41	5.40	5.40	5.40	5.40	5.40
S_{12}	−1.33	−1.33	−1.35	−1.35	−1.35	−1.35	−1.35
S_{13}	−1.33	−1.33	−1.34	−1.34	−1.34	−1.34	−1.34
S_{14}	0.31	−0.31	...	0.03	0.06	0.09	0.12
S_{15}	...	...	...	...	...	...	...
S_{16}	...	...	...	...	...	...	...
S_{22}	5.28	5.28	5.20	5.20	5.20	5.21	5.21
S_{23}	−1.45	−1.45	−1.49	−1.49	−1.49	−1.49	−1.49
S_{24}	0.97	−0.97	...	0.10	0.19	0.29	0.39
S_{25}	...	...	...	...	...	...	...
S_{26}	...	...	...	...	...	...	...
S_{33}	5.28	5.28	5.21	5.21	5.21	5.21	5.22
S_{34}	0.97	−0.97	...	0.10	0.19	0.29	0.38
S_{35}	...	...	...	...	...	...	...
S_{36}	...	...	...	...	...	...	...
S_{44}	16.46	16.46	16.22	16.22	16.23	16.24	16.26
S_{45}	...	...	...	...	...	...	...
S_{46}	...	...	...	...	...	...	...
S_{55}	25.24	25.24	16.60	16.65	16.83	17.13	17.56
S_{56}	14.76	−14.76	...	0.97	1.97	3.01	4.11
S_{66}	25.24	25.24	16.60	16.65	16.83	17.13	17.56
Piezoelectric properties							
d_{11}	...	...	...	...	...	...	...
d_{12}	...	...	...	...	...	...	...
d_{13}	...	...	...	...	...	...	...
d_{14}	...	...	...	...	...	...	...
d_{15}	72.83	72.83	30.22	30.50	31.36	32.82	34.96
d_{16}	72.83	−72.83	...	4.81	9.71	14.83	20.27
d_{21}	7.00	−7.00	...	0.71	1.41	2.12	2.82
d_{22}	31.57	−31.57	...	3.17	6.35	9.52	12.69
d_{23}	−23.58	23.58	...	−2.33	−4.66	−6.99	−9.33
d_{24}	35.14	35.14	39.37	39.33	39.20	39.00	38.70
d_{25}	...	...	...	...	...	...	...
d_{26}	...	...	...	...	...	...	...
d_{31}	7.00	7.00	12.14	12.09	11.93	11.67	11.31
d_{32}	−23.58	−23.58	1.41	1.16	0.40	−0.86	−2.62
d_{33}	31.57	31.57	5.95	6.20	6.96	8.23	10.00
d_{34}	35.14	−35.14	...	3.03	6.06	9.21	12.42
d_{35}	...	...	...	...	...	...	...
d_{36}	...	...	...	...	...	...	...
Dielectric properties							
ϵ_{11}	1540	1540	1516	1516	1517	1518	1519
ϵ_{12}	...	...	...	...	...	...	...
ϵ_{13}	...	...	...	...	...	...	...
ϵ_{22}	5145	5145	5133	5133	5133	5134	5135
ϵ_{23}	−4705	4705	...	−469	−939	−1408	−1878
ϵ_{33}	5145	5145	811	854	984	1200	1503

The two domains in the twin are $\mathbf{P}^{III} = P_S/\sqrt{2}$ [011] and $\mathbf{P}^{IV} = P_S/\sqrt{2}$ [0$\bar{1}$1] (Table III) with a charged DW oriented in [010] as shown in Fig. 3(c).

argument above, the macroscopic symmetry of the twin is orthorhombic *mm*2 for equal volume ratio and monoclinic *m* for unequal partition. As expected, the tensor components are either symmetric or antisymmetric with respect to equal partition $\nu^{(1)} = 0.5$. A large change in ϵ_{11} has been observed, which is very sensitive to the domain volume ratio change.

For $KNbO_3$, which has a $m\bar{3}m \rightarrow mm2$ phase transition, effective material properties were calculated for a twin system of P^{III} and P^{IV} (see Table III) with a [010] oriented DW. The results are given in Table VI for several values of $\nu^{(1)}$. Again, the macroscopic symmetry belongs to the orthorhombic *mm*2 class for equal partition, and is reduced to monoclinic *m* if the volume ratios are not equal. Many physical quantities change significantly with the variation of the domain volume ratio; some even change signs. This demonstrated the importance of considering the symmetry breaking caused by the domain volume ratio deviation from 50:50. Note: we have chosen a convenient coordinate system for calculations, which is not the simplest coordinate system in terms of matrix quantity representation as shown in the

tables. One can convert the matrix quantities into the simplest form by a coordinate transformation for each case.

IV. SUMMARY AND CONCLUSIONS

The effective symmetry and material properties of twin crystals have been analyzed for three symmetry classes, resulting from $m\bar{3}m \rightarrow 3m$, $m\bar{3}m \rightarrow 4mm$, and $m\bar{3}m \rightarrow mm2$ ferroelectric phase transitions. It has been shown that the macroscopic symmetry could be lower than the microscopic symmetry, particularly when the volume ratios of the two domains are different. In real materials, this nonequal partition of domain volume could be caused by any defects that provide pinning to the movement of domain walls, which leads to a symmetry reduction in terms of macroscopic physical quantities. Numerical calculations on three real materials showed that the changes in those physical properties that are nonzero at equal partition were not so drastic in the cases of $m\bar{3}m \rightarrow 3m$ and $m\bar{3}m \rightarrow 4mm$, but became noticeable for the case of $m\bar{3}m \rightarrow mm2$. As shown in Tables IV to VI, the symmetry reduction is signified by the increase of the number of nonzero components in the macroscopic property matrices when the volume ratio of the two domains deviates slightly from 50:50. The changes for those quantities that are zero in the equal volume situation are quite significant, as demonstrated through real material calculations. A more concise formula has been given here, which was derived using the method of Ref. 5 but is much simpler to use for real material property calculations in twinned crystals. The formula is also applicable to bicrystals so long as the orientations of the crystals are known.

ACKNOWLEDGMENTS

This work was supported by the National Science Foundation under Grant No. DNS 9704714 and by the Office of Naval Research under Grant Nos. N00014-98-1-0527 and N00014-96-1-1173. One of the authors (J.E.) is also grateful for partial support from the Ministry of Education of the Czech Republic (Code VS 96006, 1996).

REFERENCES

1. S.E. Park and T.R. Shrout, J. Appl. Phys. **82,** 1804 (1997).
2. J. Yin, B. Jiang, and W. Cao, Proc. SPIE, Medical Imaging **3664,** 239 (1999).
3. J. Yin, B. Jiang, and W. Cao, IEEE Trans. Ultra. Ferro. Freq. Contr. **47,** 285 (2000).
4. J. Yin and W. Cao, J. Appl. Phys. **87,** 7438 (2000).
5. J. Erhart and W. Cao, J. Appl. Phys. **86,** 1073 (1999).
6. E. Aksakaya and G.W. Farnell, J. Appl. Phys. **64,** 4469 (1988).
7. W. Cao and G.R. Barsch, Phys. Rev. B **41,** 4334 (1990).
8. W. Cao and L.E. Cross, Phys. Rev. B **44,** 5 (1991).
9. C.C. Chou and C.S. Chen, Jpn. J. Appl. Phys. **37,** 5394 (1998).
10. Y.H. Hu, H.M. Chan, Z.X. Wen, and M.P. Harmer, J. Am. Ceram. Soc. **69,** 594 (1986).
11. G. Arlt, J. Mater. Sci. **25,** 2655 (1990).
12. E.I. Eknadiosyants, A.N. Pinskaya, and V.Z. Borodin, Crystallography Reports **44,** 502 (1999).
13. J. Fousek and V. Janovec, J. Appl. Phys. **40,** 135 (1969).
14. E. Wiesendanger, Czech. J. Phys. B **23,** 91 (1973).
15. *Landolt-Börnstein Tables* (Springer Verlag, Berlin, 1969), Vol. 3, Group III.
16. J.F. Nye, *Physical Properties of Crystals* (Clarendon Press, Oxford, 1957).
17. M. Zgonik, R. Schlesser, I. Biaggio, and P. Günter, Ferroelectrics **158,** 217 (1994).

Appendix 8

P.M. Gehring, S.–E. Park, G. Shirane, "Dynamical effects of the nanometer-sized polarized domains in $Pb(Zn_{1/3}Nb_{2/3})O_3$," Physical Review B (to be published).

Physical Review B.

Dynamical effects of the nanometer-sized polarized domains in $Pb(Zn_{1/3}Nb_{2/3})O_3$

P. M. Gehring
NIST Center for Neutron Research, National Institute of Standards and Technology, Gaithersburg, Maryland 20899

S. -E. Park
Materials Research Laboratory, The Pennsylvania State University, University Park, Pennsylvania 16802
(Present address: Fraunhofer-IBMT Technology Center Hialeah, Hialeah. Florida 33010)

G. Shirane
Physics Department, Brookhaven National Laboratory, Upton, New York 11973

Recent neutron scattering measurements performed on the relaxor ferroelectric $Pb[(Zn_{1/3}Nb_{2/3})_{0.92}Ti_{0.08}]O_3$ (PZN-8% PT) in its cubic phase at 500 K. have revealed an anomalous ridge of inelastic scattering centered ~ 0.2 Å^{-1} from the zone center (Gehring *et al.*, Phys. Rev. Lett. **84**, 5216 (2000)). This ridge of scattering resembles a waterfall when plotted as a phonon dispersion diagram, and extends vertically from the transverse acoustic (TA) branch near 4 meV to the transverse optic (TO) branch near 9 meV. No zone center optic mode was found. We report new results from an extensive neutron scattering study of pure PZN that exhibits the same waterfall feature. We are able to model the dynamics of the waterfall using a simple coupled-mode model that assumes a strongly q-dependent optic mode linewidth $\Gamma_1(q)$ that increases sharply near 0.2 Å^{-1} as one approaches the zone center. This model was motivated by the results of Burns and Dacol in 1983, who observed the formation of a randomly-oriented local polarization in PZN at temperatures far above its ferroelectric phase transition temperature. The dramatic increase in Γ_1 is believed to occur when the wavelength of the optic mode becomes comparable to the size of the small polarized microregions (PMR) associated with this randomly-oriented local polarization, with the consequence that longer wavelength optic modes cannot propagate and become overdamped. Below $T_c = 410$ K, the intensity of the waterfall diminishes. At lowest temperatures ($\sim$ 30 K) the waterfall is absent, and we observe the recovery of a zone center transverse optic mode near 10.5 meV.

I. INTRODUCTION

Scientific research in the field of relaxor ferroelectrics has surged markedly over the past several years. Perhaps the primary driving force behind the rapidly increasing number of publications in this area has been the observation of an exceptionally large piezoelectric response in single crystals of the two complex perovskite systems $Pb[(Mg_{1/3}Nb_{2/3})_{1-x}Ti_x]O_3$ (PMN-xPT) and $Pb[(Zn_{1/3}Nb_{2/3})_{1-x}Ti_x]O_3$ (PZN-xPT) for compositions x that lie near the morphotropic phase boundary (MPB), which separates the rhombohedral and tetragonal regions of the phase diagram. These systems differ from the classic and well-studied simple perovskite ABO_3 compounds by virtue of the mixed-valence character of the B-site cation. In the case of PMN and PZN (x=0), the B-site is occupied by either Mg^{2+} or Zn^{2+}, and Nb^{5+} ions with a stoichiometry of 1/3 and 2/3, respectively, which is required to preserve charge neutrality. This built-in disorder sharply breaks the translational symmetry of the lattice and produces a so-called "diffuse" phase transition in which the dielectric permittivity ϵ exhibits a very large and broad peak at a characteristic temperature T_{max} that is also strongly frequency-dependent. In contrast to the normal ferroelectric parent compound $PbTiO_3$ (PT), in which the condensation of a transverse optic (TO) zone center phonon leads to a transition from a cubic paraelectric phase to a tetragonal long-range ordered state with a non-vanishing spontaneous polarization below a critical temperature $T_c = 763$ K, the prototypical relaxor compound PMN exhibits a diffuse transition at $T_{max} = 230$ K and no spontaneous polarization at any temperature studied.

Stimulated by the unusual properties of these complex systems, we performed a recent neutron inelastic scattering study to examine the lattice dynamics of a high-quality single crystal of PZN-8%PT,[1] the composition for which the piezoelectric response is largest in the PZN-xPT system.[2] The PZN-xPT phase diagram as a function of PT concentration x is shown in Fig. 1. The maximum piezoelectric activity occurs on the rhombohedral side of the MPB, which is indicated by the steep dashed line. Our measurements of the phonon dispersion of the polar TO mode in the cubic phase at 500 K revealed an unexpected ridge of scattering centered at a momentum transfer $q = 0.2$ Å^{-1}, measured from the zone center. The ridge extends in energy from $\sim$ 4 meV to 9 meV such that, when plotted as a standard phonon dispersion diagram, it resembles a waterfall in which the TO branch appears to drop precipitously into the transverse acoustic (TA) branch. This anomalous feature, hereafter referred to as the waterfall, was observed in both of the two Brillouin zones we surveyed (2,2,l), and (h,h,4), which cover the two different symmetry directions [001] and [110]. Similar data taken on a large single crystal of pure PMN at room temperature also showed the presence of a waterfall, suggesting that this feature may be common to all relaxor systems.[5]

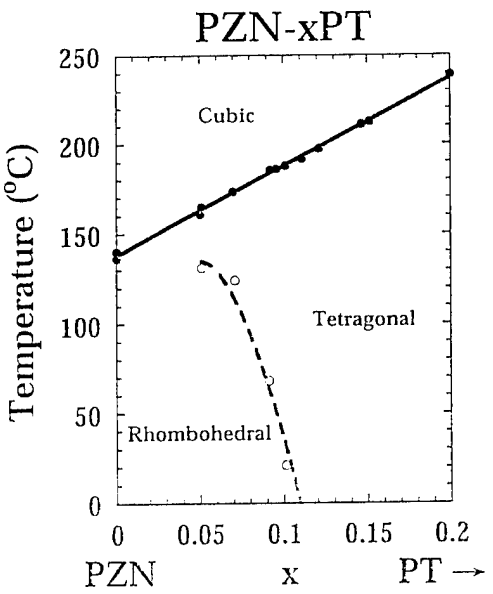

Fig. 1. Phase diagram of the PZN-PT system from Kuwata *et al.* (ref. [3]). The MPB is represented by the dashed line between the rhombohedral and tetragonal phases. An intervening monoclinic phase has been discovered in PZT by Noheda *et al.* (ref. [4]).

The waterfall observed in PZN-8%PT was speculated to represent direct microscopic evidence for small, randomly-oriented regions of local polarization within the crystal that begin to condense at temperatures far above T_c = 450 K. The existence of these regions of local polarization was first proposed by Burns and Dacol in 1983 to describe the disorder inherent to relaxor systems.[6] Using measurements of the optic index of refraction to study ceramic samples of $(Pb_{1-3x/2}La_x)(Zr_yTi_{1-y})O_3$ (PLZT), as well as single crystals of PMN and PZN,[6] they discovered that a randomly-oriented, and non-reversible local polarization P_d develops at a well-defined temperature T_d, frequently referred to as the Burns temperature, several hundred degrees above the apparent transition temperature T_c. Subsequent studies have provided additional experimental evidence supporting the existence of T_d.[7–9] The spatial extent of these locally polarized regions was conjectured to be of the order of several unit cells, and has given rise to the term "polar micro-regions," or PMR. Because the size of the PMR is finite, the propagation of long-wavelength phonons should be inhibited. This would then lead naturally to a heavily overdamped TO phonon cross section in the neighborhood of the zone center. Indeed, no well-defined TO phonon peaks were found in either PZN-8%PT or PMN for $q < 0.2$ Å^{-1}. Moreover, if one assumes the waterfall peak position in q gives a measure of the size of the PMR according to $2\pi/q$, one obtains a value of 30 Å, or about 7 – 8 unit cells, consistent with the conjecture of Burns and Dacol.

Further evidence in support of our picture correlating the waterfall with the appearance of the PMR comes from the neutron inelastic scattering data of Naberezhnov *et al.* As shown in Fig. 2, they observed a normal TO and TA phonon dispersion in the closely related relaxor ferroelectric compound PMN at 800 K > T_d = 617 K, where no polar regions remain.[10] Their data were obtained on the same crystal we studied at room temperature where the waterfall was observed. For PZN-8%PT, the formation of the PMR is estimated to occur at $T_d \sim 790$ K, which is well above the cubic-to-tetragonal phase transition at $T_c \sim 450$ K, and also beyond the temperature at which the crystal begins to decompose.

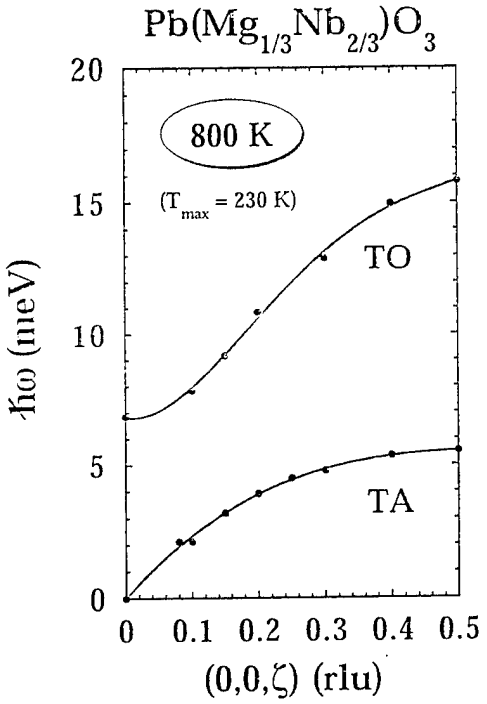

Fig. 2. Dispersion curves of the transverse acoustic (TA) and the lowest-energy transverse optic (TO) modes in PMN measured by Naberezhnov *et al.* (ref. [10]) at 800 K, far above T_d= 617 K.

In this paper we present a more complete lattice dynamical study of pure PZN, in which we also observe an anomalous ridge of scattering that closely resembles the waterfall seen in PZN-8%PT and PMN. PZN differs from PMN in that it exhibits an explicit structural phase transformation at 410 K from cubic to tetragonal symmetry. The value of T_{max} for PZN is just slightly above T_c = 410 K, and thus much higher than T_{max} = 230 K for PMN.[11] We further present a simple mode-coupling model that clearly relates this unusual feature of the TO phonon branch (the same branch that goes soft at the zone center at T_c in $PbTiO_3$) to the PMR. Our current study does not, however, cover the critical scattering at

small q below 0.075 Å^{-1}. Extensive studies in this area have already been carried out using neutron[12] and x-ray scattering[13,14] techniques. As we will show, this is the portion of the Brillouin zone where the TO mode is overdamped because of the PMR.

II. EXPERIMENTAL

Two single crystals of PZN were used in this study, the first, labelled PZN#1, weighs 4.2 grams and the second, labelled PZN#2, weighs 2.3 grams. Both crystals were grown using the high-temperature flux technique described elsewhere.[11] Each crystal was mounted onto an aluminum holder and oriented with the cubic [001] axis vertical, thereby giving access to the $(HK0)$ scattering zone. They were then placed inside a vacuum furnace capable of reaching temperatures of up to 900 K. For temperatures below room temperature, a specially designed closed-cycle helium refrigerator was used to cover the range from 25 K to 670 K.

All of the neutron scattering data presented here were obtained on the BT2 triple-axis spectrometer located at the NIST Center for Neutron Research. The (002) reflection of highly-oriented pyrolytic graphite (HOPG) was used to monochromate and analyze the incident and scattered neutron beams. An HOPG transmission filter was used to eliminate higher-order neutron wavelengths. The majority of our data were taken holding the incident neutron energy E_i fixed at 14.7 meV (λ_i = 2.36 Å) while varying the final neutron energy E_f, and using horizontal beam collimations of 60′-40′-S-40′-40′ and 60′-40′-S-40′-open.

Two basic types of inelastic scans were used to collect data on each sample. Constant-E scans were performed by holding the energy transfer $\hbar\omega = \Delta E = E_i - E_f$ fixed while varying the momentum transfer $\vec{Q}$. Constant-$\vec{Q}$ scans were performed by holding the momentum transfer $\vec{Q} = \vec{k_i} - \vec{k_f}$ ($k = 2\pi/\lambda$) fixed while varying the energy transfer ΔE. Using a combination of these scans, the dispersions of both the TA and the lowest-energy TO phonon modes were mapped out at a temperature of 500 K (still in the cubic phase, but well below the Burns temperature for PZN of $T_d \sim 750$ K).

It is worthwhile to note that the high temperature data were taken using neutron energy gain, i. e. by scanning E_f such that the energy transfer $\hbar\omega < 0$. This process is known as phonon annihilation. At high temperatures, and not too large energies, the phonon thermal population factor makes this mode of operation feasible. More importantly, the instrumental energy resolution function contains the factor $\cot 2\theta_a$, where $2\theta_a$ is the analyzer (HOPG) scattering angle. Hence the energy resolution increases with increasing energy because $2\theta_a$ decreases. The net result is an increased neutron count rate at the expense of a broader linewidth, thereby making the relatively weaker transverse optic mode easier to see.

III. INELASTIC SCATTERING DATA FROM PZN NEAR Q= (2, 0, 0)

The waterfall, previously reported in PZN-8%PT,[1] is shown for PZN#1 at 500 K in Fig. 3. The data points represent the peak scattered neutron intensity plotted as a function of $\hbar\omega$ and $\vec{q}$, where $\vec{q} = \vec{Q} - \vec{G}$ is the momentum transfer relative to the $\vec{G} = (2, 0, 0)$ Bragg reflection, measured along the cubic [010] symmetry direction. The solid dots represent data from constant-$\vec{Q}$ scans whereas the two open circles are data derived from constant-E scans. These latter two data points signal the onset of the waterfall regime in which the TO phonon branch appears to dive into the TA branch. and are thus connected by a dashed line. The lowest-energy data points trace out the TA phonon branch along [010]. Solid lines are drawn through these points as a guide to the eye, and are nearly identical to those shown for PMN in Fig. 1.

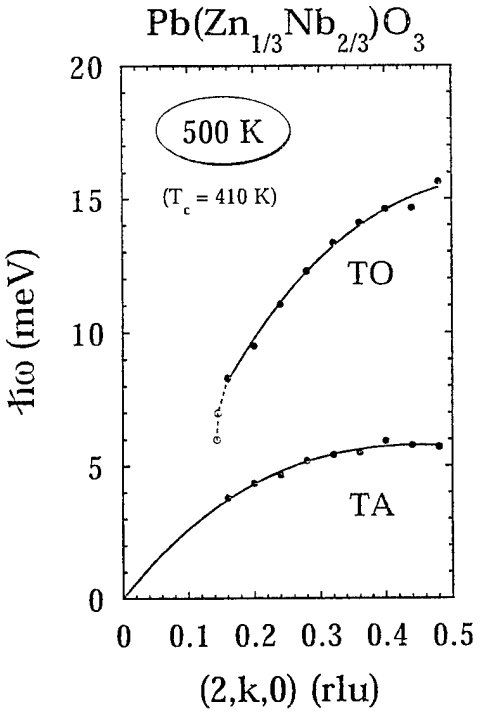

Fig. 3. Solid (open) dots represent positions of peak scattered neutron intensity taken from constant-$\vec{Q}$ (constant-E scans) at 500 K along the cubic [010] symmetry direction in PZN. Solid lines are guides to the eye indicating the TA and TO phonon dispersions.

As was the case for PZN-8%PT measured at the same temperature, the anomalous ridge of scattering in PZN is centered approximately at 0.14 reciprocal lattice units (rlu) or 0.22 Å^{-1} (1 rlu= $2\pi/a$ = 1.545 Å^{-1}). This is more clearly shown by the series of constant-E scans plotted in Fig. 4 for $\hbar\omega$ =0, -6, -8, and -12 meV (negative

values correspond to phonon annihilation as described above). We note that both of the -6 and -8 meV scans are peaked at the same value of k $(= q)$, thereby indicating the presence of the waterfall. Remarkably, the 0 meV cross section exhibits an enormous change in the vicinity of the waterfall q-vector. This demonstrates that the effects of the PMR extend in energy all the way from the TO branch through the TA branch and into the elastic channel. The -12 meV scan, by contrast, peaks at a larger momentum transfer q (~ 0.24 rlu) that lies outside the waterfall regime, and instead represents a genuinely propagating TO phonon mode.

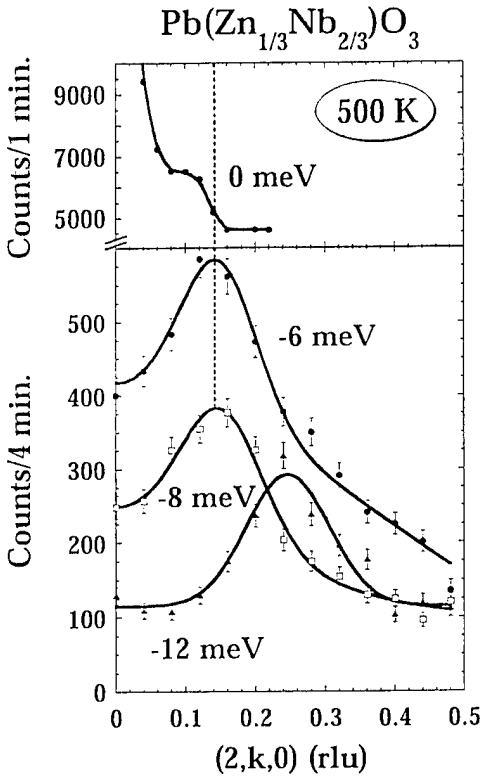

Fig. 4. Constant-E scans at 0, -6, -8, and -12 meV (phonon annihilation) measured at 500 K on PZN crystal #1.

It is important to realize that peaks in constant-E scans do not guarantee propagating modes. This can only be confirmed using constant-$\vec{Q}$ scans. Therefore we show four representative constant-$\vec{Q}$ scans in Fig. 5 for the q values 0.00, 0.16, 0.28, and 0.48 rlu. For $q > 0.16$ rlu, two distinct peaks are present, corresponding to the TA and TO phonon modes. At 0.16 rlu, one sees the TO mode beginning to become damped while the intensity of the TA mode has become relatively much more intense. For $q < 0.16$ rlu, the TA mode was indistinguishable from the elastic peak. Most striking is the absence of any peak in the constant-$\vec{Q}$ scan for $q = 0.00$ rlu. There is no clear peak for the TO mode for $q < 0.16$ rlu, indicating that these polar optic modes are heavily overdamped.

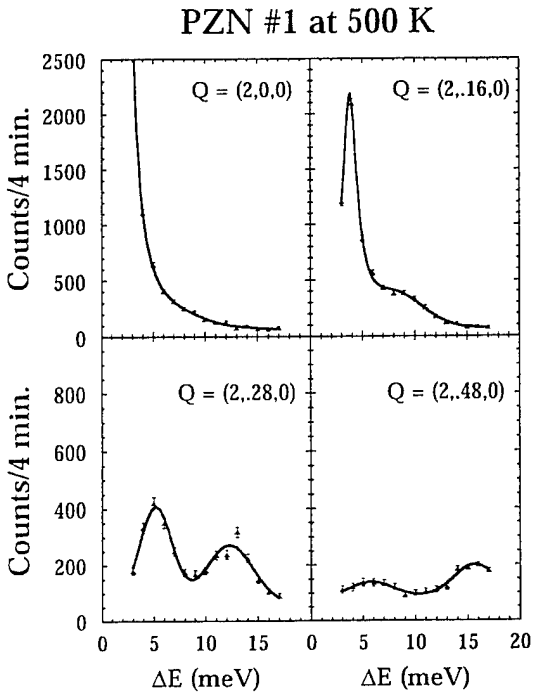

Fig. 5. Constant-$\vec{Q}$ scans at 0.00, 0.24, 0.28, and 0.48 rlu measured at 500 K on PZN crystal #1.

To illustrate this behavior as clearly as possible, a series of constant-$\vec{Q}$ scans were collected in steps of 0.04 rlu along $(2, k, 0)$ that spanned the entire Brillouin zone. After subtraction of a constant background, the data have been plotted as a contour plot in Fig. 6. For ease of comparison, the contour plot has been drawn with the same vertical and horizontal scales used in Fig.'s 2 and 3. The intensity data are represented on a logarithmic color scale with yellow representing the highest intensity, and black the lowest. At large q near the zone boundary, the TO and TA phonon branches are readily apparent as broad green features. Near the waterfall regime, the TO branch appears to drop almost vertically into the TA branch with a corresponding increase in intensity. Below $q \sim 0.14$ rlu, the intensity contours show no peak (scanning vertically) that could correspond to a propagating mode. The acoustic mode looks to be flat below 4 meV only because the color scale covers a limited intensity range above which all data are colored yellow. The intensity range was limited on purpose to make the waterfall feature more visible. Even so, one can notice a very rapid increase in the TA phonon intensity in the vicinity of the waterfall, suggesting that a transfer of intensity might be occurring between the TO and TA modes. To examine this possibility, we performed model calculations using a simple mode-coupling scheme to attempt to simulate the anomalous features reported here in the PZN compound.

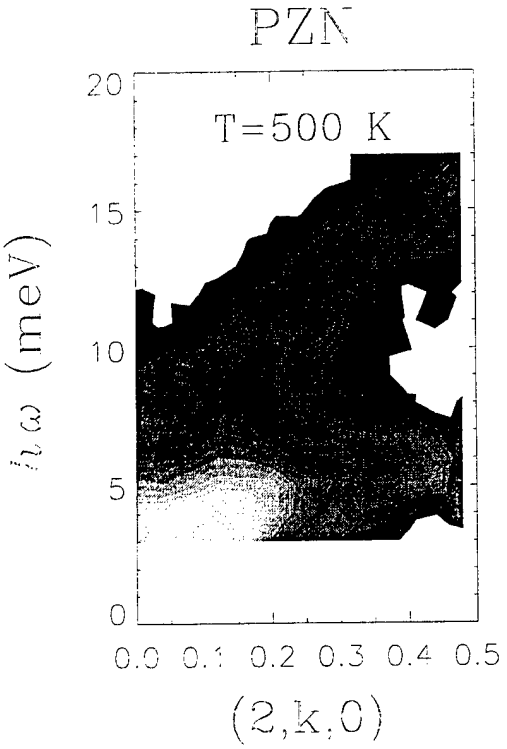

Fig. 6. Contour map of the background subtracted scattering intensity from PZN at 500 K measured near (200). The intensity is indicated by a logarithmic color scale that is limited to a narrow range in order to better show the waterfall. Yellow is the most intense.

IV. MODE-COUPLING MODEL

During the course of our experiments on relaxor ferroelectrics, a simple but effective model describing the anomalous low-frequency lattice dynamics was developed assuming a coupling between the TO and TA phonon modes. For the case of neutron energy loss, the scattering intensity distribution I for two interacting modes with frequencies Ω_1 and Ω_2, and widths Γ_1 and Γ_2, is given by the expression[15]

$$I \sim [n(\omega)+1]\frac{\omega}{A^2+\omega^2 B^2} \times \\ ([(\Omega_2^2-\omega^2)B-\Gamma_2 A]F_1^2 + 2\lambda B F_1 F_2 + \\ [(\Omega_1^2-\omega^2)B-\Gamma_1 A]F_2^2), \quad (1)$$

where A and B are given by

$$A = (\Omega_1^2-\omega^2)(\Omega_2^2-\omega^2) - \omega^2\Gamma_1\Gamma_2, \\ B = \Gamma_1(\Omega_2^2-\omega^2) + \Gamma_2(\Omega_1^2-\omega^2), \quad (2)$$

and $n(\omega)$ is simply the Bose factor $[e^{(\omega/k_BT)}-1]^{-1}$. The quantities $F_{1,2}$ are the structure factors of modes 1 and 2, and λ is the coupling strength between the two modes. Extensive model calculations based on this equation, which has been shown to describe the behavior of coupled-phonon cross sections quite well,[15,16] have been performed in collaboration with K. Ohwada at the Institute of Solid State Physics, University of Tokyo.[18]

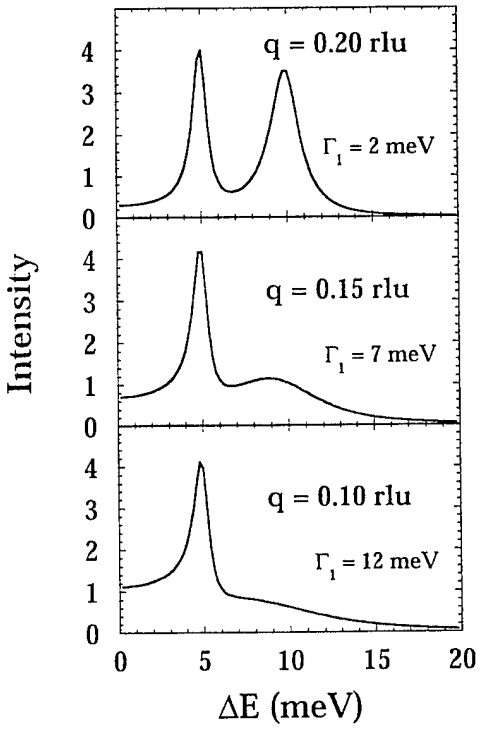

Fig. 7. Model simulations assuming a coupled-mode intensity distribution and a strongly q-dependent TO phonon linewidth Γ_1. Three constant-$\vec{Q}$ scans are shown corresponding to $q = 0.20$, 0.15, and 0.10 rlu, with $q = 0.15$ rlu taken to be the reciprocal space position of the anomalous waterfall feature.

The essential physics behind the mode-coupled model description of the waterfall is built into the linewidth of the TO mode Γ_1, which is assumed to become sharply q-dependent as the polar micro-regions begin to form at the Burn's temperature T_d. If we suppose that the PMR have an average diameter given by $2\pi/q_{wf}$, where q_{wf} represents the reciprocal space position of the waterfall, then those optic phonons having $q < q_{wf}$ will not be able to propagate easily because their wavelength exceeds the average size of the PMR. These polar lattice vibrations are effectively impeded by the boundary of the PMR. This idea has also been discussed by Tsurumi *et al.*[17] The simplest way to simulate this situation is to assume a sudden and steep increase in $\Gamma_1(q)$ at q_{wf}. For this purpose, a Fermi-distribution function of q works extremely well. Fig. 7 shows several model constant-$\vec{Q}$ simulations based on this assumption, using the values $q_{wf} = 0.15$ rlu, $\lambda = 10$, $F_1 = 1$, $F_2 = 4$, and $\Gamma_2 = 1$. For

simplicity and purposes of illustration, the dispersions of both optic and acoustic modes were ignored by holding the parameters $\Omega_{1,2}$ fixed at 10 and 5 meV, respectively, over the entire Brillouin zone. Similarly, instrumental resolution effects were not included.

For $q > q_{wf}$ one observes two broad peaks, as expected. At momentum transfers $q < q_{wf}$, however, the optic mode becomes highly overdamped and its profile extends in energy below that of the acoustic mode. Alongside each constant-$\vec{Q}$ scan is shown the corresponding value of Γ_1 used in the simulation. The waterfall thus represents the crossover between a high-q regime, in which one observes two well-defined peaks corresponding to two propagating modes, and a low-q regime, in which one observes an overdamped optic mode plus an acoustic peak. This simple model cross section describes all of the experimental observations very well. Indeed, one can favorably compare the simulated scan at $q = 0.15$ rlu in Fig. 7 with the experimental scan for $\vec{Q} = (2, 0.16, 0)$ shown in Fig. 5. One can see now that the waterfall is *not* a TO phonon dispersion at all. Instead, it is simply a redistribution of the optic mode profile that is caused by the PMR which force a sudden change in the optic mode linewidth at a specific q related to the average size of the PMR.

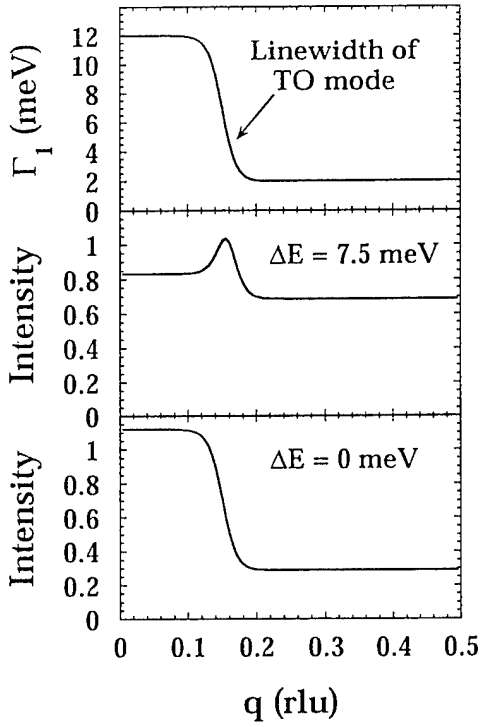

Fig. 8. Model simulations of two constant-E scans at 0 and 7.5 meV. The q-dependence of the TO linewidth Γ_1 is shown in the top panel for ease of comparison.

In order to illustrate the basic characteristics of the scattering cross section within the coupled-mode model, the q-dependence of the optic mode linewidth Γ_1 is shown in Fig. 8 along with two simulated constant-E scans at 0 and 7.5 meV. It is apparent that the sharp increase in Γ_1 has a corresponding and pronounced effect on both cross sections in the vicinity of q_{wf}. The jump in the elastic cross section occurs because of the sum rule for the scattering. Hence the extreme broadening of the TO mode that occurs near q_{wf} extends underneath the TA branch and into the elastic channel. We emphasize that despite the fact that no resolution effects, Bragg or background terms were included in these calculations, the agreement with experiment is surprisingly good. Indeed, the cross section calculated for 0 meV is striking in its similarity to the experimentally measured elastic cross section shown in the top panel of Fig. 4, and thus lends strong credence to the coupled-mode model.

V. TEMPERATURE DEPENDENCE

Our data on the temperature dependence of the waterfall in PZN are limited by the fact that PZN decomposes at a temperature less than the Burns temperature. This prevents us from performing measurements above T_d which are of interest because we wish to monitor the recovery of zone center and low-q TO phonons at temperatures where the polarized micro-regions no longer exist. PMN, by contrast, has a lower T_d. Hence Naberezhnov *et al.* were able to measure the TO phonon dispersion at 800 K $> T_d$ where they observed a normal TO phonon branch.[10] Selected phonons were briefly studied at 860 K in PZN-8%PT.[1] There the scattering intensity associated with the waterfall increased (as expected from the Bose temperature factor) beyond that measured at 500 K, and the peak position of the waterfall, measured using constant-E scans, shifted in towards the zone center, i. e. from (2,0.14,0) to (2,0.10,0). Constant-$\vec{Q}$ data at (2,0.10,0) show a broad peak around 10 meV. These data suggest that around 860 K the PMR have already begun to form inside of a "uniform," or unpolarized crystal. A complete understanding of the behavior in this temperature range must await the further study of PMN.

Below the PZN tetragonal-to-rhombohedral phase transition at 410 K the scattering intensity associated with the waterfall decreases gradually, and is almost completely gone at 100 K. This behavior is summarized in the inset to Fig. 9 where the raw intensity (no background subtraction) at $\vec{Q} = (2, -.12, 0)$ and $\hbar\omega = 7$ meV is plotted versus temperature. Figure 9 itself shows a constant-$\vec{Q}$ scan at (2,0,0) and 25 K which clearly shows the presence of a zone center TO mode.

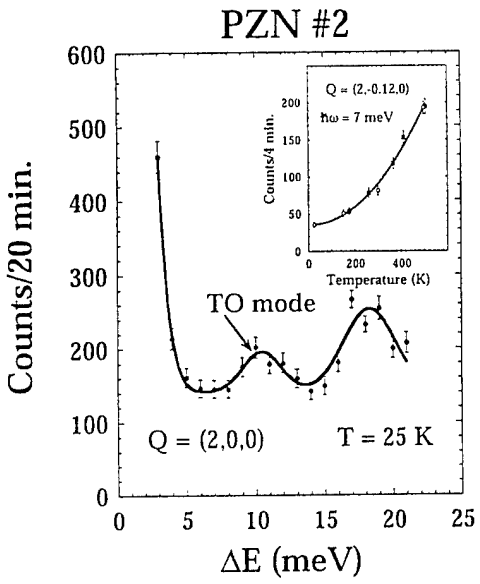

Fig. 9. Constant-$\vec{Q}$ scan at (2,0,0) and 25 K taken on PZN crystal #2 showing the recovery of the TO zone center mode at low temperature. Inset gives the temperature dependence of the raw scattering intensity measured at $\vec{Q}$ = (2,-0.12,0) at 7 meV (no background subtraction).

VI. DISCUSSION

We have discovered an anomalous ridge of scattering positioned roughly 0.2 Å^{-1} from the zone center in the relaxor systems PZN-8%PT, PZN, and also PMN in their respective cubic phases. This scattering was observed in various different Brillouin zones including (220) and (004) in PZN-8%PT, and (200), (300), and (220) in PZN. The ridge of scattering is extended in energy in such a way as to make the lowest-lying TO phonon branch appear to drop precipitously into the TA phonon branch at a specific value of q, thereby resembling a waterfall. Equally remarkable is the manifestation of a huge elastic cross section near the same value of q. An unusual feature has also been observed by Lushnikov *et al.* for pure PMN using Raman and neutron inelastic scattering techniques at 77 K over an extended energy range from 5.2 meV to 6.8 meV, which nearly coincides with that of the waterfall feature reported here.[19] This was interpreted as evidence of a fracton, i. e. an excitation on a fractal lattice. We have shown that a simple coupled-mode model can be used effectively to describe our neutron inelastic data by postulating a sharply q-dependent TO phonon linewidth Γ_1 that exhibits a large step-like increase with decreasing q upon reaching the waterfall wavevector q_{wf}. In this way we are able to relate the waterfall directly to the presence of nanometer-sized polarized micro-regions in the crystal which serve to damp the polar TO modes at low q. A brief review of the waterfall and related neutron inelastic scattering measurements on various relaxor systems has recently been submitted for publication.[20] It is hoped that our results with stimulate theoretical calculations of the precise q-dependence of Γ_1 to allow for comparison with experiment. It would be very interesting to investigate the effects of an applied electric field E on the waterfall, and we have already begun measurements to this end.

VII. ACKNOWLEDGMENTS

We would like to thank Y. Fujii, K. Hirota, B. Noheda, K. Ohwada, S. B. Vakrushev, G. Yong, and H. D. You for stimulating discussions. Financial support by the U. S. Dept. of Energy under contract No. DE-AC02-98CH10886, by the Office of Naval Research under project MURI (N00014-96-1-1173), and under resource for piezoelectric single crystals (N00014-98-1-0527) is acknowledged. We also acknowledge the support of the NIST Center for Neutron Research, U. S. Dept. of Commerce, in providing the neutron facilities used in this work.

[1] P. M. Gehring, S.-E. Park, and G. Shirane, Phys. Rev. Lett. **84**, 5216 (2000).
[2] S.-E. Park and T. R. Shrout, J. Appl. Phys. **82**, 1804 (1997).
[3] J. Kuwata, K. Uchino, and S. Nomura, Ferroelectrics **37**, 579 (1981); *ibid.* Jpn. J. Appl. Phys. **21**, 1298 (1982).
[4] See, for example, B. Noheda *et al.*, Appl. Phys. Lett. **74**, 2059 (1999).
[5] P. M. Gehring, S. B. Vakhrushev, and G. Shirane, cond-mat/0002464.
[6] G. Burns and F. H. Dacol, Phys. Rev. B **28**, 2527 (1983); *ibid.* Sol. Stat. Comm. **48**, 853, (1983).
[7] N. de Mathan *et al.*, J. Phys. Condens. Matter **3**, 8159 (1991).
[8] A. A. Bokov, Ferroelectrics **131**, 49 (1992).
[9] J. Zhao, A. E. Glazounov, Q. M. Zhang, and B. Toby, Appl. Phys. Lett. **72**, 1048 (1998).
[10] A. Naberezhnov, S. B. Vakhrushev, B. Dorner, and H. Moudden, Eur. Phys. J. B **11**, 13 (1999).
[11] S. -E. Park, M. L. Mulvihill, G. Risch, and T. R. Shrout, Jpn. J. Appl. Phys. 1 **36**, 1154 (1997).
[12] S. B. Vakhrushev, A. Naberezhnov, N. M. Okuneva, and B. N. Savenko, Phys. Solid State **37**, 1993 (1995).
[13] S. B. Vakhrushev, A. Naberezhnov, S. K. Sinha, Y. -P. Feng, and T. Egami, J. Phys. Chem. Solids **57**, 1517 (1996).
[14] H. You and Q. M. Zhang, Phys. Rev. Lett. **79**, 3950 (1997).
[15] M. Bullock *et al.*: Phys. Rev. B **57** (1998) 7916.
[16] J. Harada, J. D. Axe, and G. Shirane: Phys. Rev. B **4** (1971) 155.

[17] T. Tsurumi, K. Soejima, T. Kamiya, and M. Daimon, Jpn. J. Appl. Phys. Part 1 **33**, 1959 (1994).
[18] K. Ohwada, private communication.
[19] S. G. Lushnikov, S. N. Gvasaliya, and I. G. Siny, Physica B **263-264**, 286 (1999).
[20] G. Shirane and P. M. Gehring, J. Phys. Soc. Jpn. (accepted).

Appendix 9

B. Noheda, D.E. Cox, G. Shirane, S.–E. Park, L.E. Cross, and Z. Zhong, "Polarization rotation via a monoclinic phase in the piezoelectric 92%$PbZn_{1/3}Nb_{2/3}O_3$–8%$PbTiO_3$," Physical Review Letters, 86[17], 3891–3894(2001).

Polarization rotation *via* a monoclinic phase in the piezoelectric $92\%PbZn_{1/3}Nb_{2/3}O_3$-$8\%PbTiO_3$

B. Noheda*[1], D.E. Cox[1], G. Shirane[1], S-E. Park†[2], L.E. Cross[2] and Z. Zhong[3]
[1] *Physics Department, Brookhaven National Laboratory, Upton, NY 11973*
[2] *Materials Research Laboratory, Pennsylvania State University, University Park, PA 16802*
[3] *National Synchrotron Light Source, Brookhaven National Laboratory, Upton, NY 11973*

The origin of ultrahigh piezoelectricity in the relaxor ferroelectric $PbZn_{1/3}Nb_{2/3}O_3$-$PbTiO_3$ was studied with an electric field applied along the 001 direction. The zero-field rhombohedral R phase starts to follow the direct polarization path to tetragonal symmetry via an intermediate monoclinic M phase, but then jumps irreversibly to an alternate path involving a different type of monoclinic distortion. Details of the structure and domain configuration of this novel phase are described. This result suggests that there is a nearby R-M phase boundary as found in the $Pb(Ti,Zr)O_3$ system.

Recently two important advances have been made in searching for the origin of high piezo response in the perovskite oxides. One is a theoretical consideration [1–3] of the polarization rotation path under an electric field, emphasized by Fu and Cohen [1]. The second is the experimental discovery of a monoclinic phase in $Pb(Zr,Ti)O_3$ [4,5] close to a "morphotropic" phase boundary (MPB), a nearly vertical line between the rhombohedral and tetragonal phases. In this paper we demonstrate that these two seemingly disparate aspects are closely connected.

Solid solutions of $Pb(Zn_{1/3}Nb_{2/3})O_3$ containing a few percent of $PbTiO_3$ (PZN-xPT) are relaxor ferroelectrics with ultrahigh piezoelectric responses an order of magnitude larger than those of conventional piezoelectric ceramics [6–8]. They have a cubic perovskite-type structure at high temperatures, but undergo a diffuse ferroelectric phase transition at lower temperatures [6]. Materials in the ferroelectric region have structures with either rhombohedral or tetragonal symmetry, separated by a "morphotropic" phase boundary (MPB) at $x \simeq 10\%$, similar to that of the well-known piezoelectric system $PbZr_{1-x}Ti_xO_3$ (PZT) [9]. Extraordinarily high levels of electromechanical coupling and strain have been reported by Park and Shrout [8] in rhombohedral crystals that are poled along [001], despite the fact that the polar axis lies along [111] [7,10].

A typical strain-field loop for the rhombohedral composition PZN-8%PT (close to the MPB) with an electric field applied along [001] is plotted in Fig. 1 (top), after Durbin et al. [11]. For this poling configuration, the strain behaves linearly below a certain threshold field, which is smaller for compositions closer to the MPB [8,10]. This feature, together with the high strain levels obtained, makes these materials very promising for actuator applications. Above the threshold field, the strain shows a sharp jump, non-linear behavior and hysteresis. X-ray diffraction experiments performed on PZN-8%PT crystals under an applied electric field [11] have shown that the lattice parameter vs. field loop exactly reflects the strain behavior, confirming that the high macroscopic strain levels observed are due to the microscopic strain of the crystal lattice. The jump observed at the threshold field was attributed to a structural phase transition between the rhombohedral and the tetragonal phases. Very recently, it has been also reported that the high-field tetragonal phase changes, after removal of the field, into a mixture of a dominant monoclinic phase with a remnant tetragonal phase [12].

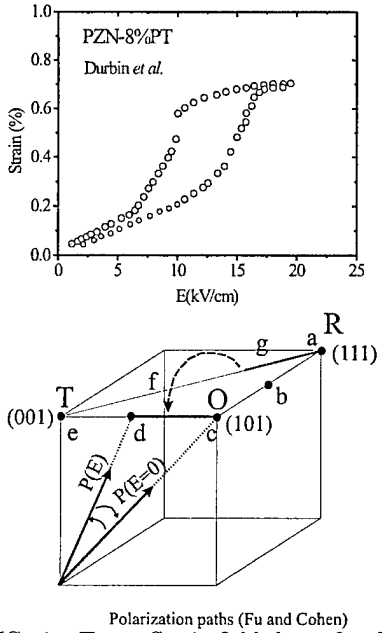

FIG. 1. Top: Strain-field loop for PZN-8%PT (after Durbin et al. [11]). Bottom: Scheme of the two possible paths (R-T and R-O-T) for the polarization direction to change from [111] in the rhombohedral (R) phase to [001] in the tetragonal (T) phase as proposed by Fu and Cohen [1]. The thickest lines represent the path followed by the polarization in PZN-8%PT under the application of the electric field, as demonstrated by the present work. The solid arrows illustrate the orientation of the polarization in a particular domain with and without an electric field.

Our current study with high energy x-rays of 67 keV gives a very different picture. We show that the rhom-

bohedral phase in the unpoled sample transforms into a purely monoclinic phase by the application of an electric field along the [001] direction which, surprisingly, remains monoclinic after the field is removed. This monoclinic phase, in which b_m is directed along the pseudo-cubic [010] axis, is not the same as that observed in PZT, in which b_m lies along pseudocubic [110] [4]. The monoclinic phase in PZT represents the a-g-f-e path (see Fig. 1 bottom) proposed by Fu and Cohen [1] for the polarization to rotate between the rhombohedral and the tetragonal phases, while the monoclinic PZN-8%PT phase represents the rotation path along a-c-d-e.

Four crystals with composition 92%$PbZn_{1/3}Nb_{2/3}O_3$ -8%$PbTiO_3$ (PZN-8%PT), grown by the high temperature flux technique [8,16], were kindly provided by the authors of Refs. [11,12]. The crystals were oriented using a Laue back-reflection camera as described previously [8], and cut into 2x2x2 mm^3 cubes with their faces perpendiculartо the ⟨100⟩ directions.

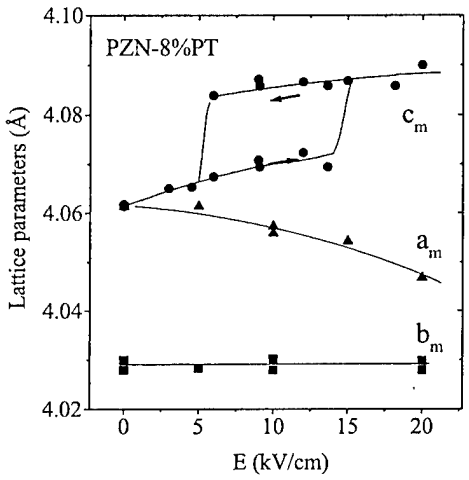

FIG. 2. Evolution of the lattice parameters, a_m,b_m and c_m, of PZN-8%PT with electric field

Synchrotron x-ray diffraction measurements were initially performed at beamline X7A, at the National Synchrotron Light Source (NSLS), with x-rays of about 18 keV from a Si(111) double-crystal monochromator. Due to the high lead content, the samples are quite opaque at these energies, with a penetration depth of only about 1 μm, at the typical scattering angles used, and the measurements are therefore sensitive to inhomogeneous piczoclectric strains close to the surface (skin effect). In order to avoid this effect, high energy x-ray experiments were perfomed at 67 keV at the superconducting-Wiggler beamline X17B at the NSLS.

The 67 keV x-rays were obtained with a Si (220) Laue-Bragg monochromator and the measurements were made on a four-circle Huber diffractometer equipped with a Si(220) analyzer, with an electric field applied to the crystal *in situ*. For this purpose thin wires were attached to the sample electrodes using a small drop of conducting epoxy, and a silicon grease with a high dielectrical breakdown was used to prevent arcing.

As-grown crystals of the composition under study are rhombohedral [6,8](see Table I). However, when an electric field above a certain value is applied, the crystal symmetry changes and the rhombohedral phase can be recovered only either by annealing above the Curie temperature or by crushing the crystal. The initial rhombohedral state and the phase transition(s) undergone during the first field cycle are currently under investigation by Ohwada [13].

Once the rhombohedral phase is irreversibly transformed into the monoclinic one, the monoclinic lattice shows reversible changes as a function of the electric field, as shown in Fig. 2 (see also Table I). The monoclinic angle, $\beta = 90.15°$, and the monoclinic axis, b_m, are field independent in the studied range between 0 and 20 kV/cm. c_m increases with the electric field and shows a jump around 15 kV/cm and hysteresis, in agreement with Durbin et al. [11], while a_m decreases as the field is increased and approaches the c_m value in the E=0 limit [14].

The domain configuration observed in this experiment is illustrated in the representations of the reciprocal space shown in Fig. 3. [15]. Usually monoclinic symmetry leads to a very complicated domain configuration. However, once the field is applied, a much simpler situation preveals. The c-axis is now fixed along the field direction. As shown in the representation of the HK0 plane in Fig. 3a, there are only two b domains related by a 90° rotation about the c-axis. Each of these b domains contains two a domains in which a_m forms angles of either β or $180° - \beta$ respectively with c_m (see Fig. 3b). The polarization vectors in each of the four domains, which rotate under the electric field within the ac plane, form identical angles with the [001] direction. It is evident from Fig. 3a that the domain twinning confers upon the lattice a pseudo-tetragonal symmetry, which might account for the previous assignment of tetragonal symmetry to this phase based on optical measurements [16].

TABLE I. Lattice parameters, unit cell volume and symmetry of PZN-8%PT as-grown, under a high field of 20 kV/cm, and after the field is removed. S denotes the crystal symmetry.

	a (Å)	b (Å)	c (Å)	α /β (°)	V (Å^3)	S
As-grown, E=0*	4.053	4.053	4.053	89.90	66.58	R
E=20kV/cm§	4.047	4.029	4.086	90.16	66.62	M
After field, E=0*§	4.061	4.030	4.061	90.15	66.46	M

*From powder diffraction. § From single crystal diffraction.

Some examples of the x-ray peak profiles are shown in Fig. 4. The longitudinal scans over the (002) reflection at 0 kV/cm and at 20 kV/cm shown in the upper left of the figure illustrate the drastic change of the c-axis with the electric field (L= 2 corresponds to the $c_m = a_m$ value at E= 0). The very narrow mosaic at high fields is apparent in the upper-right of the figure, which shows a transverse scan (L scan) over the (0 2 0) Bragg peak at E= 20 kV/cm (K= 2 corresponds to the $c_m = a_m$ value at E= 0 so K= 2.015 means $b_m/a_m = 2/2.015$). The lower part of the figure is a contour map of the H0L zone around (200) after removal of the field, which shows the b domain containing the two a domains illustrated in Fig. 3a. and 3b. The symmetric splitting along the transverse direction (L scan), corresponds to the twin angle between the a domains, so the L coordinate of 0.005 corresponds to a monoclinic angle β= 90.16°, that is found to be independent of the electric field. Although the (020) peak is very narrow, a small shoulder can be observed at positive L values (also present at 20 kV/cm, in the upper-right plot), which probably results from the crystal mosaic.

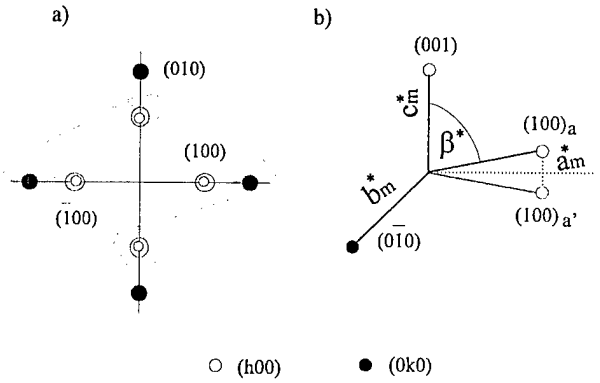

FIG. 3. (a) HK0 plane in reciprocal space for monoclinic PZN-8%PT showing the two b domains at 90°, shaded and unshaded respectively, in which H and K are interchanged with respect to each other. The double circles represent the two a domains, illustrated in Fig. 3b. b) Scheme of the reciprocal unit cell of one of the b domains showing the two a domains, a and a', respectively.

The low energy experiments at 18 keV essentially reproduce the results obtained by Durbin et al. cite-Durbin1,Durbin2. The c_m lattice parameter along the field direction [001] exhibits the same strongly non-linear field dependence illustrated in Fig. 2. Measurements made with the scattering vector perpendicular to the field direction after the field was removed, show the same characteristic diffraction features as recently reported protect [12], namely, a very broad peak on the low-angle side and a very sharp peak on the high-angle side, corresponding to H= 2.000 and K= 2.015, respectively. The broad peak changes with field while the sharp peak is field-independent, in agreement with our high-energy x-ray results described above. The markedly different widths of these two peaks led Durbin et al. to postulate the coexistence of two phases (monoclinic and tetragonal) at E= 0 kV/cm, with very different domain sizes. However, since the broadening of the (h00) peaks was not observed with high energy x-rays, it can be attributed to a "skin" effect.

Powder diffraction data collected from a sample prepared by crushing a small crystal piece after the application and removal of an electric field have confirmed that the monoclinic indexing of our single crystal experiments is correct. Lattice parameters a_m= c_m= 4.061 Å, b_m= 4.030 Å, and β= 90.15° were extracted, in complete agreement with the single crystal data. In this case, however, the monoclinic phase was found to coexist with a rhombohedral phase with a_r= 4.054 Å, and α = 89.9° (see Table I).

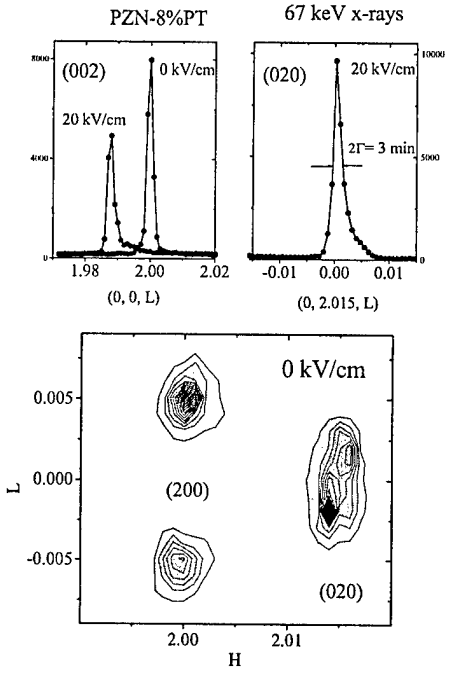

FIG. 4. Radial (L) scans over the (002) reflection at 20 kV/cm and at 0 kV/cm, after the field is removed (top left). The transverse (L) scan around (0, 2.015, 0) at 20 kV/cm is shown at the upper-right plot. At the bottom of the figure, an H0L mesh scan around the (200) Bragg reflection after the removal of the electric field. H= K= L= 2.0 have been defined to correspond to the a_m value at E= 0 kV/cm.

Comparison of our experimental results with the theoretical model of Fu and Cohen [1] brings out several interesting features. These authors calculated the free energies along the polarization rotation paths between the rhombohedral R and tetragonal T points for $BaTiO_3$

(see Fig. 1), and concluded that the R-T path (a-g-f-e) is the most energetically-favorable one. PZN-8%PT starts out at the R point in Fig. 1, since the as-grown crystal is rhombohedral, but then changes irreversibly to the O-T path (c-d-e), with monoclinic symmetry. As mentioned above, this process of change between the rhombohedral and the monoclinic phases (dashed arrow in Fig. 1) is being studied elsewhere in detail [13]. When the field is decreased, the crystal remains on the O-T path. During this process a_m and c_m gradually approach each other until they eventually reach the same value at E= 0 kV/cm [14]. When the field is increased, a_m approaches b_m (see Fig.2), while following the O-T path, approaching the T point in Fig. 1. The polarization of each domain rotates within the (010) plane, and the polarization direction gets closer to the tetragonal polar axis, [001], as the field is increased, as shown by the solid arrows in Fig. 1. However, the T point is not yet reached at the maximum electric fields (E= 20 kV/cm) used in the present study. Work is being carried out on other compositions, such as PZN-4.5%PT and PZN-9%PT, to determine the compositional range in which this behavior is observed. The major remaining question is why and how the sudden change at 15 kV/cm is reflected only in c_m. The jump observed in c_m is very sensitive to the mechanical stress and can be completely eliminated if the sample is slightly stressed [17]. Work is in progress to address this point.

The electric field experiments reported by Guo et al. [5], on rhombohedral PZT showed that, by poling at high temperatures, a monoclinic phase is also induced by the electric field and retained after the field is removed. This monoclinic cell is such that b_m lies along pseudo-cubic [110] [4], indicating that the polarization moves along the R-T (e-g-f-e) path when the field is applied. On the other hand, unpoled PZT has a monoclinic phase region from x= 0.46 to x= 0.52 at 20K [20]. The existence of an irreversible rhombohedral-to-monoclinic phase transition induced by the application of an electric field in PZN-8%PT, suggests that, as in the PZT case [5], a rhombohedral-to-monoclinic phase boundary exists close to x=8% in the unpoled PZN-xPT phase diagram. This would clarify some of the apparent puzzles reported, such as the optical observation of symmetry lowering in PZN-9%PT [18,19]. If the monoclinic phase is found to exist in unpoled PZN-9%PT, then the phase diagram of PZN-PT becomes almost identical to that of PZT. Our current results suggest that the near degeneracy between the two monoclinic paths (R-T and R-O-T) might be responsible for the larger piezoelectric response in PZN-xPT, compared with that of PZT, in which only rotation is allowed. We expect that first-principles calculations may well clarify some of these important questions.

After submission of this letter, the very relevant work by D. Vanderbilt and M.H. Cohen [21] came to our attention. By means of an eighth-order expansion of the Devonshire theory, these authors were able to predict three different monoclinic phases. Two of these, M_A and M_C, correspond, respectively, to that previously observed in PZT and the one in PZN-8%PT described above.

We would like to thank M. Durbin, Y. Fujii, P. Gehring, R. Guo, J. Hastings, K. Hirota, K. Ohwada, D. Vanderbilt and T. Vogt for helpful discussions. Financial support by the U.S. DOE under contract No. DE-AC02-98CH10886, by ONR Grant No. N00014-98-1-0527 and project MURI (N00014-96-1-1173) is also acknowledged.

[1] H. Fu and R.E. Cohen, Nature **403**, 281 (2000).
[2] A. Garcia and D. Vanderbilt, Appl. Phys. Lett. **72**,2981 (1998).
[3] L. Bellaiche, A. Garcia, and D. Vanderbilt, Phys. Rev. Lett. **84**,5427 (2000).
[4] B. Noheda, J. A. Gonzalo, L.E. Cross, R. Guo, S-E. Park, D.E. Cox, and G. Shirane. Phys. Rev. B **61**,8687 (1999)
[5] R. Guo, L.E. Cross, S-E. Park, B. Noheda,D.E. Cox, and G. Shirane, Phys. Rev. Lett. **84**,5423 (2000)
[6] J. Kuwata, K. Uchino, and S. Nomura, Ferroelectrics, **37**, 579 (1981).
[7] J. Kuwata, K. Uchino, and S. Nomura, Japan. J. of Applied Phys. **21**,1298 (1982).
[8] S-E. Park and T.R. Shrout, J. Appl. Phys. **82**,1804 (1997).
[9] B. Jaffe, W.R. Cook, and H. Jaffe, Piezoelectric Ceramics, Academic Press, London (1971).
[10] S-F. Liu, S-E. Park, T. R. Shrout, and L. E. Cross, J. Appl. Phys. **85**,2810 (1999).
[11] M.K. Durbin, E.W. Jacobs, J.C. Hicks, and S.-E. Park, Appl. Phys. Lett. **74**,2848 (1999).
[12] M.K. Durbin, J.C. Hicks, S-E. Park, and T.R. Shrout, J. Appl. Phys., **87**,8159 (2000)
[13] K. Ohwada, (private communication).
[14] In the limit at which $a_m = c_m$ and $\beta > 90°$, the crystal symmetry becomes orthorhombic, corresponding to the O point in Fig.1 bottom.
[15] The real and the reciprocal lattice parameters are related by: $a_m^*=2\pi/(a_m \sin\beta)$, $b_m^*=2\pi/b_m$, $c_m^*=2\pi/(c_m \sin\beta)$ and $\beta^* = 180° - \beta$
[16] D-S. Paik, S-E. Park, S. Wada, S-F. Liu, and T. R. Shrout, J. Appl. Phys. **85**,1080 (1999).
[17] D. Viehland, J. Appl. Phys. **88**, 4794 (2000).
[18] Y. Uesu, Y. Yamada, K. Fujishiro, H. Tazawa, S. Enokido, J.-M. Kiat, and B. Dkhil, Ferroelectrics **217**,319 (1998)
[19] K. Fujishiro, R. Vlokh, Y. Uesu, Y. Yamada, J.-M. Kiat, B. Dkhil and Y. Yamashita, Jpn. J. Appl. Phys. **37**,5246 (1998).
[20] B. Noheda, D.E. Cox, G. Shirane, R, Guo, B. Jones, and L.E. Cross, Phys. Rev. B. **63**, (to appear 01/01/2001).
[21] D. Vanderbilt and M.H. Cohen, Phys. Rev. B. (in press), cond-mat/0009337.

Appendix 10

M.K. Durbin, J.C. Hicks, S.–E. Park, and T.R. Shrout, "X-ray diffraction and phenomenological studies of the engineered monoclinic crystal domains in single crystal relaxor ferroelectrics," Journal of Applied Physics, Vol. 87[11], 8159–8164 (June 2000).

X-ray diffraction and phenomenological studies of the engineered monoclinic crystal domains in single crystal relaxor ferroelectrics

M. K. Durbin and J. C. Hicks[a)]
SPAWAR System Center, San Diego, California 92152

S.-E. Park and T. R. Shrout
Materials Research Laboratory, The Pennsylvania State University, University Park, Pennsylvania 16802

(Received 21 September 1999; accepted for publication 29 February 2000)

We present x-ray diffraction data, which demonstrate that after high field poling, solid solutions of lead zinc niobate with 8% lead titanate (PZN–PT) consist of a mixture of a dominant monoclinic phase and a remnant tetragonal phase. To understand the origin of this engineered monoclinic phase we studied a Devonshire phenomenological model that predicts the field induced phase transitions in PZN–PT. Although previous attempts to use this model for these materials have matched the phase diagram and dielectric behavior, we show that the coefficients used in those models cannot be reconciled with recent data on electric field behavior. By modifying the coefficients we are able to explain the phase diagram, dielectric behavior, and high field phase transitions in compositions near the morphotropic phase boundary. Using these coefficients, we find no stable monoclinic phase present in the model. This contradiction is explained by noting that within the engineered domain state the tetragonal regions strain the rhombohedral regions, resulting in a metastable monoclinic phase. © *2000 American Institute of Physics.* [S0021-8979(00)06811-0]

I. INTRODUCTION

Complex perovskite materials have been the subject of much recent investigation because of their useful dielectric, piezoelectric and electrostrictive properties.[1–5] In particular, certain solid solutions of lead zinc niobate with lead titanate (PZN–PT) have shown extremely high electromechanical coupling with low hysteresis when poled along the ⟨001⟩ direction rather than the polar ⟨111⟩ direction.[2] The high coupling has been attributed in part to the existence of a morphotropic phase boundary (MPB), where two phases—a rhombohedral phase and a tetragonal phase—are near each other in energy. Compositions near the MPB also exhibit an electric field induced phase transition from rhombohedral to tetragonal when poled along the ⟨001⟩ direction.[3,4,6]

Using x-ray powder diffraction, Noheda *et al.* recently discovered a monoclinic phase in lead zirconate titanate (PZT). The new phase occurs near the MPB of PZT, and is bordered by the PZT rhombohedral and tetragonal phases.[7] Fujishiro *et al.* have observed monoclinic or triclinic domains in PZN–9%PT using polarized light microscopy.[8] The domains are observed at temperatures where the tetragonal and rhombohedral phases coexist. In this paper we report on a single crystal x-ray diffraction experiment which confirms that the coexistence of rhombohedral and tetragonal domains in PZN–8%PT results in a monoclinic distortion of the rhombohedral phase. In order to better understand the relationship between the rhombohedral, tetragonal and monoclinic phases, we have examined a simple phenomenological model of PZN–PT. The model was initially developed by Abe *et al.*,[9] and was based on the Devonshire model,[10] assuming that the energy expansion coefficients for a given composition could be determined by taking a linear combination of the coefficients of the unmixed materials.[11,12] Yamamoto and Terashima expanded on the model, modifying the coefficients to give more reasonable dielectric data[13] for high PT compositions (>10 mol%). Both groups were able to predict basic aspects of the phase diagram and dielectric behavior for these materials. We have examined their model and included a monoclinic phase as a possible solution (as was done by Belokopytov[14]). We also have used the model to predict the recently observed behavior of these materials under applied electric field. Comparing the results to known data yields modified coefficients for the model that are consistent with the observed phase transition, as well as with the dielectric behavior and phase diagram.

II. EXPERIMENT

Several samples of composition 92% $Pb(Zn_{1/3}Nb_{2/3})O_3$–8% $PbTiO_3$ (PZN–8%PT) were prepared as described in a previous work.[3] The final polished single crystal was a cube with sides of ≈2.4 mm. The samples were coated on the (001) and $(00\bar{1})$ faces with gold and poled just above the coercive field. The transverse sides were polished along the ⟨100⟩, ⟨010⟩, $\langle\bar{1}00\rangle$ and $\langle 0\bar{1}0\rangle$ directions. It should be noted here that since the crystal is pseudocubic in all phases (distortions to monoclinic, rhombohedral, tetragonal, etc., are small), all references to crystal orientation in this paper are in the cubic system. Prior to x-ray measurements, the polarization and strain versus electric field were measured at 0.1 Hz using a conventional Sawyer–Tower circuit and a linear voltage differential transformer (LVDT), respectively. For poling at high fields the electroded samples were placed between a brass shim covered with soft indium

a)Author to whom correspondence should be addressed; electronic mail: hicks@nosc.mil

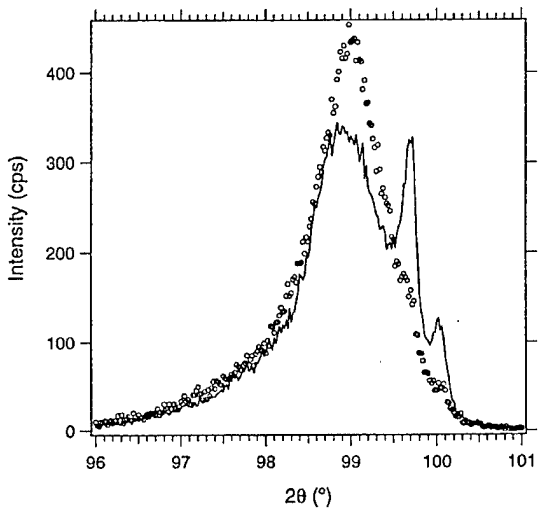

FIG. 1. X-ray diffraction scans from the (040) peak of a transverse face of PZN–8%PT, before poling the sample above the Rh to Tet transition (circles), and after poling above the phase transition (line).

solder and a gold-coated spring-loaded clip. The brass shim was connected to ground. The clip was soldered to a high voltage cable connected to a Trek Model 6093 1000:1 voltage amplifier driven by a Hewlett–Packard Model E3610A variable power supply. The sample was surrounded by a soft silicone compound to prevent arcing. Before and after high field poling, the sample was mounted on a single crystal goniometer on a Rigaku rotating anode two-circle diffractometer. A curved graphite monochromator selected the CuK_α wavelength of 1.541 Å. Instrumental resolution was determined from a quartz standard to be $\approx 0.1°$ full width at half maximum (FWHM).

III. MONOCLINIC PHASE: EXPERIMENTAL OBSERVATION

Figure 1 shows two scans of the (040) peak from a transverse face of a single crystal of PZN–8%PT. Both scans were taken at zero field. For the first scan (circles) the sample had been carefully poled to just above its coercive field (2.5 kV/cm) but well below the phase transition field (≈ 10 kV/cm), so as to avoid introducing any remnant tetragonal phase. The peak maximum corresponds to a spacing of 4.050 Å, which is consistent with the expected rhombohedral phase. The second data set (line) was taken after the sample had been poled to 12 kV/cm (above the field-induced phase transition). Although the main peak is almost exactly the same as before the high field poling, there are two additional sharp peaks that demonstrate the coexistence of a new phase. The two peaks represent a single crystal spacing that is split because Cu$K_{\alpha 1}$ radiation has a slightly different wavelength than Cu$K_{\alpha 2}$ radiation, so they diffract from a crystal spacing at slightly different angles. The graphite monochromator reduces the intensity of the $K_{\alpha 2}$ radiation to roughly 40% of the $K_{\alpha 1}$ radiation, but cannot eliminate it. The expected separation of the peaks due to $K_{\alpha 1}$ and $K_{\alpha 2}$ at 99° is 0.34°, which agrees quite well with the separation shown by the two narrow peaks. The position of the narrow peaks is consistent with peaks observed in the high field tetragonal phase.[6] The width of the two sharp peaks is resolution limited, indicating that they result from domains of at least 500 Å in size. The main peak at 98.8° has a FWHM of at least 1°. This is much broader than the instrumental resolution of 0.1°, and indicates that the domains that diffract in this direction have correlations of under 100 Å. This agrees well with the domain size expected in these relaxor materials.[4] The splitting of 0.34° expected because of the difference in energy between the Cu $K_{\alpha 1}$ and $K_{\alpha 2}$ radiation will not be apparent for such a broad peak (although it will contribute some to the breadth of the peak, making domain size estimations only approximate). The position of the peak remains the same before and after application of a high field. Thus, we see that near the morphotropic phase boundary a coexistence between two phases can be introduced. The evidence presented here for the transverse face of the crystal (orthogonal to the applied field) suggests that this coexistence occurs between the expected rhombohedral phase with small domains and a tetragonal phase with large domains which remain after the high field poling. We need to consider the longitudinal direction as well in order to fully determine the symmetry of the two coexisting phases.

By comparing the diffraction from all six faces of the sample described above, we have determined that the application of an electric field introduces a distortion in the rhombohedral phase. This distorted phase has monoclinic symmetry. Figure 2 shows two sets of scans of the (200) peaks from all six faces of the sample. Figure 2(a) is of the situation with no remnant tetragonal phase, i.e., no coexistence. The peaks overlap each other fairly well, indicating that the rhombohedral symmetry holds as expected. The peak overlap also indicates that our alignment procedure is reproducible and precise. The rhombohedral symmetry is confirmed by previous work of ours on similar samples oriented in the ⟨110⟩ direction, which shows a split (330) peak.[6] The peak maximum corresponds to a lattice spacing of 4.05 Å, consistent with previous work.[3] Figure 2(b) shows the situation after high field poling. The longitudinal and transverse peaks no longer overlap each other. The scans of the longitudinal faces have clearly been affected by the poling: their positions have been shifted relative to before poling [see Fig. 2(a)], so that they no longer overlap the scans from the transverse faces. They now correspond to a spacing of 4.061 Å. This small but significant shift is a clear indication that the rhombohedral symmetry has been broken. We can rule out tetragonal symmetry because our previous work shows that samples with (110) oriented transverse faces show a peak splitting which is inconsistent with tetragonal symmetry.[6] This leaves monoclinic symmetry as the only lattice structure consistent with the data. Fujishiro *et al.* also noticed that one of the coexisting structures in poled PZN–9%PT exhibits a rotation of the optical indicator under polarized light microscopy that is consistent with a monoclinic distortion.[8]

IV. THEORY

In an effort to understand the x-ray diffraction results discussed above we studied the phenomenological model

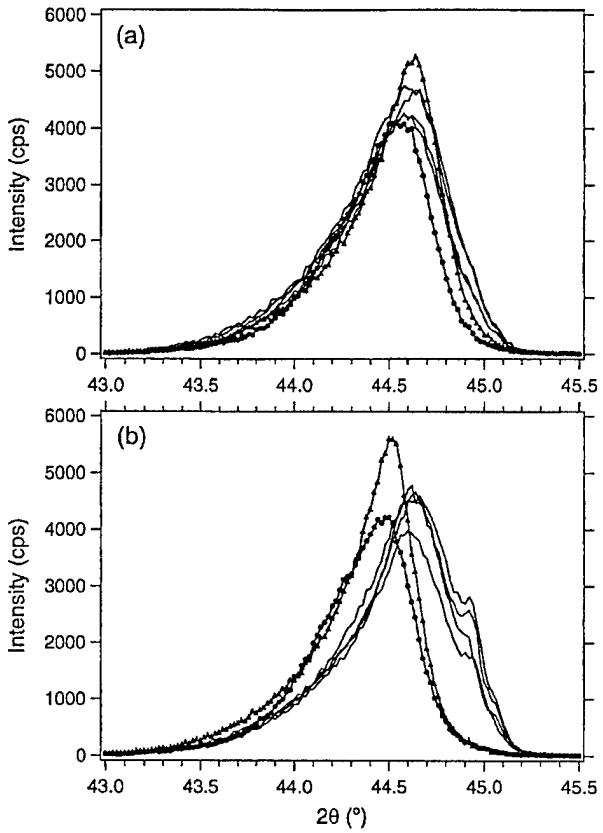

FIG. 2. X-ray diffraction scans from the (200), (020), etc. peaks (all six faces) of a single crystal of PZN–8%PT: (a) before high field poling of the sample, and (b) after poling above the phase transition. Lines represent scans of the four transverse faces of the crystal, lines with markers represent scans of the two longitudinal faces.

used by Devonshire, and adopted by Abe *et al.*, and Yamamoto *et al.* for PZN–PT. This model starts by expanding the Gibbs' free energy in terms of dielectric displacement (or polarization, in the absence of field). We consider an expansion up to sixth order with full cubic symmetry. This can be expressed as

$$G=\tfrac{1}{2}\alpha D^2+\tfrac{1}{4}\xi_{11}(D_x^4+D_y^4+D_z^4)+\tfrac{1}{2}\xi_{12}(D_x^2D_y^2+D_x^2D_z^2+D_y^2D_z^2)+\tfrac{1}{6}\zeta_{111}(D_x^6+D_y^6+D_z^6)+\tfrac{1}{2}\zeta_{112}[D_x^4(D_y^2+D_z^2)+D_y^4(D_x^2+D_z^2)+D_z^4(D_x^2+D_y^2)]+\tfrac{1}{2}\zeta_{123}D_x^2D_y^2D_z^2, \quad (1)$$

where G is the free energy, D_i are the dielectric displacement components, α,ξ_{ij}, and ζ_{ijk} are the dielectric stiffness and higher order stiffnesses. We assume that the only temperature dependence is contained in α, which varies according to the Curie–Weiss law, $\alpha=(T-T_0)/C$, where T is temperature, T_0 is the Curie–Weiss temperature, and C is the Curie constant. By differentiating Eq. (1) with respect to the three orthogonal components of D we obtain the three equations of state:

$$\frac{\partial G}{\partial D_x}=E_x=D_x\{\alpha+\xi_{11}D_x^2+\xi_{12}(D_y^2+D_z^2)+\zeta_{111}D_x^4+\zeta_{112}[D_y^4+D_z^4+2D_x^2(D_y^2+D_z^2)]+\zeta_{123}D_y^2D_z^2\},$$

$$\frac{\partial G}{\partial D_y}=E_y=D_y\{\alpha+\xi_{11}D_y^2+\xi_{12}(D_x^2+D_z^2)+\zeta_{111}D_y^4+\zeta_{112}[D_x^4+D_z^4+2D_y^2(D_x^2+D_z^2)]+\zeta_{123}D_x^2D_z^2\}, \quad (2)$$

$$\frac{\partial G}{\partial D_z}=E_z=D_z\{\alpha+\xi_{11}D_z^2+\xi_{12}(D_x^2+D_y^2)+\zeta_{111}D_z^4+\zeta_{112}[D_x^4+D_y^4+2D_z^2(D_x^2+D_y^2)]+\zeta_{123}D_x^2D_y^2\}.$$

For the purposes of this paper, we consider a field applied along the $\hat{z}$ direction, i.e. $\mathbf{E}=E\hat{z}$. In this case, we expect to have $D_x=D_y$, and the set of three equations reduces to two. When $E=0$, there are five possible solutions to this set of equations. They are

$$D_x=D_y=D_z=0, \quad (3)$$

$$D_x=D_y=0, \quad D_z=P_t, \quad (4a)$$

$$\alpha+\xi_{11}P_t^2+\zeta_{111}P_t^4=0, \quad (4b)$$

$$D_x=0, \quad D_y=D_z=P_o/\sqrt{2}, \quad (5a)$$

$$\alpha+\tfrac{1}{2}(\xi_{11}+\xi_{12})P_o^2+\tfrac{1}{4}(\zeta_{111}+3\zeta_{112})P_o^4=0, \quad (5b)$$

$$D_x=D_y=D_z=P_r/\sqrt{3}, \quad (6a)$$

$$\alpha+\tfrac{1}{3}(\xi_{11}+2\xi_{12})P_r^2+\tfrac{1}{9}(\zeta_{111}+6\zeta_{112}+\zeta_{123})P_r^4=0, \quad (6b)$$

$$D_x=D_y=(P_m/\sqrt{2})\sin(\theta), \quad D_z=P_m\cos(\theta), \quad (7a)$$

$$\alpha'+\xi'_{11}P_m^2+\zeta'_{111}P_m^4=0, \quad (7b)$$

where the coefficients for the monoclinic phase are defined as

$$\sin^2(\theta)=2\frac{\zeta_{111}-\zeta_{112}+(\xi_{11}-\xi_{12})/P_m^2}{(\zeta_{111}-3\zeta_{112}+\zeta_{123})},$$

$$\alpha'=\alpha+\frac{(\xi_{11}-\xi_{12})^2(2\zeta_{111}-\zeta_{123})}{(\zeta_{111}-3\zeta_{112}+\zeta_{123})^2} \quad (8)$$

$$\xi'_{11}=\xi_{11}+\frac{2(\xi_{12}-\xi_{11})(\zeta_{112}-\zeta_{111})(\zeta_{111}+3\zeta_{112}-2\zeta_{123})}{(\zeta_{111}-3\zeta_{112}+\zeta_{123})^2},$$

$$\zeta'_{111}=\zeta_{111}+\frac{3(\zeta_{112}-\zeta_{111})^2(2\zeta_{112}-\zeta_{123})}{(\zeta_{111}-3\zeta_{112}+\zeta_{123})^2}. \quad (9)$$

Equation (3) represents the cubic paraelectric solution. Equations 4(a), 5(a), 6(a) and 7(a), represent the symmetries of the remaining solutions, tetragonal, orthorhombic, rhombohedral and monoclinic, respectively. Equations 4(b), 5(b), 6(b) and 7(b) must be solved to give the spontaneous polarization in each ferroelectric phase. The results of Equations 4(b), 5(b), 6(b) and 7(b) can be inserted back into Eq. (1) to

TABLE I. Expansion coefficients of PZN from two previous studies as well as this study, and coefficients for PT.

Parameter	PZN[a]	PZN[b]	PZN (new)	PT[c]
T_0 (°C)	130	130	130	478.8
C (10^5 °C)	4.7	4.7	4.7	1.5
$\xi_{11}\left(\frac{10^8 m^5}{C^2 F}\right)$	−1.37	−1.37	−1.2	−2.9
$\xi_{12}\left(\frac{10^8 m^9}{C^2 F}\right)$	−1.0	−1.4	−1.3	15.0
$\zeta_{111}\left(\frac{10^8 m^5}{C^4 F}\right)$	10.3	6.0	7.8	15.6
$\zeta_{112}\left(\frac{10^8 m^9}{C^4 F}\right)$	6.8	6.8	9.1	−3.4
$\zeta_{123}\left(\frac{10^8 m^9}{C^4 F}\right)$	−10	0	−10	0

[a]See Ref. 9.
[b]See Ref. 13.
[c]See Ref. 15.

determine the value of the free energy for each solution. The Hessian matrix of second derivatives of the free energy determines which solutions are minima. For our two variables, the Hessian is defined as

$$H=\begin{pmatrix} \frac{\partial^2 G}{\partial D_x \partial D_x} & \frac{\partial^2 G}{\partial D_z \partial D_x} \\ \frac{\partial^2 G}{\partial D_x \partial D_z} & \frac{\partial^2 G}{\partial D_z \partial D_z} \end{pmatrix},$$

and the conditions for a stable minimum are that $\det |H| > 0$, $H_{xx} > 0$ and $H_{zz} > 0$. A comparison of the free energies of each of the local minima will give a global minimum, which determines the equilibrium state. If the coefficients in Eq. (1) are known for a material, then the preferred phase at any given temperature and field can be determined.

V. DETERMINING THE VALUES OF THE EXPANSION COEFFICIENTS

It is time consuming and unproductive to determine the coefficients for each composition of a solid solution. However, it is often possible to use simple mixing laws so that only the coefficients of the constituent materials need to be known.[11,12] To calculate the phase diagram for PZN–PT, Abe *et al.* and Yamamoto *et al.* assumed a linear dependence of the solution coefficients on the unmixed PZN and PT coefficients.[9,13] These were expressed as: $\xi_{11}^{\mathrm{PZN}-x\%\mathrm{PT}} = (1-x)\xi_{11}^{\mathrm{PZN}} + x\xi_{11}^{\mathrm{PT}}$ and

$$\frac{G^{\mathrm{PZN}-x\%\mathrm{PT}}}{\xi_{11}^{\mathrm{PZN}-x\%\mathrm{PT}}} = (1-x)\frac{G^{\mathrm{PZN}}}{\xi_{11}^{\mathrm{PZN}}} + x\frac{G^{\mathrm{PT}}}{\xi_{11}^{\mathrm{PT}}}.$$

The second equation merely indicates that each coefficient is to be normalized by ξ_{11} before applying the linear mixing.

The only unknown quantities in the theory are the dielectric stiffnesses for PZN. The coefficients for PT are known from single crystal studies,[15] and are not in question. The difficulty of producing single crystal PZN means that coefficients for that endpoint have to be determined by studying solid solutions that can be produced as single crystals. Table I shows the values of the expansion coefficients for PZN as determined by Abe *et al.* and Yamamoto and Terashima, as well as our best estimates of the coefficient values, determined in Sec. V A by modeling the behavior of the materials under field. The phase diagrams calculated using these values, as well as the experimental phase diagram, are shown in Fig. 3. As the figure demonstrates, widely vary-

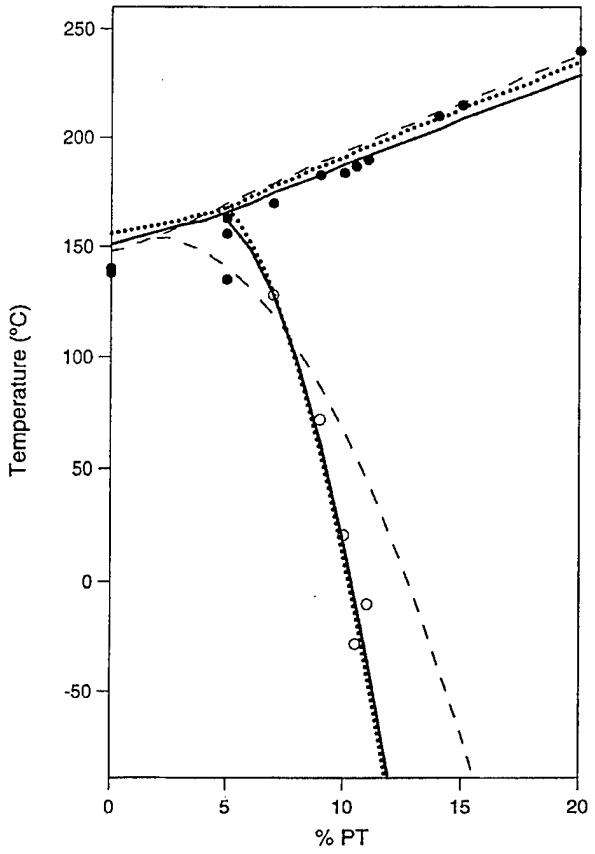

FIG. 3. Phase diagram for the solid solution PZN–PT. The horizontal axis shows the percent PT in the composition. Symbols represent data taken from Kuwata *et al.*, (see Ref. 2) the dashed line is from the phenomenological model presented in Abe *et al.*, (see Ref. 9) the dotted line is using the coefficients of Yamamoto *et al.*, (see Ref. 13) and the bold solid line is the same model using new coefficients developed by matching high field behavior.

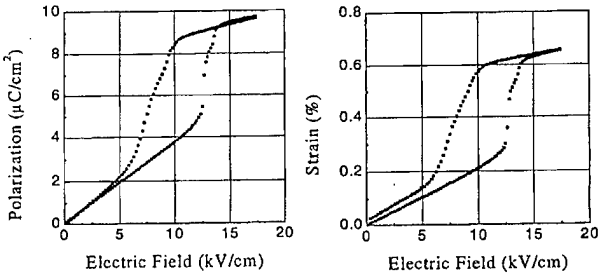

FIG. 4. Sample bulk data from a 2 mm^3 poled sample of PZN–8%PT. Data were taken using an LVDT and a Sawyer–Tower circuit (see Refs. 3 and 4).

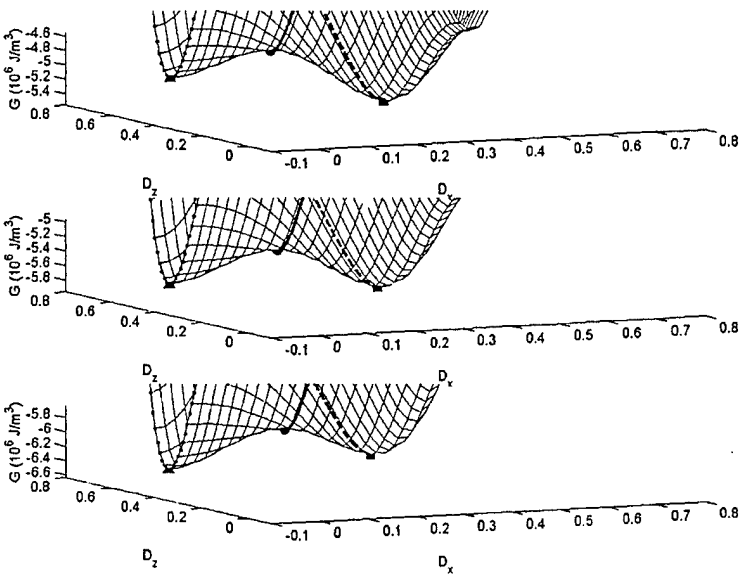

FIG. 5. Three dimensional (3D) plots of the calculated free energy for PZN–8%PT as a function of dielectric displacement in the $\hat{x}$ and $\hat{z}$ directions (symmetry allows us to assume $D_x = D_y$) under three different applied fields: (a) $E = 0$ kV/m, (b) $E = 12$ kV/cm, (c) $E = 24$ kV/cm. The coefficients used to calculate $G(D_x, D_z)$ are from Table I, column 3. The two dimensional lines that overlay the 3D plot are guides to the eye, and pass through the tetragonal (dotted), monoclinic (solid) and rhombohedral (dashed) solutions. We can see by inspection that the tetragonal phase is a local minimum at $E = 0$, and a global minimum at $E = 18$ kV/cm. The monoclinic phase is a saddle point at all fields.

ing sets of coefficients yield similar phase diagrams, emphasizing the point that the phase diagram alone cannot be used to determine the coefficients.

The dielectric constant for a ceramic is obtained by taking the logarithmic mean of the diagonalized components of the dielectric susceptibility tensor, $\chi_{ij} = \partial^2 G / \partial D_i \partial D_j$.[9] Yamamoto and Terashima achieved significant improvements in the coefficients by considering the change in dielectric constant at the ferroelectric phase transition.[13] However, for the sake of brevity we merely comment that our coefficients yield similar temperature dependent dielectric constants as those of Yamamoto *et al.*[9]

A. Electric field induced phase transition

Finally, the behavior of the materials when subject to an electric field can be determined by solving Eq. (2) for nonzero values of **E**. Recent work has demonstrated that rhombohedral compositions of PZN–PT near the morphotropic phase boundary undergo a transition to a tetragonal phase when a sufficiently high electric field is applied along the (001) direction.[3,4,6] Sample strain and polarization data which demonstrate this phase transition are shown in Fig. 4. In principle, this behavior is consistent with the phenomenological model. An applied field in the $\hat{z}$ direction will act to stabilize the (local) tetragonal minimum, eventually making it a global minimum, which causes a phase transition. A typical sequence demonstrating this at room temperature for the coefficients shown in column 3 of Table I is shown in Fig. 5. Plots of the free energy derived from Eq. (1) using the coefficients in Table I for two different compositions are shown in Fig. 6. Vertical lines in Fig. 6 indicate the observed positions of the phase transition in each material (10 kV/cm in PZN–8%PT and 32.5 in PZN–4.5%PT). The theoretically predicted phase transition occurs in each plot where the rhombohedral energy (dashed line) and tetragonal energy (solid line) cross. It is clear that neither of the two previous estimations of the expansion coefficients for PZN is at all consistent with the observed electric field induced phase

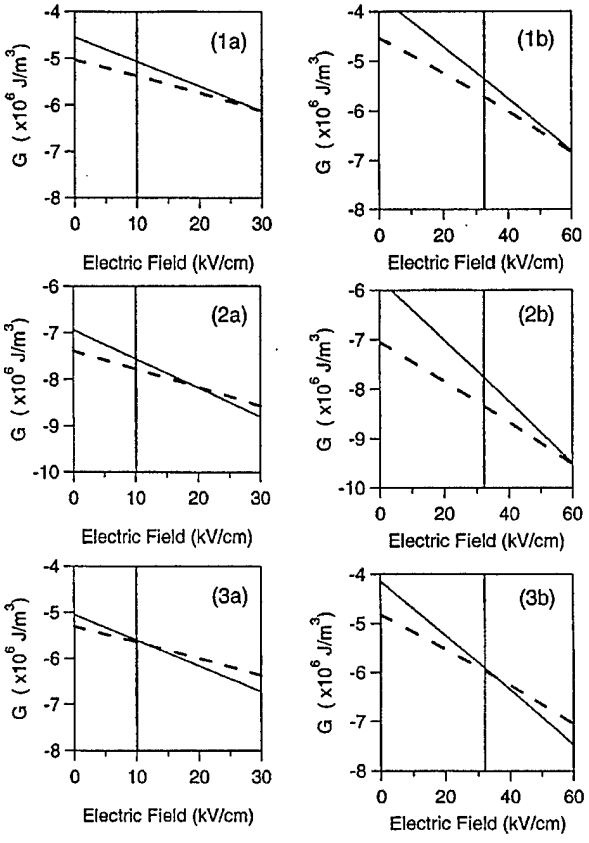

FIG. 6. Plots of the minimum free energy in the rhombohedral (dashed line) and tetragonal (solid line) phases, as calculated from the phenomenological model using three different sets of coefficients: (1) from Abe *et al.* (see Ref. 9), (2) Yamamoto *et al.* (see Ref. 13), (3) coefficients chosen to match the observed field of transition (while still matching the phase diagram and dielectric behaviors, as shown in Fig. 3). The left plots (1a, 2a, 3a) are for PZN–8%PT, and the right plots (1b, 2b, 3b) are for PZN–4.5%PT. The vertical lines mark the approximate position of the observed field induced phase transitions for each composition (see Refs. 3, 4, and 6).

transition. We made adjustments to the coefficients to achieve the plots shown in Fig. 6(c). These new coefficients (shown in column 3 of Table I) do an excellent job of reproducing the phase transition behavior, phase diagram, and dielectric behavior of these materials, within the limitations of the model.

We note that, as shown in Fig. 4, the field induced phase transition occurs with significant hysteresis. The phenomenological model can only describe where an erstwhile local minimum becomes a global minimum, and cannot be used to determine the extent of the field hysteresis. However, it is clear from the plots in Fig. 5 that the two minima are close in energy. The fact that there is strong hysteresis, and the fact that Fujishiro *et al.* observed a coexistence between rhombohedral and tetragonal phases is not surprising.

VI. MONOCLINIC PHASE-THEORETICAL CONSIDERATIONS

The free energy predicted by the phenomenological theory permits the existence of a monoclinic phase, but it is only stable under certain conditions. The coefficients developed above, which lead to reasonable predictions of many pieces of data, are not consistent with a stable monoclinic phase. Moreover, from a glance at the free energies shown in Fig. 5 it is unlikely that a monoclinic phase can be stable at the same time that a rhombohedral phase is stable but rather must be a saddle point. It is similarly unlikely that the coefficients change enough under high field poling to make the monoclinic solution from Eq. 7(b) stable. However, the large width of the dominant phase peak (shown in Fig. 2) indicates that it consists of very small domains, with dimensions less than 1 μm, consistent with earlier observations.[16] The domain walls of the rhombohedral phase are expected to be tetragonal by symmetry, and the growth of the coexisting tetragonal phase is expected to occur at the domain walls. Because the rhombohedral domains are small, they can be influenced in their entirety by the strains at the domain walls, so that there would be no coexistence of all three types of symmetry. Therefore, we believe that the remnant tetragonal phase strains the lattice of the rhombohedral phase, forcing it to adopt the monoclinic symmetry.

VII. CONCLUSIONS

We have shown x-ray diffraction evidence that after poling by a high electric field in the (001) direction, PZN–8%PT possesses some remnant tetragonal phase mixed in with the dominant phase. Moreover, the dominant phase is not rhombohedral, as it is for a newly annealed crystal, but monoclinic. We have also shown that a simple Devonshire phenomenological model can explain the phase diagram, dielectric behavior, and field induced phase transition. Although the model is consistent with a coexistence between the rhombohedral and tetragonal phases, it indicates that a stable monoclinic phase cannot exist for this material. However, this does not contradict the x-ray results because the observed phase does not possess the monoclinic symmetry [see Eq. 7(a)] that comes from solving the zero field equations of state [Eqs. (2)]. Instead, the diffraction shows a slightly distorted version of the rhombohedral zero field solution represented by Eq. 6(a). We interpret this result as a strained rhombohedral phase with the strains resulting from domain walls that consist of a tetragonal phase. Thus, this engineered metastable monoclinic phase would likely exist even in the absence of tetragonal domains due to the resultant stains from the domain walls. A richer model (perhaps one that accounts for interactions between domains of different symmetry) might be able to give more quantitative insight into the situation.

ACKNOWLEDGMENTS

This work was supported by the Office of Naval Research under Code No. 332. Thanks go to Hua Lei for her help with sample preparation.

[1] S. Nomura, T. Takahashi, and Y. Yokomizo, J. Phys. Soc. Jpn. **27**, 262 (1969).
[2] J. Kuwata, K. Uchino, and S. Nomura, Ferroelectrics **37**, 579 (1981).
[3] S.-E. Park and T. R. Shrout, J. Appl. Phys. **82**, 1804 (1997).
[4] S.-F. Liu, S.-E. Park, T. R. Shrout, and L. E. Cross, J. Appl. Phys. **85**, 2810 (1999).
[5] S. Saitoh, T. Kobayashi, K. Harada, S. Shimanuki, and Y. Yamashita, IEEE Trans. Ultrason. Ferroelectr., Freq. Control **45**, 1071 (1998).
[6] M. K. Durbin, E. W. Jacobs, J. C. Hicks, and S.-E. Park, Appl. Phys. Lett. **74**, 2848 (1999).
[7] B. Noheda, D. E. Cox, G. Shirane, J. A. Gonzalo, L. E. Cross, and S.-E. Park, Appl. Phys. Lett. **74**, 2059 (1999).
[8] K. Fujishiro, R. Vlokh, Y. Uesu, Y. Yamad, J. Kiat, B. Dkhil, and Y. Yamashita, Proceeding 9th European Meeting on Ferroelectricity, Prague, Czech Republic, July 1999.
[9] K. Abe, O. Furukawa, and H. Imagawa, Ferroelectrics **87**, 55 (1988).
[10] A. F. Devonshire, Philos. Mag. Suppl. **3**, 85 (1954).
[11] A. Amin, Ferroelectrics **54**, 207 (1984).
[12] T. Matsubara and K. Yoshimitsu, Prog. Theor. Phys. **64**, 380 (1980).
[13] T. Yamamoto and Y. Terashima, Jpn. J. Appl. Phys., Part 1 **31**, 3252 (1992).
[14] G. V. Belokopytov, Moscow Univ. Phys. Bull. **52**, 49 (1997).
[15] M. J. Haun, E. Furman, S. J. Jang, and L. E. Cross, Ferroelectrics **99**, 55 (1989).
[16] S. Wada, S.-E. Park, L. E. Park, and T. R. Shrout, Ferroelectrics **221**, 147 (1999).

Appendix 11

Yu Lu, D.–Y. Jeong, Z.–Y. Cheng, Q.M. Zhang, H.–S. Luo, Z.–W. Yin, and D. Viehland, "Phase transitional behavior and piezoelectric properties of the orthorhombic phase of $Pb(Mg_{1/3}Nb_{2/3})O_3$–$PbTiO_3$ single crystals," Applied Physics Letters, 78[20], 3109–3111 (May 2001).

Phase transitional behavior and piezoelectric properties of the orthorhombic phase of $Pb(Mg_{1/3}Nb_{2/3})O_3$–$PbTiO_3$ single crystals

Yu Lu, D.-Y. Jeong, Z.-Y. Cheng, and Q. M. Zhang[a)]
Materials Research Laboratory, The Pennsylvania State University, University Park, Pennsylvania 16802

Hao-Su Luo and Zhi-Wen Yin
Laboratory of Functional Inorganic Materials, Shanghai Institute of Ceramics, Chinese Academy of Science, Shanghai, China

D. Viehland
Naval Seacommand, Division Newport, Newport, Rhode Island 02841

(Received 21 December 2000; accepted for publication 24 March 2001)

We report on the observation of an orthorhombic ferroelectric phase in $0.67Pb(Mg_{1/3}Nb_{2/3})O_3$ $-0.33PbTiO_3$ single crystals, whose polarization is along ⟨011⟩ direction and stability can be altered by poling conditions. We studied the piezoelectric properties on poled ⟨011⟩ crystals, in both monodomain and polydomain states, and found that the piezoelectric d_{32} coefficient, which is the piezoelectric response in perpendicular to the poling direction, is positive in both cases. Based on the phenomenological theory, we show that this is possible in a crystal with the electrostrictive coefficients $Q_{11}>Q_{44}-Q_{12}$. © *2001 American Institute of Physics.* [DOI: 10.1063/1.1372360]

We report in this letter on the phase transition behavior and piezoelectric responses of $Pb(Mg_{1/3}Nb_{2/3})O_3$–$PbTiO_3$ (PMN–PT) single crystals, for compositions close to the morphotropic phase boundary (MPB) between rhombohedral ferroelectric (FE_r) and tetragonal ferroelectric (FE_t) phases. Recent discoveries in mixed B-site cation ferroelectric perovskites have stimulated significant research activities.[1–4] In $Pb(Zn_{1/3}Nb_{2/3})O_3$–$PbTiO_3$ (PZN–PT) and PMN–PT single crystals, an electromechanical coupling factor of greater than 0.9 has been reported in the FE_r phase near the MPB for specimens poled along ⟨001⟩.[1–3] Similar enhancements in the electromechanical properties were also reported when crystals were poled at finite angles with respect to the spontaneous polarization direction, although the coupling factors of these finite miss-oriented crystals were lower (~0.8).[5–7]

Naturally, a question to ask is what is unique about the PZN–PT and PMN–PT crystalline solutions and the role of the MPB. In 0.92PZN–0.08PT crystals (which at $T=25\,°C$ is in the FE_r phase and near a MPB), recent investigations have demonstrated the presence of monoclinic domains, and orthorhombic ferroelectric (FE_o) and monoclinic ferroelectric (FE_m) states.[8–10] This opens an interesting possibility that those states, even metastable, may be regarded as intermediate states and responsible for the high piezoelectric and electromechanical responses in PZN–PT and PMN–PT single crystals near the MPB.

In $Pb(Zr_{1-x}Ti_x)O_3$, which is another related ferroelectric perovskite material, high electromechanical properties have been widely studied over many years for compositions close to the MPB between FE_r and FE_t phases.[11] Much effort has been expended in determining the mechanism responsible for these significant enhancements. Recently, a FE_m state has been reported over a very narrow composition range near MPB. In this FE_m state, the polarization was confined to the ⟨*hhk*⟩ plane, which is one of the planes that can "bridge" the tetragonal ⟨001⟩ and rhombohedral ⟨111⟩ directions.[4,12] It was suggested that this "bridging" effect, via the FE_m state, is responsible for the enhanced electromechanical properties.[12]

This investigation reports the phase transition behavior and piezoelectric responses in PMN–PT single crystals of approximate compositions of 0.67PMN–0.33PT, which are close to the MPB. Dielectric and piezoelectric methods have been used to study crystals with various poling histories. We have observed, by dielectric and optical microscopy techniques, an intermediate FE_o state whose phase stability depends upon its poling history and mechanical condition. In addition, it was observed that this monodomain FE_o does not exhibit enhanced piezoelectricity and its piezoelectricity can be described quite well by the phenomenological theory.[13,14]

Crystals were grown by the Bridgman method.[15] Various crystals were oriented along the ⟨001⟩, ⟨110⟩, and ⟨111⟩ directions. Typical specimen dimensions were $2\times2\times2\,mm^3$. Crystals were poled at room temperature, with monodomain conditions achieved in both ⟨111⟩ and ⟨110⟩ oriented crystals. Dielectric characterization (at 1 kHz) was carried out using a standard LCR meter (HP4284A) equipped with a temperature chamber (Delta 9023). Piezoelectric coefficients were measured at 1 kHz using a laser dilatometer.[16] Domain patterns were characterized by a Zeiss Axioskop cross-polarized optical microscope (100× amplification).

Figures 1(a)–1(d) show the dielectric constant and loss as functions of temperature for poled ⟨111⟩, ⟨011⟩($E_{poling}>5$ kV/cm), ⟨011⟩($E_{poling}=4$ kV/cm), and ⟨001⟩ oriented PMN–PT crystals, respectively. It is important to emphasize that the difference between Figs. 1(b) and 1(c) (which are both for ⟨011⟩ orientations) is only the poling field (E_{poling}). Each figure exhibited a transition at 145 °C which is the FE_t to cubic transformation,[17,18] and a second dielectric anomaly at ~80 °C. For ⟨111⟩ and ⟨011⟩($E_{poling}<4$ kV/cm)

a)Electronic mail: qxz1@psu.edu

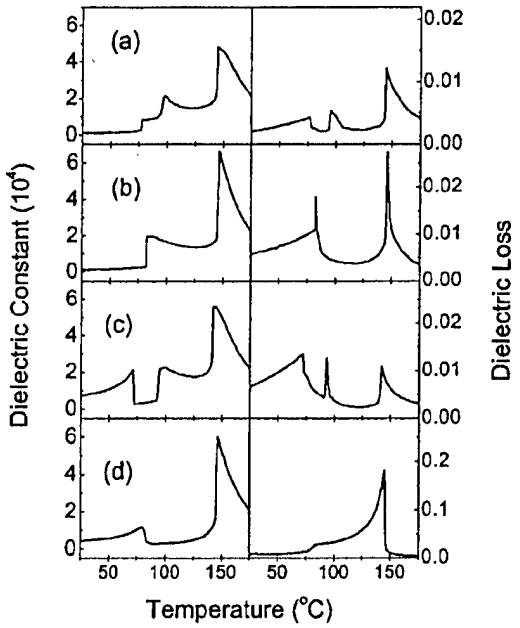

FIG. 1. The dielectric constant and dielectric loss measured at 1 kHz as functions of temperature for 0.67PMN–0.33PT single crystals (a) poled and measured along the [111] direction (monodomain rhombohedral phase); (b) poled and measured along [011] (monodomain orthorhombic phase); (c) poled along [011] direction to form ⟨111⟩ twined crystal and measured along [011]; and (d) poled and measured along [001] (polydomain crystal).

orientations, an additional third anomaly was found at ~100 °C.

For ⟨011⟩-oriented crystals poled at $E_{poling}<4$ kV/cm, optical microscopy revealed the presence of a polydomain condition with domains oriented along the ⟨111⟩, typical of that of a FE_r state. These domain orientations are schematically illustrated in Fig. 2(a). However, for $E_{poling}>5$ kV/cm, ⟨011⟩-oriented crystals were observed under cross-polarized light to be in a monodomain state with the polarization along the ⟨011⟩. This domain orientation is schematically illustrated in Fig. 2(b). It should be mentioned that even small variations in the PT content resulted in deviations from this monodomain condition and the disappearance of the FE_o state at 25 °C, demonstrating that this state only exists over a narrow composition range near the MPB. Accordingly, at room temperature most of the crystals poled along ⟨011⟩ were polydomain and FE_r.

The differences in the dielectric responses of the ⟨011⟩

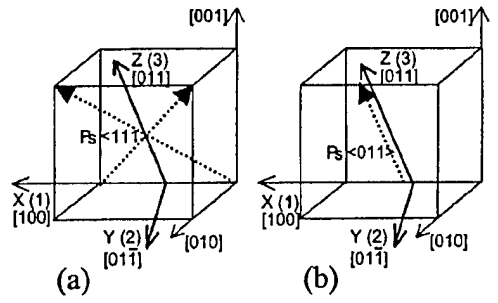

FIG. 2. Schematic drawings for [011] poled crystals in (a) twined crystals and (b) monodomain crystals. The dashed arrows indicate the remanent polarization direction and orthorhombic coordinate system used to describe the piezoelectric coefficients is also presented.

TABLE I. Piezoelectric coefficients of 0.67PMN–0.33PT single crystals poled along [011] direction at room temperature.

	d_{33} (pm/V)	d_{32} (pm/V)	d_{31} (pm/V)	$\epsilon_{33}^{(\sigma)}/\epsilon_0$[a]
Monodomain	250	40	−220	880
Polydomain (experimental)	1780	1100	−2740	
Polydomain (calculated)	1770	980	−2760	

[a]ϵ_0 is the vacuum permittivity.

crystals due to the various poling histories can be explained on the basis of these optical microscopy observations. For $E_{poling}<4$ kV/cm [Fig. 1(c)], the FE_r state is stable at room temperature. Upon heating to ~80 °C, a transition occurs to a FE_o state. On further increase of temperature to ~100 °C, a secondary transformation to a FE_t state occurred. In contrast, for $E_{poling}>5$ kV/cm [Fig. 1(b)], a monodomain FE_o state can be induced at room temperature. Upon heating to 80 °C, a transition occurs to a FE_t state. Interestingly, the FE_o–FE_t transition temperature in the monodomain condition was significantly lower (80 °C) than in the polydomain condition (100 °C). Clearly, the phase transformational pathway is altered by whether the specimen is elastically constrained (polydomain) or free to deform (monodomain).[9]

The dielectric constant for the poled ⟨111⟩ crystals [Fig. 1(a)] exhibited a similar transition sequence as the polydomain ⟨011⟩ [Fig. 1(c)]. In both cases, the FE_r to FE_t transition proceeded through an intermediate FE_o state, with the FE_o state being present for $\sim 80<T<100$ °C. The dielectric constant for poled ⟨001⟩ crystals was shown in Fig. 1(d). Only one FE–FE transition was observed, which occurred at 80 °C. This transition temperature is close to that of the FE_o–FE_t along the ⟨011⟩ ($E_{poling}>5$ kV/cm, monodomain), and with that of the FE_r–FE_o along the ⟨111⟩ and ⟨011⟩ ($E_{poling}<4$ kV/cm, polydomain).

The results in Fig. 1 demonstrate a complex transformation sequence that is dependent upon orientation and electrical history. An intermediate FE_o state exists between the FE_r and FE_t ones, whose temperature range of existence varies, suggesting metastability. Furthermore, these results indicate that the margin of stability in the FE_r, FE_o, and FE_t states may all be sufficiently fragile that changes in orientation, electrical history, or mechanical constraints may change the free energy balance. The reason why ceramic specimens have not revealed a FE_o state in the last 20 years[17,18] may then reflect the fact that under all circumstances the polarization is elastically constrained, preventing strain accommodation.

To determine the influence of monodomain versus polydomain conditions upon the electromechanical properties of ⟨011⟩ oriented crystals, the piezoelectric coefficients (d_{33}, d_{31}, and d_{32}) were measured. The results are given in Table I. First, the values of all coefficients were much lower in the monodomain FE_o state than the polydomain FE_r one. The results were a little unusual in that $d_{32}>0$ for both the mono and polydomain conditions, and also in that $|d_{31}|>|d_{33}|$ for the polydomain condition.

In order to explain the observed piezoelectric properties in poled ⟨011⟩ crystals in both the poly and monodomain states, we derived expressions for the piezoelectric coeffi-

cients from phenomenological theory.[13,14] Along the ⟨011⟩ in the monodomain condition, the piezoelectric responses were found to be

$$\begin{aligned} d_{33}^{(o)} &= \sqrt{2}(Q_{11}+Q_{12}+Q_{44})\epsilon_{33}^{(o)}P_r^{(o)}, \\ d_{32}^{(o)} &= \sqrt{2}(Q_{11}+Q_{12}-Q_{44})\epsilon_{33}^{(o)}P_r^{(o)}, \\ d_{31}^{(o)} &= 2\sqrt{2}Q_{12}\epsilon_{33}^{(o)}P_r^{(o)}, \end{aligned} \tag{1}$$

where the superscript (o) stands for properties that are referenced with respect to the coordinate system of the FE_o state (see Fig. 2), $\epsilon_{33}^{(o)}$ is the dielectric permittivity of the FE_o state, $P_r^{(o)}$ is the remanent polarization of the FE_o state (0.39 C/m^2),[9] and Q_{11}, Q_{12}, and Q_{44} are the electrostrictive coefficients (in the pseudocubic coordinates) expressed in matrix notation. For ferroelectric perovskites, it is known that $Q_{11}>0$, $Q_{44}>0$, $Q_{12}<0$, and $|Q_{11}|>2|Q_{12}|$.[13] Therefore, under the condition that $Q_{11}>Q_{44}-Q_{12}$, Eq. (1) predicts that $d_{32}^{(o)}$ is positive. Using Eq. (1) and the data in Table I, the values of the electrostrictive coefficients can be estimated: $Q_{11}=0.06\,m^4/C^2$, $Q_{12}=-0.025\,m^4/C^2$, and $Q_{44}=0.024\,m^4/C^2$, respectively.

For the ⟨011⟩-oriented FE_r polydomain state, assuming that there are [111] and $[\bar{1}11]$ domains only, the piezoelectric coefficients were derived as

$$\begin{aligned} d_{33}^{(o)} &= \sqrt{2}/3[(Q_{11}+Q_{44})(\epsilon_{11}^{(R)}+2\epsilon_{33}^{(R)}) \\ &\quad +Q_{12}(4\epsilon_{33}^{(R)}-\epsilon_{11}^{(R)})]P_r^{(R)}, \\ &\approx \sqrt{2}/3(Q_{11}+Q_{44}-Q_{12})\epsilon_{11}^{(R)}P_r^{(R)}, \\ d_{32}^{(o)} &= \sqrt{2}/3[(Q_{11}-Q_{44})(\epsilon_{11}^{(R)}+2\epsilon_{33}^{(R)}) \\ &\quad +Q_{12}(4\epsilon_{33}^{(R)}-\epsilon_{11}^{(R)})]P_r^{(R)}, \\ &\approx \sqrt{2}/3(Q_{11}-Q_{44}-Q_{12})\epsilon_{11}^{(R)}P_r^{(R)}, \\ d_{31}^{(o)} &= 2\sqrt{2}/3[Q_{11}(\epsilon_{33}^{(R)}-\epsilon_{11}^{(R)})+Q_{12}(2\epsilon_{33}^{(R)}+\epsilon_{11}^{(R)})]P_r^{(R)}, \\ &\approx 2\sqrt{2}/3(-Q_{11}+Q_{12})\epsilon_{11}^{(R)}P_r^{(R)}, \end{aligned} \tag{2}$$

where $\epsilon_{33}^{(R)}$ and $\epsilon_{11}^{(R)}$ are the dielectric permittivity measured in the FE_r state along and perpendicular to the [111] polarization direction, respectively, and $P_r^{(R)}$ is the remanent polarization of the rhombohedral phase ($\sim$0.39 C/m^2).[9] In the second part of each relationship in Eq. (2), we have made use of the fact that $\epsilon_{11}^{(R)} \gg \epsilon_{33}^{(R)}$. The values of $d_{33}^{(o)}$, $d_{33}^{(o)}$, and $d_{33}^{(o)}$ for the FE_r polydomain condition can be estimated by placing the values of the electrostriction coefficients estimated in the proceeding paragraph into Eq. (2). These calculated values for the piezoelectric coefficients are given in Table I where $\epsilon_{11}^{(R)}/\epsilon_0=10\,000$ is used. Inspection of the data in the table reveals remarkable agreement, in particular in consideration of the use of a single crystalline single domain phenomenological approach to the properties of polydomain conditions.

This work was supported by the Office of Naval Research.

[1] J. Kuwata, K. Uchino, and S. Nomura, Jpn. J. Appl. Phys., Part 1 **21**, 1298 (1982).
[2] S. Park and T. R. Shrout, J. Appl. Phys. **82**, 1804 (1997).
[3] S. Park and T. Shrout, IEEE Trans. Ultrason. Ferroelectr. Freq. Control **44**, 1140 (1997).
[4] B. Noheda, D. E. Cox, G. Shirane, J. Gonzalo, L. Cross, and S. Park, Appl. Phys. Lett. **74**, 2059 (1999).
[5] K. Nakamura and Y. Kawamura, in *1999 IEEE Ultrasonics Symposium Proceedings*, edited by S. C. Schneider, M. Levy, and B. R. McAvoy (IEEE, New York, 1999), pp. 1013–1018.
[6] S. Park, S. Wada, L. Cross, and T. Shrout, J. Appl. Phys. **86**, 2746 (1999).
[7] X.-H. Du, J. Zheng, U. Belegundu, and K. Uchino, Appl. Phys. Lett. **72**, 2421 (1998).
[8] M. K. Durbin, J. C. Hicks, S. Park, and T. Shrout, J. Appl. Phys. **87**, 8159 (2000).
[9] D. Viehland, J. Appl. Phys. **88**, 4794 (2000).
[10] B. Noheda, D. Cox, G. Shirane, S. Park, L. E. Cross, and Z. Zhong (unpublished).
[11] B. Jaffe, W. Cook, Jr., and H. Jaffe, *Piezoelectric Ceramics* (Academic, New York, 1971), Chap. 7.
[12] R. Guo, L. Cross, S. Park, B. Noheda, D. Cox, and G. Shirane, Phys. Rev. Lett. **84**, 5423 (2000).
[13] A. F. Devonshire, Philos. Mag. **3**, 85 (1954).
[14] F. Jona and G. Shirane, *Ferroelectric Crystals* (Dover, New York, 1993), Chap. IV.
[15] Z. Yin, H. Luo, P. Wang, and G. Xu, Ferroelectrics **229**, 207 (1999).
[16] Q. M. Zhang, W. Pan, and L. Cross, J. Appl. Phys. **63**, 2492 (1988).
[17] S. W. Choi, T. Shrout, S. Jang, and A. Bhalla, Ferroelectrics **100**, 29 (1989).
[18] O. Noblanc, P. Gaucher, and G. Calvarin, J. Appl. Phys. **79**, 4291 (1996).

Appendix 12

Yu Lu, D.–Y. Jeong, Z.–Y. Cheng, T. Shrout, and Q.M. Zhang, "Phase Stabilities of "Morphotorpic" Phases in $Pb(Zn_{1/3}Nb_{2/3})O_3$–$PbTiO_3$ Single Crystals," submitted to Applied Physics Letters (2001).

Phase Stabilities of "Morphotropic" Phases in $Pb(Zn_{1/3}Nb_{2/3})O_3$-$PbTiO_3$ Single Crystals

Yu Lu, D.-Y. Jeong, Z.-Y. Cheng, T. Shrout, and Q. M. Zhang

Materials Research Laboratory, The Pennsylvania State University

University Park, Pennsylvania 16802

Abstract:

Based the optic and dielectric data acquired under different mechanical and electric conditions and temperature, we show that an orthorhombic phase exists near the morphotropic phase boundary (MPB) (on both the rhombohedral and tetragonal sides of MPB). Because of the proximity of the free energy of this phase to the two other morphotropic phases, i.e., the rhombohedral and tetragonal phases, the experimentally observed phases and phase diagrams near MPB depend crucially on the mechanical and electric conditions as well as sample history.

PACS No: 77.80.Bh, 77.65.Bn, 61.50.-f, 77.84.Bw

The large electromechanical responses observed in ferroelectric perovskite $A(B'B'')O_3$ and $A(B'B''B''')O_3$ materials near the morphotropic phase boundary (MPB) between the ferroelectric rhombohedral (FE_r) and tetragonal (FE_t) phases have been the topic of many investigations for many decades.[1-3] Traditionally, MPB is regarded as a simple boundary of first order transition between the two morphotropic phases. However, recently Noheda et al. reported that the MPB in $Pb(Zr_{1-x}Ti_x)O_3$ (PZT) exhibited a more complex transition sequence and a ferroelectric monoclinic (FE_m) phase was observed over a very narrow composition range near MPB between FE_r and FE_t phases.[4,5] It was suggested that the "bridging" effect of the FE_m phase between the tetragonal <001> and rhombohedral <111> polarization directions is responsible for the enhanced electromechanical properties in PZT near MPB. More recently, in FE_r composition of $Pb(Mg_{1/3}Nb_{2/3})O_3$-$PbTiO_3$ (PMN-PT) and $Pb(Zn_{1/3}Nb_{2/3})O_3$-$PbTiO_3$ (PZN-PT) near MPB, experiment evidence also shows the presence of a ferroelectric orthorhombic FE_o phase in between FE_r and FE_t phases.[6,7] From both fundamental science and practical application points of view, it is important to understand and determine the stability range of each of these "morphotropic" phases under different electric and mechanical conditions. It is the objective of this letter to experimentally address this issue. It will be shown that because of the proximity of the free energies between the morphotropic phases, the experimentally observed phase and phase transition sequence near MPB will depend crucially on the electric and mechanical conditions.

PZN-PT single crystals were grown by the flux method.[3] The single crystals at compositions of PZN-4.5%PT, PZN-8%PT, and PZN-10%PT were chosen for the present study. The crystals were orientated along the pseudo-cubic <001>, <110> and <111> directions. The typical samples size is about 2x2x2 mm^3 and Pt sputtered electrodes were used

for the electric characterization. The dielectric property as a function of temperature was measured using HP multi-frequency LCR meter at 1 kHz (HP 4284A) equipped with a temperature chamber and the temperature scan rate was 1 °C/min. All the dielectric data were recorded in the heating run from room temperature to higher temperature. The domain patterns of the crystals at room temperature under different poling conditions and orientations were characterized by a cross-polarized optic microscope (100x magnification) (Zeiss Axioskop).

In this study, in addition to the FE_r and FE_t phases, the optic data indicate the existence of an orthorhombic phase (FE_o), consistent with the results in references 6 and 7. To understand the optic results, we plot in figure 1 the optic indicatrix for the three crystal phases. For the optic observation reported in this letter, except otherwise specified, the single crystals were aligned so that the poling electric field is in the same direction as the polarizer for the incident light. Therefore, when the crystals were poled along [111] to the FE_r phase, the optic extinction will be observed along [01 $\bar{1}$] and [2 $\bar{1}$ $\bar{1}$] directions. Analogously, for crystals in the FE_o phase and poled along [011], the optic extinction will be observed along [100] and [01 $\bar{1}$] directions. Therefore, the optic data can unambiguously establish the crystal phase for a single domain single crystal.

Presented in figures 2 and 3 are the dielectric data acquired from single crystals of PZN-8PT and PZN-10PT oriented and poled along the three crystallography directions: <011>, <111>, and <001>, respectively. We first discuss the results from the crystals oriented and poled along <011> direction.

(i) For PZN-8PT crystals orientated along <011> and poled under different electric field E, the experimentally observed phases and phase transition temperatures depend crucially on the poling field level except the FE_t-Cubic transition, which remains at 170 °C. For poling fields

E>10 kV/cm, the optic observation shows total extinction along [100] and [0 $\bar{1}$ $\bar{1}$] directions, indicating a FE_o can be trapped at room temperature. In the dielectric data, two transitions (105 °C and 170 °C) were observed as the temperature is raised (figure 2(a)). Because the room temperature phase is FE_o, the transition at 105 °C should be from FE_o to FE_t (FE_o-FE_t).

For PZN-8PT crystals oriented still along [011] but with lower poling field (E < 10 kV/cm), the optic and dielectric data exhibit quite different behavior from those at E>10 kV/cm. For crystals poled in the field range (2 kV/cm <E <10 kV/cm), three dielectric transition peaks (94 °C, 111 °C, and 170 °C) were observed (figure 2(b)). Apparently, the phase at temperatures between 111 °C and 170 °C is FE_t. At room temperature, optic observation shows total extinction along [011] when the polarizer is aligned along [100] direction and polydomain patterns for observations made along [100] and [01 $\bar{1}$], indicating that the crystal is in FE_r phase with the polarization direction along [111] and [$\bar{1}$ 11] (figure 1(d)). Because of the complicated multidomain pattern, the phase in temperatures between 94 °C and 111 °C can't be determined optically here. From the data of PZN-10PT, it can be deduced that this is FE_o phase.

For PZN-8PT unpoled or poled at field E<2 kV/cm, optic data show multidomain state in the crystals and it is in FE_r phase from the early experimental results.[2,3,8] Two transitions (75 °C and 170 °C) were observed in the dielectric data, indicating that the crystal is at FE_r at temperatures <75 °C and in between 75 °C and 170 °C, it is in FE_t, respectively.

The results indicate that after high poling field (E>10 kV/cm), a FE_o phase can be induced and stabilized at room temperature. In the intermediate poling field, an ordered FE_r state is formed at room temperature which leads to the transition to the FE_o phase at temperatures

above 94 C. At low poling fields (E<2 kV/cm), the crystal is in a randomly oriented FE_r state and no FE_o phase is allowed at all temperatures.

(ii) For PZN-10PT oriented and poled along <011> direction, when the poling field is below 5 kV/cm, there is only one dielectric transition FE_t-Cubic at 185 °C (the data are not shown) and at below 185 °C, the crystal is in FE_t phase as expected. However, when poled at E>5 kV/cm, the optic observation reveals that the crystal is in FE_o phase. As the temperature increases, the dielectric data exhibit a FE_o-FE_t transition at 55 °C, followed by the FE_t-Cubic transition at 188 °C (figure 3(a)).

(iii) For PZN-4.5PT, optic and dielectric data indicate that the crystal is in FE_r phase for all the orientations. The transition to FE_t phase is at 115 °C and FE_t-Cubic phase is at 150 °C.

Based on the data here, the phase diagrams for PZN-PT crystals oriented and poled along <011> under fields (E>10 kV/cm and E=4 kV/cm) are proposed in figures 4(a) and 4(b).

We now discuss the data for crystals oriented and poled along <111> direction. For PZN-8PT, optic observation indicates a single domain FE_r phase at room temperature for a poled crystal. Interestingly, the dielectric data (figure 2(c)) also reveal three transitions (91 °C, 111.5 °C, and 170 °C) and the transition temperatures here are quite similar to those observed in multidomain <011> oriented and poled crystals (figure 2(b)). Apparently, the transition at 170 °C is from FE_t to the cubic. Because of the complicated multidomain pattern, the phase at temperatures between 91 °C and 111.5 °C can't be determined optically here and we suggest that this is a phase similar to the FE_o phase as observed in <011> oriented and poled crystals and denote it as FE_o'.

For <111> oriented PZN-10PT crystals, optic observation shows no sign of single domain state for crystals poled to fields to more than 10 kV/cm. However, the dielectric data of poled

crystals display two transitions (78 °C and 188 °C, see figure 3(b)). It is well known that the one at 188 °C is from FE_t to cubic transition. The existence of the additional transition at 78 °C implies that the room temperature phase is not FE_t and the optic data indicate that it is not a FE_r either. From the data of <111> oriented and poled PZN-8PT crystals, it is likely that at this composition, FE_o, becomes a room temperature trapped phase. And the phase diagram for <111> oriented and poled crystals is proposed in figure 4(c).

For <001> oriented crystals, early X-ray results taken from PZN-8PT have indicated that at low poling fields (E<10 kV/cm), the crystals are in the FE_r phase.[8] For these crystals, the dielectric data are presented in figure 2(d). At room temperature, the dielectric constant is relatively high due to the tilting of the remanent polarization P_s direction with respect to the applied electric field (E parallel to <001> and P_s parallel to <111>). At 100.5 °C, a transition to FE_t phase is accompanied by a large drop of the dielectric constant, consistent with the fact that now P_s is parallel to the applied field. For PZN-10PT, both the dielectric and optic data indicate that the room temperature FE_t phase is directly transitioned to the cubic paraelectric phase as the temperature is raised to above 185 °C. The phase diagram for <001> oriented and poled crystal (E<10 kV/cm) is proposed in figure 4(d).

The complicated phases and phase transition sequences near MPB for different electric poling and crystal orientations are caused by the closeness in the free energy among the "morphotropic" phases and the presence of high degree of defect fields in the relaxor, which causes local energy variation and traps metastable phases. In other words, the mechanical and electric boundary conditions can greatly influence the experimentally observed phases near MPB for this crystal system, which may explain the very compliant (high) electromechanical responses in this crystal. Furthermore, the observed phenomena could also be common to other

relaxor ferroelectric single crystals and indicate that there is no universal phase diagram in those systems.

This work was supported by the Office of Naval Research.

References:

1. B. Jaffe, W. Cook, Jr., and H. Jaffe, *Piezoelectric Ceramics* (Academic Press Limited, New York, 1971).

2. J. Kuwata, K. Uchino, and S. Nomura, Jpn. J. Appl. Phys., Part 1, **21**, 1298 (1982).

3. S. Park and T. R. Shrout, J. Appl. Phys., **82**, 1804 (1997).

4. B. Noheda, D. E. Cox, G. Shirane, J. Gonzalo, L. Cross, and S. Park, Appl. Phys. Lett. **74**, 2059 (1999).

5. R. Guo, L. Cross, S. Park, B. Noheda, D. Cox, and G. Shirane, Phys. Rev. Lett. **84**, 5423 (2000).

6. B. Noheda, D. E. Cox, G. Shirane, S.-E. Park, L. E. Cross, and Z. Zhong, Phys. Rev. Lett. **86**, 3891 (2001).

7. Yu Lu, D.-Y. Jeong, Z. Y. Cheng, Q. M. Zhang, H. Luo, Z. Yin, and D. Viehland. Appl. Phys. Lett. **78**, 3109 (2001).

8. M. K. Durbin, J. C. Hicks, S.-E. Park, and T. R. Shrout. J. Appl. Phys. **87**, 8159 (2000).

Figure captions:

Figure 1: Schematics of optical indicatrix for (a) tetragonal phase (FE_t), (b) rhombohedral phase (FE_r), (c) orthorhombic phase (FE_o) of PZN-PZ single crystals. (d) Schematic drawing for [011] poled crystals in FE_r twined crystals, dashed arrows indicating the remanent polarization directions.

Figure 2: Dielectric data of PZN-8%PT measured along different crystal orientations and electric poling conditions: (a) <011> direction poled with high fields (E>10 kV/cm), (b) <011> direction poled with fields 2 kV/cm<E<10 kV/cm, (c) <111> poled (E~5 kV/cm), (d) <001> poled (E~10 kV/cm).

Figure 3: Dielectric data of PZN-10%PT measured along different crystal orientations and electric poling conditions: (a) <011> direction poled (E>5 kV/cm), (b) <111> direction poled (E>5 kV/cm), (c) <001> direction poled. The weak peaks observed in the dielectric loss at temperatures near 160°C are indication of the possible trapped phases in the crystal.

Figure 4: The phase diagrams for PZN-PT (X is the mol% of PT) measured along different crystal orientations and electric poling conditions. The solid lines for the morphotropic phase boundary are obtained from <001> oriented and poled crystals which is the same as the early results. (a) Oriented and poled along <110> direction (E>10 kV/cm). (b) Oriented and poled along <110> (E=4 kV/cm). (c) Oriented and poled along <111> at room temperature. (d) Oriented and poled along <100> direction. The black dots are data points from the dielectric

data and dashed and solid lines are suggested phase boundaries. In the figure, C, T, O, and R stand for cubic, FE_t, FE_o and FE_r phases and O' for $FE_{o'}$.

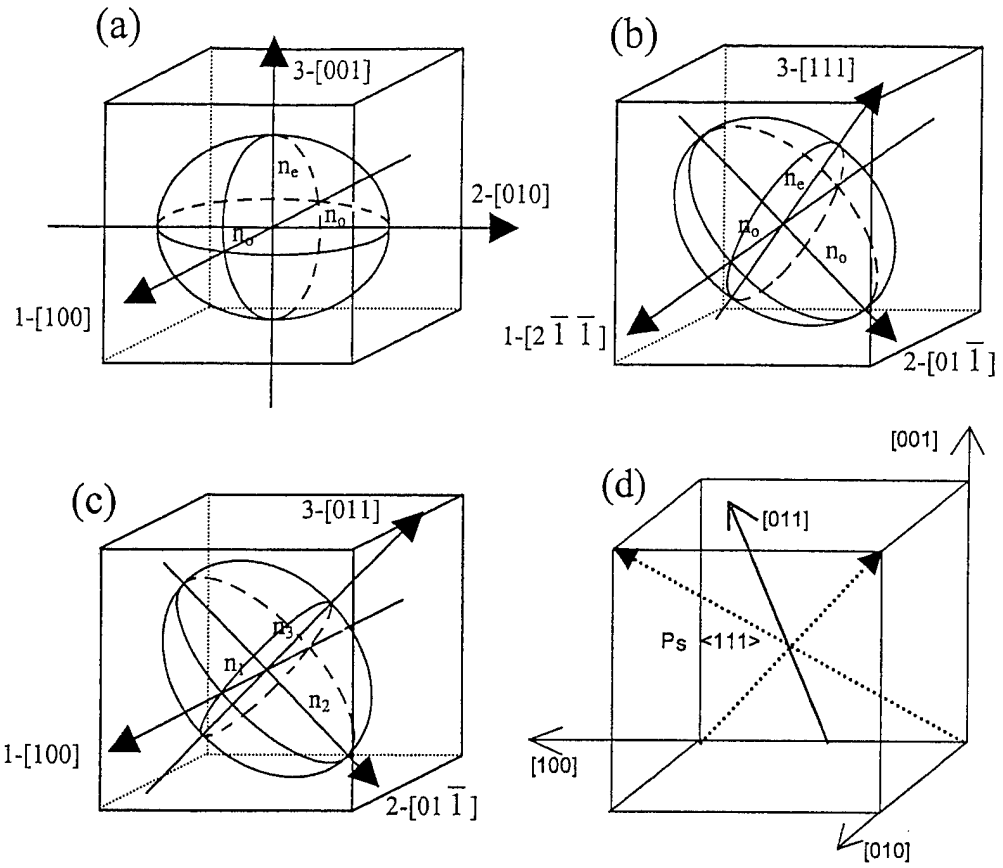

Fig. 1 Yu Lu, et al.

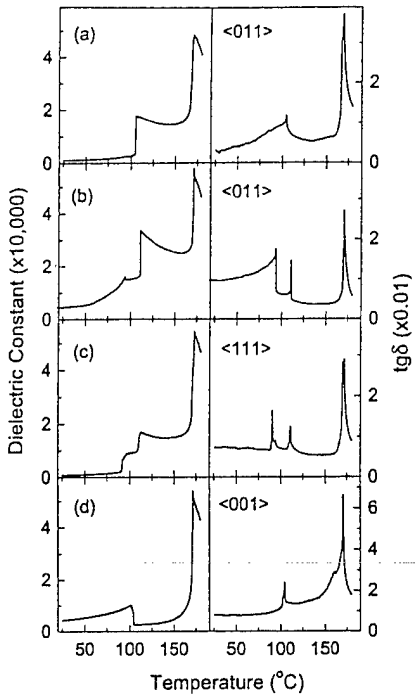

Fig. 2 Yu Lu, et al.

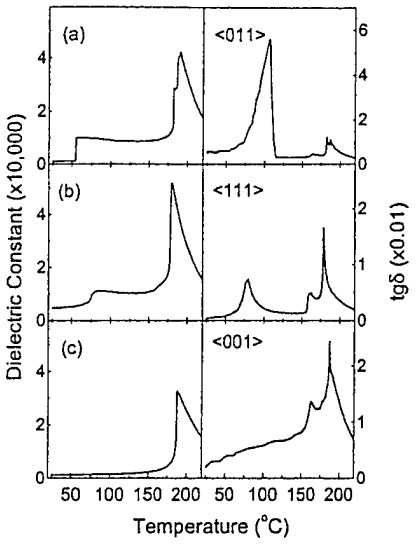

Fig. 3 Yu Lu, et al

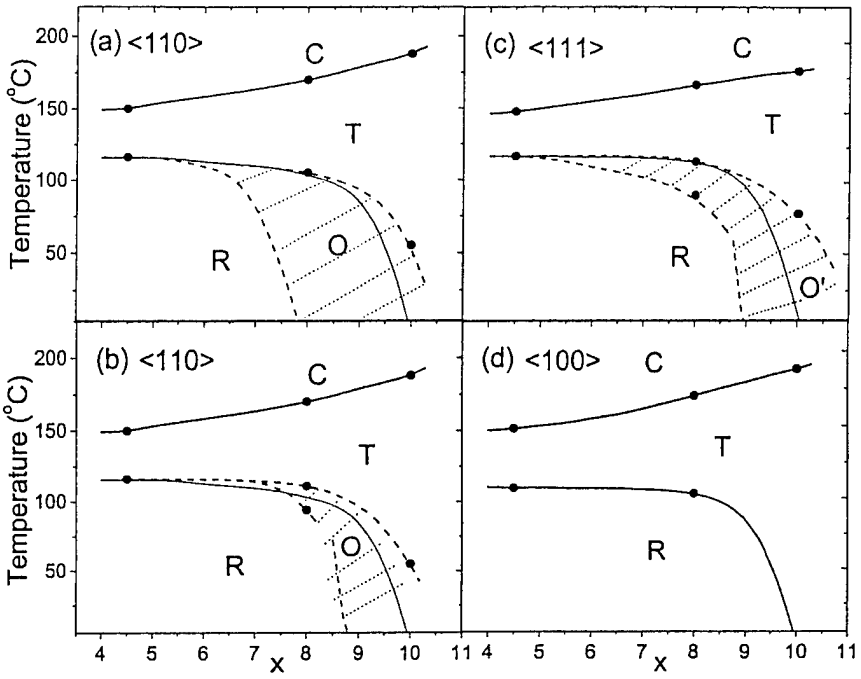

Fig. 4 Yu Lu, et al.

Appendix 13

Zhi Yu, Ruyan Guo, A.S. Bhalla, "Growth of $Ba(Ti_{1-x}Zr_x)O_3$ single crystals by the laser heated pedestal growth technique," Journal of Crystal Growth **233**, 460–465 (2001).

ELSEVIER

Journal of Crystal Growth 233 (2001) 460–465

JOURNAL OF CRYSTAL GROWTH

www.elsevier.com/locate/jcrysgro

Growth of $Ba(Ti_{1-x}Zr_x)O_3$ single crystals by the laser heated pedestal growth technique

Zhi Yu, Ruyan Guo, A.S. Bhalla*

253 Materials Research Laboratory, The Pennsylvania State University, University Park, PA 16802-4801, USA

Received 30 January 2001; accepted 4 June 2001
Communicated by R.S. Feigelson

Abstract

Single crystals of the ferroelectric $Ba(Ti_{1-x}Zr_x)O_3$ ($x = 0.05$ and 0.08) were grown by the laser heated pedestal growth (LHPG) technique. The perovskite structure of the crystals was identified by the X-ray diffraction technique. Crystals were examined by Laue patterns and scanning electron microscopy (SEM), which indicated that the single crystals were of good crystallinity and compositional homogeneity. The anisotropic dielectric and piezoelectric behavior was characterized. The $Ba(Ti_{1-x}Zr_x)O_3$ single crystals possessed a high-level hysteresis-free electromechanical strain and are promising lead-free ferroelectric crystals for the piezoelectric transducer applications. © 2001 Elsevier Science B.V. All rights reserved.

PACS: 77.84.Dy; 77.65.Bn; 81.10.Fq

Keywords: A1. Characterization; A2. Laser heated pedestal growth; B1. Perovskites; B2. Dielectric materials; B2. Lead-free materials; B2. Piezoelectric materials

1. Introduction

Lead oxide-based perovskite compounds and solid solutions, like $Pb(Zn_{1/3}Nb_{2/3})O_3$–$PbTiO_3$, exhibit optimized strain level and piezoelectric activity in their single crystal [1,2] form. However, the toxicity of lead has been an increasing concern and thus a driving force to find lead-free substitutes. One of the most important lead-free piezoelectric material is barium titanate ($BaTiO_3$) or its solid solutions, such as $BaTiO_3$–$BaZrO_3$ ceramics [3]. Millimeter-sized $Ba(Ti_{1-x}Zr_x)O_3$ crystals grown by the templated grain growth method have been recently reported [4]. To date, however, the quality of the bulk $Ba(Ti_{1-x}Zr_x)O_3$ single crystals still needs further improvement.

The laser heated pedestal growth (LHPG) technique is a modified floating zone melting process using a laser beam as the heating source [5,6]. The LHPG technique takes advantage of crucible-free feature for the crystal growth of refractory materials. The growth rate for small diameter (~mm) single crystals is rather high (generally ≥ 10 mm/h). Solid solution compositions in polycrystalline form can be readily prepared and used as the source for crystal growth. Using this method, single crystal fibers such as $BaTiO_3$ [7], $Ba(Mg_{1/3}Ta_{2/3})O_3$ [8], $Sr(Al_{1/2}Ta_{1/2})O_3$,

*Corresponding author. Tel.: +1-814-865-9232; fax: +1-814-865-2326.
E-mail address: asb2@psu.edu (A.S. Bhalla).

PII: S0022-0248(01)01520-2

$Sr(Al_{1/2}Nb_{1/2})O_3$ [9], $CaTiO_3$ [10] and doped or undoped $LiNbO_3$ [11–14] have been successfully grown.

In this work, we adopted the LHPG method for the growth of $Ba(Ti_{1-x}Zr_x)O_3$ ($x = 0.05$ and 0.08) single crystals, and studied the phase structure, crystal quality and the dielectric properties. The results are compared with those for $Ba(Ti_{1-x}Zr_x)O_3$ ceramics [3,15–18].

2. Experimental procedure

$Ba(Ti_{1-x}Zr_x)O_3$ ($x = 0.05$ and 0.08) ceramics were prepared by conventional ceramics processing via solid-state reaction. The starting materials $BaCO_3$ (99.997%), TiO_2 (99.995%) and ZrO_2 (99.978%) were weighed and wet mixed in alcohol. After drying, the powders were calcined at 1200°C. The calcined powders were mixed again, dried and pressed into disks of 35 mm diameter and ~1.2 mm thick. The pellets were sintered at 1335–1580°C for 2–8 h. The ceramic pellets with density higher than 90% were polished and cut into square rods as feeds with dimension of about $1 \times 1 \times 25\,mm^3$.

The LHPG equipment used in this work is composed of a tunable gas CO_2 laser source (Edinburgh Instrument, PL6, 180 W), an optical layout and a growth chamber. The circular laser radiation of the TEM_{00} mode was used and the laser power could be adjusted through gas pressure and/or discharge current. The laser beam was then transformed into an annulus by a reflaxicon [5]. The annulus was directed onto a parabolic mirror that focused the radiation back to its focal point, and thus the hot zone was formed. After the ceramic feed rod was aligned and its tip was introduced into the hot zone and melted, a crystal seed rod was properly contacted with the melted zone of the feed rod and then the growth was initiated. Equal pulling and feeding rates were used in this study. The molten zone temperature was monitored during growth by using an optical pyrometer with a resolution of ±10°C.

The phase and crystallographic structure of both the ceramics and the crushed single crystals were examined by X-ray diffraction analysis (XRD) using CuK_α radiation. The cross-section of the as-grown crystal was observed by scanning electron microscopy (SEM) and the distribution of elements was analyzed by energy dispersion spectra (EDS). The crystal orientation was identified by Laue back reflection technique (Northstar real-time orientation system).

Thermal expansion was measured for crystals with lengths of 6–7 mm using a dilatometer with linear variable differential transducer. The sample was first heated to 580°C before slow cooling to −180°C. The thermal expansion data were collected in first heating and then in cooling cycle at a rate of 2°C/min.

Gold electrodes were sputtered on the plates of crystal specimens for the dielectric measurements. The complex-dielectric constant of the samples was measured using an HP4284 LCR meter in the temperature range −100°C to +175°C with the cooling/heating rate of 1°C/min. The hysteresis loop and strain as a function of electric field were measured at room temperature by a modified Sawyer–Tower circuit and a linear variable differential transducer driven by a lock-in amplifier. The voltage was supplied using a Trek high voltage DC amplifier.

3. Results and discussion

Single-phase ceramic rods were used as feeding rods and either ⟨0 0 1⟩ or ⟨1 1 0⟩ oriented $SrTiO_3$ single crystal rods were used as seed crystals.

After selection of the TEM_{00} mode and the alignment of the optical beam path, the hot zone was defined. Then the alignment of the feed rod and the seed was carried out, and the assembly was introduced into the hot zone.

$BaTiO_3$ and $BaZrO_3$ form a complete solid solution system [19]. The melting temperatures of the end members are 1625°C and 2620°C, respectively [20,21]. The melting temperature of the solid solution is determined by Zr content in the solid solution. The suitable laser power level was selected to form a stable molten zone for each composition. For $x = 0.05$ and 0.08, the molten zone temperature was 1780±30°C and 1810±30°C, respectively.

Once the molten zone was stable, either ⟨1 1 0⟩ or ⟨1 0 0⟩ oriented $SrTiO_3$ seed rod was pulled upward. Both seeds can successfully initiate the growth. The pulling/feeding rates used in this work were between 11 and 15 mm/h. During growth, the temperature distribution was uniform as examined by temperature measurements at different locations of the zone within the resolution of the pyrometer of ±10°C. The shape of the molten zone was also uniform as observed from the front and back view. During the stable growing period, the shape and the temperature of the molten zone were constant. Continuous growth could be realized and crystals 20 mm long and with ~1 mm diameter were obtained, with the length restricted by the dimension of the feed ceramic rods.

The pictures of as-grown $Ba(Ti_{1-x}Zr_x)O_3$ crystals with $x = 0.05$ and 0.08 are shown in Fig. 1. The crystals are transparent for $x = 0.05$ and translucent for $x = 0.08$, as seeded by either the ⟨1 1 0⟩ or ⟨0 0 1⟩ oriented $SrTiO_3$ single crystals. The as-grown crystals were uniform in diameter, but with small facets on the side. For ⟨1 1 0⟩ seeded case, the growth was more stable and fewer cracks were observed than for the ⟨0 0 1⟩ $SrTiO_3$ seeded growth.

The Laue back reflection patterns indicated that the grown fibers were of high quality. The growth direction was identified as either pseudocubic ⟨1 1 0⟩ or ⟨0 0 1⟩, being the same as the direction of the seed crystal. Fig. 2 shows the Laue pattern of the [0 0 1] $SrTiO_3$ seeded growth. The Laue back-reflection photograph was collected when the X-ray beam was perpendicular to the growth direction, hitting on the facet (1 1 0 face) on the side of the as-grown crystal.

XRD analysis of the crushed crystal powder showed that the grown $Ba(Ti_{1-x}Zr_x)O_3$ crystals were of perovskite structure with dominant orthorhombic phase for $x = 0.05$ and rhombohedral phase for $x = 0.08$, consistent with what was identified by dielectric properties [22,23]. There is, however, peak broadening indicating coexistence of phases. Lattice parameter refinement is currently being carried out. The room temperature XRD patterns are shown in Fig. 3.

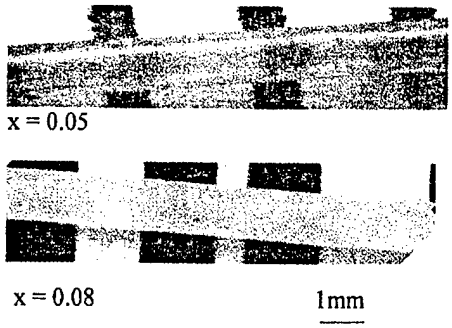

Fig. 1. Photos of as-grown $Ba(Ti_{1-x}Zr_x)O_3$ crystals with $x = 0.05$ and 0.08.

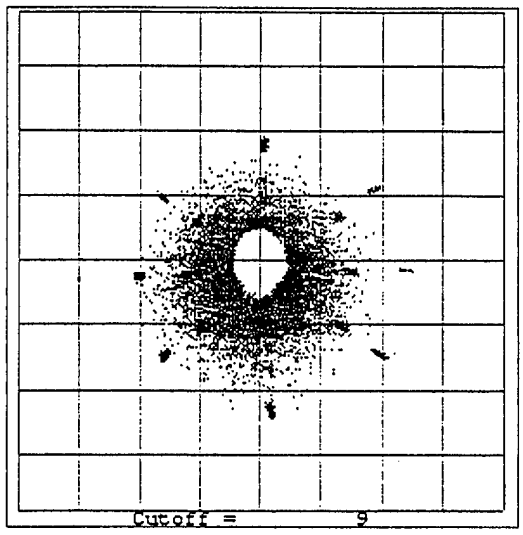

Fig. 2. Real time Laue back-reflection pattern of the $Ba(Ti_{1-x}Zr_x)O_3$ ($x = 0.05$) as-grown crystal for the [0 0 1] $SrTiO_3$ seeded growth, where the X-ray beam was perpendicular to the growth direction, hitting on the facet (1 1 0 face) on the side of the as-grown crystal.

The polished cross-section of the $x = 0.05$ crystal fiber was observed by scanning electron microscopy (SEM). The microstructure is uniform, without segregation of any second phase, as shown in Fig. 4. The EDS spectra show that the distribution of various elements Ba, Zr and Ti is also uniform in the cross-section, as shown in Fig. 4. The Zr content detected by EDS is in reasonable agreement with the nominal composition.

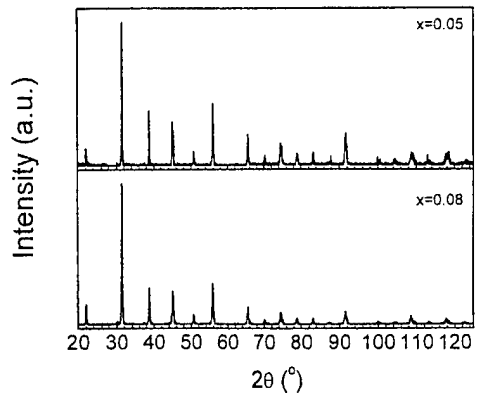

Fig. 3. The XRD patterns for the $Ba(Ti_{1-x}Zr_x)O_3$ ($x = 0.05$ and 0.08) crystals.

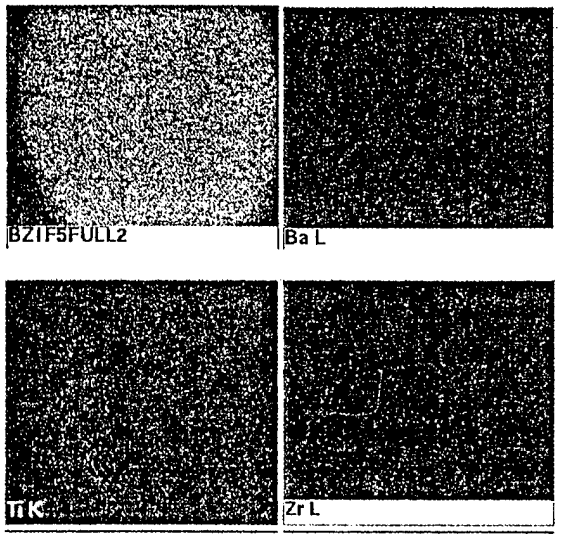

Fig. 4. SEM micrograph for the polished cross-section (upper left) of the $Ba(Ti_{1-x}Zr_x)O_3$ ($x = 0.05$) crystal and the distribution of Ti, Zr and Ba elements detected by EDS.

The thermal expansion of the crystals with $x = 0.05$ and 0.08 is shown in Fig. 5. The three-phase transition (cubic–tetragonal–orthorhombic–rhombohedral) temperatures are $T_c = 112/110°C$, $T_2 = 50/30°C$, and $T_3 = -20/-30°C$ for heating/cooling cycles, respectively, for $x = 0.05$. The thermal hysteresis at the two transitions around T_2 and T_3 is more significant. The T_2 and T_3

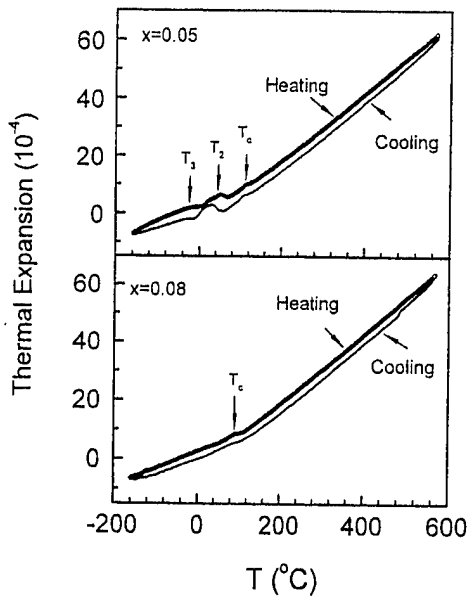

Fig. 5. Thermal expansion of the crystals with $x = 0.05$ and 0.08 as a function of temperature.

obtained here are lower than those identified from dielectric data (see below), however, the paraelectric to ferroelectric phase transition temperature is almost the same with that from dielectric data. For $x = 0.08$, only the paraelectric to ferroelectric phase transition can be seen and the small hysteresis occurs at the phase transition during heating and cooling. The average thermal expansion coefficient as calculated from Fig. 5 for $x = 0.08$ is about $12 \times 10^{-6}/°C$ in the paraelectric phase from 120 to 500°C. This is similar to the thermal expansion coefficient of $BaTiO_3$ [20].

The temperature dependence of dielectric constant (ε) for $x = 0.05$ and 0.08 measured upon cooling cycle is shown in Fig. 6. The data for corresponding ceramics used to grow crystals are also plotted. The dielectric properties show anisotropic behavior along different crystal orientations. The phase transition temperatures are $T_c = 110°C$, $T_2 = 50°C$ and $T_3 = 0°C$ for $x = 0.05$ and $T_c = 102°C$ and $T_2 = 71°C$ for $x = 0.08$, respectively, which are in agreement with that of ceramics in the present work and the literature [3,16,18].

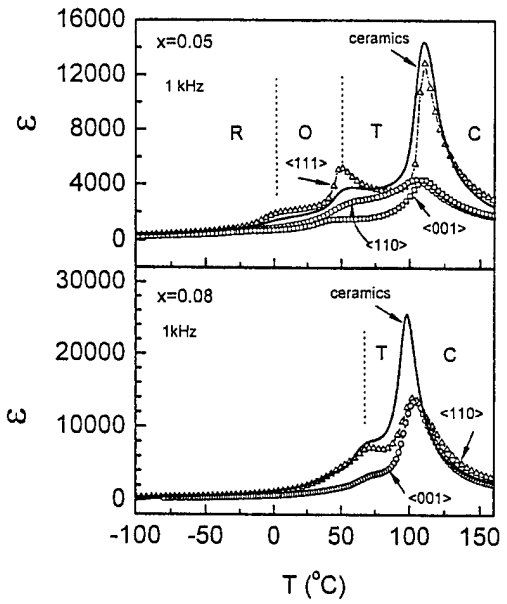

Fig. 6. Temperature dependence of dielectric constant (ε) at 1 kHz for the $Ba(Ti_{1-x}Zr_x)O_3$ crystals and ceramics with $x = 0.05$ and 0.08. (C: Cubic; T: tetragonal; O: orthorhombic; R: rhombohedral.)

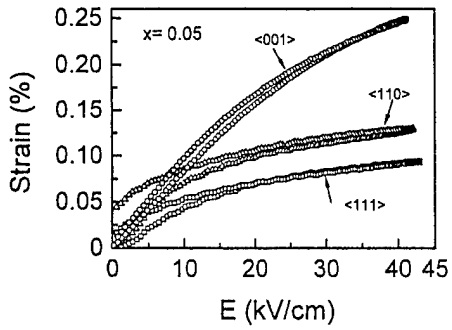

Fig. 7. The unipolar strain vs. electric field (E) for the $Ba(Ti_{1-x}Zr_x)O_3$ single crystals with $x = 0.05$ along various crystal orientations.

The growth of single crystals also allowed us to study the piezoelectric strain along different crystalline orientations. The room temperature unipolar strain (x) vs. electric field (E) behavior for $Ba(Ti_{1-x}Zr_x)O_3$ single crystals with $x = 0.05$ for different orientations is shown in Fig. 7. In the non-polar $\langle 0\,0\,1 \rangle$ direction, the strain exhibits the highest value among the three measured directions, which at room temperature is of orthorhombic symmetry (more than 2 times higher than that in the polar $\langle 1\,1\,0 \rangle$ direction) for $x = 0.05$ crystals. This shows that in lead-free crystals the crystal orientation determines the piezoelectric behavior as in the lead-containing ferroelectric relaxor based materials [2]. It is also shown that the strain level is reasonably high ($\sim$0.25%) and almost hysteresis-free. No obvious saturation up to 40 kV/cm for $\langle 0\,0\,1 \rangle$ orientation was observed. The piezoelastic coefficient derived from the low field x–E slope yielded $d_{33} = \sim 800$ pC/N, which is notably high for non-lead compositions.

4. Conclusions

Single crystals of $Ba(Ti_{1-x}Zr_x)O_3$ with $x = 0.05$ and 0.08 were successfully grown by the LHPG technique, and the compositions of the grown crystals are found to be uniform and retain the starting compositions. Dielectric, piezoelectric and thermal expansion properties of the single crystals have been measured. The results are overall in agreement with those obtained from the corresponding ceramic, with, however, anisotropic details.

The $Ba(Ti_{1-x}Zr_x)O_3$ single crystals possess high level hysteresis-free electromechanical strain and are promising lead-free ferroelectric materials for piezoelectric transducer applications.

Acknowledgements

One of the authors (Zhi Yu) would like to thank Dr. Chen Ang for his stimulating discussion during the course of this work. This work is supported by the Office of Naval Research under Grant No. N00014-98-1-0527.

References

[1] J. Kuwata, K. Uchino, S. Nomura, Jpn. J. Phys. Part 1 21 (1982) 1298.
[2] S.E. Park, T.R. Shrout, J. Appl. Phys. 82 (1997) 1804.
[3] R.C. Kell, N.J. Hellicar, Acustica 6 (1956) 235.

[4] P.W. Rherig, S.E. Park, S.T. McKinstry, G.L. Messing, B. Jones, T.M. Shrout, J. Appl. Phys. 86 (1999) 1657.
[5] J. Yamamoto, A.S. Bhalla, Mater. Res. Bull. 24 (1989) 761.
[6] J. Yamamoto, Ph.D. Thesis, The Pennsylvania State University, 1989.
[7] M. Saifi, B. Dubois, E.M. Vogel, F.A. Thiel, J. Mater. Res. 1 (1986) 452.
[8] R. Guo, A.S. Bhalla, L.E. Cross, J. Appl. Phys. 75 (1994) 4704.
[9] R. Guo, A.S. Bhalla, J. Sheen, F.W. Ainger, S. Erdei, E.C. Subbarao, L.E. Cross, J. Mater. Res. 10 (1995) 18.
[10] Y. Jiang, R. Guo, A.S. Bhalla, J. Electroceramics 2 (3) (1998) 199.
[11] Y.S. Luh, R.S. Feigelson, M.M. Fejer, R.L. Byer, J. Crystal Growth 78 (1986) 135.
[12] Y.S. Luh, M.M. Fejer, R.L. Byer, R.S. Feigelson, J. Crystal Growth 85 (1987) 264.
[13] M. Matsukura, Z. Chen, M. Adachi, A. Kawabata, Jpn. J. Appl. Phys. 36 (1997) 5947.
[14] Y.-J. Lai, J.-C. Chen, K.-C. Liao, J. Crystal Growth 198/199 (1999) 531.
[15] T.N. Verbitshais, S.S. Zhdanov, Iu.N. Venevtsev, S.P. Solsviev, Sov. Phys.- Cryst. 3 (1958) 182.
[16] D. Hennings, A. Schnell, G. Simon, J. Am. Ceram. Soc. 65 (1982) 539.
[17] S.M. Neirman, J. Mater. Sci. 23 (1988) 3973.
[18] J. Ravez, A. Simon, Eur. J. Solid State Inorg. 34 (1997) 1199.
[19] M. McQuarrie, F.W. Behnke, J. Am. Ceram. Soc. 37 (1954) 539.
[20] B. Jaffe, W. Cook, H. Jaffe, Piezoelectric Ceramics, Academic Press, London, 1971.
[21] H. von Wartenberg, W. Gurr, Z. Anorg. Allg. Chem. 196 (1931) 381.
[22] Zhi Yu, Ruyan Guo, A.S. Bhalla, J. Appl. Phys. 88 (2000) 410.
[23] Zhi Yu, Ruyan Guo, A.S. Bhalla, Appl. Phys. Letts. 77 (2000) 1535.

Appendix 14

Jianyi Cui, Ruyan Guo, and Amar Bhalla, "The Growth and Characterizatin of Lead Magnesium Niobate–Lead Titanate by Laser Heated Pedestal Growth Technique," submitted to Journal of Crystal Growth (2001).

Submitted *J. Crystal Growth* (2001).

The Growth and Characterization of Lead Magnesium Niobate – Lead Titanate by Laser Heated Pedestal Growth Technique

Jianyi Cui, Ruyan Guo and Amar Bhalla
Materials Research Laboratory, The Pennsylvania State University, University Park, Pennsylvania 16802

Abstract

PMN-PT crystal fibers of perovskite phase with length up to 7 mm were grown in this work by the LHPG technique. It is the first successful demonstration of growing highly volatile lead-containing solid solution perovskite crystals by an open crucible/crucible-free system. The control of lead evaporation and the stabilization of perovskite phase were realized. Aided by SEM, dielectric, ferroelectric and strain properties measurements, a detailed analysis on the forming phase(s) and crystal qualities was provided. Growth parameters, particularly the excess lead oxide necessary to achieve dynamic balance of Pb content in melt during growth, and the suitable flux system, were studied and reported.

Introduction

Relaxor-PT type perovskites are well known ferroelectric materials for their high dielectric permittivity, electrostrictive coefficient, and electrooptic coefficient near room temperature. The ultrahigh coupling and piezoelectric properties of PMN-PT single crystals were first reported in 1989[1]. In composition near the morphotropic phase boundary between rhombohedral and tetragonal phases(PMN33PT), single crystals exhibit extraordinarily large electromechanical properties[2]. Driven by technological importance, single crystal form of the solid solution between lead magnesium niobate and lead titanate [(1-x)%PMN-x%PT] is investigated. Currently, however, the application of PMN-PT single crystals is

limited by the composition uniformity and availability, both of which dependent on growth techniques.

At present, the stable growth of compositionally homogenous crystals faces some difficulties. Three major methods – flux method, modified Bridgman method and Seeded polycrystal conversion method – are used to produce PMN-PT single crystals. In flux method[1,3], the crystals sizes yielded are in general in the range of cubic millimeters with or without the presence of pyrochlore phase. B-site ions magnesium, niobium and titanium reveal locally compositional fluctuation up to 5%, which influence the crystals properties significantly. The difficulty of separating crystals from the flux and chemical inhomogeneity caused by incongruently melting system and slow growth rate are other difficulties for this method. The most successful method at present is Modified Bridgman technique[4,5,6]. However, high cost due to the use of Platinum crucible, and difficulty of growth orientation and compositional homogeneity control severely obstruct the application. Seeded polycrystal conversion method[7,8,9] is still in the initial stage. So far, only millimeter size crystal is grown. In order to overcome the limitation of methods above, a different approach, laser heated pedestal growth (LHPG) technique is studied to grow PMN-PT single crystal fibers near a morphotropic phase boundary.

Backgrounds

Laser Heated Pedestal Growth technique is basically a crucible free novel crystal growth method. Therefore, the control of high evaporation of lead oxide was a major concern in this work. A modified traveling flux method, which was realized by adding the flux into ceramic performs, was introduced to solve this problem.

In order to compensate the loss of lead oxide during the crystal growth, higher initial concentration of lead oxide was added when preparing for the ceramics. By previous study, the addition of another component, boric acid, was proven to be a good flux additive to stabilize the growth zone and decrease the growth temperature due to its network structure. Hence, boric acid (oxide) plus

lead oxide flux system was investigated here to grow PMNPT single crystal fibers. However, excessive boric acid may lead to the formation of pyrochlore phase, which influences the materials performance severely. Therefore, adjusting of the flux concentration, its influence on the forming phase and the grown crystal qualities were discussed in this paper.

Experiments

Preparation of Ceramic Preforms

Ceramic processing was applied to provide preforms of feed for LHPG single crystal fibers growth.

Ceramic specimens were prepared by solid state reaction. High purity (>99.99%) magnesium oxide (MgO), titanium oxide (TiO_2), niobium oxide (Nb_2O_5) lead oxide (PbO) and flux components were used as starting materials. The columbite two-step method[10] was adopted to minimize the formation of pyrochlore phase in the ceramic samples. Powder X-ray diffraction was used extensively to characterize the crystallographic phases. The flux concentration, whose components were excess lead oxide and boric acid was shown in Table 1. Two factors were considered here: the concentration of excess lead oxide and the relative ratio between boric acid and excess lead oxide. Stoichmetric PMN30PT [$0.7Pb(Mg_{1/3}Nb_{2/3})O_3$ - $0.3PbTiO_3$] was used as the standard. Relatively to the PMN30PT concentration, the excess lead oxide concentration was sorted into 4 groups, named Group A, B, C, and D, which represented 10, 25, 50 100 mol % extra lead oxide. While numerical number represented the relative ratio between boric acid and extra lead oxide. Group 1, 2 and 3 stand for the ratio of 0, 1:5 and 1:1 respectively.

The sintering parameters were shown in Table 2. After checking with XRD to confirm the right phase, ceramic disk was then cut into the thin rods with dimension of 1x1x20 mm^3.

Table 1: Designed flux composition of PMN30PT ceramic

Boric Acid : PbO \ PbO	10 mol% (Group A)	25 mol% (Group B)	50 mol% (Group C)	100 mol% (Group D)
0 (Group 1)	—	—	—	—
1:5 (Group 2)	2 mol%	5 mol%	10 mol%	20 mol%
1:1 (Group 3)		25 mol%		

Table 2: Sintering parameters of flux-added PMN30PT ceramics

	A	B	C	D
1	1200°C / 2 hr	1150°C / 2 hr	1100°C / 2 hr	1050°C / 2 hr
2	1150°C / 2 hr	1100°C / 2 hr	1050°C / 2 hr	1000°C / 2 hr
3		1050°C / 2 hr		

Laser Heated Pedestal Growth

The LHPG equipment used in this study consisted of a laser generation system (Edinburgh Model PL6 step-tunable CW CO_2 laser, TE_{00} mode), an optical layout and a growth chamber (ultra-high vacuum, stainless steel walls).

In this study, <001> orientated PMN33PT single crystal seed was used. Prior to each growth event, the bottom of the seeds that were contaminated by the previous growth event was removed by grinding. The seed was kept unmelted when initiating the growth process. Seeding rates of 20 mm/hr is used to get a stable growth. Feeding rates were adjusted to match the seeding rates. The resulting seeding/feeding rates in group one materials were about 20/30 mm/hr, while the growth rates in group two and group three were 20/22 mm/hr.

The resulting growth temperatures during stable growth are listed in Table 3.

Characterization of crystal samples

Powder X-ray diffraction technique was employed to identify the crystallographic phase of the crystals grown. The phase distribution was further detected by Scanning Electron Microscopy (SEM) and Electron Probe Analysis (EP). Dielectric and ferroelectric measurements are also performed on the specific portion of grown crystals (The details was discussed in Results & Discussion section).

Table 3: Growth temperature of different compositions

	A	B	C	D
Group 1	~ 1500°C	~ 1500°C	~ 1500°C	~ 1500°C
Group 2	~ 1450°C	~ 1430°C	~ 1430°C	~ 1430°C
Group 3		~ 1350°C		

Results and Discussions

Ceramic performs

Powder X-ray patterns (Fig 1) showed PMN-PT and excess lead oxide phases in both group one and group two ceramic samples. While the formation of pyrochlore phase was shown in the third group, which agree with the claim of Dong and Ye[3] that pyrochlore phases had the tendency to form with higher boric oxide ratio. Morphologically, all ceramic samples were of high porosity. However, those with boric acid showed reduced porosity, which may have played a role in stable growth that was observed in group two and three, i.e., the fluctuation caused by structural inhomogeneity of feed rods was less severe with boric acid.

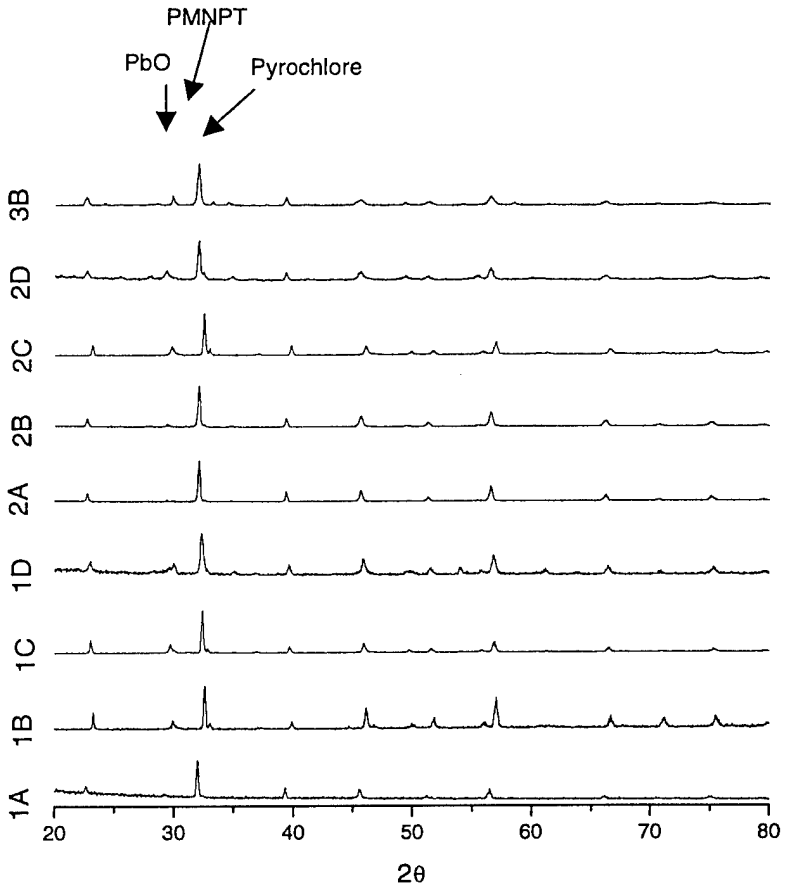

Fig 1.Powder X-ray patterns of ceramic pellets

X-ray measurement of crystals

Powder X-ray diffraction technique was employed to check the crystallographic phase of the crystals grown (Fig 2 for group one, Fig 3 for group two). The crystal fibers were grounded previous to each test. Fibers with composition 1D were not obtained due to the instability of the growth.

From X-ray profile of group one crystals, the ratio of perovskite phase increased consistently with increasing of excess lead oxide, which indicated that a higher level lead concentration was needed to compensate the lead loss during the crystal growth. However, during the LHPG, growth stability decreased with higher lead contents was observed, which raised the difficulty to obtain the crystals. For samples of group two and group three with boric acid flux though, there was no significant decrease of stability observed as the excess lead oxide was increased. As mentioned above, the increasing viscosity of the molten zone

by the addition of boric oxide might be the desirable factor to overcome the severe volatility of lead oxide. There were no additional peaks in X-ray diffraction produced due to the addition of boric acid. The reason was possibly the glassy phase of boric oxide[11] and so it could not be detected by powder X-ray diffraction technique. In another case, the boric oxide could also be evaporated out during the growth.

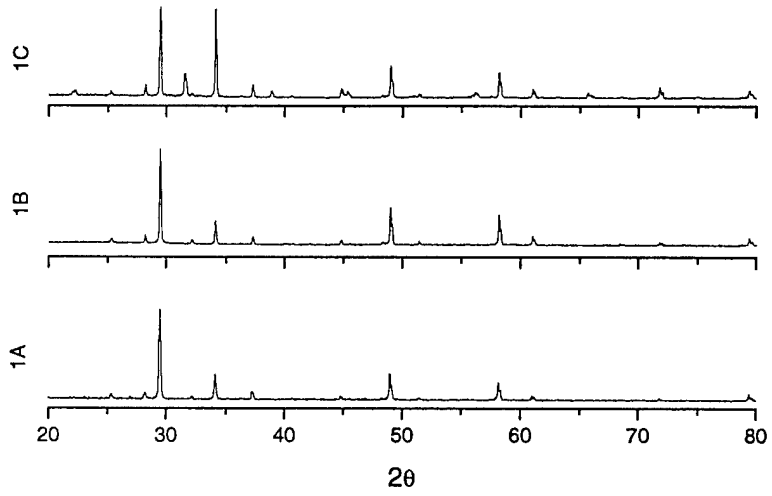

Figure 2: Powder X-ray diffraction patterns of crystals from group one by LHPG

The attention was focused on group two with composition 2D, which represented flux composition of 100% excess lead oxide and 20% boric oxide. Using the feed rod of composition 2D with PMN-PT single crystal seed, a crystal of essentially perovskite phase and up to 7 millimeters in length was obtained (Fig 3 2D_p). This crystal was believed to be the first evidence that demonstrated the feasibility of lead-containing perovskite crystal growth in an open system by LHPG technique. However, pyrochlore phase, as shown in Fig 3, noted as 2D, was also obtained using the same feed rods, but different growth parameters.

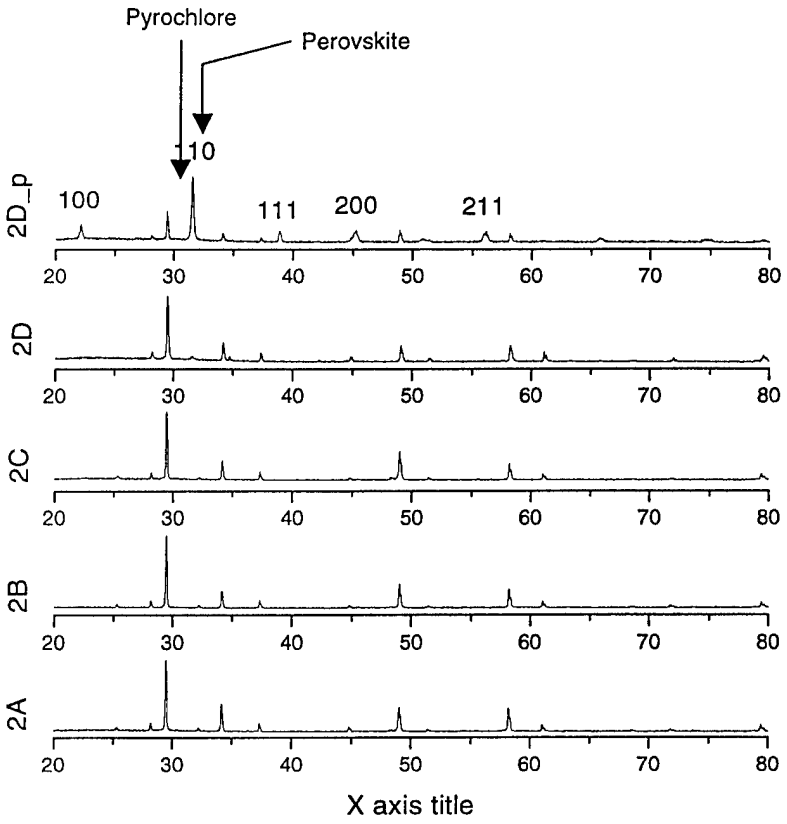

Figure 3: Powder X-ray diffraction patterns for group two LHPG grown crystals (The peaks were indexed by perovskite phase)

By Lauè X-ray back scattering, the orientation of the grown fibers was determined to be <112> when growth was initiated with PMN30PT <001> orientation.

Phases segregation

The secondary electron images of the middle part of sample 2D_p was shown in Fig 4. An essentially one phase was observed in the cross-section. By quantitative analysis (Fig 5), two minor phases were identified beside the main perovskite phase. Further study of elements maps were shown in Fig 6 (bright color represents the high concentration), which showed a continuous perovskite PMN-PT phase imbedded with regions of MgO segregation and MgO depletion. This magnesium segregation could be attributed to the poor dispersability and

reactivity of magnesium oxide, which were also noted in the study on ceramics [12,13].

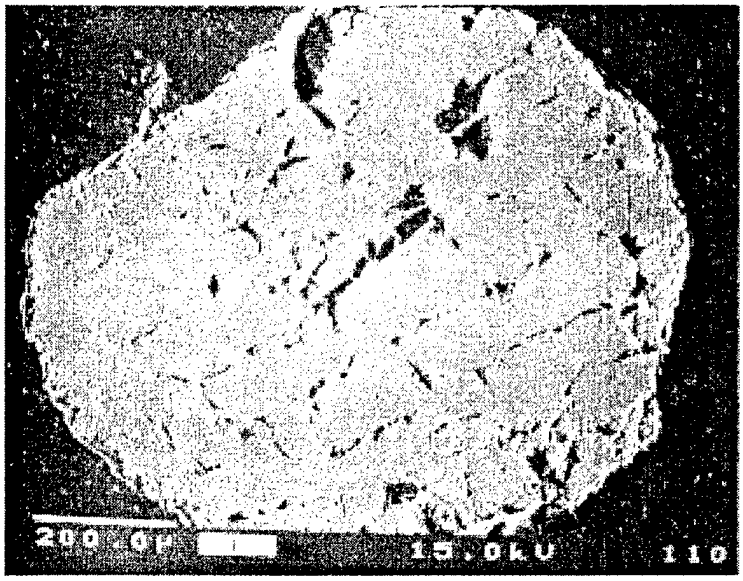

Figure 4: SE image on the middle section of sample 2D_p

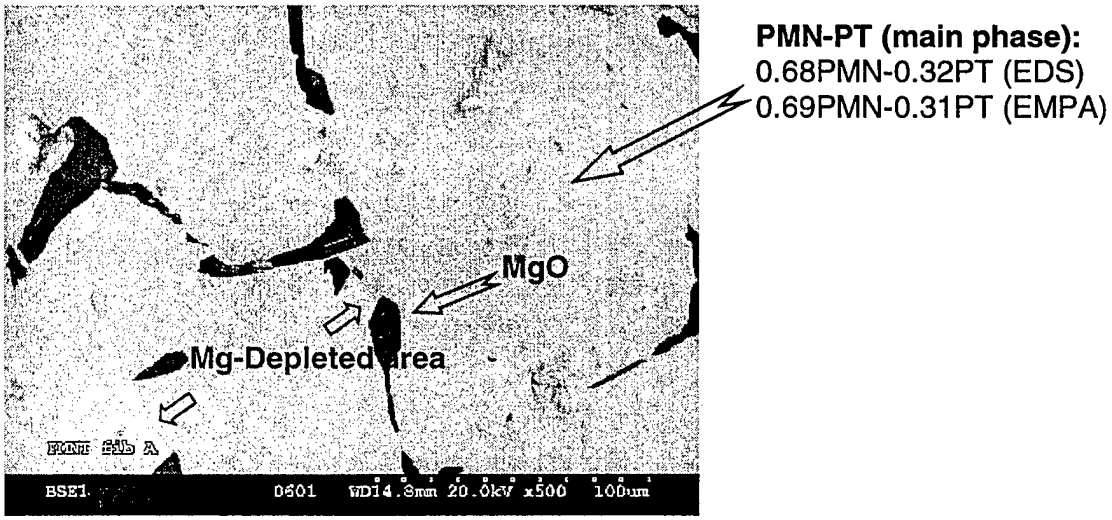

Figure 5: Composition Analysis on the middle section of sample 2D_p

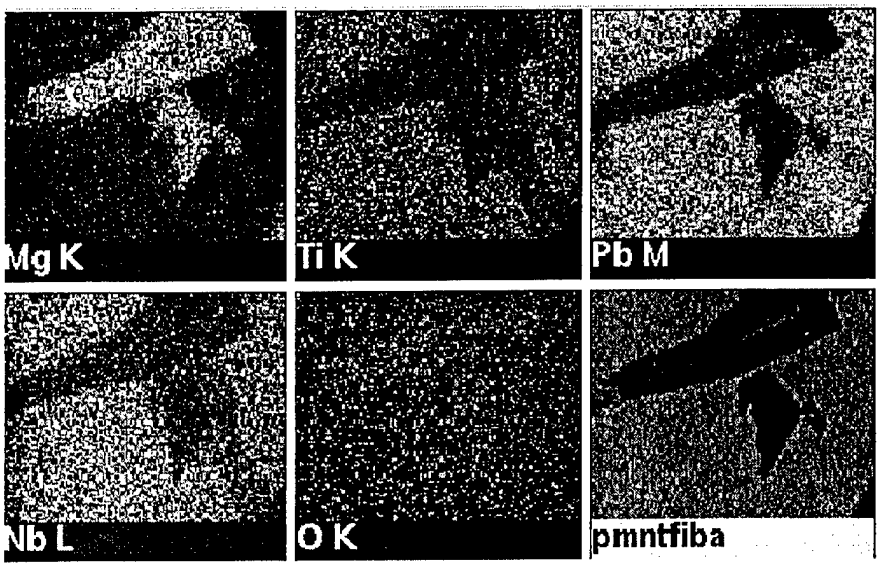

Figure 6: Element map on the middle section of sample 2D_p

No boron was detected in the cross-section of both top and middle part of the sample, which showed the utility of modified traveling flux method.

Dielectric Measurement

Dielectric measurement was performed on middle part of sample 2D_p. Sample 2D_p was silver electroded prior to the experiment. The measurement was performed from room temperature to 200°C at four different frequencies of 1k, 10k, 100k and 1M Hz, which were designed to display the relaxor features (Fig 7).

From the measurement results, several points should be noted: 1. Dielectric constant versus temperature curves showed two peaks: a strong one around a temperature of 190°C and a weak one around 75°C at the frequency of 1kHz. They corresponded to the two peaks reported in the PMN33PT composition [1], but with a shift of nearly 20°C to the high temperature end. From SEM pictures, three phases, PMN-PT, MgO and MgO depleted phase, were observed. Because of their different dielectric permittivity and conductivity, the Maxwell-Wagner effect from interfacial polarization may contribute to the overall

dielectric behavior, as well as on T_C, particularly in low frequency range. Because of these effects the typical relaxor behavior of tanδ vs. frequency was masked substantially. 2. The maximum value of dielectric constant was much lower than the value reported for the flux grown single crystals; however, the room temperature value was comparable. 3. The dielectric loss at temperatures below 150°C was moderately low. The high dielectric loss at higher temperatures may be attributed to the use of air-dry silver electrode during the measurement and the Maxwell-Wagner polarization discussed as above. 4. The most important information obtained from the dielectric measurements was the verification of bulk continuous perovskite phase during the growth, which was near the target composition of PMN30PT.

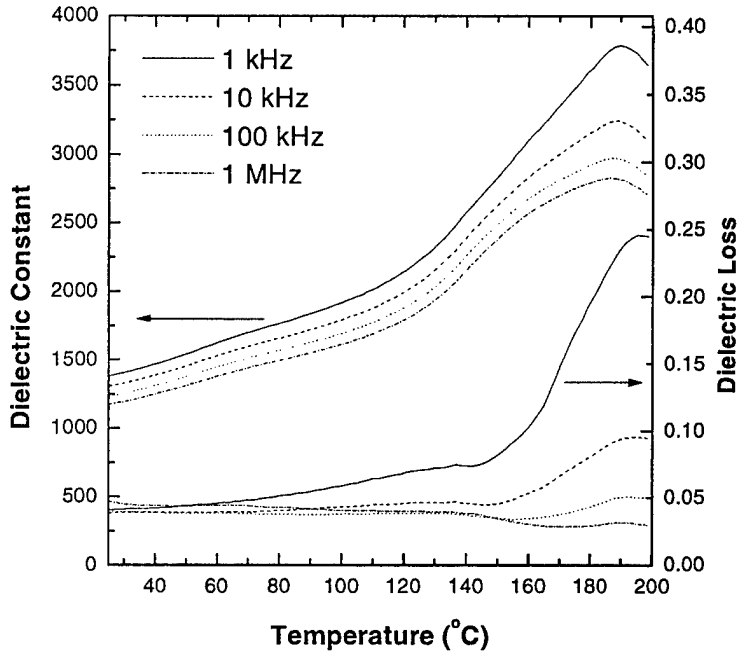

Figure 7: Dielectric measurement on the middle section of sample 2D_p

Ferroelectric Measurement

The polarization (Fig 8) and strain (Fig 9) versus electric field measurements were performed on the same sample that was used for dielectric measurements. To avoid the damage of sample, the electric field applied was limited to 17kV/cm.

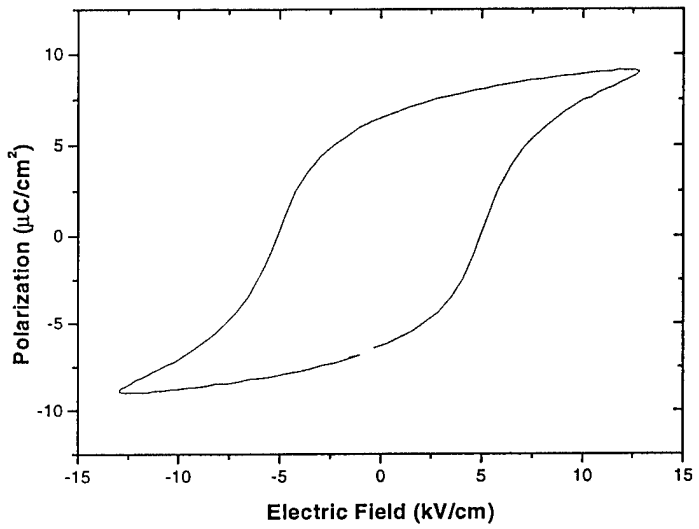

Figure 8: Polarization vs. electric field hysteresis loop at 200Hz on the middle section of sample 2D_p

From Fig 8 and 9, the bulk quality of ferroelectric perovskite phase was authenticated in the grown fiber. Again, well established polarization ~ electric field hysteresis loop showed that continuous perovskite structure existed in the fiber. However, the remanent polarization value was not high, at the low electric field applied. Checking with strain level of the grown crystals, up to 0.11% unsaturated strain under electric field 17kV/cm was obtained, which indicated a good strain response of electric field even though the segregated magnesium oxide and magnesium-depleted phases were co-found within the PMN-PT main phase.

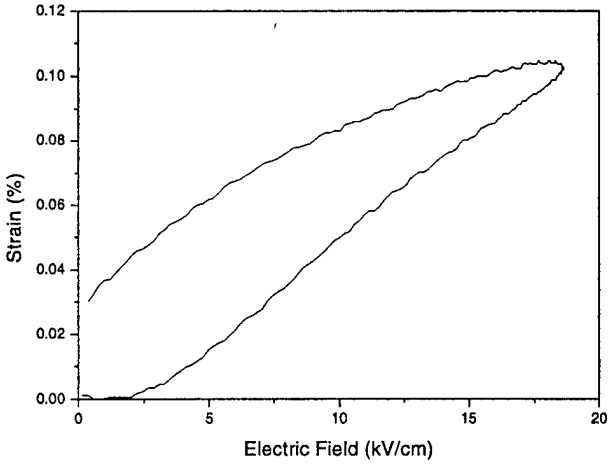

Figure 9: Strain vs. electric field measurement at 0.2 Hz, unipole of middle part sample 2D_p

From the measurement results, a view of mainly perovskite phase single crystals fibers with some additional non-ferroelectric phases was constructed. So far, the growth stability of perovskite phase in an open crucible system was established, however, the phase purity and crystal quality need to be further improved.

Conclusion

Based on the current result on PMN-PT crystal growth by the LHPG technique, the first stage of success has been achieved. The perovskite phase has been stabilized in grown fibers for several millimeters in length. The feasibility of high volatile materials crystal growth by open crucible technique has been demonstrated.

In this work, PMN-PT single crystal fibers near target composition 30%PT up to 7 mm were grown by LHPG technique. This is the first time a lead-containing ferroelectric perovskite crystal is grown by an open crucible technique. Modified flux method was introduced in this study in order to decrease the growth temperature and stabilize the perovskite phase during the growth process. It has

been shown that the combination of lead oxide and boric acid could effectively compensate the lead loss and stabilize the growth. The forming phase was confirmed by SEM together with EDS and EMPA microscopically. Dielectric, ferroelectric and strain properties were measured as well to further verify the chemical and phase analysis results. Currently, the flux containing 100 mol% excess lead oxide with 20 mol% boric acid was used for the successful growth. From the experiment, 100 mol% excess lead oxide was shown to be enough to compensate the lead loss.

However, overcoming the existence of segregated phases and precise controlling of growth orientation are perhaps the most important issues for the future work.

Acknowledgments

The authors would like to acknowledge Professor Amar S. Bhalla for his important comments. Gratitude is also extended to the members of the Ferroelectrics group for providing insight suggestions and discussions. This work is supported by Office of Naval Research.

Reference

1. T.R. Shrout, Z.P. Chang, N. Kim, and S. Markgraf, *Ferroelectrics Letters*, 12 (1990) 63
2. S.-E. Park and T.R. Shrout, *IEEE Transactions on Ultrasonics, Ferroelectrics, and Frequency Control*, 44[5] (1997) 1140
3. M. Dong and Z.-G. Ye, *Journal of Crystal Growth*, 209 (2000) 81
4. H. Luo, G. Xu, P. Wang, and Z. Yin, *Ferroelectrics*, 231 (1999) 97
5. Z.-W. Yin, H.-S. Luo, P.-C. Wang, and G.-S. Xu, *Ferroelectrics*, 229 (1999) 207
6. H. Luo, G. Xu, H. Xu, P. Wang and Z. Yin, *Japanese Journal of Applied Physics*, 39 (2000) 5581
7. A. Khan, F.A. Meschke, T. Li, A.M. Scotch, H.M. Chan, and M.P. Harmer, *Journal of the American Ceramic Society*, 82 (1999) 2958

8. T. Li, A.M. Scotch, H.M. Chan, and M.P. Harmer, *Journal of the American Ceramic Society*, 81 (1998) 244
9. T. Li, S. Wu, A. Khan, A.M. Scotch, H.M. Chan, and M.P. Harmer, *Journal of Materials Research*, 14 (1999) 3189
10. S.L. Swartz and T.R. Shrout, *Materials Research Bulletin*, 17 (1982) 1245
11. *Encyclopedia of Chemical Technology, 4th edition.* V4 p368
12. S.M. Gupta and A.R. Kulkarni, *Materials Chemistry and Physics*, 39 (1994) 98
13. T.R. Shrout and A. Halliyal, *American Ceramic Society Bulletin*, 66 (1987) 704

Appendix 15

Jeong Hwan Park, Fei Xu, and Susan Trolier-McKinstry, "Dielectric and piezoelectric properties of sol-gel derived lead magnesium niobium titanate films with different textures," Journal of Applied Physics, 89[1], 568–574 (January 2001).

Dielectric and piezoelectric properties of sol–gel derived lead magnesium niobium titanate films with different textures

Jeong Hwan Park, Fei Xu, and Susan Trolier-McKinstry[a)]
Materials Research Laboratory, The Pennsylvania State University, University Park, Pennsylvania 16802

(Received 23 December 1999; accepted for publication 18 September 2000)

The piezoelectric and dielectric constants for $Pb(Mg_{1/3}Nb_{2/3})O_3$–$PbTiO_3$ (PMN–PT, 70/30) films with different orientations were measured. PMN–PT films were deposited on Pt(111)-passivated silicon substrates using a modified sol–gel process. The room temperature dielectric constants K for the {100}-oriented films were 2500–2600, while K for {111}-oriented films were 1900–2000. In both cases $\tan\delta$ was less than 0.03. The dependence of the piezoelectric coefficient d_{31} of the PMN–PT films on the poling fields was investigated. The d_{31} coefficients of {100}-oriented PMN–PT films were found to range from −28 to −69 pC/N with poling field. The {100}-oriented PMN–PT films showed larger piezoelectric coefficient than {111}-oriented films. The d_{33} coefficients of the 1.5 μm thick {100} oriented PMN–PT films were ~170–183 pC/N. The aging rate of $-d_{31}$ was ~4%–10%/decade. © *2001 American Institute of Physics.*
[DOI: 10.1063/1.1324685]

INTRODUCTION

There has been significant interest in Pb-based ferroelectric thin films such as $Pb(Mg_{1/3}Nb_{2/3})O_3$ (PMN), $PbTiO_3$ (PT), $PbZrO_3$, and $Pb(Zr_{0.5}Ti_{0.5})O_3$ (PZT) because of their potential advantages for electro-optic and microelectronic applications, including capacitors, pyroelectric detectors, surface acoustic wave devices, nonvolatile semiconductor memories, and piezoelectric devices.[1,2] Of these, piezoelectric thin films have attracted considerable attention since they can add functionality to microfabricated devices such as microsensors and actuators. Microfabricated devices incorporating ferroelectric actuation or sensing typically include compositions from the $Pb(Zr, Ti)O_3$ system.[3–5] In that case, it was demonstrated that properties such as the dielectric constant, pyroelectric coefficients, piezoelectric constants, and P–E hysteresis could be improved by preferentially controlled orientation.[6–9]

Recently, ultralarge piezoelectric responses have been observed in single crystal solid solutions of relaxor ferroelectrics and PT. For example, for single crystals of the rhombohedral $Pb(Zn_{1/3}Nb_{2/3})O_3$–$PbTiO_3$ system, Park *et al.* have reported that a d_{33} piezoelectric coefficient as high as 2600 pC/N can be obtained when oriented and measured along the [001] direction.[10,11] They suggested that no driving force exists for non-180° domain wall motion in the case of a well-poled (001)-oriented rhombohedral crystal measured normal to the face. This is interesting from the standpoint of piezoelectric films since ferroelastic wall motion is difficult to achieve in many ferroelectric thin films.[12] Maria *et al.* have also demonstrated that d_{31} piezoelectric coefficients as high as −180 pC/N can be realized in (001) epitaxial rhombohedral PMN–PT thin films on $SrRuO_3$/(001)$LaAlO_3$ substrates.[13] Taking these results into account, similar advantages in piezoelectric characteristics can be expected for highly {100}-oriented relaxor-PT film relative to polycrystalline ones.

Thus an investigation of the dielectric and electromechanical properties of oriented PMN–PT films by sol–gel has been initiated. The specific composition investigated was 70%PMN–30%PT, which lies on the rhombohedral side of the room temperature morphotrophic phase boundary between PMN and PT. In this study, the effects of crystallographic texture ({100} and/or {111} fiber texture) on the dielectric and piezoelectric properties of the PMN–PT thin films have been characterized. In addition, aging of the piezoelectric coefficients in {100} and {111} oriented films has been investigated.

EXPERIMENTAL PROCEDURE

Lead acetate trihydrate, $Pb(C_2H_3O_2)_2\cdot 3H_2O$, magnesium ethoxide, $Mg(OC_2H_5)_2$, niobium ethoxide, $Nb(OC_2H_5)_5$, and i.e. $Pb(C_2H_3O_2)_2\cdot 3H_2O$ titanium(IV) isopropoxide, $Ti(OCH(CH_3)_2)_4$ (Aldrich Chemical, Milwaukee, WI) were used as starting materials. 2-methoxyethanol was used as a solvent (Aldrich Chemical, Milwaukee, WI) and formamide as a drying control chemical additive. PMN–PT solutions were synthesized with a 70:30 ratio (on the rhombohedral side of the morphotropic phase boundary) using a modification of the route described elsewhere.[8,14]

Stable polymeric methoxyethoxide complex precursors were synthesized through distillation and refluxing of the starting materials in 2-methoxyethanol under a dry N_2 atmosphere. A flow chart for the chemical solution processing of PMN–PT precursors is presented in Fig. 1. To compensate for lead loss during rapid thermal annealing, 15 mol % excess lead was added to the precursor solution. 0.5 M solutions were synthesized and then spin coated at 2500 rpm for 30 s on Pt(111)-coated {100} silicon substrates 1500 Å Pt/200 Å Ti/1 μm SiO_2/Si. Following pyrolysis at 360 °C

a)Author to whom correspondence should be addressed; electronic mail: stmckinstry@psu.edu

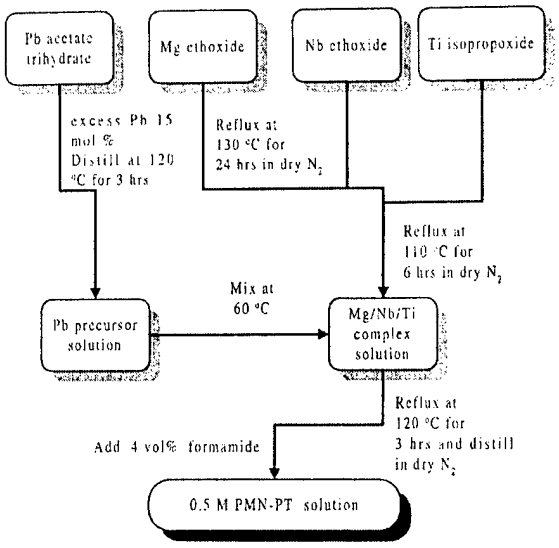

FIG. 1. Schematic diagram of PMN–PT (70/30) precursor solution by sol–gel processing.

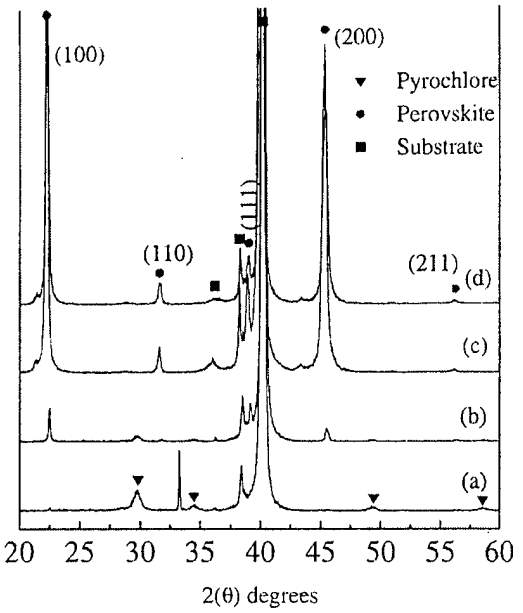

FIG. 2. XRD patterns of sol–gel derived PMN–PT films without a perovskite seed layer as a function of temperature: (a) 650 °C, (b) 700 °C, (c) 750 °C, and (d) 800 °C.

for 3 min, additional layers were spin coated to build up the desired thickness. Films were crystallized by rapid thermal annealing (Heatpulse 610, A.G. Associates, San Jose, CA) at 650–800 °C for 60 s. Individual crystallization steps were conducted for thicker films after every fourth coating to minimize cracking of the resulting film. The final film thicknesses were about 1.2–1.5 μm thick. In some cases, a very thin PT layer (~30 nm) was deposited and heat treated at 550 °C for 30 s, prior to deposition of PMN–PT films.

The structure and crystallinity of the films were characterized by x-ray diffraction (XRD) (Rigaku Co., Tokyo, Japan, Cu $K\alpha$ radiation, 40 kV, 50 mA). A second diffractometer (Philips, Eindhoven, Netherlands) was employed for θ–2θ scans and pole figures. The film morphology was observed by scanning electron microscopy (SEM) (Hitachi, S4200, Japan). Electrical measurements were made through the film thickness using Pt top electrodes 1.6 mm in a diameter prepared by sputtering through a shadow mask. Electrical contact was made to the bottom electrode with a probe wire, whereas the top contact was made with a microprobe tip. Low field dielectric properties were determined by an impedance analyzer (Model 4184A, Hewlett-Packard, Palo Alto, CA) with an oscillation of 30 mV and frequencies of 0.1–10 kHz as a function of temperature (−50–180 °C). High and low temperature measurements were made using a laboratory oven with both refrigerating and heating capabilities. High field hysteresis properties were characterized using a RT66A (Radiant Technology, Albuquerque, NM) ferroelectric test system. The coercive field of the film was measured and used to calculate the poling field to be applied for the subsequent piezoelectric characterization. The d_{31} coefficients of the thin films were characterized using a modification of wafer flexure method described previously.[15] For this investigation, all samples were poled with the top electrode negative at room temperature with various electric fields. The poling time used for the experiments was taken to be 5 min. In this method, a piece of a PMN–PT coated wafer was glued to a 3 in. Si(100) substrate. This substrate was suspended over the cavity, and the pressure inside the cavity was changed periodically, yielding a biaxial stress in the film. The microstrain generated at the film surface was calibrated using a strain gauge attached to bare Si single crystal substrate combined with a lock-in amplifier (model 7260 EG&G Instrument) and a strain indicator (model 3800, Vishay measurements, Raleigh, NC). The aging of the d_{31} coefficients was measured 0.5–3000 min after the poling field was removed.

d_{33} coefficients were also measured using the pneumatic pressure method. For this experiment the back of the wafer was polished using diamond paste (0.5–1 μm), and the sample (3 cm×3 cm) was then inserted between two cavities, using lubricated O-rings as pressure seals. High-pressure gas was introduced into the cavities, and the net amount of charge fluctuation was measured after releasing the pressure. The detailed experimental procedure for measurement of d_{33} was described elsewhere.[16]

RESULTS AND DISCUSSION

Figure 2 shows the XRD patterns for PMN–PT films with various annealing temperatures. All peak indexing for the perovskite films is done on the basis of the pseudocubic unit cell. The pyrochlore phase was dominant when the annealing temperature was lower than 700 °C, as shown by the strong pyrochlore (222) peak in Fig. 2(a). Above 700 °C, highly {100}-oriented PMN–PT films (f_{100}~92%) on Pt(111)-coated Si substrate were obtained with increasing crystallization temperature. These {100}-oriented films were nearly phase-pure perovskite within XRD detection limits.

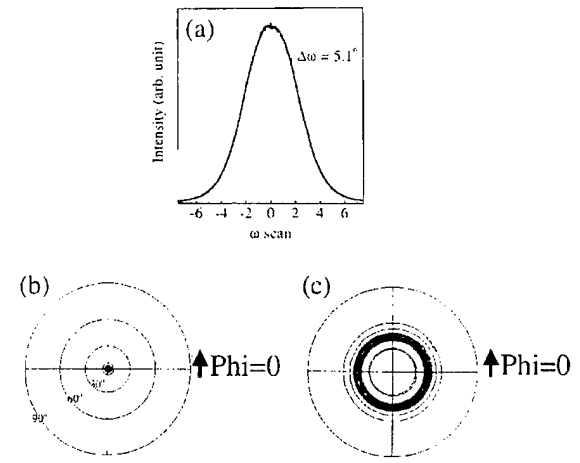

FIG. 3. (a) (200) plane rocking curve of the {100} oriented PMN–PT film, (b) (100) pole figure of the {100}-oriented PMN–PT film, and (c) (110) pole figure of the {100}-oriented PMN–PT film.

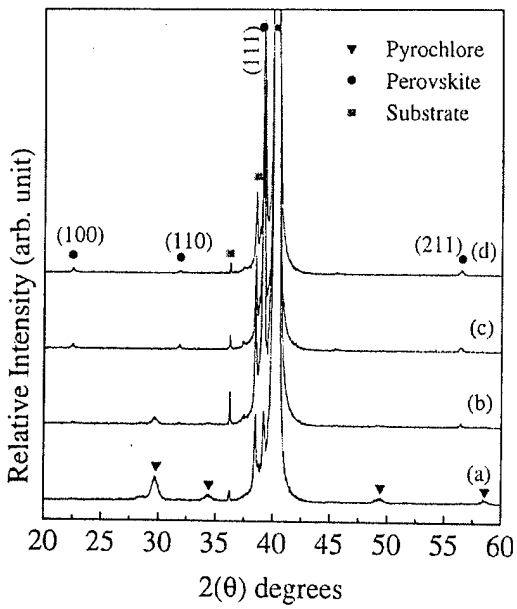

FIG. 4. XRD patterns of sol–gel derived PMN–PT films with a perovskite seed layer as a function of temperature: (a) 650 °C, (b) 700 °C, (c) 750 °C, and (d) 800 °C.

XRD ω scans of the (200) plane were collected for a {100}-oriented PMN–PT film crystallized at 750 °C on a Pt(111) substrate to examine the crystallinity and degree of film orientation. Next, to investigate the in-plane alignment of the oriented films prepared on Pt(111) substrates, (100) and (110) pole figure analyses were performed as shown in Fig. 3. Figure 3(a) shows the rocking curve for the {100} oriented film measured at $2\theta = 45.35°$. The rocking curve width (FWHM) of the film heat treated at 750 °C is about 5.1° and shows relatively good alignment (grain orientation) perpendicular to the substrate surface. Figures 3(b) and 3(c) show the pole figures obtained at $2\theta = 22.15°$ and 31.48° (100 and 110 peaks) for the PMN–PT film. From the (100) and (110) pole figures, it can be shown that the 100 peak is within 5° of the surface normal, and the 110 peak was found 45° away, corresponding to the calculated values. The circular pole contours indicated that the PMN–PT film grew with ⟨100⟩ perpendicular to the substrate surface but with random orientation in the plane. From the above observations, it can be seen that the PMN–PT films are fiber textured on Pt(111)-passivated substrates.

For perovskite PMN–PT deposition by sol–gel, a high nucleation energy barrier must be overcome by relatively higher annealing temperatures than are used for PT or PZT deposition.[17] This high nucleation energy barrier can be reduced by the use of a template layer with a good match in lattice and structure. Ishikawa *et al.*[18] have reported that the use of a PT seeding layer reduces the nucleation temperature of perovskite PZT films and changes their texture development. Furthermore, Cattan *et al.*[19] have shown that for PZT films grown on PT films with a thickness above 200 Å, the PT buffer layer promoted (111) PZT orientation. Therefore, the ready formation of perovskite PT and the tendency toward development of {111} texture on Pt(111) coated substrate should both decrease the nucleation barrier for PMN–PT perovskite formation and allow development of alternative film orientations.

Figure 4 shows XRD patterns of PMN–PT films on Pt(111)-coated substrates with a PT buffer layer. The very thin PT buffer layer (~30 nm) was heat treated at 550 °C for 30 s by rapid thermal annealing before deposition of the PMN–PT film.

As shown in Fig. 4(a), the perovskite 111 peak was detected even at a crystallization temperature of 650 °C for PMN–PT films with a perovskite buffer layer. This is lower than the temperature required for PMN–PT films without a perovskite buffer layer [Fig. 2(a)]. Other research groups have also reported the benefit of a perovskite PT interlayer in promoting the perovskite phase.[8,18,20]

The perovskite peak intensity corresponding to {111} perovskite was found to increase with increasing annealing temperature. Above 750 °C, highly {111}-oriented PMN–PT films ($f_{111} \sim 95\%$) were phase-pure perovskite within XRD detection limits. The resulting {111} PMN–PT texture may be due to a strongly textured PT thin film. The {111} texture of the PT thin film on (111) Pt substrates may be attributed to the small lattice mismatch between PT ($a = 3.961$ Å) and Pt ($a = 3.923$ Å).

Figure 5 shows SEM photographs of {100}-oriented and {111}-oriented PMN–PT films. The cross sectional view of the film in Fig. 5 shows that the thickness was about 1.2 μm. The {100} film consisted of small and large grains, with a grain size distribution of 150–500 nm. On the other hand, the {111}-oriented films, with an average grain size of ~50 nm, showed much smaller and more uniform grains than {100}-oriented films. There may be a difference in the nucleation density for the two processing routes. The grain size distributions of the {100}- and {111}-oriented films did not change significantly with film thickness. A similar observation between the orientation and grain size distribution has

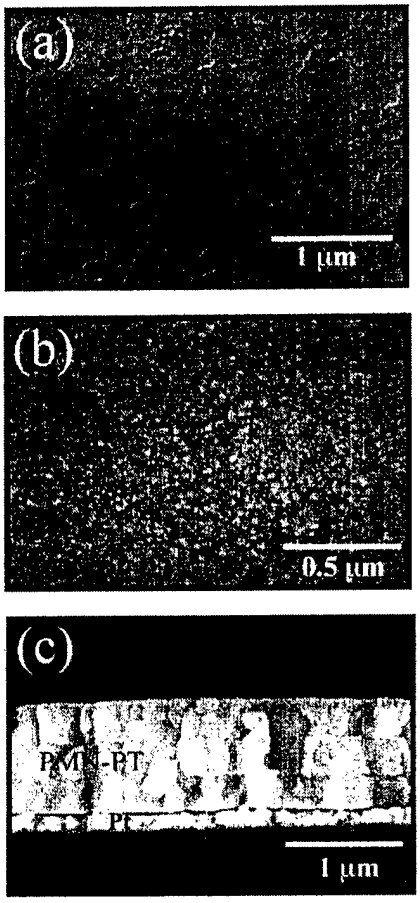

FIG. 5. SEM photographs of {100}- and {111}-oriented PMN–PT films: (a) {100} oriented PMN–PT film, (b) {111}-oriented PMN–PT film, and (c) cross-sectional view of the films.

also been reported in sol–gel derived PZT and PMN–PT (50/50) films.[7,8]

Figure 6 shows the temperature dependence of the dielectric constant for the 1.2 μm thick {100}- and {111}-oriented PMN–PT films as a function of frequency. The dielectric constants of {100}-oriented and {111}-oriented films were ~2500 and ~2000 at 1 kHz and room temperature, respectively. The dielectric constants for {100}-oriented films were, in general, higher than those of {111}-oriented films. This was consistent for many independent measurements of the temperature dependent dielectric behaviors of the films. In terms of the loss values of differently oriented PMN–PT films, the temperature dependence was quite similar for both film orientations. No noticeable trends in tan δ values with different orientation of the films were found in this present study.

As shown in Fig. 6, the curves at different frequency show broad maxima, with a T_{max} of ~115 °C. These films show the dispersive dielectric data characteristic of relaxor ferroelectrics below T_{max}. This is more dispersion that is seen in bulk crystals of the same composition, but is consistent with other data on PMN–PT (70/30) films. The transition temperature is somewhat lower than that of bulk ceramics of equivalent composition (140 °C).[21]

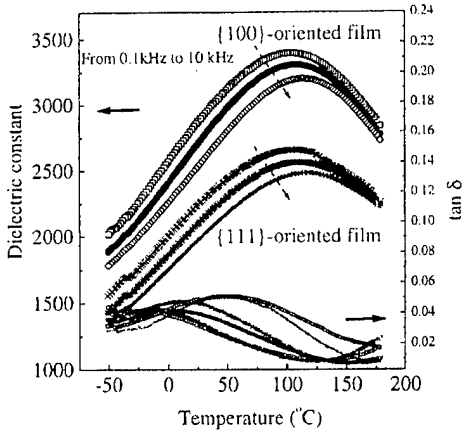

FIG. 6. The temperature dependences of the dielectric constants and tan δ for {100}- and {111}-oriented PMN–PT films.

Figure 7 shows the polarization reversal for PMN–PT films with different orientations. As shown in Fig. 7, {100}-oriented films showed lower remanent polarizations than {111}-oriented films. The values of maximum polarization P_{max} and remanent polarization P_r of the {111}-oriented film were ~41 and ~11.7 μC/cm^2 at 200 kV/cm, respectively. The values of P_{max} and P_r of the {100}-oriented film were ~36 and ~10 μC/cm^2 at the same applied field, respectively. Regardless of the preferred orientation of these films on Si, the remanent polarization values of these films on the same composition were lower compared to those of epitaxial PMN–PT films of the same composition on $LaAlO_3$ substrates prepared by pulsed laser deposition.[22] This might be due, in part, to the tensile stress developed in the film due to the thermal expansion mismatch with the Si substrate during cooling.[23,24]

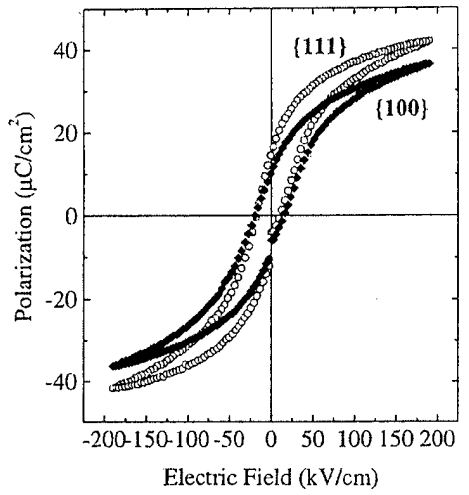

FIG. 7. Comparison of high-field hysteresis properties for the {100}- and {111}-oriented PMN–PT films.

Several methods to characterize the piezoelectric properties of thin films have been reported including double beam laser interferometry[25] and charge-based techniques.[26] Among them, Xu *et al.*[16] and Shepard *et al.*[15] have described measurement of thin film piezoelectric properties by the pneumatic pressure method and the wafer flexure technique as previously reported. Both methods measure the effective piezoelectric response of thin films on their substrates. The effective piezoelectric coefficient d_{33} of a piezoelectric film measured by the pneumatic pressure method[16] is determined by introducing high pressure gas to cavities on either side of a film-coated wafer in other to generate a uniaxial stress, and the resulting charge is collected.

d_{33} is then calculated from

$$d_{33}=\frac{Q}{\Delta PA}, \tag{1.1}$$

where Q is the pressure-induced charge collected by the charge integrator, ΔP is the pressure change inside the cavity, and A is the area of the top electrode.

In contrast, the wafer flexure method entails suspending a film-coated wafer over a cavity and oscillating the cavity pressure to flex the wafer. The effective piezoelectric coefficient d_{31} of the films can be determined by the stress–strain relationship using plate theory.[27] The in-plane stress (σ_1) of the film at the center point generated by the oscillating pressure (5 Hz) in the cavity is

$$\sigma_1=\frac{E\varepsilon}{1-\nu}. \tag{2.1}$$

Assuming that the biaxial stress σ_{tot} is the same in two perpendicular directions on the sample surface

$$\sigma_{tot}=\sigma_1+\sigma_2, \tag{2.2}$$

where E is the Young's modulus of the film, ν is Poisson's ratio of the sample ($\nu\sim 1/3$), and ε is the in-plane strain in the sample mounted on the stress rig measured with a strain gauge. The strain gauge was attached to the center of the sample surface using superglue.

d_{31} is thus given by

$$d_{31}=\frac{Q}{2\sigma_1 A}. \tag{2.3}$$

As shown in Eqs. (2.1)–(2.3), this measurement technique requires information about the film elastic modulus. If this information is known, d_{31} values of the films can be measured quickly, even using a small piece of the sample.

The d_{33} coefficients of 1.5 μm thick {100}- and {111}-oriented films were characterized by the pneumatic pressure method.[16] Both films were poled at 85 kV/cm for 30 min and the generated charges were measured using a 10^{-8} F integrating capacitor. For the {100}- and {111}-oriented PMN–PT films, the values of d_{33} measured were 170–183 and 90–100 pC/N, respectively. This measurement technique does not require knowledge of the film or substrate elastic modulus as shown in Eq. (1.1). For the same films poled under the same conditions, the values of d_{31} of the {100}- and {111}-oriented PMN–PT films were −95–−100 and −55–−60 pC/N, respectively. These values were calculated assuming a Young's modulus for the films of 35 GPa, the number reported by Park and Shrout[28] for the same composition of single crystalline PMN–PT (70/30) oriented along ⟨001⟩.

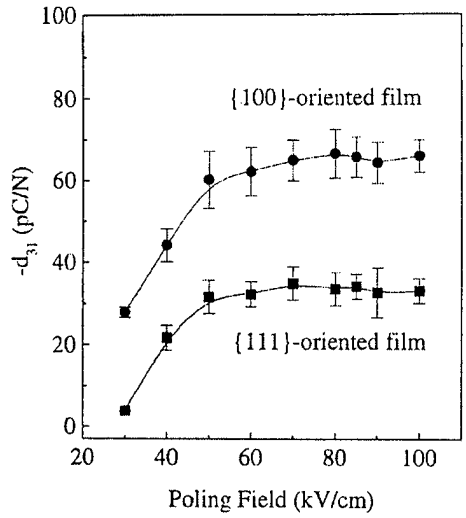

FIG. 8. Poling curves for the {100}- and {111}-oriented PMN–PT films with various poling fields for 5 min.

In general, in many perovskite ferroelectrics, including piezoelectric PMN-PT ceramics and $0.955Pb(Zn_{1/3}Nb_{2/3})O_3$–$0.045PbTiO_3$ single crystals, $d_{31}\sim -0.43d_{33}$.[29–31] There are some literature sources which give different d_{33}/d_{31} ratios for PMN–PT, particularly when samples prepared by different groups or poled under different conditions are compared.[32] However, for a given sample, this ratio is a good approximation. This is supported by the observation of low hydrostatic d coefficients $d_h=d_{33}+2d_{31}$ for PMN–PT ceramics near the morphotropic phase boundary[29] (similar low values are observed in ⟨001⟩ piezoelectric single crystals of lead zinc niobate–lead titanate).[33] That is, for a single sample, d_{33} is close to $-2d_{31}$. Thus, the available data for a ⟨001⟩ oriented single crystal relaxor ferroelectric-$PbTiO_3$ solid solution was taken as a first approximation (i.e., $d_{31}\sim -0.43d_{33}$). Assuming that this value is appropriate for thin films, the actual d_{31} values of the {100} and {111}-oriented PMN–PT films should be −73 to −78 and −39 to −43 pC/N, respectively. This suggests that the appropriate Young's moduli to use in the d_{31} calculations are ~44 and ~49 GPa for {100} and {111} films. That is, for polycrystalline PMN–PT films, it may be appropriate to use a Young's modulus of 45 GPa to calculate d_{31} values by the wafer flexure technique.

The d_{31} coefficients of 1.2 μm thick {100}- and {111}-oriented films by the wafer flexure technique were characterized as a function of poling field. Figure 8 show the poling curves for the PMN–PT films. These values were calculated assuming a Young's modulus for the {100}- and {111}-oriented films of 44 and 49 GPa, respectively, which were the values experimentally determined by analyzing the d_{33} and d_{31} values obtained using the pneumatic pressure and wafer flexure technique, as mentioned above.

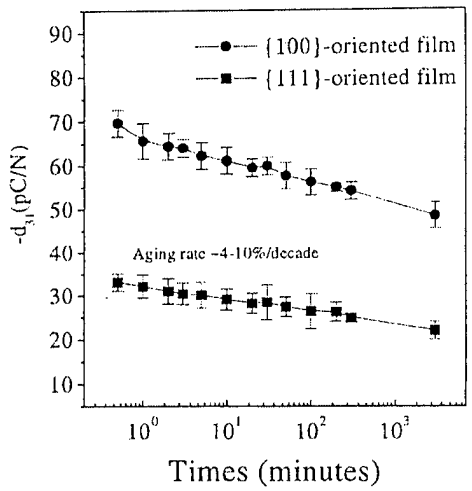

FIG. 9. Aging curves for {100}- and {111}-oriented PMN–PT films.

The measured phase angle θ corresponds to the phase of the piezoelectric response (charge or current) with respect to the pressure oscillation. The poling direction is therefore differentiated by the measurement phase angle. In the case of {100}-oriented samples, the direction of the preferred orientation is from the film/substrate interface to the surface. Therefore, d_{31} was characterized after poling with the top electrode negative. As shown in Fig. 8, the piezoelectric coefficient of the films increases in a logarithmic fashion with poling field. For all films tested here the piezoelectric coefficients were largely saturated after poling at 60–80 kV/cm. For a {100}-oriented film 1.2 μm thick, a larger piezoelectric coefficient ($-d_{31}=\sim 69$ pC/N) was obtained relative to those of {111}-oriented films ($-d_{31}=\sim 35$ pC/N) at a poling field of 85 kV/cm for 5 min. Since the typical d_{31} value of a 1 μm thick PZT (52/48) film was around -40 pC/N, even the lower PMN–PT is still comparable to that for sol–gel PZT films of the same thickness.[15] This result also supports that the idea of crystallographic engineering is applicable to thin films as well as bulk crystals. That is, the differences in properties between {100} and {111} fiber textured samples suggest that the high piezoelectric coefficients reported here are not due simply to the lower T_{max} of PMN–PT relative to PZT.

The film thickness also affected the dielectric and piezoelectric properties of the PMN–PT films. Thicker layers had larger remanent polarizations and lower coercive fields. In addition, the piezoelectric coefficients of {100}-oriented film increased more rapidly with thickness compared to those of {111}-oriented films.

Figure 9 shows the different aging behavior of {100}- and {111}-oriented films. There were no significant discrepancies in aging rate between {100}- and {111}-oriented films. The aging rate of the {100}-and {111}-oriented films is about 4%–10% decade. However, the aging rate is considerable when compared to the nearly 0% reported for epitaxial {100} PMN–PT films on $LaAlO_3$ which had strongly imprinted hysteresis loops. It is believed that the aging rates observed here are due to progressive depoling of the films, as has previously been reported for PZT films.[34]

CONCLUSIONS

The crystalline characteristics and dielectric properties of {100} fiber textured PMN–PT films grown on Pt (111)-coated substrates by sol–gel are described. It was shown that the introduction of a perovskite PT thin film as a buffer layer assists the nucleation of {111} textured PMN–PT films. The dielectric constant for {100}-oriented films is, in general, higher than those of {111}-oriented films. However, {100}-oriented films showed lower remanent polarizations in comparison with {111}-oriented films. Both of these observations are consistent with a substantial in-plane tensile stress in the ferroelectric films. The d_{31} coefficients of highly {100}-oriented PMN–PT films were found to range from -28 to -69 pC/N with increasing poling field and saturated at fields of 60–80 kV/cm. The {100}-oriented PMN–PT films showed larger piezoelectric coefficients than {111}-oriented films. The aging rate of piezoelectric coefficients $-d_{31}$ for the {100}- and {111}-oriented PMN–PT films were about 4%–10%/decade. Based on the results of d_{33} measurements of the PMN–PT films with different orientation, Young's moduli of 44–49 GPa may be used to estimate plausible d_{31} values of PMN–PT (70/30) films.

ACKNOWLEDGMENTS

The authors gratefully acknowledge support from the Office of Naval Research for this work. The authors would like to thank Dr. Seung-Eek Park for his helpful discussion on the anisotropic properties of single crystals.

[1] J. F. Scott and C. A. Paz de Araujo, Science **246**, 1400 (1989).
[2] D. Dimos, S. J. Lockwood, and R. W. Schwartz, IEEE Trans. Compon. Packag. Manuf. Technol., Part A **A18**, 174 (1995).
[3] H. D. Chen, K. R. Udayakumar, C. J. Gaskey, and L. E. Cross, Appl. Phys. Lett. **67**, 3411 (1995).
[4] S. Watanabe and T. Fujii, Rev. Sci. Instrum. **67**, 3898 (1996).
[5] C.-R. Cho, L.-F. Francis, and M. Jang, Jpn. J. Appl. Phys., Part 2 **38**, L751 (1999).
[6] X.-H. Du, J. Zheng, U. Belegunda, and K. Uchino, Appl. Phys. Lett. **72**, 2421 (1998).
[7] K. Aoki, Y. Fukuda, K. Numata, and A. Nishimura, Jpn. J. Appl. Phys., Part 1 **33**, 5155 (1994).
[8] J. H. Park, D. H. Kang, and K. H. Yoon, J. Am. Ceram. Soc. **82**, 2116 (1999).
[9] F. Xu, Ph.D. thesis, The Pennsylvania State University, 1999.
[10] S. E. Park and T. R. Shrout, IEEE Trans. Ultrason. Ferroelectr. Freq. Control **44**, 140 (1997).
[11] S. E. Park and T. R. Shrout, J. Appl. Phys. **82**, 1804 (1997).
[12] S. Trolier-McKinstry, J. F. Shepard, J. L. Lacey, T. Su, G. Zavala, and J. Fender, Ferroelectrics **206–7**, 381 (1998).
[13] J.-P. Maria, Ph.D. thesis, The Pennsylvania State University, 1998.
[14] K. D. Budd, S. K. Dey, and D. A. Payne, Br. Ceram. Proc. **36**, 107 (1985).
[15] J. F. Shephard, Jr., F. Xu, I. Kanno, and S. Trolier-McKinstry, J. Appl. Phys. **85**, 6711 (1999).
[16] F. Xu, F. Chu, and S. Trolier-McKinstry, J. Appl. Phys. **86**, 588 (1999).
[17] Z. Huang, Q. Zhang, and R. W. Whatmore, J. Appl. Phys. **85**, 7355 (1999).
[18] K. Ishikawa, K. Sakura, D. Fu, and S. Yamada, Jpn. J. Appl. Phys., Part 1 **37**, 5128 (1998).
[19] E. Cattan, G. Velu, B. Jaber, D. Remiens, and B. Thierry, Appl. Phys. Lett. **70**, 1718 (1997).
[20] K. H. Yoon, J. H. Shin, J. H. Park, and D. H. Kang, J. Appl. Phys. **83**, 3626 (1998).

[21] T. R. Shrout, Z. P. Chang, N. Kim, and S. Markgraf, Ferroelectr. Lett. Sect. **12**, 63 (1990).
[22] J-P. Maria, W. Hackenberger, and S. Trolier-McKinstry, J. Appl. Phys. **84**, 5147 (1998).
[23] T. Kumazawa, Y. Kumagai, H. Miura, and M. Kitano, Appl. Phys. Lett. **72**, 608 (1998).
[24] J. F. Shepard, Jr., S. Trolier-McKinstry, and M. A. Hendrickson, The 10th International Symposium on Applications of Ferroelectrics, New Brunswick, NJ, 1996, pp. 161–165.
[25] Z. Kighelman, D. Damjanovic, A. Seifert, L. Sagalowicz, and N. Setter, Appl. Phys. Lett. **73**, 2281 (1999).
[26] I. Kanno, S. Fujii, T. Kamada, and R. Takayama, Appl. Phys. Lett. **70**, 1378 (1997).
[27] S. Timoshenko and S. Woinowsky-Krieger, *Theory of Plates and Shell* (McGraw-Hill, New York, 1959).
[28] S. E. Park and T. R. Shrout, U.S. Navy Workshop on Acoustic Transduction Materials and Devices, University Park, PA, 13–15 April 1999.
[29] Edo Electroceramics Piezoelectric Products catalog. Data for EC-98, http://www.edoceramic.com
[30] S.-F. Liu, S.-E. Park, T. R. Shrout, and L. E. Cross, J. Appl. Phys. **85**, 2810 (1999).
[31] B. Jaffe, W. R. Cook, Jr., and H. Jaffe, *Piezoelectric Crystals* (Academic, New York, 1971).
[32] Landolt-Bornstein III/18, *Elastic, Piezoelectric, and Related Constants of Crystals* (Springer, New York, 1984).
[33] S.-F. Liu, S.-E. Park, T. R. Shrout, and L. E. Cross, J. Appl. Phys. **85**, 2810 (1999).
[34] A. L. Kholkin, A. K. Tagantsev, E. L. Colla, D. V. Taylor, and N. Setter, Integr. Ferroelectr. **15**, 317 (1997).

Appendix 16

Takeshi Yoshimura and Susan Trolier-McKinstry, "Transverse piezoelectric properties of epitaxial $Pb(Yb_{1/2}Nb_{1/2})O_3$–$PbTiO_3$ (50/50) films," Journal of Crystal Growth **229**, 445–449 (2001).

ELSEVIER

Journal of Crystal Growth 229 (2001) 445–449

JOURNAL OF CRYSTAL GROWTH

www.elsevier.nl/locate/jcrysgro

Transverse piezoelectric properties of epitaxial $Pb(Yb_{1/2}Nb_{1/2})O_3$–$PbTiO_3$ (50/50) films

Takeshi Yoshimura*, Susan Trolier-McKinstry

Materials Research Laboratory, The Pennsylvania State University, University Park, PA 16802-4801, USA

Abstract

The transverse piezoelectric properties of $(1-x)Pb(Yb_{1/2}Nb_{1/2})O_3$–$xPbTiO_3$ (PYbN–PT, $x = 0.5$) epitaxial films grown on (0 0 1)$SrRuO_3$/(0 0 1)$LaAlO_3$ (indices given for the pseudocubic unit cell) were investigated by the wafer flexure technique. PYbN–PT films and $SrRuO_3$ bottom electrodes were deposited by pulsed laser deposition. At a deposition pressure of 400 mTorr, (0 0 1) PYbN–PT epitaxial films with high phase purity and good crystalline quality were obtained for a wide range of deposition rates (40–100 nm/min) and temperatures (620–660°C). The remanent polarization of the film was as high as 30 $\mu C/cm^2$. The e_{31} coefficient and the aging rate were strongly dependent on the poling direction. The maximum e_{31} coefficient was $-11.0\ C/m^2$. The minimum aging rate of the piezoelectric coefficients for the films was 2% per decade.

PACS: 77.84.Dy; 77.55.+f; 77.65.Bn; 81.15.Fg

Keywords: A3. Vapor phase epitaxy; B1. Perovskites; B1. Lead compounds; B2. Piezoelectric materials; B2. Relaxor ferroelectrics

1. Introduction

Single crystals of relaxor ferroelectrics—$PbTiO_3$ solid solutions such as $Pb(Mg_{1/3}Nb_{2/3})O_3$–$PbTiO_3$ (PMN–PT) and $Pb(Zn_{1/3}Nb_{2/3})O_3$–$PbTiO_3$ (PMN–PT) exhibit very large piezoelectric responses [1]. For micro-electromechanical systems (MEMS), the ferroelectric materials are required in thin film form and it is desirable to generate large strains or to sense small ones [2,3]. Although $Pb(Zr,Ti)O_3$ (PZT) films have been widely studied for piezoelectric applications, the piezoelectric properties for PZT films appear, for the most part, to be limited to those of hard PZT ceramics.

Therefore, epitaxial relaxor ferroelectric films are interesting for this area. Maria et al. [4] have reported a d_{31} coefficient of −180 pC/N in PMN–PT epitaxial films. This value is in excess of even the largest values reported for PZT films [5]. Bornand et al. [6–8] have reported growth and ferroelectric properties of $(1-x)Pb(Yb_{1/2}Nb_{1/2})O_3$–$xPbTiO_3$ (PYbN–PT) epitaxial films by pulsed laser deposition. Since PYbN–PT has the highest Curie point (~360°C) near the morphotropic phase boundary ($x \sim 0.5$) [9,10], MEMS devices with good temperature stability can be expected. However there are no reports about the piezoelectric properties of PYbN–PT films. In the present study, we have investigated the ferroelectric and piezoelectric properties of epitaxial PYbN–PT films. As the ⟨0 0 1⟩ orientation in

*Corresponding author. Tel.: +1-814-865-5361.
E-mail address: txy7@psu.edu (T. Yoshimura).

0022-0248/01/$ - see front matter
PII: S0022-0248(01)01200-3

rhombohedrally distorted perovskites has been shown to yield the highest piezoelectric coefficients [1], (0 0 1) epitaxial 0.5PYbN–0.5PT films were prepared and piezoelectric properties were investigated.

2. Experimental procedure

PYbN–PT epitaxial films and $SrRuO_3$ bottom electrodes were prepared by the pulsed laser deposition method. A KrF excimer laser (Lambda Physik Compex 102) with a 248 nm wavelength was used. (0 0 1) $LaAlO_3$ single crystal wafers were used as the substrates. In this paper, the Miller indices of all materials are given in terms of a pseudocubic unit cell. Substrates were fixed to a stainless steel block-style heater using silver paste and placed parallel and opposite to the rotating target. Oxygen and ozone gases were introduced to the deposition chamber using a commercial ozone generator (PCI).

$SrRuO_3$ bottom electrodes (300 nm thick) were deposited using stoichiometric $SrRuO_3$ ceramic targets (Target Materials Inc.). Details on the deposition are given elsewhere [6,7,11]. To deposit PYbN–PT films on $SrRuO_3/LaAlO_3$, sintered ceramics of PYbN–PT with the 50 : 50 composition, including 25 wt% excess PbO, were used as the targets. The excess PbO compensated lead loss in the films during growth. After deposition, the films were quickly cooled under an atmosphere of 200 Torr oxygen/ozone mixture. The specific deposition conditions of the $SrRuO_3$ bottom electrode and PYbN–PT films are given in Table 1.

The crystalline phases and orientation of the films were evaluated by the X-ray diffraction method. The $\theta-2\theta$ scans and ω scans were conducted by using a Scintag Pad V diffractometer. The ϕ scans for texture analyses were performed using an X'PERT Phillips four circle diffractometer. Cu-K_α radiation was used. Circular Pt top electrodes ($\phi = 0.1-0.6$ mm) were sputtered on the film surface through a shadow mask. The dielectric constant and dissipation factor were measured by an impedance analyzer (HP4192A). Polarization hysteresis measurements were made using a Radiant Technologies RT66A standard ferroelectrics tester.

Table 1
Deposition conditions for $SrRuO_3$ and PYbN–PT epitaxial films

	$SrRuO_3$	PYbN–PT
Temperature	730°C	620–660°C
Atmosphere	100% O_2	10% O_3–90% O_2
Pressure	200 m Torr	400 mTorr
Laser energy density	1.2 J/cm^2	1.5 J/cm^2
Laser frequency	10 Hz	2–5 Hz
Number of laser shots	15000	2700
Target	Stoichiometric	25% excess PbO
Target to substrate distance	8 cm	4.5 cm
Thickness	300 nm	900 nm

The effective $e_{31(\mathrm{eff})}$ coefficients of the films were characterized using a modification of the wafer flexure method described previously [12]. For this measurement, the PYbN–PT film was glued to a 3″ Si(1 0 0) substrate. This substrate was suspended over a cavity, and the pressure inside the cavity was changed periodically, yielding a biaxial stress in the film. The charge induced via the piezoelectric effect of the film was measured by a lock-in amplifier (Model 7260 EG&G Instrument). The strain generated at the film surface was calibrated using a strain gauge attached to the samples. An effective $e_{31(\mathrm{eff})}$ coefficient $e_{31(\mathrm{eff})} = \mathrm{charge/strain}$ was calculated form the resulting data. The aging of the $e_{31(\mathrm{eff})}$ coefficients was measured after the poling field was removed.

3. Results and discussion

A recent study reported that epitaxial PYbN–PT films were obtained at temperatures in the range of 560–660°C with deposition pressures of 300 mTorr [8,9]. In bulk processing, higher temperatures and oxygen pressures were needed to form the perovskite phase [2]. Therefore, a deposition pressure of 400 mTorr and temperatures of 660°C were utilized to obtain high quality PYbN–PT films. Fig. 1 shows XRD $\theta-2\theta$ patterns of PYbN–PT films deposited at laser frequency

range of 2–5 Hz. The growth rate was 3.3 Å/pulse. Although a small peak corresponding to pyrochlore was present at 34.7°, highly (0 0 1) oriented PYbN–PT films were obtained at each laser frequency. The quantity of pyrochlore phase, full width at half maximum (FWHM) of the $\theta-2\theta$ scan and rocking curve for PYbN–PT 002 are shown in Table 2. The quantity of pyrochlore phase was estimated by the ratio of the $\theta-2\theta$ diffraction peaks of the pyrochlore phase (34.7°) to PYbN–PT (0 0 2). The PYbN–PT film deposited at 3 Hz has the lowest quantity of pyrochlore phase. The measured FWHM is limited by the instrument resolution.

The in-plane orientation of PYbN–PT films was studied by ϕ scans of the PYbN–PT (3 0 3) peak (see Fig. 2). Four equally spaced peaks separated by 90° indicate the heteroepitaxy of the PYbN–PT films on the substrates. There was no indication of misoriented grains in the plane. Fig. 3 is a $\theta-2\theta$ pattern of PYbN–PT film deposited at 620°C and a laser frequency of 3 Hz. Although a small peak of PYbN–PT (1 1 0) was observed, the quantity of pyrochlore phase was less than the detection limits of X-ray diffraction. FWHM of $\theta-2\theta$ scan and

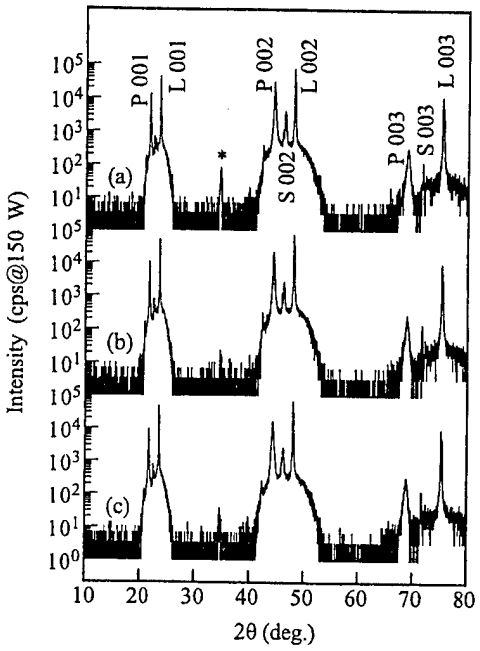

Fig. 1. $\theta-2\theta$ diffraction patterns of PYbN–PT films deposited at a substrate temperature of 660°C and laser frequencies of (a) 2 Hz, (b) 3 Hz, and (c) 5 Hz. P: perovskite PYbN–PT, S: $SrRuO_3$, L: $LaAlO_3$, and *: pyrochlore.

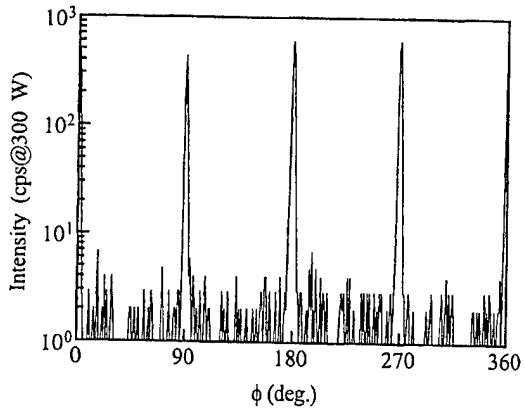

Fig. 2. ϕ scan of {1 0 1} for the PYbN–PT film deposited at a substrate temperature of 660°C and a laser frequency of 3 Hz.

Table 2
The effect of growth conditions on the quantity of pyrochlore and FWHM of $\theta-2\theta$ scan and ω scan of PYbN–PT (0 0 2)

Temperature (°C)	Laser frequency (Hz)	% Pyrochlore	$\Delta(2\theta)$	$\Delta\omega$
660	2	0.13	0.22°	0.51°
660	3	0.04	0.16°	0.53°
660	5	0.2	0.15°	0.51°
620	3	<0.02	0.17°	0.64°

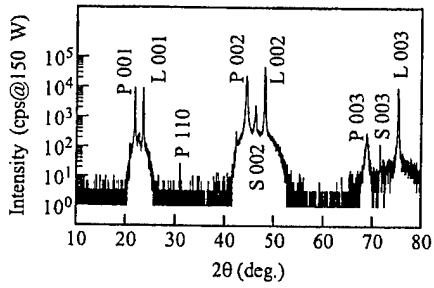

Fig. 3. $\theta-2\theta$ diffraction pattern of PYbN–PT film deposited at a substrate temperature of 620°C and a laser frequency of 3 Hz.

rocking curve of this film are also shown in Table 2. As compared to the growth conditions reported previously, PYbN–PT perovskite thin films with high phase purity were obtained for a wide range of deposition rates and temperatures at high deposition pressures (400 mTorr).

Fig. 4 shows the polarization hysteresis loops for PYbN–PT films deposited at a laser frequency of 3 Hz and substrate temperatures of 620°C and 660°C. The remanent polarization (Pr) of the 660°C-deposited film is higher than that of the 620 °C-deposited film. Although the saturation properties of the polarizations for both films were almost the same, the hysteresis loop of the 620°C-deposited film was tilted. The dielectric constant of PYbN–PT films deposited at 620°C and 660°C was 1000 and 750, respectively at a measurement frequency of 10 kHz. The dissipation factor of both films was about 5%.

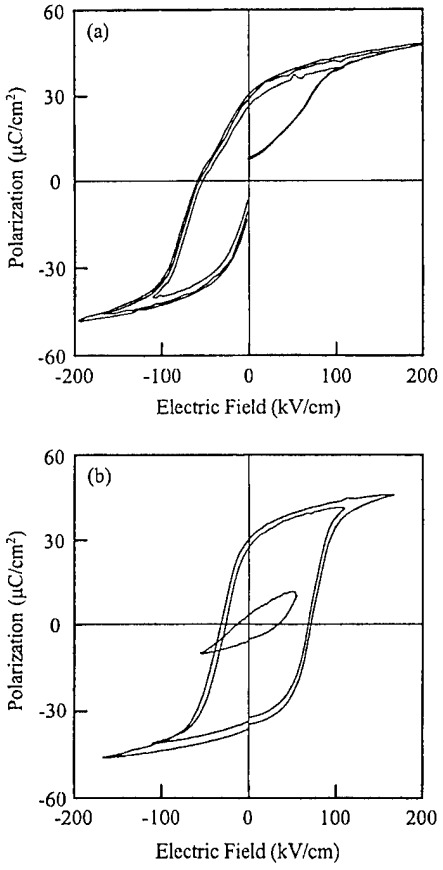

Fig. 4. Polarization hysteresis loops of PYbN–PT films deposited at (a) 620°C and (b) 660°C.

Prior to measurement of the piezoelectric coefficients, a DC voltage was applied to the top electrode of the films for poling. Fig. 5 shows the variation of the $e_{31(eff)}$ coefficients for the PYbN–PT film deposited at 660°C as a function of the poling voltage and time. The higher $e_{31(eff)}$ ($-11.0\,C/m^2$) was obtained by poling with the top electrode negative. This result is in agreement with the hysteresis loop shown in Fig. 4(b). The value was also higher than that reported for randomly oriented PZT films with the same thickness [13]. Fig. 6 shows the aging behaviors of the piezoelectric coefficients for the PYbN–PT film deposited at 660°C. The film was poled for 20 min with a field of $\pm$ 167 kV/cm. The aging behaviors also showed a strong asymmetry. Since the hysteresis loop for this film was shifted to 40 kV/cm along the field axis as shown in Fig. 4(b), the decrease in the $e_{31(eff)}$ for the positive poling was much higher than that for the negative poling. The aging rate was 2% per decade when poled with a negative voltage. The dependence of the aging rate on the imprint is comparable to that previously reported for sputtered PZT [14,15].

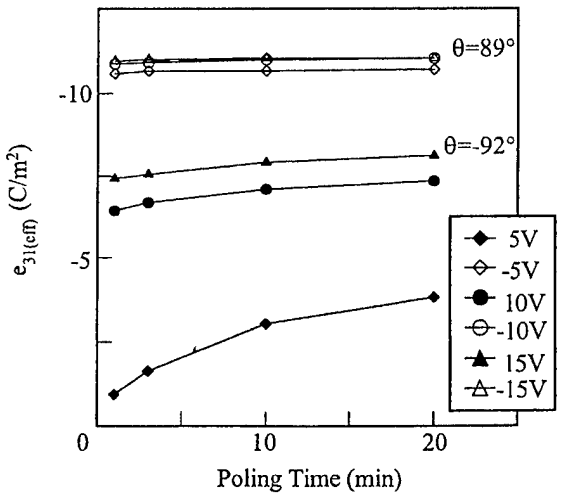

Fig. 5. The $e_{31(eff)}$ coefficients of 0.9 μm-thick PYbN–PT films deposited at 660°C as a function of the poling voltage and time. θ: phase angle of current with respect to applied stress.

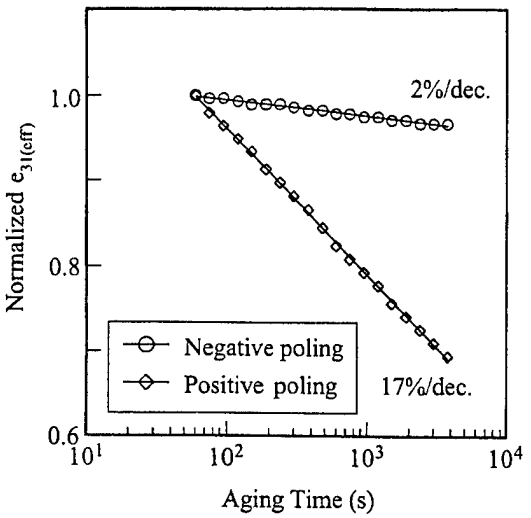

Fig. 6. Aging behavior of the piezoelectric coefficient of PYbN–PT films deposited at 660°C. The film was poled for 20 min with a field of ± 167 kV/cm.

4. Conclusions

$Pb(Yb_{1/2}Nb_{1/2})O_3$–$PbTiO_3$ (PYbN–PT) epitaxial films with 50 : 50 composition were fabricated on (0 0 1)$SrRuO_3$/(0 0 1)$LaAlO_3$ by the pulsed laser deposition. High quality PYbN–PT films were easily obtained at higher deposition pressures compared to the growth condition reported previously. The ferroelectric properties of the films depended on the growth conditions. PYbN–PT films deposited at higher temperatures have higher remanent polarizations ($\sim 30\,\mu C/cm^2$). The piezoelectric coefficient ($e_{31(eff)}$) was measured by the wafer flexure technique. To the authors' knowledge, this is the first report of the piezoelectric coefficients of PYbN–PT films. The $e_{31(eff)}$ coefficients and the aging rate were strongly dependent on the poling direction. This was explained by the shift of the polarization hysteresis loop (the internal electric field). The maximum $e_{31(eff)}$ coefficients were $-11.0\,C/m^2$. The minimum aging rate of the piezoelectric coefficients for the films was 2% per decade.

Acknowledgements

The authors are grateful to B. Jones and M. Angelone for their cooperation in the ceramic target synthesis and texture analyses, respectively. Support for this work was provided by the Office of Naval Research (US) under the Contract No. N00014-98-1-0527.

References

[1] S.E. Park, T.R. Shrout, J. Appl. Phys. 82 (1997) 1804.
[2] J.P. Maria, W. Hackenberger, S. Trolier-McKinstry, J. Appl. Phys. 84 (1998) 5147.
[3] P. Muralt, J. Micromech. Microeng. 10 (2000) 136.
[4] J.P. Maria, Ph.D. Thesis, The Pennsylvania State University, 1998.
[5] J. Kanno, S. Fujii, T. Kamada, R. Takayama, Appl. Phys. Lett. 70 (1997) 1378.
[6] V. Bornand, S. Trolier-McKinstry, Thin Solid Film 370 (2000) 70.
[7] V. Bornand, S. Trolier-McKinstry, J. Appl. Phys. 87 (2000) 3958.
[8] V. Bornand, S. Trolier-McKinstry, K. Takemura, C.A. Randall, J. Appl. Phys. 87 (2000) 3958.
[9] T. Yamamoto, S. Ohashi, Jpn. J. Appl. Phys. 34 (1995) 5349.
[10] H. Lim, H.J. Kim, W.K. Choo, Jpn. J. Appl. Phys. 34 (1995) 5449.
[11] J.P. Maria, S. Trolier-McKinstry, D.G. Schlom, M.E. Hawley, G.W. Brown, J. Appl. Phys. 83 (1998) 4373.
[12] J.F. Shepard Jr., P.J. Moses, S. Trolier-McKinstry, Sens. Actuators A 71 (1998) 133.
[13] P. Muralt, IEEE Trans Ultrasonics, Ferroelectrics, Frequency Control 47 (2000) 903.
[14] A. Kholkin, E. Colla, K. Brooks, P. Muralt, M. Kohli, T. Maeder, D. Taylor, N. Setter, Microelectron. Eng. 29 (1995) 261.
[15] J.F. Shepard Jr., F. Chu, I. Kanno, S. Trolier-McKinstry, J. Appl. Phys. 85 (1999) 6711.

Appendix 17

Koichi Takemura, Metin Ozgul, Veronique Bornand, Susan Trolier-McKinstry, and Clive A. Randall,"Fatigue Anisotropy in single crystal $Pb(Zn_{1/3}Nb_{2/3})O_3$–$PbTiO_3$," Journal of Applied Physics, 88[12] (December 2000).

Fatigue anisotropy in single crystal $Pb(Zn_{1/3}Nb_{2/3})O_3$–$PbTiO_3$

Koichi Takemura,[a] Metin Ozgul, Veronique Bornand, Susan Trolier-McKinstry, and Clive A. Randall[b]
Center for Dielectric Studies, Materials Research Laboratory, The Pennsylvania State University, University Park, Pennsylvania 16802-4800

(Received 22 February 2000; accepted for publication 3 August 2000)

Fatigue rates in the $Pb(Zn_{1/3}Nb_{2/3})O_3$–$PbTiO_3$ perovskite solid solution were investigated for different compositions in the rhombohedral and tetragonal phases in a variety of directions, at various field levels. It was found that the fatigue rates depend on both the ferroelectric phase and crystallographic orientation. In the rhombohedral phase when the field is applied along the $[001]_C$ direction (where the direction is given in terms of the cubic prototype), excellent fatigue resistance was obtained. © *2000 American Institute of Physics.* [S0021-8979(00)06321-0]

I. INTRODUCTION

Ferroelectric fatigue is the gradual decrease of switchable charge with polarization reversal under bipolar drive. Early studies of fatigue were mostly confined to single crystals, and fatigue was observed to be a general phenomenon in ferroelectrics. In general, freezing of the switchable polarization is believed to occur through the pinning of domain walls with point defects and space charge.[1–8]

In ferroelectric thin film studies, fatigue as well as imprint and retention are widely recognized as major problems to overcome with ferroelectric nonvolatile random access memories (FeRAMs). IN FeRAM devices, polarization reversal is utilized for read/write operations and the two remanent polarization states correspond to "0" or "1" in the binary memory. Ferroelectric fatigue makes it difficult to distinguish between the two states, and consequently limits the lifetime of the memories.[9–11]

There have been innovative advances to overcome the problem of fatigue in perovskite films, such as the utilization of top and bottom oxide electrodes, RuO_2,[12,13] IrO_2,[14] $SrRuO_3$,[15] and $(La,Sr)CoO_3$,[16,17] which have all been successfully tested. The mechanism responsible for the improved fatigue resistance with oxide electrodes is not fully elucidated; one possibility is that such electrodes can act as oxygen sources, and so help limit pinning of the domain walls associated with point defects. Alternative ferroelectrics have also been explored, such as $SrBi_2Ta_2O_9$ (SBT) and $SrBi_2Nb_2O_9$ (SBN).[18–20] These materials have the spontaneous polarization lying in the a-b plane of the orthorhombic unit cell. There are only four possible polarization states with SBT or SBN.[21] In the polycrystalline case, the remanent polarization is small, unless care is taken to control the crystallization orientation. The SBN family can be co-processed with Pt electrodes and retains good fatigue even in this case. There are, however, technological issues associated with the lower polarizations levels, the high crystallization temperatures, and Bi–Pt reactions.[22]

The objective of this study was to revisit fatigue in perovskite single crystals based on $Pb(Zn_{1/3}Nb_{2/3})O_3$–$PbTiO_3$, (PZN-PT) system. These material systems have recently become important owing to the excellent electromechanical performance obtained with engineered domain structures.[23,24]

II. EXPERIMENTAL PROCEDURE

PZN-PT crystals were grown by a high temperature flux technique.[25,26] The ferroelectric crystal compositions studied include 100% PZN(PZN), 95.5% PZN-4.5% PT(PZN-4.5 PT), 92% PZN-8% PT(PZN-8 PT), and 88% PZN-12% PT(PZN-12 PT). At room temperature, PZN and PZN-4.5 PT crystals are rhombohedral (pseudocubic), PZN-8 PT is near the morphotropic phase boundary (MPB) (still rhombohedral), and PZT-12 PT is tetragonal. For the sake of consistency, all of the orientations given throughout the remainder of the article will be given in terms of the prototype cubic perovskite axes. This will be denoted by the subscript C when orientations are given. All the crystals were oriented within $\pm 2°$ along the $[111]_C$ or $[001]_C$ axes by the back-reflection Laue method. Plate-shaped samples were obtained by cutting off the oriented crystals, which were then polished with 3 μm alumina powder to obtain flat and parallel surfaces. Pt 100 nm thick was sputtered as an electrode. The thickness of the samples ranged from 200 to 600 μm, and the electrode area ranged from 0.7 to 7 mm^2. The samples were annealed at 250 °C in air for 16 h in order to remove residual strain and defects that were introduced during crystal growth and polishing.

Polarization hysteresis loops were measured at room temperature using a modified Sawyer–Tower circuit. In particular, the electric field (E) was applied as a triangular bipolar wave form using a high voltage dc amplifier (Trek Model 609C-6 or Kepco Model BOM 1000M). The frequency of the alternating field was 10 Hz for polarization measurements as well as the switching in fatigue measurements. During measurement, the samples were immersed in Fluorinert to prevent arcing. The remanent polarization (P_r)

[a]Present address: ULSI Device Development Division, NEC Electron Devices, NEC Corporation, 1120 Shimokuzawa, Sagamihara 229-1198, Japan.
[b]Electronic mail: car4@psu.edu

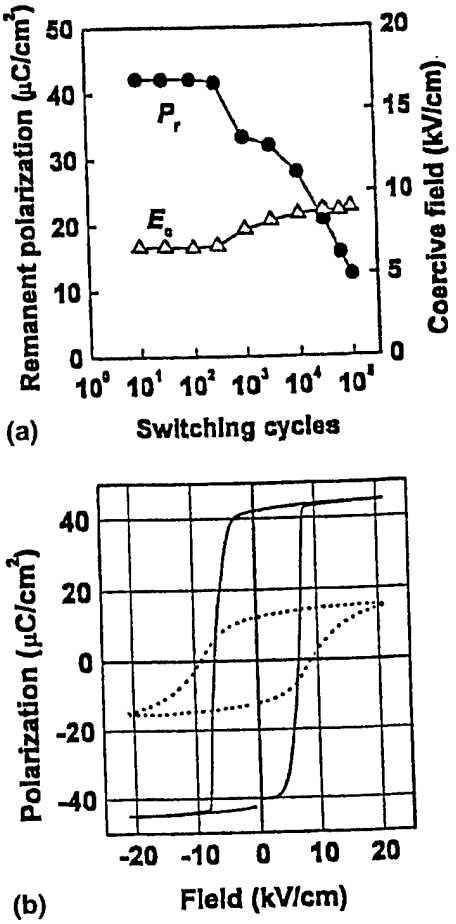

FIG. 1. Switching cycle dependence of (a) remanent polarization, P_r (solid circles), and coercive field, E_c (open triangles), (b) hysteresis loops for $[111]_C$-oriented PZN-4.5 PT single crystals. In Fig. 1(b), the solid line is the hysteresis loop after ten cycles, and the broken line is that after 1×10^5 cycles.

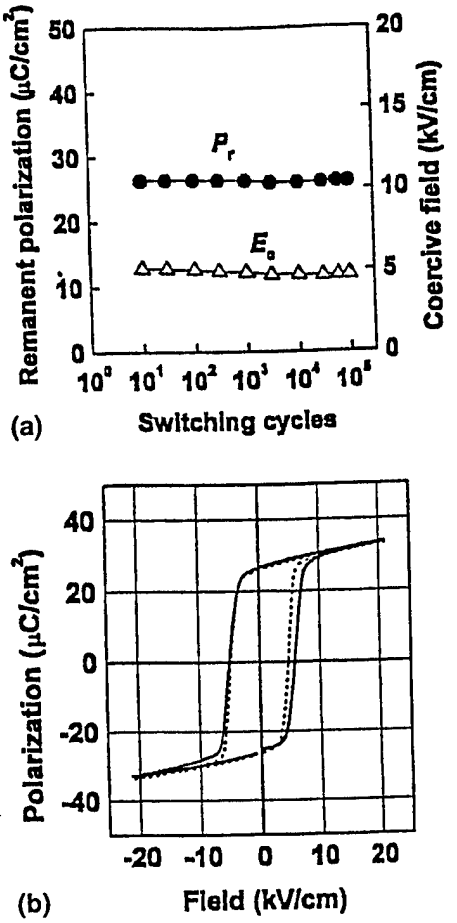

FIG. 2. Switching cycle dependence of (a) remanent polarization, P_r (solid circles), and coercive field, E_c (open triangles), (b) hysteresis loops for $[001]_C$-oriented PZN-4.5 PT single crystals. In Fig. 2(b), the solid line is the hysteresis loop after ten cycles, and the broken line is that after 1×10^5 cycles.

and the coercive fields (E_c) were computed from the hysteresis loops obtained. On a limited number of samples, the strain-field hysteresis loop was monitored with a linear variable differential transducer to ensure complete switching under the bipolar drive at each driving field frequency and amplitude.

III. RESULTS AND DISCUSSION

A. Composition and orientation dependence

Figures 1 and 2 show P_r, E_c, and hysteresis loops for $[111]_C$- and $[001]_C$-oriented PZN-4.5 PT crystals as a function of the number of switching cycles. The amplitude of the alternating triangular electric field (E_{max}) was 20 kV/cm, and the frequency of the field was 10 Hz. The initial P_r value for the $[111]_C$-oriented crystal ($P_{r,[001]}$) is approximately equal to $1/\sqrt{3}$ of $P_{r,[111]}$. In $[111]_C$-oriented crystals, the remanent polarization during cycling is along $[111]_C$ for $\mathbf{E}\|[111]$, or $[\bar{1}\bar{1}\bar{1}]_C$ for $\mathbf{E}\|[\bar{1}\bar{1}\bar{1}]$. Thus, the domains switch between $[111]$ and $[\bar{1}\bar{1}\bar{1}]$ states. In $[001]_C$-oriented crystals, the spontaneous polarization lies along one of four possible polar directions, for example, $[111]_C$, $[\bar{1}11]_C$, $[1\bar{1}1]_C$, or $[\bar{1}\bar{1}1]_C$ for $\mathbf{E}\|[001]$. With a reverse electric field, then these domains switch to $[\bar{1}\bar{1}\bar{1}]_C$, $[1\bar{1}\bar{1}]_C$, $[\bar{1}1\bar{1}]_C$, or $[11\bar{1}]_C$, and this can be done via 180°, 71°, or 109° switching processes, assuming rhombohedral symmetry.

As shown in Fig. 1, the P_r values for $[111]_C$-oriented crystals are almost constant up to 10^3 cycles and then decrease rapidly with further switching cycles. The $[111]_C$-oriented crystals obviously fatigue. The E_c values increase after the onset of fatigue. In contrast, the P_r and E_c values for $[001]_C$-oriented crystals are almost constant up to 10^5 switching cycles as shown in Fig. 2(a). The shape of the hysteresis loop does not change even after 10^5 cycles as shown in Fig. 2(b). The E_c value slightly decreases with switching cycles. As will be discussed below, this decrease in E_c as a function of cycling was observed for $[001]_C$-oriented crystals measured with a wide variation in field amplitudes. We infer that some domain walls are weakly pinned in the initial state, causing some resistance to switching, but during cycling these domain walls are detached from the original pinning sites. Possible origins for the pinning include impurities, oxygen or lead vacancies, or damage produced during crystal growth, polishing, or electroding.

The same orientation dependence of fatigue is also observed in pure PZN single crystals, as shown in Figs. 3 and

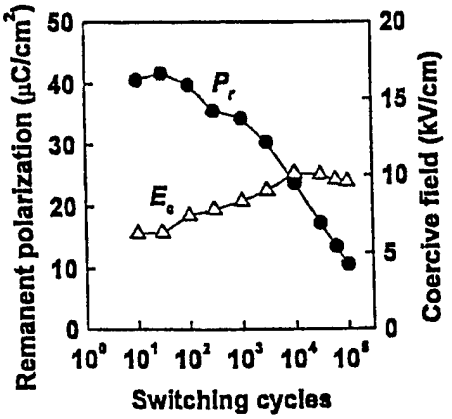

FIG. 3. Switching cycle dependence of P_r (solid circles) and E_c (open triangles) for $[111]_C$-oriented PZN single crystals.

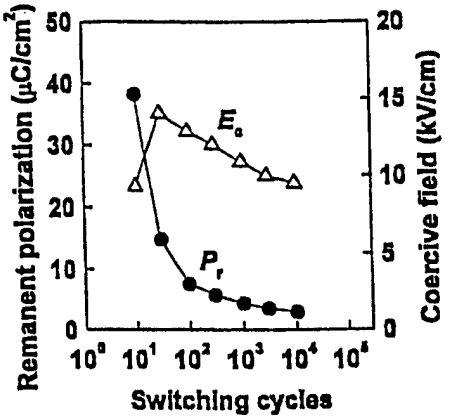

FIG. 5. Swithcing cycle dependence of P_r (solid circles) and E_c (open triangles) for $[001]_C$-oriented PZN-12 PT single crystals.

4. Fatigue in rhombohedral PZN(-PT) single crystals, therefore, is not dominated by the nature of the ferroelectricity, that is to say relaxor or normal behavior.[27,28]

Unlike the rhombohedral phase, fatigue is observed in $[001]_C$-oriented PZN-12 PT tetragonal crystals as shown in Fig. 5. In tetragonal PZN-12 PT, the polar direction is along $[001]_C$. Thus, domain switching involves polarization directions normal to the electrode-crystal interface, and presumably is accomplished predominantly through 180° domain wall motion. The origin of fatigue in tetragonal PZN-PT crystals is believed to be similar to that found in tetragonal $BaTiO_3$ single crystals.

The switching behavior of P_r and E_c in a $[001]_C$-oriented PZN-8 PT crystal (near the MPB composition) is shown in Fig. 6(a). Whereas the P_r values are almost constant up to 10^5 cycles, the hysteresis loop changes as shown in Fig. 6(b). There is some indication of the development of a pinning phenomenon, as is evidenced by the narrowing of the waist of the hysteresis loop.

The above results indicate again that the rate of fatigue is strongly dependent on both the ferroelectric phase and the crystal orientation in relaxor-PT single crystals. The $[001]_C$-oriented rhombohedral phase showed no notable fatigue up to 10^5 cycles for the slow alternating field required to switch the polarization in the crystal capacitors.

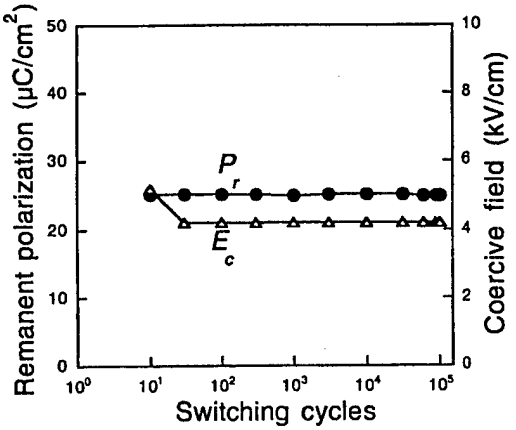

FIG. 4. Switching cycle dependence of P_r (solid circles) and E_c (open triangles) for $[001]_C$-oriented PZN single crystals.

B. Switching condition dependence of fatigue

In ferroelectric thin films, the magnitude of the applied fields can influence the fatigue rates.[29,30] Figure 7 shows that the $[111]_C$-oriented PZN-4.5 PT single crystals fatigue for a

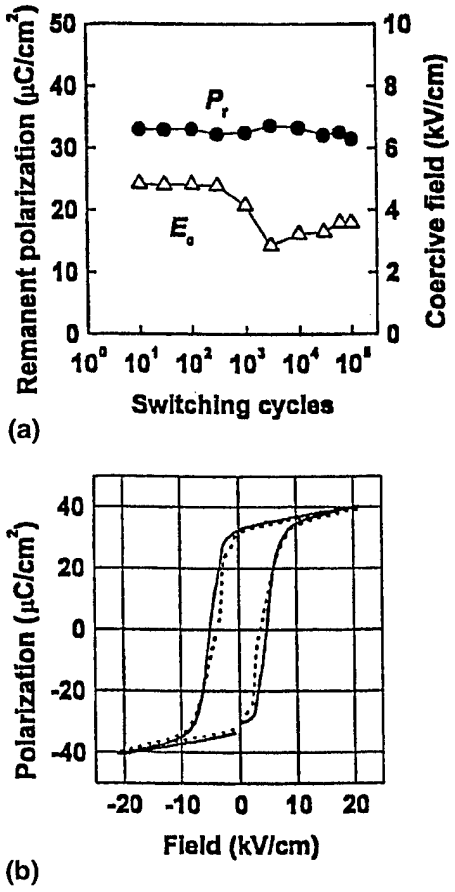

FIG. 6. Switching cycle dependence of (a) remanent polarization, P_r (solid circles), and coercive field, E_c (open triangles), (b) hysteresis loops for $[001]_C$-oriented PZN-8 PT single crystals. In Fig. 6(b), the solid line is the hysteresis loop after ten cycles, and the broken line is that after 1×10^5 cycles.

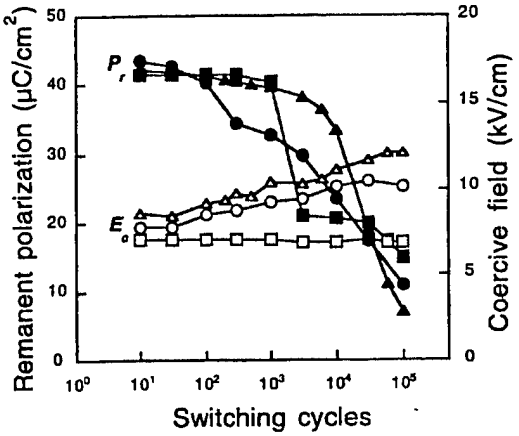

FIG. 7. Switching cycle dependence of P_r (solid symbols) and E_c (open symbols) for $[111]_C$-oriented PZN-4.5 PT single crystals under various switching field strengths (■,□; 10 kV/cm, ●,○; 20 kV/cm, ▲,△; 30 kV/cm). The switching frequency was 10 Hz.

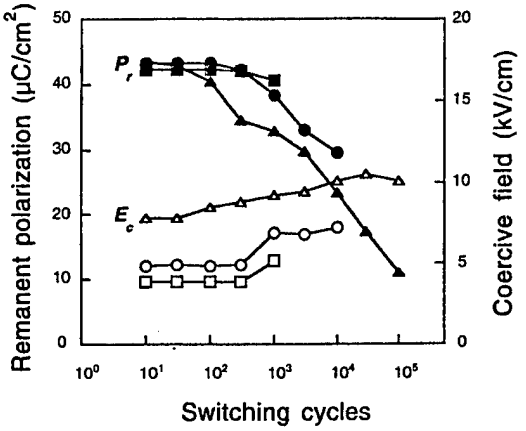

FIG. 9. Switching cycle dependence of P_r (solid symbols) and E_c (open symbols) for $[111]_C$-oriented PZN-4.5 PT single crystals measured at various switching frequencies (■,□; 0.1 Hz, ●,○; 1 Hz, ▲,△; 10 Hz). E_{max} was 20 kv/cm.

wider range of E_{max} values. $[001]_C$-oriented PZN-4.5 PT crystals, in contrast, do not fatigue under various E_{max} levels, as shown in Fig. 8. We therefore can infer that the crystal orientation, rather than E_{max}, governs the fatigue resistance for these PZN-PT crystals, provided the E_{max} does not induce ferroelectric phase transitions.[31] Figures 9 and 10 show the switching cycle dependence of P_r and E_c values for $[111]_C$- and $[001]_C$-oriented PZN-4.5 PT single crystals measured at various switching frequencies between 0.1 and 10 Hz. In the present study, fatigue lifetime does not depend on the switching frequency for $[111]_C$-oriented crystals.

It has been shown previously that large strain changes of 0.1% accompany polarization reversal in $[111]_C$-oriented crystals.[23] Strain sometimes results in microcracking, and microcracks have often been associated with fatigue in bulk ceramics.[32] Figure 11 shows that annealing improves the P_r value of a fatigued $[111]_C$-oriented PZN-4.5 PT crystal. When a fatigued crystal was annealed at 450 °C for 16 h in air, P_r increased to more than 80% of the initial P_r value. This result proves that the fatigue observed in the present study is recoverable, and rules out fatigue by microcracking. Therefore, fatigue in the $[111]_C$-oriented PZN-4.5 PT single crystals is believed to result from domain wall pinning via defects during polarization reversal, as has been reported in earlier single crystal studies.

C. Optimum orientation of crystals

Figure 12(a) shows the fatigue behavior for PZN-4.5 PT single crystals oriented along $[001]_C+\alpha$, where α is the degree of deviation from $[001]_C$ ($\alpha=0°$) toward $[111]_C$ ($\alpha=54.7°$), as shown in Fig. 12(b). The initial P_r and E_c values increase with α, and the initial P_r magnitude is consistent with projection of the $P_{r,[111]}$, i.e., $P_{r,[111]}\cos(54.7°-\alpha)$. The fatigue rate is enhanced when crystals are oriented with $\alpha \geq 15°$. The induction period before fatigue onset gradually decreases with increasing α. Fatigue in the rhombohedral PZN-PT single crystals is systematically dependent on crystallographic orientation, with $[001]_C$-oriented rhombohedral ferroelectric single crystals believed to have the lowest fatigue rate.

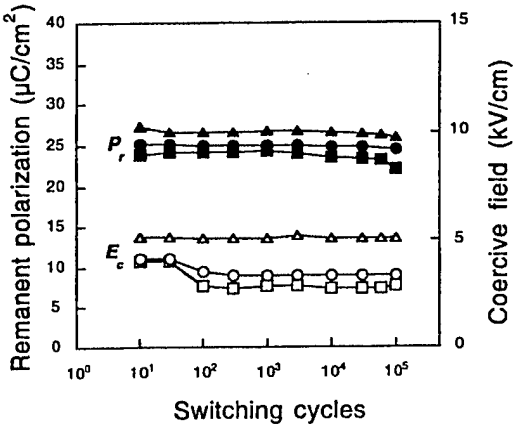

FIG. 8. Switching cycle dependence of P_r (solid symbols) and E_c (open symbols) for $[001]_C$-oriented PZN-4.5 PT single crystals under various switching field strengths (■,□; 5 kV/cm, ●,○; 10 kV/cm, ▲,△; 20 kV/cm). The switching frequency was 10 Hz.

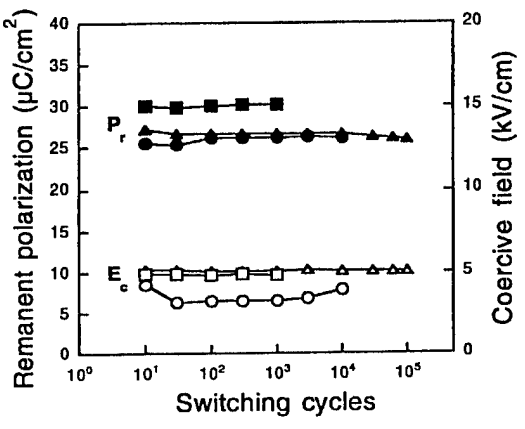

FIG. 10. Switching cycle dependence of P_r (solid symbols) and E_c (open symbols) for $[001]_C$-oriented PZN-4.5 PT single crystals measured at various switching frequencies (■,□; 0.1 Hz, ●,○; 1 Hz, ▲,△; 10 Hz). E_{max} was 20 kv/cm.

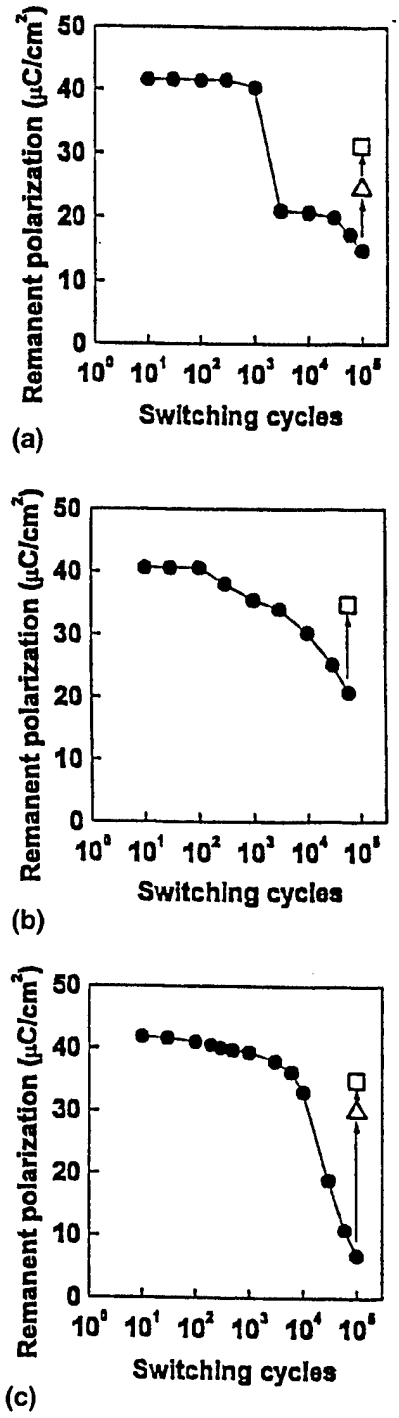

FIG. 11. Recovery of remanent polarization, P_r, for $[111]_C$-oriented PZN-4.5 PT single crystals fatigued under different E_{max} conditions; (a) 10 kV/cm, (b) 20 kV/cm, and (c) 30 kV/cm. After fatigue, the crystal was annealed at 250 °C (open triangle), and then 450 °C (open square) for 16 h in air.

D. Domain structure in field cycled PZN-PT crystals

Optical microscopy has shown in the $[111]_C$-oriented PZN-4.5 PT crystal the domain density increases with cycling and fatigue, whereas in the $[001]_C$-oriented PZN-4.5 PT crystal, the density of domain walls decreases. In the case of $[111]_C$-oriented crystals, it is anticipated that as domain walls are pinned by the fatigue process, new domains are activated from preexisting nuclei, initially enabling the maximum polarization to be reversed for each cycle. As cycling

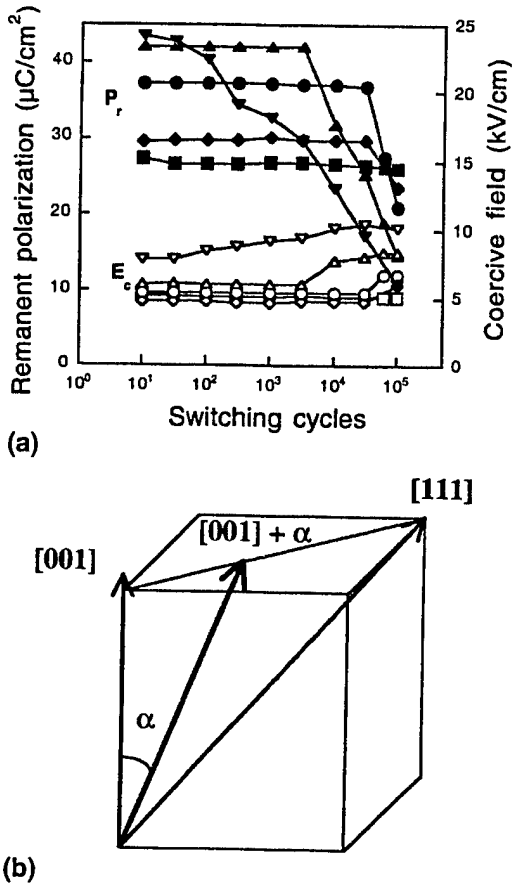

FIG. 12. (a) Effect of deviation from $[001]_C$ direction on fatigue for PZN-4.5 PT single crystals. (b) The deviation angle from $[001]_C$ toward $[111]_C$ (α) is defined. Solid markers show P_r, and open markers show E_c (■,□; $\alpha=0°$ [001], ◆,◇; $\alpha=15°$, ●,○; $\alpha=30°$, ▲,△; $\alpha=45°$, ▼,▽; $\alpha=54.7°$ [111]). The switching frequency was 10 Hz and E_{max}=20 kV/cm.

continues the process of pinning, activation of new domains, and then ultimately freezing, the result is a high density of frozen-in domain walls in fatigued crystals. Recently, in our group, switching analysis of $[111]_C$- and $[001]_C$-oriented PZN-PT crystals has shown that the mobility of domain walls in $[001]_C$ cuts is much higher.[33] This results in the ferroelectric being able to lower its total energy by systematically having the fastest domain walls control the switching and the domains can grow to define the largest volumes in the crystal and reduce the total domain wall density. This is consistent with observations made with optical microscopy, where only a few domains are observed in $[001]_C$-oriented crystals driven under bipolar fields to 10^3-10^5 cycles. Clearly more work needs to be conducted to establish the orientation and nature (i.e., charged or uncharged) of the residual domain walls in both fatigued and unfatigued crystals of both orientations. Higher resolution techniques that can verify the local domain structures will also be necessary, together with a determination of the switching mechanism.

IV. CONCLUSIONS

Fatigue in PZN-PT single crystals was studied at room temperature for a variety of crystallographic orientations, electric field strengths, frequencies, and compositions. It is

observed that the rhombohedral PZN-PT crystals oriented with the field along $[001]_C$ have no fatigue. At room temperature, $[111]_C$-oriented rhombohedral PZN-PT fatigues as does tetragonal PZN-PT in $[001]_C$ and $[111]_C$ directions. Close to the morphotropic phase boundary the presence of tetragonal phase will dominate and complicate the fatigue process; this will be addressed in a future paper.

The fatigue free nature of the rhombohedral phase in the $[001]_C$ orientation is suggested to be related to the engineered domain configuration, and to the observation that the $[001]_C$ direction has a high domain mobility. Following these studies, epitaxial ferroelectric thin films of $Pb(Yb_{1/2}Nb_{1/2})O_3$–$PtTiO_3$ have been fabricated and tested to verify fatigue at higher switching frequencies and thinner crystals. The results are consistent with the fundamental observations made here.[34]

ACKNOWLEDGMENTS

The authors would like to thank Professor T. R. Shrout and Dr. S.-E. Park for their helpful suggestions, and by S.-F. Liu and H. Lei for supplying single crystals. This work was partially supported by DARPA, Grant No. N00014-98-1-0527 and a grant-in-aid from NEC Corporation.

[1] E. Fatuzzo and W. J. Merz, *Ferroelectricity* (Wiley, New York, 1967).
[2] F. Jona and G. Shirane, *Ferroelectric Crystals* (Pergamon, Oxford, 1962) and (MacMillan, New York, 1962).
[3] D. S. Campbell, Philos. Mag. **79**, 1157 (1962).
[4] W. J. Merz and J. R. Anderson, Bell Lab. Rec. **33**, 335 (1955).
[5] R. Williams, J. Phys. Chem. Solids **26**, 399 (1965).
[6] J. R. Anderson, G. W. Brady, W. J. Merz, and J. P. Remeika, J. Appl. Phys. **26**, 1387 (1955).
[7] H. L. Stadler, J. Appl. Phys. **29**, 743 (1958).
[8] J. F. Scott and C. A. Pas de Araujo, Science **246**, 140 (1989).
[9] S. B. Desu, Phys. Status Solidi A **151**, 467 (1995).
[10] P. K. Larsen, G. J. M. Dormans, D. J. Taylor, and P. J. van Veldhoven, J. Appl. Phys. **76**, 2405 (1994).
[11] D. P. Vijay and S. B. Desu, J. Electrochem. Soc. **140**, 2640 (1993).
[12] T. Nakamura, Y. Nakao, A. Kamisawa, and H. Takasu, Jpn. J. Appl. Phys., Part 1 **33**, 5207 (1994).
[13] H. N. Al-Shareef, K. R. Bellur, A. I. Kingon, and O. Auciello, Appl. Phys. Lett. **66**, 239 (1995).
[14] T. Nakamura, Y. Nakano, A. Konisawa, and H. Takasu, Appl. Phys. Lett. **65**, 1552 (1994).
[15] J. T. Cheung, P. E. D. Morgan, and R. Neurgaonkar, Proceedings of the 4th International Symposium on Integrated Ferroelectrics, Colorado Springs, CO, 1992, p. 518.
[16] R. Ramesh, H. Gilchrist, T. Sands, V. G. Keranidas, R. Haakenaasen, and D. K. Fork, Appl. Phys. Lett. **63**, 3592 (1993).
[17] C. B. Eom, R. B. Van Dover, J. M. Phillips, D. J. Werder, J. H. Marshall, C. H. Chen, R. J. Cava, R. M. Fleming, and D. K. Fork, Appl. Phys. Lett. **63**, 2570 (1993).
[18] S. Aggarwal, I. G. Jenkins, B. Nagaraj, C. J. Kerr, C. Canedy, R. Ramesh, G. Valasquez, L. Boyer, and J. T. Evans, Jr., Appl. Phys. Lett. **75**, 1787 (1999).
[19] R. Dat, J. K. Lee, O. Auciella, and A. I. Kingon, Appl. Phys. Lett. **67**, 572 (1995).
[20] C. A. Paz de Araujo, J. K. Cuchiaro, L. D. McMillan, M. C. Scott, and J. F. Scott, Nature (London) **374**, 627 (1995).
[21] R. E. Newnham, R. W. Wolfe, R. S. Horsey, F. A. Diaz-Colon, and M. I. Kay, Mater. Res. Bull. **8**, 1183 (1973).
[22] J. F. Scott, Ferroelectrics **206-207**, 365 (1990).
[23] S.-E. Park and T. R. Shrout, J. Appl. Phys. **82**, 1804 (1997).
[24] T. Kobayashi, S. Saitoh, K. Harada, S. Shimanuki, and Y. Yamashita, Proceedings of the 1998 11th IEEE International Symposium on Applications of Ferroelectrics (ISAF-XI), August 24–27, 1998.
[25] M. L. Mulvihill, S.-E. Park, G. Rish, Z. Li, K. Uchino, and T. R. Shrout, Jpn. J. Appl. Phys., Part 1 **35**, 51 (1996).
[26] S.-E. Park, M. L. Mulvihill, G. Risch, and T. R. Shrout, Jpn. J. Appl. Phys., Part 1 **36**, 1154 (1997).
[27] L. E. Cross, Ferroelectrics **76**, 241 (1987).
[28] C. A. Randall and A. S. Bhalla, Jpn. J. Appl. Phys., Part 1 **29**, 327 (1990).
[29] X. Du and I. W. Chen, J. Appl. Phys. **83**, 7789 (1998).
[30] I. K. Yoo and B. Desu, Phys. Status Solidi **133**, 565 (1992).
[31] S.-F. Liu, S.-E. Park, T. R. Shrout, and L. E. Cross, J. Appl. Phys. **85**, 2810 (1999).
[32] D. Wang, Y. Fotinich, and G. P. Carman, J. Appl. Phys. **83**, 5342 (1998).
[33] H. Yu, V. Gopalan, and C. A. Randall, J. Appl. Phys. (submitted).
[34] V. Bornand, S. Trolier McKinstry, K. Takemura, and C. A. Randall, J. Appl. Phys. **87**, 3965 (2000).

Appendix 18

Koichi Takemura, Metin Ozgul, Veronique Bornand, Susan Trolier-McKinstry, and Clive A. Randall, "Fatigue Anisotropy in $Pb(B1,B2)O_3$–$PbTiO_3$ Single Crystals and Epitaxial Films," Proceedings, 9th US-Japan Seminar on Dielectric and Piezoelectric Ceramics, Okinawa, (November 3-5, 1999)

Proc. 9th US-Japan Seminar on Dielectric and Piezoelectric Ceramics, Okinawa, Nov. 3-5, 1999.

Fatigue Anisotropy in $Pb(B1,B2)O_3$ - $PbTiO_3$ Single Crystals and Epitaxial Films

Koichi Takemura*, Metin Ozgul, Veronique Bornand, Susan Trolier-McKinstry, and Clive A. Randall**

Materials Research Laboratory, The Pennsylvania State University, University Park, PA 16802-4800, U.S.A.

**Fax: 1-814-865-2326, e-mail: carl@psu.edu

* Present address: Functional Materials Research Laboratories, NEC Corporation, 4-1-1 Miyazaki, Miyamae-ku, Kawasaki 216-8555, Japan.

Fax: 81-44-856-2216, e-mail: takemura@fml.cl.nec.co.jp

Fatigue properties for rhombohedral $Pb(Zn_{1/3}Nb_{2/3})O_3$ - $PbTiO_3$ single crystals have been studied. Fatigue depends on crystal orientation, and rhombohedral pseudocubic <001>-oriented crystals do not fatigue up to 10^5 cycles, whereas <111>- and <110>-oriented crystals fatigue. The orientation dependence appears to result from differences in the domain configuration and switching process. Epitaxially-grown rhombohedral <001>-oriented $Pb(Yb_{1/2}Nb_{1/2})O_3$ - $PbTiO_3$ films on $SrRuO_3/LaAlO_3$ substrate with Pt top electrodes are also shown not to fatigue up to 10^{11} switching cycles. <111>-oriented films fatigue. Crystal anisotropy can be used to suppress the fatigue phenomena in non-volatile ferroelectric memories.

1. INTRODUCTION

Fatigue is the gradual decrease of remanent polarization with bipolar switching of a ferroelectric material. The mechanism of fatigue is not fully understood, but is generally regarded to be a systematic freezing out of switchable polarization through domain wall pinning with point defects and space charge.

Early studies of fatigue were mostly confined to single crystals, and fatigue was observed to be a general phenomenon in ferroelectrics [1,2]. More recent studies have focussed on thin film ferroelectrics, owing to the opportunity of memory devices. Non-volatile ferroelectric memories (FeRAM) have advantages over other memory schemes, such as Flash memories. However, there are two major problems with the FeRAM devices, namely fatigue and imprint. Imprint is the systematic off-set in the hysteresis loop that is developed by exposure to a unipolar field.

In the case of fatigue, there have been advances in the problem, through innovative utilization of top and bottom oxide electrodes, such as RuO_2 [3], $SrRuO_3$ [4], and $(La,Sr)CoO_3$ [5]. These electrodes appear to limit the reduction of ferroelectrics such as $Pb(Zr,Ti)O_3$ (PZT), and thus limit the increase of oxygen vacancies, that aid in the pinning of domain structures, and ultimately fatigue. Alternative ferroelectrics have also been explored such as $SrBi_2Ta_2O_9$ (SBT) and $SrBi_2Nb_2O_9$ (SBN) [6]. These materials have polarization lying in the *a-b* plane of the unit cell. In the SBT and SBN materials, there are relatively few allowed directions for the spontaneous polarization. Therefore, orientation has to be carefully controlled. Although it can be co-processed with Pt-electrodes, the high crystallization temperature and Bi-Pt reactions of the film limit performance [7].

This study returns to the utilization of single crystals to understand fatigue. However, unlike the earlier studies, we have examined the effect of anisotropy and domain engineering. The concept of domain engineering in ferroelectrics has gained popularity during the last few years in the periodic domain structures for second harmonic generation, and in high piezoelectric activity $Pb(Zn_{1/3}Nb_{2/3})O_3$ - $PbTiO_3$ (PZN-PT) single crystals. The PZN-PT crystals demonstrate very high d_{33} coefficients for the rhombohedral phase when poled in the pseudocubic <001> direction. Coefficients as high as 2500 pC/N have been obtained [8].

This paper describes fatigue behavior in rhombohedral PZN-PT single crystals and rhombohedral $Pb(Yb_{1/2}Nb_{1/2})O_3$ - $PbTiO_3$ (PYbN-PT) thin films. In both cases, it was observed that the pseudocubic <001>-oriented materials are fatigue-free.

2. EXPERIMENTAL PROCEDURE

PZN-PT crystals were grown by a high temperature flux technique [8]. The crystals were oriented along the pseudocubic <001>, <111>, or <110> axis by the back-reflection Laue method. Plate-shaped measurement samples were obtained by cutting off the oriented crystals, which were then polished with 3 μm alumina powder to obtain flat and parallel surfaces. 100-nm-thick Pt was sputtered as an electrode. The thickness of the samples ranged from 200 μm to 600 μm, and the electrode area ranged from 0.7 mm^2 to 7 mm^2.

Polarization and strain hysteresis loops were measured at room temperature using a modified Sawyer-Tower circuit and linear variable differential transducer.

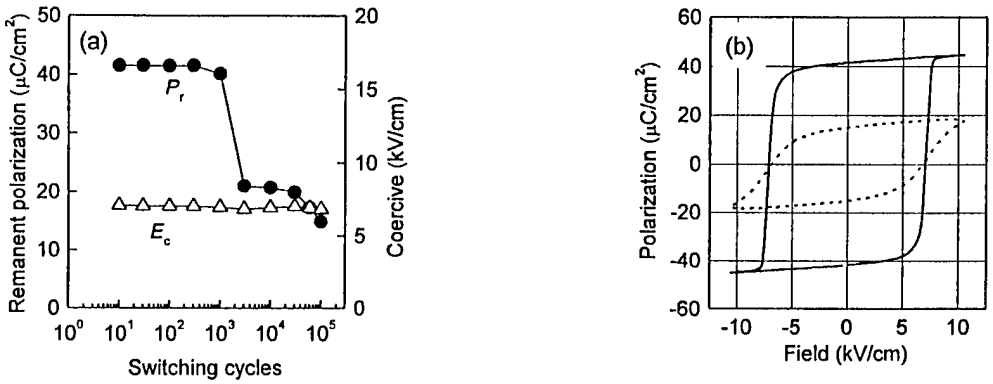

Fig. 1 Switching cycle dependence of P_r, E_c, and hysteresis loops for <111>-oriented PZN - 4.5 PT single crystals. In Fig. 1(b), the solid line is the hysteresis loop after 10 cycles, and the broken line is that after 1×10^5 cycles.

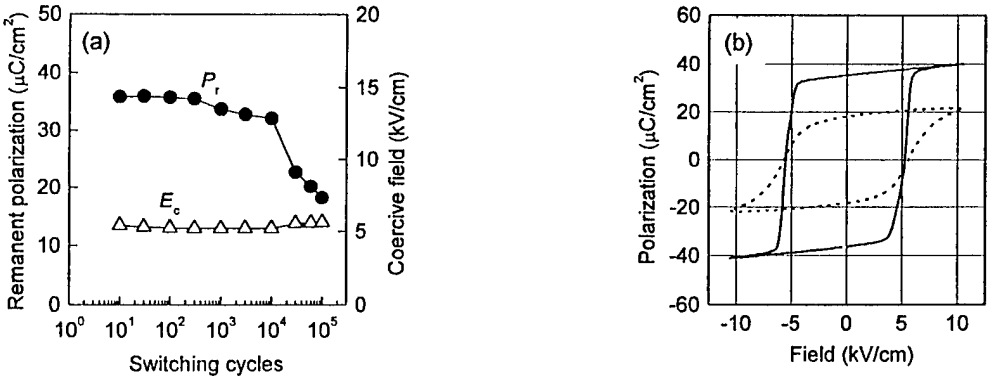

Fig. 2 Switching cycle dependence of P_r, E_c, and hysteresis loops for <110>-oriented PZN - 4.5 PT single crystals. In Fig. 2(b), the solid line is the hysteresis loop after 10 cycles, and the broken line is that after 1×10^5 cycles.

Electrical fields with a triangle bipolar waveform were applied using a high voltage dc amplifier (Trek Model 609C-6 or Kepco Model BOM 1000M). The frequency of the alternating field was 10 Hz for polarization measurement and switching in fatigue measurements, and 0.1 Hz for strain measurement. During measurement, the samples were immersed in Fluorinert to prevent arcing. The remanent polarization (P_r) and the coercive fields (E_c) were computed from the hysteresis loops obtained.

60 % PYbN - 40 % PT/SRO heterostructures were sequentially deposited by the pulsed laser deposition process onto pseudocubic <001>-oriented $LaAlO_3$ and <111>-oriented $SrTiO_3$ substrates. According to the substrate orientation, perovskite PYbN-PT films exhibit a strong <001>- or <111>-texture [9].

3. RESULTS AND DISCUSSION

3.1 PZN-PT Single Crystals

Figures 1 - 3 show P_r, E_c, and hysteresis loops for pseudocubic <111>-, <110>- and <001>-oriented 95.5 % PZN - 4.5 % PT (PZN - 4.5 PT) crystals depending on the number of switching cycles. The amplitude of the alternating triangular electric field (E_{max}) is 10 kV/cm. Because <111> is the polar direction for rhombohedral ferroelectric crystals, the initial P_r value ($P_{r,<111>}$) is the highest of the three. The initial P_r values for <110>- and <001>-oriented crystals are consistent with $\sqrt{2}/\sqrt{3}$ and $1/\sqrt{3}$ of $P_{r,<111>}$, respectively.

As shown in Figs. 1 and 2, the P_r values for the <111>- and <110>-oriented crystals are almost constant up to 10^3 cycles and then decrease with switching cycles. The <110>- and <111>-oriented crystals obviously fatigue. The E_c values for these crystals are almost independent of the switching cycles.

In contrast, the P_r and E_c value for the <001>-oriented crystal are almost constant up to 10^5 switching cycles as shown in Fig. 3(a). The shape of the hysteresis loop does not change even after 10^5 cycles as shown in Fig. 3(b). The E_c value decreases slightly after 10 switching cycles. The same results for E_c are also observed in Fig. 5 for a switching study with a wide variation in field amplitude. It seems that some domain walls are weakly pinned in the initial state, causing some resistance to domain wall motion, but after a few cycles these domain walls are detached from the original defect

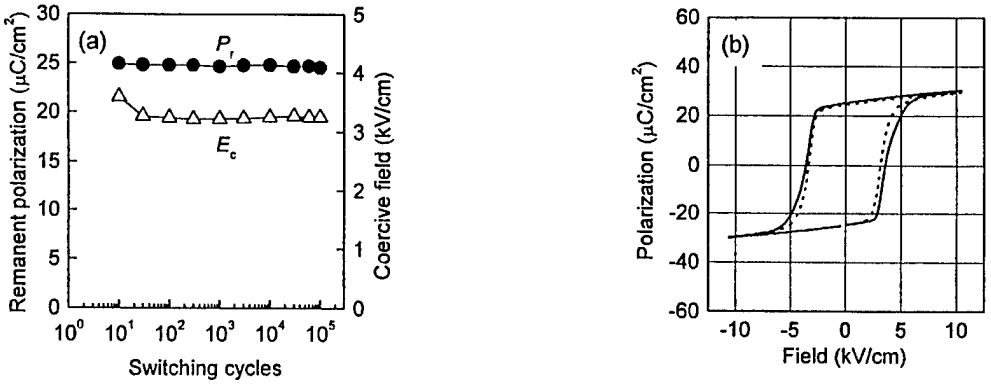

Fig. 3 Switching cycle dependence of P_r, E_c, and hysteresis loops for <001>-oriented PZN - 4.5 PT single crystals. In Fig. 3(b), the solid line is the hysteresis loop after 10 cycles, and the broken line is that after 1×10^5 cycles.

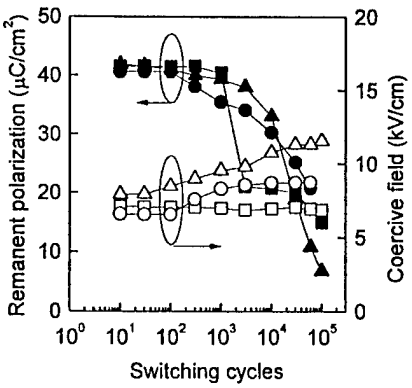

Fig. 4 Switching cycle dependence of P_r (solid symbols) and E_c (open symbols) for <111>-oriented PZN - 4.5 PT single crystals under various switching field strengths (■,□; 10 kV/cm, ●, ○; 20 kV/cm, ▲,△; 30 kV/cm).

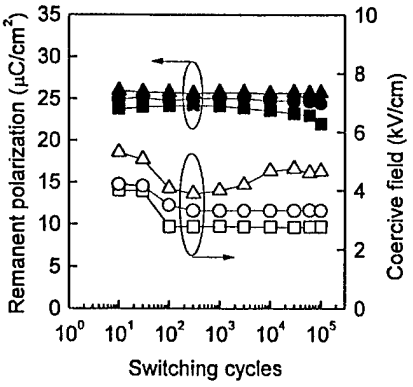

Fig. 5 Switching cycle dependence of P_r (solid symbols) and E_c (open symbols) for <001>-oriented PZN - 4.5 PT single crystals under various switching field strengths (■,□; 5 kV/cm, ●,○; 10 kV/cm, ▲,△; 20 kV/cm).

pinning sites. Possible origins for the pinning include such as impurities, oxygen or lead vacancies, or damage produced during crystal growth, polishing, or electroding.

In ferroelectric thin films, E_{max} often influences fatigue lifetime [10,11]. Figure 4 shows that the <111>-oriented crystals fatigue regardless of the E_{max} values. In contrast, the <001>-oriented crystals do not fatigue under various E_{max} as shown in Fig. 5. We therefore can conclude that the crystal orientation rather than E_{max} governs the fatigue behavior for these crystals. The E_{max} dependence of the fatigue lifetime for the <111>-oriented crystals is not clear. Increasing E_{max} often accelerates fatigue, as observed in thin film studies [10,11]. It is generally believed that carrier injection creates oxygen vacancies and then leads to the pinning of domain walls. In the present study, the applied field strength is one order smaller than that for thin films and the fatigue lifetime does not depend on E_{max}; therefore intrinsic defects rather than the oxygen vacancies created by carrier injection play an important role in the domain wall pinning. After the onset of fatigue, the E_c values for the <111>-oriented crystals increase. The magnitude of E_c increases with E_{max}.

<111>-oriented PZN - 4.5 PT single crystals exhibit a strain change of 0.2 % in a switching cycle. Large strains sometimes result in microcracking, and microcracks have often been observed in fatigued bulk ceramics [12]. To check whether microcracking influenced the current results, fatigued samples were annealed at 250 °C and 450 °C, for 16 hr in air. Figure 6 shows that annealing improves the P_r value of the fatigued <111>-oriented PZN - 4.5 PT crystal. This crystal was fatigued by applying 30 kV/cm triangular switching fields prior to annealing. After 10^5 switching cycles, the fatigue P_r value had reduced to approximately 16 % of the initial value. P_r increases to more than 80 % of the initial P_r value after annealing. This result suggests that the fatigue observed in the present study on PZN-PT single crystals is recoverable,

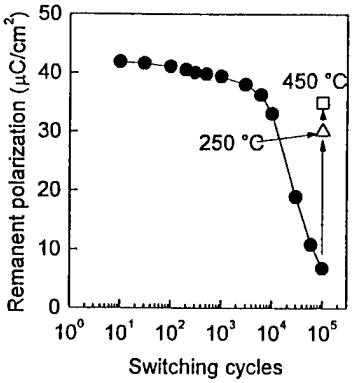

Fig. 6 Recovery of P_r for <111>-oriented PZN - 4.5 PT single crystals. After fatigue, the crystal was annealed at 250 °C, and then 450 °C for 16 h in air.

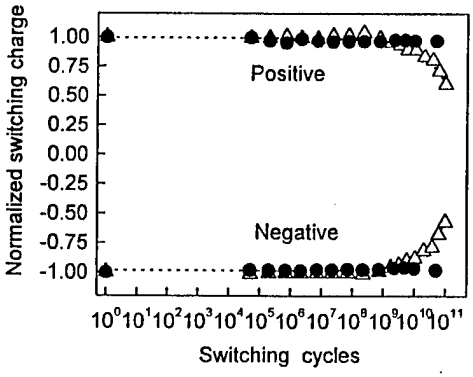

Fig. 7 Normalized switching charge of PYbN-PT thin films as a function of switching cycles. ● ; <001>-oriented heterostructure, △; <111>-oriented heterostructure.

and rules out fatigue by microcracking.

The same orientation dependence of fatigue is also observed in pure PZN single crystals. Therefore, fatigue in rhombohedral PZN-PT single crystals is surely dominated by the orientation of the crystals and not by the nature of the ferroelectricity, that is to say relaxor or normal [13,14].

3.2 PYbN-PT Epitaxial Films

Based on the single crystal observations, we expanded our investigation to epitaxial thin films with PYbN-PT. In good agreement with the single crystals, a significant orientation effect can be observed in the fatigue behavior of capacitors consisting of PYbN-PT heteroepitaxial thin films with conducting oxide $SrRuO_3$ bottom electrodes and Pt top electrodes.

The changes of net switching charge as a function of switching cycles for the two types of capacitors are compared in Fig. 7. Whereas the capacitor with the <001>-orientation does not fail up to nearly 10^{11} cycles, the <111>-oriented PYbN-PT/SRO layered structure presents a marked degradation after 10^9 cycles and shows more than 40 % decay after 10^{11} cycles. These results suggest that a significant impact on fatigue characteristics can be expected from the proper control of orientation in ferroelectric epitaxial thin films.

4. CONCLUSION

Fatigue properties for rhombohedral PZN-PT single crystals have been studied. Fatigue depends on the crystal orientation; pseudocubic <001>-oriented crystals do not fatigue up to 10^5 cycles, whereas <111>- and <110>-oriented crystals fatigue.

Epitaxially-grown <001>-oriented PYbN-PT films do not fatigue up to 10^{11} switching cycles even when Pt is used as the top electrode. The orientation dependence of fatigue is also observed in ferroelectric thin films.

ACKNOWLEDGMENT

The authors would like to thank Prof. T. R. Shrout and Dr. S.-E. Park for their helpful suggestions, and Mr. S.-F. Liu and Ms. H. Lei for supplying single crystals. This work was partially supported DARPA and a grant from NEC Corporation.

REFERENCES

[1] F. Jona and G. Shirane, "Ferroelectric Crystals," Pergamon Press, Oxford (1962).

[2] E. Fatuzzo and W. J. Merz, "Ferroelectricity," John Wiley & Sons, Inc., New York (1967).

[3] H. N. Al-Shareef, B. A. Tuttle, T. J. Headley, D. Dimos, J. A. Voigt, and R. D. Nasby, *J. Appl. Phys.*, **79**, 1013 (1996).

[4] C. B. Eom, R. B. V. Dover, J. M. Phillips, R. M. Fliming, R. J. Cava, J. H. Marshall, D. J. Werder, C. H. Chen, and D. K. Fork, *Mater. Res. Soc. Symp. Proc.*, **310**, 145 (1993).

[5] H. N. Al-Shareef, B. A. Tuttle, W. L. Warren, D. Dimos, M. V. Raymond, and M. A. Rodriguez, *Appl. Phys. Lett.*, **68**, 272 (1996).

[6] C. A. Pas de Araujo, J. D. Cuchiaro, L. D. McMillan, M. C. Scott and J. F. Scott, *Nature*, **374**, 627 (1995).

[7] J. F. Scott, *Ferroelectrics*, **206-207**, 365 (1998).

[8] S.-E. Park and T. R. Shrout, *J. Appl. Phys.*, **82**, 1806 (1997).

[9] V. Bornand and S. Trolier-McKinstry, *submitted to J. Appl. Phys.*

[10]R. D. Nasby, J. R. Schwank, M. S. Rodgers, and S. L. Miller, *Proc. 3rd Int. Symp. Integr. Ferroelectr.*, Colorado Springs, p. 376 (1991).

[11]T. Mihara, H. Watanabe, H. Yoshimori, C. A. Araoujo, B. M. Melnick, and L. D. McMillan, *Proc. 3rd Int. Symp. Integr. Ferroelectr.*, Colorado Springs, p. 116 (1991).

[12]D. Wang, Y. Fotinich, and P. Carman, *J. Appl. Phys.*, **83**, 5342 (1998).

[13]L. E. Cross, *Ferroelectrics*, **76**, 241, (1987).

[14]C. A. Randall and A. S. Bhalla, *Jpn. J. Appl. Phys.*, **29**, 327 (1990).

Appendix 19

Metin Ozgul, Koichi Takemura, Susan Trolier-McKinstry, and Clive A. Randall, "The Study of Fatigue Anisotropy in Pb(Zn1/3Nb2/3)O3–PbTiO3 Ferroelectric Single Crystal," Proceedings, 10th US-Japan Seminar on Dielectric and Piezoelectric Ceramics, Providence, RI, 253–256, (September 26–29, 2001).

Proceedings, 10th US-Japan Seminar on Dielectric & Piezoelectric Ceramics, Providence, RI, Sept. 26-29, 2001

The Study of Fatigue Anisotropy in $Pb(Zn_{1/3}Nb_{2/3})O_3$-$PbTiO_3$ Ferroelectric Single Crystals

Metin Ozgul*, Koichi Takemura, Susan Trolier-McKinstry, and Clive A. Randall**

Center for Dielectric Studies, Materials Research Institute, The Pennsylvania State University, University Park, PA 16802-4800, U.S.A.

*Fax: 1-814-8652326, email: mxo158@psu.edu

**Present address: ULSI Device Development Division, NEC Electron Devices, NEC Corporation, 1120 Shimokuzawa, Sagamihara 229-1198, Japan.

Polarization fatigue anisotropy has been studied in $Pb(Zn_{1/3}Nb_{2/3})O_3$–$PbTiO_3$ (PZN-PT) single crystal ferroelectrics. It was recently found that ferroelectrics with the rhombohedral phase in the PZN-PT solid solution have essentially no polarization fatigue in the $[001]_C$ directions (orientations will be given in terms of the prototype cubic (m3m) axes and denoted by the subscript C). In this study, we expand upon this observation to correlate fatigue rates more completely with respect to composition, orientation, temperature, and electric field strength. It is inferred that an engineered domain state in a relaxor based ferroelectric crystals with the spontaneous polarization inclined to the normal of the electrode is associated with negligible or no fatigue at room temperature. However, if thermal history, temperature, or field strength induces a phase transition that produces a polarization parallel to the normal of electrode, these orientations fatigue. In summary, this article gives information on the polarization states and orientations that control fatigue in ferroelectric crystals with a relaxor end member.

1.INTRODUCTION

Ferroelectric fatigue is the systematic decrease of switchable polarization in a ferroelectric material undergoing bipolar drive. This phenomenon has received a great deal of investigation over the past ten years to aid the development of thin film ferroelectric random access memories. Fatigue is generally believed to be due, at least in part charge injection and the accumulation of space charge that pins domain walls or retards the nucleation of reversed domains.[1-4]

There have been a number of strategies used to improve fatigue resistance in ferroelectrics; these include:

(i) Doping the ferroelectric with donor dopants, e.g., La or Nb in $Pb(Zr,Ti)O_3$ (PZT).[5,6]

(ii) Using oxide electrodes such as RuO_2,[7] IrO_2,[8] $SrRuO_3$,[9] and $(La,Sr)CoO_3$,[10] for PZT thin film ferroelectrics.

(iii) Employing nonfatiguing ferroelectrics with Pt electrodes, e.g., $SrBi_2Ta_2O_9$ or $SrBi_2Nb_2O_9$.[11, 12]

Our recent studies have explored a fourth possible method to control fatigue, namely, the use of domain engineering and crystal anisotropy.[13-16] In this case, the spontaneous polarization vectors are inclined relative to the normal of the electrode plane. The objective of this article is to build upon the previous studies, which were confined to room temperature fatigue rates, and field levels that did not induce ferroelectric-ferroelectric phase switching. Here we are concerned with the influence of temperature and phase transitions on fatigue rates in crystals measured in different directions and with different compositions.

2. EXPERIMENTAL PROCEDURE

The ferroelectric system selected for this study is the $Pb(Zn_{1/3}Nb_{2/3})O_3$–$PbTiO_3$ (PZN-PT) perovskite type solid solution. PZN-PT single crystals are of interest owing to their extraordinary piezoelectric properties, (piezoelectric coefficients $d_{33} \approx 2500$ pC/N and electromechanical coupling coefficients $K_p^2 \geq 90\%$ in the $[001]_C$ direction in the rhombohedral ferroelectric phase).[17]

Crystals of (1-x)PZN-xPT (x=0.00, 0.045, 0.080, 0.10, and 0.12) were grown using the high temperature flux technique.[17] As shown in Fig. 1, at room temperature and weak field levels, PZN and PZN-4.5PT crystals are rhombohedral (pseudocubic), PZN-8PT is near the morphotropic phase boundary (MPB) (still rhombohedral), and PZT-12 PT is tetragonal. All the crystals were oriented within $\pm 2^0$ along the

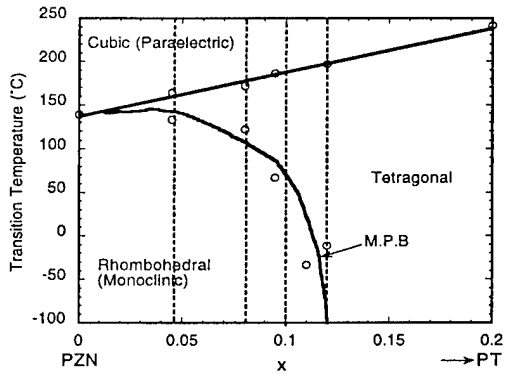

Fig. 1 Phase diagram of the $Pb(Zn_{1/3}Nb_{2/3})O_3$-$PbTiO_3$ system near the MPB (from Ref. 18).

$[111]_C$, $[110]_C$, or $[001]_C$ axes by the back-reflection Laue method. Plate-shaped samples were polished with silicon carbide and alumina powders (down to ~1 μm) to achieve flat and parallel surfaces onto which silver paste electrodes were applied. Silver paste electrodes were preferred due to the fact that they can be removed easily by washing with acetone without changing the nature of the crystal/electrode interface after the experiments. Similar results are obtained with Pt electrodes.[15] The thickness of samples used in this study ranged from 200 μm to 1 mm.

High field measurements including polarization and strain hysteresis utilized a modified Sawyer-Tower circuit and linear variable differential transducer driven by a lock-in amplifier (Stanford Research Systems, Model SR830). Electric fields (E) with a triangle bipolar waveform were applied using a high voltage dc amplifier (Trek Model 609C-6). The frequency of the alternating field was 10 Hz for polarization measurements as well as switching during fatigue measurements, and 0.2 Hz for strain measurements. During measurements, the samples were submerged in Fluorinert, an insulating liquid, to prevent arcing. To study the influence of temperature on fatigue, the Fluorinert liquid was heated or cooled using an oven and liquid nitrogen cryostat, respectively.

The remanent polarizations (P_r) and the coercive fields (E_c) were computed from the recorded hysteresis loops. Fatigue is defined as the change in remanent polarization as a function of the number of switching cycles. All the changes are given as normalized values represented as percentages of the initial remanent polarization or coercive field.

3. RESULTS AND DISCUSSION

3.1 Temperature dependence of fatigue

Figure 2 shows the temperature dependence of fatigue rates in $[111]_C$ oriented PZN-4.5PT crystals for temperatures ranging from 23 (RT) to 100 °C. Fatigue is observed at room and 75 °C temperature within the first 10^5 cycles for a triangular ac field of amplitude 20 kV/cm and frequency 10 Hz. In the $[111]_C$ rhombohedral crystals the fatigue rate is reduced at higher temperatures, as shown in Fig. 2. At temperatures ≥85 °C, fatigue is eliminated. Here, the higher temperatures enable domain switching to overcome the pinning forces. Also at high temperatures, the probability of nucleation (or activating more preexisting nuclei) increases, which also may enable polarization switching to occur throughout the ferroelectric crystals. Collectively, at these higher temperatures the spontaneous polarization does not fatigue as fast as at lower temperatures.

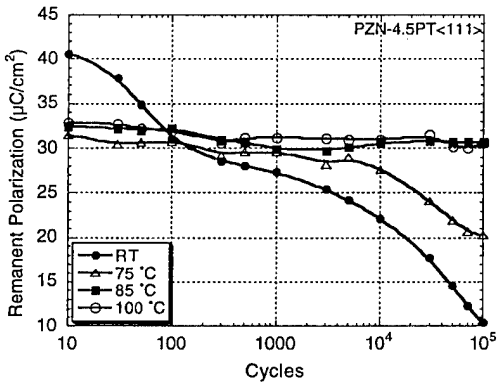

Fig. 2 Fatigue rates as a function of temperature and the number of switching cycles.

3.2 Field induced phase transitions and their impact on fatigue rates

In the rhombohedral phase region the $[111]_C$ oriented crystals fatigue regardless of the applied electric field strength.[15] In this case, the $[111]_C$ oriented crystals have a polarization vector parallel to the electric field and switching is presumably dominated by 180° domain walls. If an electric field is applied along the $[001]_C$ and $[110]_C$ direction, the rhombohedral crystals do not show fatigue at low field strengths. In this case the electric field develops an engineered domain structure with polarization vectors

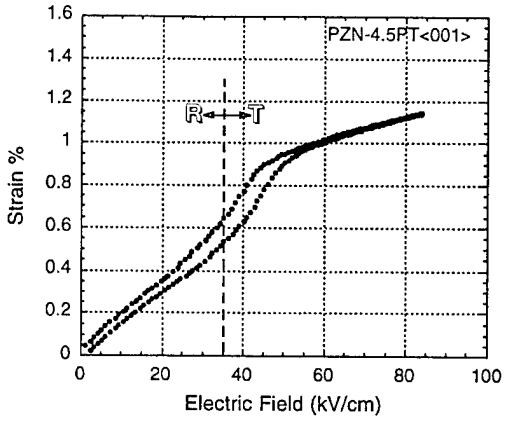

Fig. 3 High field strain vs unipolar electric field behavior in PZN-4.5PT<001>$_C$ single crystals

inclined with respect to the normal vector of the electrode plane.

However, it is known from the work of Park and co-workers[17] that under sufficiently high fields in specific directions, the rhombohedral ferroelectric phase can undergo field forced phase transitions. This can change the nature of the engineered domain state; for example in the [001]$_C$ direction it is possible to induce a tetragonal phase at room temperature with unipolar electric field strengths of >~30 kV/cm. High field strain versus unipolar electric field behavior is given in Fig. 3 for PZN-4.5PT<001>$_C$ crystals indicating the evidence for this phase transformation. PZN-4.5PT<001>$_C$ crystals normally do not fatigue under small electric fields but show remarkable remanent polarization loss when driven at relatively higher fields as illustrated in Fig. 4. Similar experiments

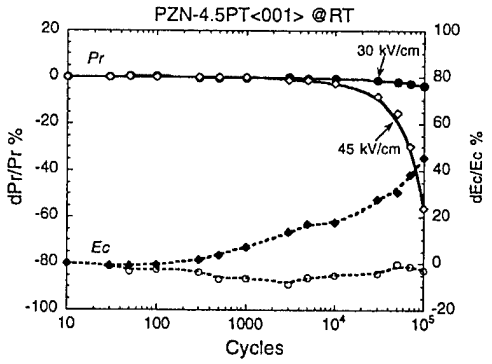

Fig. 4 Fatigue behavior change in PZN-4.5PT<001>$_C$ crystal due to phase switching at higher electric fields; (a) 30 kV/cm (no fatigue) and (b) 45 kV/cm (fatigue).

were performed in [110]$_C$ oriented PZN-4.5PT crystals. Even though rhombohedral PZN-4.5PT <110>$_C$ crystals do not fatigue at low fields, very pronounced fatigue occurred under electric field levels sufficiently high to induce another phase, i.e., the orthorhombic phase. In the case of unipolar drive, different strain-field slopes are noted with a hysteretic transition between the rhombohedral and field induced phase. The field levels for the transformation under unipolar conditions is higher than under ac conditions. Hysteresis losses may locally heat to enable lower temperature transitions. The transition from a ferroelectric rhombohedral to ferroelectric tetragonal (or orthorhombic) phase eventually leads to fatiguing of the crystals.

All of the above results suggest that in these crystals an engineered domain state with the polarization inclined to the electrode is necessary to minimize or eliminate fatigue. This now has been confirmed at a variety of temperatures, compositions, and in both single crystal[15,16] and epitaxial thin film form.[14] The mechanism by which these engineered domain states limit fatigue is not understood. One possibility is that the inclined polarization states redistribute the space charge accumulation and thereby reduce the fatigue rate at a given temperature and composition.

3.3 Influence of fatigue history

The curved morphotropic phase boundary of the PZN-PT system permits fatigue to be studied in single crystals at different temperatures and ferroelectric phases. [001]$_C$ PZN-8PT crystals were induced into the tetragonal phase at 125 °C and cycled with amplitude 20 kV/cm at 10 Hz. After 10^5 cycles, the crystal was substantially (~35%) fatigued. Then, these samples were cooled into the rhombohedral phase at room temperature and again driven under bipolar drive. The samples continued to fatigue as shown in Fig. 5 (in comparison with the crystal cycled only at room temperature). The fatigue at higher temperatures stabilizes local tetragonal regions, which are then retained on cooling into the rhombohedral phase field. The above experiments demonstrate that there are exceptions to high temperature retardation of fatigue rates. This is the case when domain engineered crystals undergo a phase transition to produce polarization vectors parallel to the electric field. Further, the thermal history can also influence the fatigue. If a crystal can undergo a field that induces a domain state that

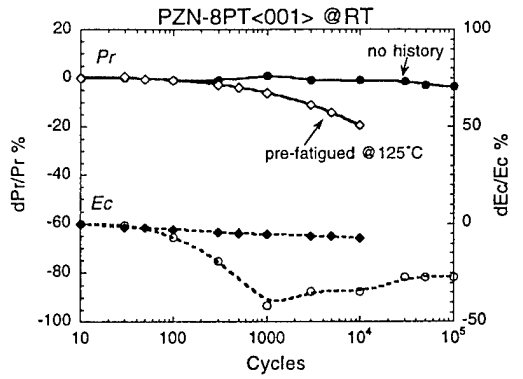

Fig. 5 Comparison of room temperature fatigue behavior of PZN-8PT<001>$_C$ crystals (20 kV/cm, 10 Hz) indicating the influence of fatigue history; (a) cycled only at room temperature and (b) crystals pre-fatigued at 125 °C.

fatigues, this ultimately controls the fatigue process, acting as a nucleation site for pinned domains in the whole crystal.

4. CONCLUSIONS

All of the above illustrates the role of fatigue anisotropy and domain engineering in $Pb(Zn_{1/31}Nb_{2/3})O_3$–$PbTiO_3$ crystals. Fatigue is induced if a polarization vector is normal to the electrode plane and is parallel to the electric field vector. Fatigue rates are suppressed in some directions, provided the thermal energy can overcome pinning effects or alter active nucleation probability. In the compositions close to the MPB, alternating electric fields can induce a ferroelectric phase with polarization parallel to the electric field direction, e.g. a rhombohedral to tetragonal phase transition in a $[001]_C$ crystal. This then can give rise to polarization fatigue. It is hypothesized that if a ferroelectric crystal with a relaxor end member has engineered domains with polarization inclined to the electrode normal, charge injection is either reduced and/or charge is redistributed, and/or domain switching mobility is enhanced, thereby limiting fatigue.

ACKNOWLEDGMENTS

The authors would like to thank Professor T.R. Shrout and Dr. S.-E. Park for their helpful suggestions, and H. Lei and P. Wu for supplying single crystals. This work was achieved with the financial support of The Ministry of Turkish National Education and of DARPA (Grant No. N00014-98-1-0527).

REFERENCES

[1] E. Fatuzzo and W. J. Merz, *Ferroelectricity* (Wiley, New York, 1967).
[2] J. F. Scott and C. A. Pas de Araujo, Science **246**, 140 (1989).
[3] W. L. Warren, D. Dimos, B. A. Tuttle, R. D. Nasby, and G. E. Pike, Appl. Phys. Lett. **65**, 1018 (1994).
[4] J. F. Scott, J. Phys. Chem. Solids **57**, 1439 (1996).
[5] K. Amanuma, T. Hase, and Y. Miyasaka, Jpn. J. Appl. Phys., Part 1 **33**, 5211 (1994).
[6] I. K. Yoo, S. B. Desu, and J. Xing, in *Ferroelectric Thin Films III*, MRS Symp. Proc. Vol. 310, edited by B. A. Tuttle, E. R. Myers, S. B. Desu, and P. K. Larsen (Materials Research Society, Pittsburgh, PA,1993), p.165.
[7] D. P. Vijay and S. B. Desu, J. Electrochem. Soc. **140**, 2640 (1993).
[8] K. Kushida-Abdelghafar, M. Hiratani, and Y. Fujisaki, J. Appl. Phys. **85**, 1069 (1999).
[9] S. Aggarwal, I. G. Jenkins, B. Nagaraj, C. J. Kerr, C. Canedy, R. Ramesh, G. Valasquez, L. Boyer, and J. T. Evans, Jr., Appl. Phys. Lett. **75**, 1787 (1999). 518.
[10] J. Yin, T. Zhu, Z. G. Liu, and T. Yu, Appl. Phys. Lett. **75**, 3698 (1999).
[11] R. Dat, J. K. Lee, O. Auciello, and A. I. Kingon, Appl. Phys. Lett. **67**, 572 (1995).
[12] C. A. Pas de Araujo, J. D. Cuchiaro, L. D. McMillan, M. C. Scott and J. F. Scott, Nature (London) **374**, 627 (1995).
[13] K. Takemura, M. Ozgul, V. Bornand, S. Trolier-McKinstry, and C. A. Randall, Proceedings of the 9th US-Japan Workshop on Dielectric and Piezoelectric Ceramics, Okinawa, Japan, 1999.
[14] V. Bornand, S. Trolier McKinstry, K. Takemura, and C. A. Randall, J. Appl. Phys. **87**, 3965 (2000).
[15] K. Takemura, M. Ozgul, V. Bornand, S. Trolier-McKinstry, and C. A. Randall, J. Appl. Phys. **88**, 7272 (2000).
[16] M. Ozgul, K. Takemura, S. Trolier-McKinstry, and C. A. Randall, J. Appl. Phys. **89**, 5100 (2001).
[17] S.-F. Liu, S.-E. Park, T. R Shrout, and L. E. Cross, J. Appl. Phys. **85**, 2810 (1999)..
[18] J. Kuwata, K. Uchino, and S. Nomura, Ferroelectrics **37**, 579 (1981).

Appendix 20

Metin Ozgul, Koichi Takemura, Susan Trolier-McKinstry, and Clive A. Randall, "Polarization fatigue in $Pb(Zn_{1/3}Nb_{2/3})O_3$–$PbTiO_3$ ferroelectric single crystals," Journal of Applied Physics, 89[9], 5100–5106 (May 2001).

Polarization fatigue in $Pb(Zn_{1/3}Nb_{2/3})O_3-PbTiO_3$ ferroelectric single crystals

Metin Ozgul, Koichi Takemura,[a] Susan Trolier-McKinstry, and Clive A. Randall[b]
Center for Dielectric Studies, Materials Research Laboratory, The Pennsylvania State University, University Park, Pennsylvania 16802-4800

(Received 9 June 2000; accepted for publication 2 November 2000)

$Pb(Zn_{1/3}Nb_{2/3})O_3-PbTiO_3$ (PZN–PT) single crystal ferroelectrics have been studied to determine the relative rates of polarization fatigue. It was recently found that ferroelectrics with the rhombohedral phase in the PZN–PT solid solution have essentially no polarization fatigue in the $[001]_C$ directions (all of the orientations in this article will be given in terms of the prototype cubic ($m3m$) axes, denoted by the subscript C). In this study, we expand upon this observation to correlate fatigue rates more completely with respect to composition, orientation, temperature, and electric field strength. It is inferred that an engineered domain state in relaxor based ferroelectric crystals with the spontaneous polarization inclined to the normal of the electrode is associated with negligible or no fatigue at room temperature. However, if thermal history, temperature, or field strength induces a phase transition that produces a polarization parallel to the normal of electrode, these orientations fatigue. The relative fatigue rates are also studied as a function of temperature. In directions, such as $[111]_C$ in the ferroelectric rhombohedral phase, the polarization fatigues at room temperature, but as temperature is increased the fatigue rate systematically decreases. This is explained in terms of a thermally activated process that limits the net fatigue rate of ferroelectrics. In summary, this article gives information on the polarization states and orientation that control fatigue in ferroelectric crystals with a relaxor end member. © *2001 American Institute of Physics.* [DOI: 10.1063/1.1335819]

I. INTRODUCTION

Ferroelectric fatigue is the systematic reduction of switchable polarization in a ferroelectric material undergoing bipolar drive. Figure 1 shows a schematic of the polarization decay in a ferroelectric material as a function of the number of cycles and also the corresponding evolution of the hysteresis loops. This phenomenon has received a great deal of investigation over the past ten years to aid the development of thin film ferroelectric random access memories. Fatigue is generally agreed to be the result of charge injection and the accumulation of space charge that pins domain walls or retards the nucleation of reversed domains to permit switching.[1–11]

There have been a number of strategies used to improve fatigue resistance in ferroelectrics; these include:

(i) Doping the ferroelectric with donor dopants, e.g., La[12,13] or Nb[14] in $Pb(Zr,Ti)O_3$ (PZT).
(ii) Oxide electrodes, RuO_2,[15–17] IrO_2,[18,19] $SrRuO_3$,[20] and $(La,Sr)CoO_3$,[21–23] for PZT thin film ferroelectrics.
(iii) Nonfatiguing ferroelectrics with Pt electrodes, e.g., $SrBi_2Ta_2O_9$ or $SrBi_2Nb_2O_9$.[24–26]

Our recent studies have explored a fourth possible method to resist fatigue, namely, the use of domain engineering and crystal anisotropy.[27–29] In this case, the spontaneous polarization vectors are inclined relative to the normal of the electrode plane. The objective of this article is to build upon the domain engineering and crystal orientation studies, which were previously confined to room temperature fatigue rates, and field levels that did not induce ferroelectric-ferroelectric phase switching. Here we are concerned with the influence of temperature and phase transitions on fatigue rates in crystals measured in different directions and with compositions.

II. EXPERIMENTAL PROCEDURE

The ferroelectric system selected for this study is the $Pb(Zn_{1/3}Nb_{2/3})O_3-PbTiO_3$ (PZN–PT) solid solution. This is a perovskite material with lead occupying the twelvefold coordinated site, and Zn–Nb and Ti occupying the octahedral site with intermediate scale cation ordering, depending on Ti content.[30] PZN–PT single crystals are of interest owing to their extraordinary piezoelectric properties (piezoelectric coefficients $d_{33} \approx 2500$ pC/N and electromechanical coupling coefficients $K_p^2 \geq 90\%$ in the $[001]_C$ direction in the rhombohedral ferroelectric phase).[31]

Crystals of $(1-x)$PZN–xPT ($x=0.00$, 0.045, 0.080. 0.10, and 0.12) were grown using the high temperature flux technique.[32] As shown in Fig. 2, PZN and PZN–4.5PT crystals are rhombohedral (pseudocubic) at room temperature. As the PT increased beyond 8%, the composition of crystals approaches to the morphotrophic phase boundary (MPB) separating rhombohedral and tetragonal ferroelectric phases. PZN–8PT crystals are in the rhombohedral phase field but PZN–10PT crystals are close to the phase boundary at room temperature and therefore small chemical inhomogeneities in the crystal will lead to mixed phases. PZN–12PT crystals are in a tetragonal ferroelectric phase field at room temperature.

[a]Present address: ULSI Device Development Division, NEC Electron Devices, NEC Corporation, 1120 Shimokuzawa, Sagamihara 229-1198, Japan.
[b]Electronic mail: CAR4@PSU.EDU

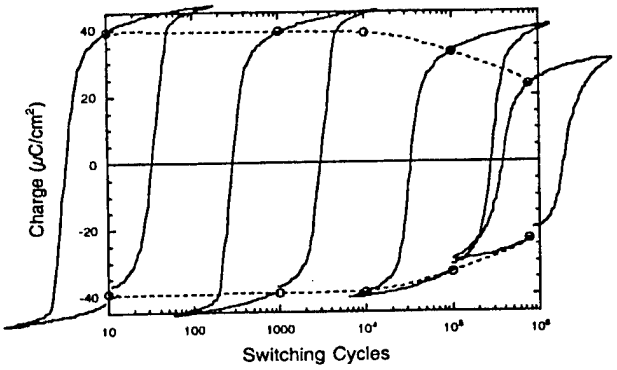

FIG. 1. A schematic illustration of polarization decay as a function of the number of the switching cycles.

The crystal samples were oriented along the $[111]_C$, $[110]_C$, and $[001]_C$ axes within $\pm 2°$ by using a Laue Camera (Multiware Laboratories Ltd., real-time Laue machine).

For electrical characterization, plate-shape samples were cut off from the oriented samples and prepared by polishing with silicon carbide and alumina polishing powders (down to ~ 1 μm) to achieve flat and parallel surfaces onto which silver paste electrodes were applied. Silver paste electrodes were preferred due to the fact that they can be removed easily by washing with acetone without changing the nature of the crystal/electrode interface after the experiments although similar results are obtained with Pt electrodes.[27,29] The thickness of samples used in this study ranged from 200 μm to 1 mm.

High field measurements including polarization and strain hysteresis utilized a modified Sawyer–Tower circuit and linear variable differential transducer driven by a lock-in amplifier (Stanford Research Systems, Model SR830). Electric fields (E) as high as ~ 85 kV/cm were applied in strain measurements using an amplified unipolar wave form at 0.1 Hz. In particular, the electric field was applied with a triangular bipolar wave form for the polarization switching and fatigue experiments. A high voltage dc amplifier (Trek Model 609C-6) was used in both strain and polarization fatigue property measurements. The magnitude and the frequency of the applied ac field were generally 20 kV/cm and 10 Hz, respectively, unless otherwise stated. During measurements, the samples were submerged in Fluorinert, an insulating liquid, to prevent arcing. To study the influence of temperature on fatigue, the Fluorinert liquid was heated or cooled from the room temperature using an oven and liquid nitrogen cryostat, respectively. The experiments were performed at temperatures ranging from -70 to 150 °C depending on the crystal composition.

The remanent polarizations (P_r) and the coercive fields (E_c) were computed from the recorded hysteresis loops. Fatigue rate is defined as the change in remanent polarization as a function of the number of switching cycles. All the changes are given as normalized values represented as percentages of initial remanent polarization or coercive field.

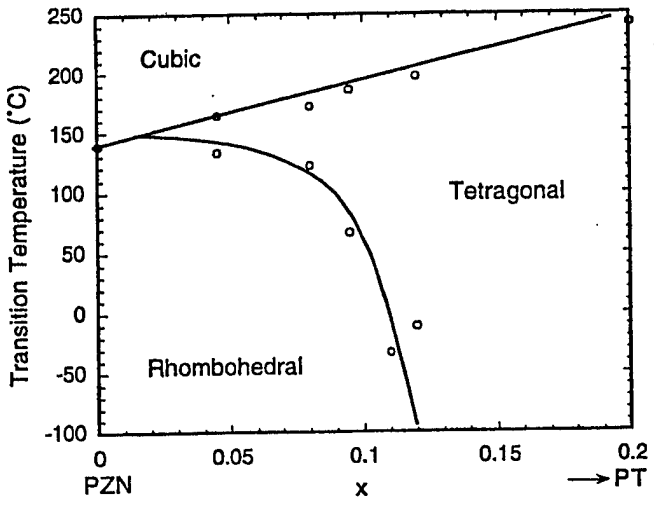

FIG. 2. Phase diagram of the $Pb(Zn_{1/3}Nb_{2/3})O_3$–$PbTiO_3$ system near the MPB (from Ref. 33).

III. RESULTS AND DISCUSSION

A. Temperature dependence of fatigue

Figure 3 shows the virgin hysteresis loops and loops after 10^5 cycles at different temperatures: 23, 65, 75, 85, and 100 °C, respectively, in PZN–4.5PT crystals in $[111]_C$ orientation. Fatigue is observed at room temperature with the first 10^5 cycles for a triangular ac field, amplitude 20 kV/cm and frequency 10 Hz, and for temperatures below 85 °C. In the $[111]_C$ rhombohedral case, the fatigue rate is reduced at higher temperatures, as shown in Fig. 4. The higher temperatures enable domain switching to overcome the pinning forces of the accumulated defects or space charge. Also at high temperatures, the probability of nucleation (or activating more preexisting nuclei) increases, thereby enabling polarization switching to occur throughout the ferroelectric crystals. Collectively, at these higher temperatures the spontaneous polarization does not fatigue at rates as fast as at lower temperatures.

Furthermore, in the case of tetragonal PZN–10PT (at 75 °C) crystals undergo fatigue in the $[001]_C$ direction; again the fatigue rate is reduced as temperature is increased, for similar reasons as explained above for $[111]_C$ directions for rhombohedral crystals at temperatures of 75 °C and above. In the case of tetragonal PZN–PT switching studies at room temperature, the switching frequently causes microcracking, the stress fields about the microcracks can pin polarization switching and is an additional source of fatigue. In single crystal samples undergoing fatigue, it is important to separate the influence of microcracking over space charge or point defect domain pinning. This can be readily done by a heat treatment that rejuvenates the polarization switching, the thermal energy here would not repair the cracks but can redistribute point defects and space charge by diffusion. So rejuvenation of polarization infers that no microcracking is involved in the fatigue of the polarization switching.

Using rejuvenation and switching studies in a variety of compositions, temperatures and directions, it is clear that fatigue anisotropy exists in each phase. In orientations that have fast fatigue rates, this can be reduced by raising the temperature.

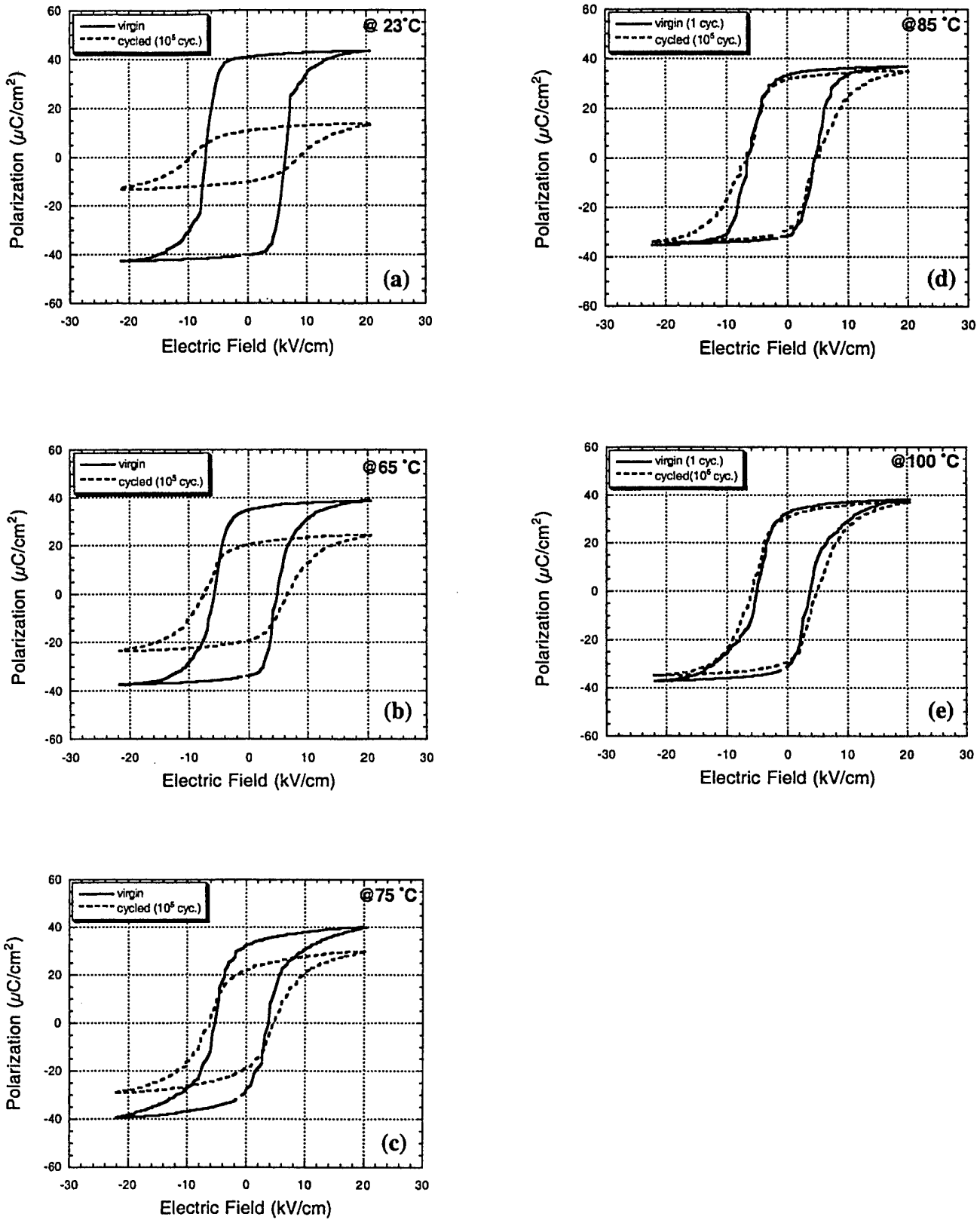

FIG. 3. The influence of switching temperature on fatigue in rhombohedral PZN–4.5PT crystal along with $[111]_C$ orientation; (a) room temperature (23 °C), (b) 65 °C, (c) 75 °C, (d) 85 °C, and (e) 100 °C.

B. Field induced phase transitions and their impact on fatigue rates

Figure 2 recalls the phase diagram of the PZN–PT solid solution at low temperatures and for low electric fields levels (<1 kV/cm). In the rhombohedral phase region the $[111]_C$ oriented crystals fatigue regardless of the applied electric field strength. In this case, the $[111]_C$ oriented crystals have a polarization vector parallel to the electric field and switch-

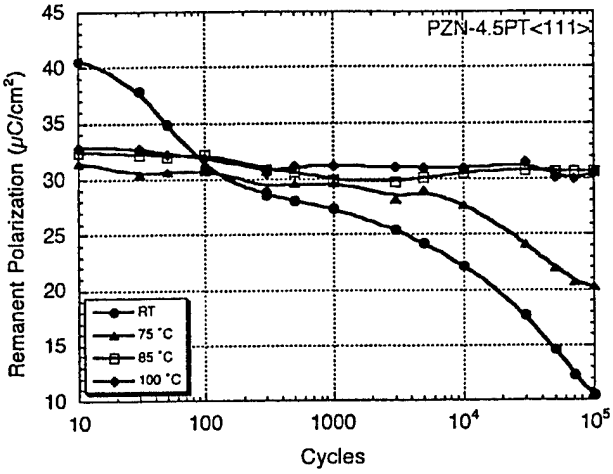

FIG. 4. A plot of fatigue rates as a function of temperature and the number of switching cycles.

ing is presumably dominated by 180° domain walls. If an electric field is applied along the $[110]_C$ and $[001]_C$ directions, the rhombohedral crystals do not show fatigue at low field strengths. In both of these cases the electric field develops an engineered domain structure with polarization vectors inclined with respect to the normal vector of the electrode plane.

However, it is known from the work of Park and co-workers[34] that under sufficiently high fields in specific directions, the rhombohedral ferroelectric phase can undergo field-forced phase transitions. This can change the nature of the engineered domain state; for example in the $[110]_C$ direction it is possible to induce an orthorhombic phase and in the $[001]_C$ direction a tetragonal phase can be induced at room temperatures with unipolar electric field strengths of ~15 and 30 kV/cm, respectively. High field strain versus unipolar electric field behavior is given in Fig. 5 for PZN–4.5PT crystals with $[110]_C$ orientation indicating the evi-

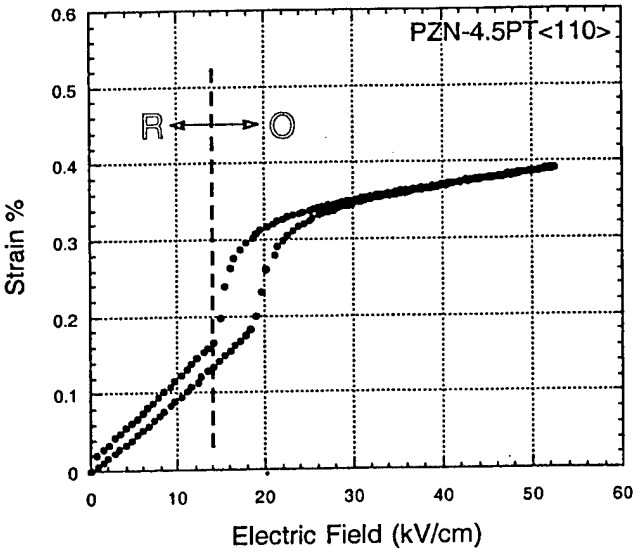

FIG. 5. High field strain vs unipolar electric field behavior for PZN–4.5PT single crystals with $[110]_C$ orientation. A high unipolar electric field induces a phase transition (rhombohedral→orthorhombic) at a critical voltage.

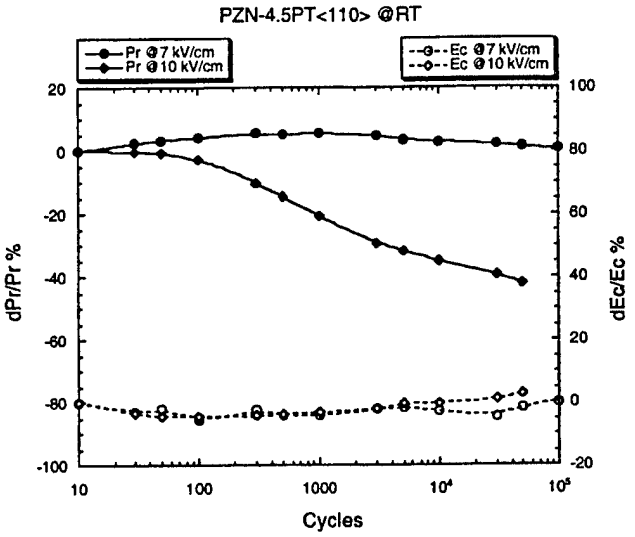

FIG. 6. Polarization fatigue behavior change in $[110]_C$ oriented PZN–4.5PT single crystals due to field induced phase switching under two different bipolar electric fields; (a) 7 kV/cm (no fatigue) and (b) 10 kV/cm (fatigue).

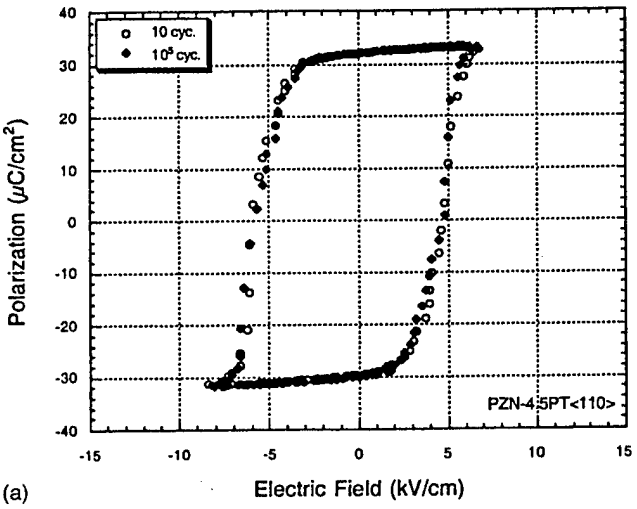

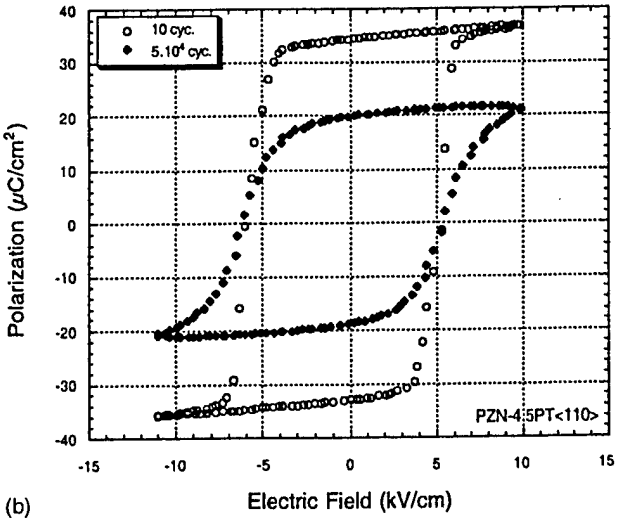

FIG. 7. Hysteresis loop change in PZN–4.5PT⟨110⟩ single crystals after bipolar cycling below and above the critical voltage; (a) stable remanent polarization and coercive field after 10^5 cycles under 7 kV/cm ac field and (b) polarization fatigue after 5×10^4 cycles under 10 kV/cm ac field.

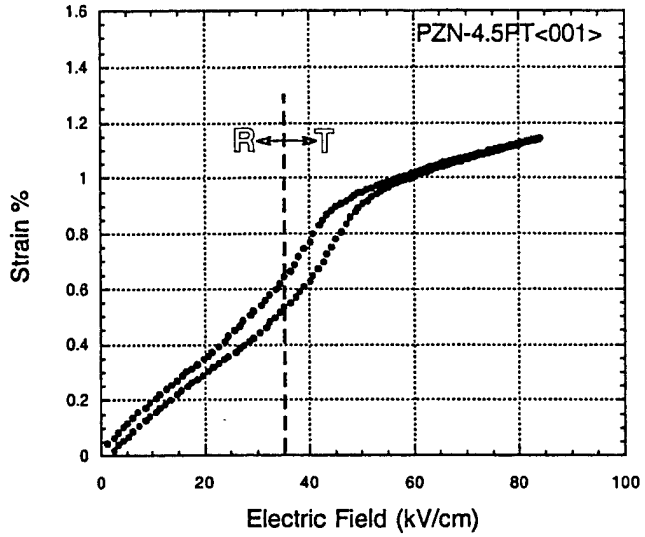

FIG. 8. High field strain vs unipolar electric field behavior for PZN–4.5PT single crystals with $[001]_C$ orientation. A high unipolar electric field induces a phase transition (rhombohedral→tetragonal) at a critical voltage.

dence for this phase transformation. PZN–4.5PT crystals normally do not fatigue under small electric fields but show remarkable remanent polarization loss when driven at relatively higher fields as illustrated in Fig. 6. Hysteresis loops for $[110]_C$ oriented PZN–4.5PT crystals before and after cycling under different field levels are also given in Fig. 7. Similar experiments were performed in $[001]_C$ oriented PZN–4.5PT crystals. Even though rhombohedral PZN–4.5PT crystals do not fatigue at room temperature, very pronounced fatigue occurred under electric field levels sufficiently high to induce another phase. The unipolar strain versus field curve in Fig. 8, the remanent polarization values as a function of the number of cycles in Fig. 9, and the hysteresis behavior before and after cycling in Fig. 10 illustrate the important role of field induced phase transitions on fatigue. In the case of unipolar drive different strain-field

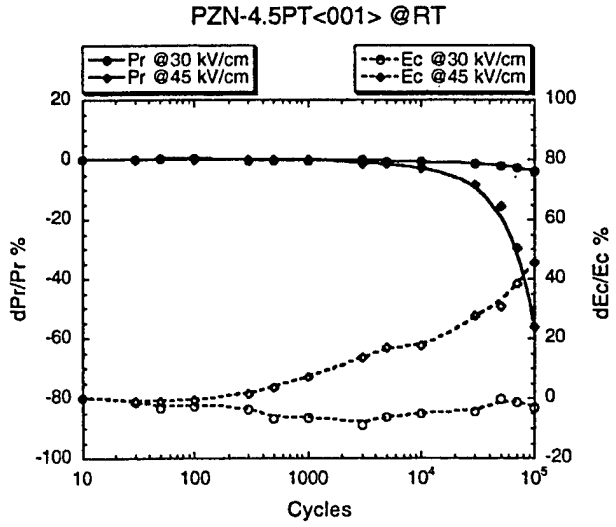

FIG. 9. Polarization fatigue behavior change in $[001]_C$ oriented PZN–4.5PT single crystals due to field induced phase switching under two different bipolar electric fields; (a) 30 kV/cm (no fatigue) and (b) 45 kV/cm (fatigue).

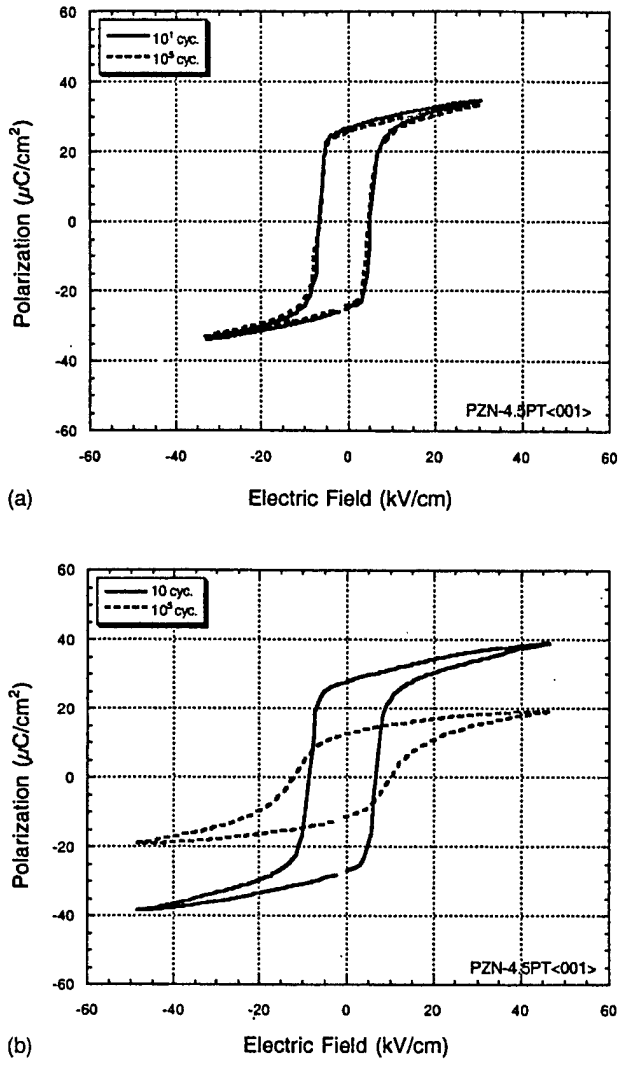

FIG. 10. Hysteresis loop change in PZN–4.5PT$\langle 001 \rangle_C$ single crystals after bipolar cycling below and above the critical voltage; (a) stable remanent polarization and coercive field after 10^5 cycles under 30 kV/cm ac field and (b) polarization fatigue after 10^5 cycles under 45 kV/cm ac field.

slopes are noted with a hysteretic transition between the rhombohedral and field induced phase. The field levels for the transformation under unipolar conditions is higher than under ac conditions. Hysteresis losses may locally heat to enable lower temperature transitions. The transition from a ferroelectric rhombohedral to ferroelectric tetragonal (or orthorhombic) phase eventually creates a fatiguing of the crystals. The rate at which the tetragonal phase is induced from the rhombohedral phase depends on the compositions, temperature, and magnitude of the electric field. Figure 11 shows field induced fatigue in rhombohedral PZN–10PT crystal at low temperatures (~−70 °C). The tetragonal phase is easily induced at this composition which is very close to morphotrophic phase boundary. Once the remanent tetragonal phase is induced it initially causes an increase in the remanent polarization, then the fatigue process starts, and this gives a systematic reduction in the polarization as a function of cycles, above a certain number of cycles.

All of the above results suggest that, in these crystals, an engineered domain state with the polarization inclined to the

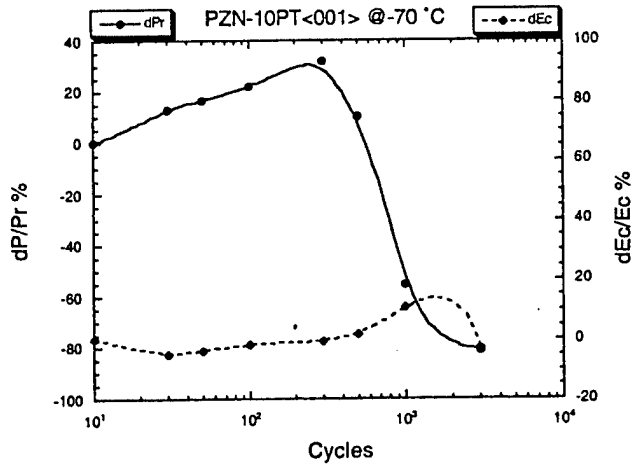

FIG. 11. Polarization fatigue behavior of PZN–10PT$\langle 001\rangle_C$ single crystals at ~−70 °C. The field induced tetragonal phase dominates over rhombohedral structure and produces very fast fatigue.

electrode is necessary to minimize or eliminate fatigue. This now has been confirmed at a variety of temperatures, compositions, and in both single crystal[27,29] and epitaxial thin film form.[28] The precise mechanism by which these engineered domain states limit fatigue is not understood. One possibility is that the inclined polarization states redistribute the space charge accumulation and thereby reduce the fatigue rate at a given temperature and composition. It still is under investigation, but it is also hypothesized that the engineered domain structures with the rhombohedral symmetry can have a higher percentage of charged domain walls. Charged walls could act as sinks to the injected charge in these systems. Another intriguing possibility is the multiple routes for domain switching that may exist in PZN–PT relaxor crystals, the complex dendritic domain wall structures observed under pulsed conditions indicate this great flexibility in switching paths,[35] and also indicate a switching process with a very high effective domain wall mobility.[36] This may also change the nature of the switching and thereby alter the fatigue mechanisms.

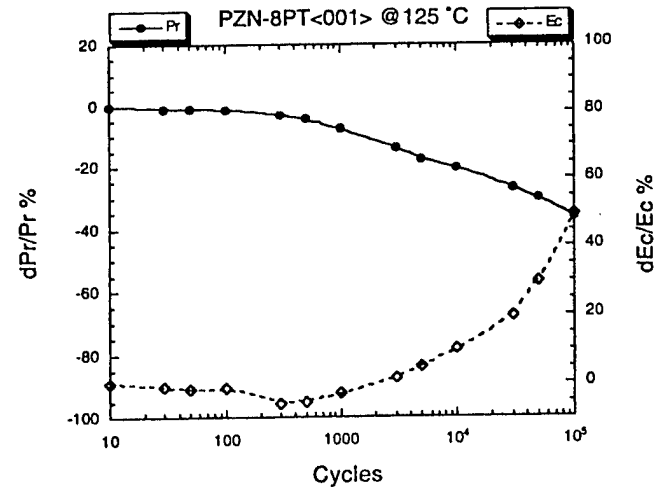

FIG. 12. Polarization fatigue behavior of PZN–8PT$\langle 001\rangle_C$ single crystals at 125 °C. Thermally induced tetragonal phase shows remarkable fatigue.

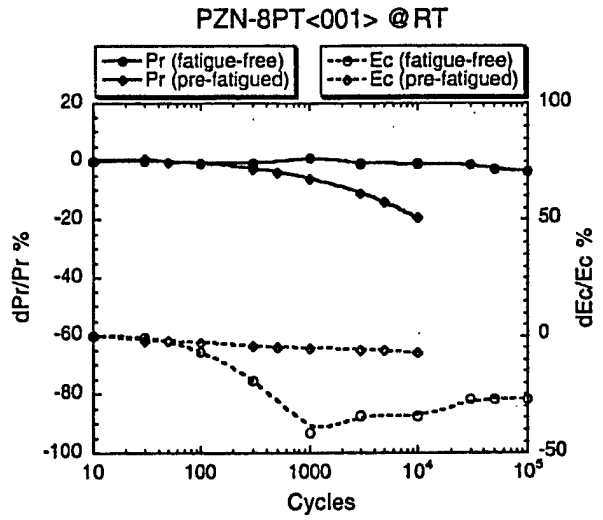

FIG. 13. Comparison of room temperature polarization fatigue behavior of PZN–8PT$\langle 001\rangle_C$ crystals (20 kV/cm, 10 Hz) indicating the influence of fatigue history; (a) cycled only at room temperature and (b) crystals prefatigued at 125 °C.

C. Influence of fatigue history

The curved morphotropic phase boundary of the PZN–PT system permits fatigue to be studied in single crystals at different temperatures and ferroelectric phases. Crystals with composition PZN–8PT and $[001]_C$ orientation were phase induced into the tetragonal phase at 125 °C under bipolar fields with amplitude 20 kV/cm at 10 Hz. After 10^5 cycles, the crystal was substantially (~35%) fatigued as shown in Fig. 12. Then, these samples were cooled into the rhombohedral phase at room temperature and then driven under bipolar drive. The samples then continued to fatigue as shown in Fig. 13 in comparison with the crystal cycled only at room temperature. The fatigue at higher temperatures stabilizes local tetragonal regions, which are then cooled into

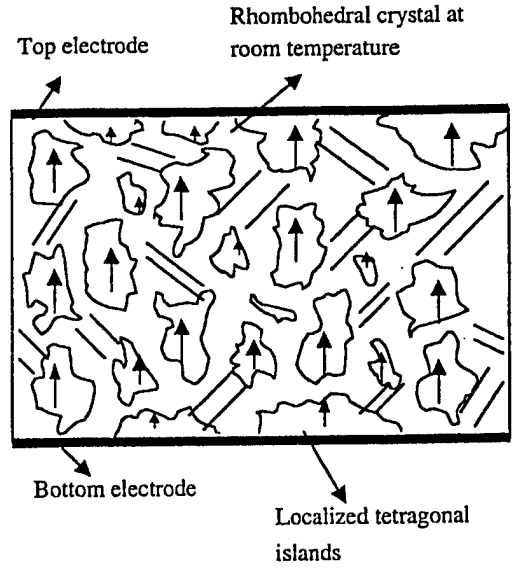

FIG. 14. A schematic illustration of room temperature mixed phase structure of PZN–8PT$\langle 001\rangle_C$ crystal after fatiguing at high temperature tetragonal phase region causing localized tetragonal phase stabilization.

the rhombohedral phase field, as schematically illustrated in Fig. 14. The above experiments demonstrate that there are exceptions to high temperature retardation of fatigue rates. This is the case when domain engineered crystals undergo a phase transition to produce polarization vectors parallel to the electric field. Further, the thermal history can also influence the fatigue. If a crystal can undergo a field that induces a domain state that fatigues, this ultimately controls the fatigue process, acting as a nucleation site for pinned domains in the whole crystal.

IV. CONCLUSIONS

All of the above illustrate the role of fatigue anisotropy and domain engineering in $Pb(Zn_{1/3}Nb_{2/3})O_3$–$PbTiO_3$ crystals. Fatigue is induced if a polarization vector is normal to the electrode plane and is parallel to the electric field vector. Fatigue rates are suppressed in some directions, provided the thermal energy can overcome pinning effects or alter active nucleation probability at the electrode interface without inducing polarization parallel to the applied field. In the compositions close to the MPB, alternating electric fields can induce a ferroelectric phase with polarization parallel to the electric field direction, e.g., a rhombohedral to tetragonal phase transition in a $[001]_C$ crystal. This then can give rise to polarization fatigue. In special directions, such as $[110]_C$, a rhombohedral phase can be field induced into a metastable orthorhombic phase that has polarization parallel to the normal of the electrode plane and thereby undergo fatigue. In the case of electric fields inducing mixed ferroelectric phases, the fatigue is dominated by the polarization direction parallel to the electric field direction. It is hypothesized that if a ferroelectric crystal with a relaxor end member has engineered domains with polarization inclined to the electrode normal, charge injection is either reduced and/or charge is redistributed, and/or domain switching mobility is enhanced, thereby limiting fatigue.

A comprehensive mechanism that explains fatigue is still awaiting the feroelectrics community, however, these studies on ferroelectric phase and orientation, builds up the experimental background that ultimately has to be explained in a complete fatigue model.

ACKNOWLEDGMENTS

This work was achieved with the financial support of The Ministry of Turkish National Education and DARPA single crystal fund (Grant No. N00014-98-1-0527). The authors would like to thank Professor T. R. Shrout and Dr. S.-E. Park for helpful suggestions, and H. Lei and P. Wu for supplying single crystals.

[1] W. J. Merz and J. R. Anderson, Bell Lab. Rec. **33**, 335 (1955).
[2] J. R. Anderson, G. W. Brady, W. J. Merz, and J. P. Remeika, J. Appl. Phys. **26**, 1387 (1955).
[3] H. L. Stadler, J. Appl. Phys. **29**, 743 (1958).
[4] D. S. Campbell, Philos. Mag. **79**, 1157 (1962).
[5] F. Jona and G. Shirane, *Ferroelectric Crystals* (Pergamon, Oxford, 1962).
[6] R. Williams, J. Phys. Chem. Solids **26**, 399 (1965).
[7] E. Fatuzzo and W. J. Merz, *Ferroelectricity* (Wiley, New York, 1967).
[8] J. F. Scott and C. A. Pas de Araujo, Science **246**, 140 (1989).
[9] W. L. Warren, D. Dimos, B. A. Tuttle, R. D. Nasby, and G. E. Pike, Appl. Phys. Lett. **65**, 1018 (1994).
[10] W. L. Warren, D. Dimos, B. A. Tuttle, G. E. Pike, R. W. Schwartz, P. J. Clews, and P. C. McIntyre, J. Appl. Phys. **77**, 6695 (1995).
[11] J. F. Scott, J. Phys. Chem. Solids **57**, 1439 (1996).
[12] W. C. Stewart and L. S. Cosentino, Ferroelectrics **1**, 149 (1970).
[13] K. Amanuma, T. Hase, and Y. Miyasaka, Jpn. J. Appl. Phys., Part 1 **33**, 5211 (1994).
[14] I. K. Yoo, S. B. Desu, and J. Xing, in *Ferroelectric Thin Films III*, MRS Symp. Proc. Vol. 310, edited by B. A. Tuttle, E. R. Myers, S. B. Desu, and P. K. Larsen (Materials Research Society, Pittsburgh, PA, 1993), p. 165.
[15] D. P. Vijay and S. B. Desu, J. Electrochem. Soc. **140**, 2640 (1993).
[16] T. Nakamura, Y. Nakano, A. Kanisawa, and H. Takasu, Jpn. J. Appl. Phys., Part 1 **33**, 5207 (1994).
[17] H. N. Al-Shareef, K. R. Bellu, A. I. Kingon, and O. Auciello, Appl. Phys. Lett. **66**, 239 (1995).
[18] T. Nakamura, Y. Nakao, A. Kanisawa, and H. Takasu, Appl. Phys. Lett. **65**, 1522 (1994).
[19] K. Kushida-Abdelghafar, M. Hiratani, and Y. Fujisaki, J. Appl. Phys. **85**, 1069 (1999).
[20] J. T. Cheung, P. E. D. Morgan, and R. Neurgaonkar, Proceedings of the 4th International Symposium on Integrated Ferroelectrics, Colorado Springs, CO, 1992, p. 518.
[21] R. Ramesh, H. Girchlist, T. Sands, V. G. Keramidas, R. Haakenaasen, and D. K. Fork, Appl. Phys. Lett. **63**, 3592 (1993).
[22] C. B. Eom, R. B. V. Dover, J. M. Phillips, D. J. Werder, J. H. Marshall, C. H. Chen, R. M. Fleming, and D. K. Fork, Appl. Phys. Lett. **63**, 2570 (1993).
[23] J. Yin, T. Zhu, Z. G. Liu, and T. Wu, Appl. Phys. Lett. **75**, 3698 (1999).
[24] S. Aggarwal, I. G. Jenkins, B. Nagaraj, C. J. Kerr, C. Canedy, R. Ramesh, G. Valasquez, L. Boyer, and J. T. Evans, Jr., Appl. Phys. Lett. **75**, 1787 (1999).
[25] R. Dat, J. K. Lee, O. Auciello, and A. I. Kingon, Appl. Phys. Lett. **67**, 572 (1995).
[26] C. A. Pas de Araujo, J. D. Cuchiaro, L. D. McMillian, M. C. Scott, and J. F. Scott, Nature (London) **374**, 627 (1995).
[27] K. Takemura, M. Ozgul, V. Bornand, S. Trolier-McKinstry, and C. A. Randall, Proceedings of the 9th US-Japan Workshop on Dielectric and Piezoelectric Ceramics, Okinawa, Japan, 1999.
[28] V. Bornand, S. Trolier McKinstry, K. Takemura, and C. A. Randall, J. Appl. Phys. **87**, 3965 (2000).
[29] K. Takemura, M. Ozgul, V. Bornand, S. Trolier-McKinstry, and C. A. Randall, J. Appl. Phys. **88**, 7272 (2000).
[30] C. A. Randall, A. S. Bhalla, T. R. Shrout, and L. E. Cross, J. Mater. Res. **5**, 829 (1990).
[31] S.-E. Park and T. R. Shrout, Mater. Res. Innovations **1**, 20 (1997).
[32] M. L. Mulvihill, S.-E. Park, G. Rish, and T. R. Shrout, Jpn. J. Appl. Phys., Part 1 **35**, 561 (1996).
[33] J. Kuwata, K. Uchino, and S. Nomura, Ferroelectrics **37**, 579 (1981).
[34] S.-F. Liu, S.-E. Park, T. R. Shrout, and L. E. Cross, J. Appl. Phys. **85**, 2810 (1999).
[35] H. Yu and C. A. Randall, J. Appl. Phys. **86**, 5733 (1999).
[36] H. Yu, V. Gopalan, J. Sindel, and C. A. Randall, J. Appl. Phys. **89**, 561 (2001).

Appendix 21

Yu Lu, Z.–Y. Cheng, Y. Barad, and Q.M. Zhang, "Photoelastic effects in tetragonal $Pb(Zn_{1/3}Nb_{2/3})O_3$–$PbTiO_3$ single crystals near the morphotropic phase boundary," Journal of Applied Physics, 89[9], 5075–5078 (May 2001).

Photoelastic effects in tetragonal $Pb(Zn_{1/3}Nb_{2/3})O_3$–$PbTiO_3$ single crystals near the morphotropic phase boundary

Y. Lu,[a] Z.-Y. Cheng, Y. Barad, and Q. M. Zhang
Materials Research Laboratory and Electrical Engineering Department, Pennsylvania State University, University Park, Pennsylvania 16802

(Received 15 January 2001; accepted for publication 15 February 2001)

In order to explore the photoelastic effects of the ferroelectric single crystal $Pb(Zn_{1/3}Nb_{2/3})O_3$–$PbTiO_3$ (PZN–PT), the piezo-optical coefficients π were characterized for 0.9PZN–0.1PT and 0.88PZN–0.12PT under uniaxial stress using an interferometer method. The results show that the crystal exhibits very large π values (for example, π_{33} can reach 19.8 $\times 10^{-12}$ m^2/N), indicating that this material is a good candidate for stress sensors and acousto-optic modulators. © *2001 American Institute of Physics.* [DOI: 10.1063/1.1363684]

I. INTRODUCTION

The phenomenon of photoelastic behavior in crystals is attractive for many applications, such as stress sensors and light modulators.[1,2] In order to improve the performance of these devices, new materials with a large photoelastic effect are highly desirable. Recently, there has been an increased interest in $Pb(Zn_{1/3}Nb_{2/3})O_3$–$PbTiO_3$ (PZN–PT) single crystals because the crystals exhibit very large piezoelectric constants, high electromechanical coupling factors, and massive electro-optic effects.[3–6] The unique feature of these materials is that high quality single crystals can be grown at compositions close to the tetragonal–rombohedral morphotropic phase boundary (MPB), where very large ferroelastic coupling is expected for this class of crystals because of a large lattice constant change between the two morphotropic phases.[7,8] In general, materials with large ferroelastic responses may also have high photoelastic effects. Especially, for materials near MPB, the large lattice parameter changes with composition will result in large changes in the refractive index. Equivalently, the stress induced phase transition (shift of the MPB with stress) will also bring additional and large refractive index changes, which enhances the overall photoelastic effects. Therefore, it is interesting to investigate the photoelastic effect of PZN–PT single crystals near MPB.

PZN–PT single crystals are the solid solutions of lead zinc niobate and lead titanate and the crystals used here were grown by a high temperature flux method.[4] Among them, 0.9PZN–0.1PT was chosen since this composition is close to MPB in the tetragonal side at room temperature, and 0.88PZN–0.12PT was also measured for comparison.[7] The sample was poled along its spontaneous polarization direction (⟨001⟩ direction) to form a single domain state, then carefully polished to optical grade as described in Ref. 5. The typical specimen dimension is $3 \times 3 \times 3$ mm^3.

II. PHOTOELASTIC EFFECT AND ITS MEASUREMENT

Photoelastic effect describes the change of the refractive index as a result of mechanical stress. Under an applied stress T_{kl}, the change of refractive index n_{ij} is given by[2]

$$\Delta B_{ij} = \Delta\left(\frac{1}{n_{ij}^2}\right) = \pi_{ijkl} T_{kl}, \tag{1}$$

where B_{ij} is the optical dielectric impermeability, which is equal to $1/n_{ij}^2$; π_{ijkl} is the piezo-optical coefficient (i, j, k, and $l = 1-3$). In this work, the piezo-optical coefficients, $\pi_{13}(=\pi_{1133})$, $\pi_{33}(=\pi_{3333})$, $\pi_{11}(=\pi_{1111})$, and π_{31} $(=\pi_{3311})$ were characterized at room temperature at a wavelength of 623.8 nm utilizing uniaxial stress measurements. As schematically shown in Fig. 1, by applying the compressional stress along the three axis (T_{33}) which is along the sample poling direction, the piezo-optical coefficient π_{33} can be obtained from the change of the extraordinary refractive index n_e; and π_{13} can be determined from the change of the ordinary refractive index n_0.

To generate the required uniaxial stress on the crystal, a special setup was carefully designed. In this setup, a piezoelectric actuator (Thorlabs Inc., AE0505D08) was used to generate a dynamic force by applying an ac electric driving voltage to the actuator, and the stress was measured using a high performance load cell (Omegadyne Inc., LC302-25). The refractive index change was measured at a wavelength of 623.8 nm using a computer-controlled scanning Mach–Zender interferometer, as schematically shown in Fig. 2, similar to the one reported in the Ref. 5. Since the dynamic force was used in the experiment, a lock-in amplifier was used to detect the modulated interference output signal at the frequency of the applied stress, which significantly improves the sensitivity of the measurement. Therefore, the stress applied to the sample can be very small ($\geqslant$1 kPa was used, which is actually limited by the resolution of the load cell) eliminating the possibility of stress depoling the crystal, especially when applying the compressional stress along the poling direction. For the setup designed here, the frequency of the dynamic force can be varied from 1 to 100 Hz and the results reported were obtained at 10 Hz.

[a]Electronic mail: YXL27@PSU.EDU

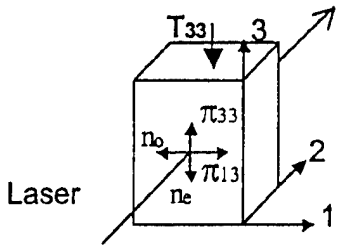

FIG. 1. Schematic drawing for the measurement of π_{33} and π_{13} where the uniaxial stress is applied along the three axis. The laser light propagation direction and the light polarization direction for the measurement of π_{33} and π_{13} are indicated.

TABLE I. Piezo-optical coefficients of single crystal PZN–PT at room temperature ($\times 10^{-12}$ m^2/N).

0.9PZN–0.1PT		0.88PZN–0.12PT	
π_{33}^E	19.8	π_{33}^E	18.2
π_{13}^E	−1.6	π_{13}^E	−0.9
π_{11}^E	2.3	π_{11}^E	0.8
π_{31}^E	−10.4	π_{31}^E	−9.3
π_{33}^D	6.2	π_{33}^D	6.0
π_{13}^D	−2.5	π_{13}^D	0.2
π_{11}^D	2.4	π_{11}^D	1.3
π_{31}^D	−4.6	π_{31}^D	−3.9

It should be mentioned that, in this interferometer technique, the directly measured optical path length change is the result of two effects, i.e., the change in the refractive index (piezo-optical effect) and the change in the sample dimension (elastic deformation of the sample due to stress). In order to extract the refractive index change due to the piezo-optical effect, the sample dimensional change along the optical path under the same applied stress was measured using a double beam interferometer method.[9] After this correction, the piezo-optical coefficient π can be obtained.

III. EXPERIMENTAL RESULTS AND DISCUSSION

For piezoelectrics, there are two types of the π coefficients, i.e., π^E and π^D, due to the different electric boundary conditions of the sample in the measurement. Because of the piezoelectric effect, a voltage will be generated under the applied stress if the measurement is carried out in an open circuit condition (constant electric displacement, D) and in this case, π^D is measured. On the other hand, if the measurement is carried out in the short circuit condition (constant electric field, E), where the sample surfaces at the positive and negative polarization directions are electroded and the two electroded surfaces are connected (shorted), π^E is measured. As will be shown later, the difference between π^E and π^D is determined by the electro-optical and piezoelectric effects. That is, the stress-generated electric field on the sample in the open circuit condition also results in a change of refractive index through the electro-optic effect. In this investigation, the piezo-optical coefficients π_{11}, π_{31}, π_{13}, and π_{33} under both the constant electric field and the constant electric displacement conditions were measured. Table I summarizes the final results for 0.9PZN–0.1PT and 0.88PZN–0.12PT single crystals.

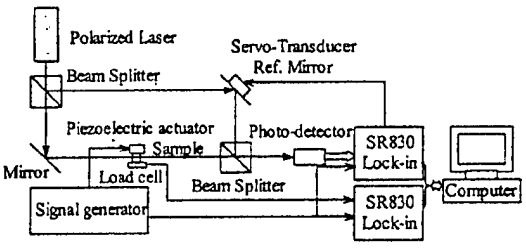

FIG. 2. Schematic drawing of the computer-controlled scanning Mach–Zender interferometer for piezo-optical measurement.

To provide an understanding of the measured results, a phenomenological treatment will be used to link the change of optical properties of the crystals to the applied stress, electric field, as well as the remanent polarization.[10] From the symmetry consideration, the change of the optical impermeability for the PZN–PT single crystals can be written as

$$\Delta B_{ij} = \pi^0_{ijkl} T_{kl} + g_{ijmn} P_m P_n + f_{ijklmn} T_{kl} P_m P_n, \qquad (2)$$

where π^0_{ijkl} is the piezo-optical coefficient of the prototype phase (cubic for PZN–PT single crystals studied here) where $P_m = 0$, P_m is the polarization component along the m axis, g_{ijmn} is quadratic polarization-optic (PO) constant, and f_{ijklmn} is the first order cross term between T and P. In Eq. (2), all the higher order terms have been omitted. Based on the results in this study, we find the three terms in Eq. (2) are on the same order of magnitude. To simplify the formula, a matrix notation will be used in following derivations (i.e., $11 \rightarrow 1$, $22 \rightarrow 2$, $33 \rightarrow 3$).[11]

For the uniaxial stress used here, only T_1 or T_3 is the nonzero stress component. In the prototype cubic phase where the spontaneous polarization is zero,

$$\Delta B_1 = \pi^0_{11} T_1 + \pi^0_{13} T_3,$$
$$\Delta B_3 = \pi^0_{31} T_1 + \pi^0_{33} T_3. \qquad (3)$$

For the prototype cubic phase, $B_1 = B_3$, T_1 and T_3 are interchangeable, and hence the piezo-optical coefficients $\pi^0_{33} = \pi^0_{11}$, and $\pi^0_{31} = \pi^0_{13}$, respectively.

In the ferroelectric tetragonal phase where the total polarization is P_3,

$$\Delta B_1 = \pi^0_{11} T_1 + \pi^0_{13} T_3 + g_{13} P_3^2 + f_{113} T_1 P_3^2 + f_{133} T_3 P_3^2,$$
$$\Delta B_3 = \pi^0_{13} T_1 + \pi^0_{11} T_3 + g_{33} P_3^2 + f_{313} T_1 P_3^2 + f_{333} T_3 P_3^2. \qquad (4)$$

In order to obtain the expressions for the piezo-optical coefficients in the tetragonal phase, the total polarization, which includes the spontaneous polarization P_s and the induced polarization due to the external field, should be calculated. Under the constant electric field condition (constant E), the total polarization P_3 can be derived from the piezoelectric constitutive equation as $P_3 = P_s + d_{31} T_1 + d_{33} T_3$, where d_{31} and d_{33} are the piezoelectric constants of the crystal.[11] Substituting P_3 into Eq. (4) yields

TABLE II. Electro-optic coefficients (r_{ij}), piezoelectric constants (d_{ij}), and dielectric constant (K_3) in PZN–PT single crystals.

Composition	d_{31} (pC/N)	d_{33} (pC/N)	r_{33} (pm/V)	r_{13} (pm/V)	K_3
0.9PZN–0.1PT	−247	770	177	0	1000
0.88PZN–0.12PT	−210	610	134	7	800

$$\begin{aligned}\Delta B_1 &= g_{13}P_s^2+(\pi_{11}^0+2g_{13}P_sd_{31}+f_{113}P_s^2)T_1\\ &\quad+(\pi_{13}^0+2g_{13}P_sd_{33}+f_{133}P_s^2)T_3,\\ \Delta B_3 &= g_{33}P_s^2+(\pi_{13}^0+2g_{33}P_sd_{31}+f_{313}P_s^2)T_1\\ &\quad+(\pi_{11}^0+2g_{33}P_sd_{33}+f_{333}P_s^2)T_3.\end{aligned}\tag{5}$$

The first term in Eq. (5) represents the spontaneous birefringence by the PO effect due to the spontaneous polarization in the ferroelectric phase. The second and third terms are the refractive index changes as a consequence of the applied stress under constant electric field, which are photoelastic effects. Hence, the piezo-optical coefficients π^E can be expressed as

$$\begin{aligned}\pi_{11}^E &= \pi_{11}^0+2g_{13}P_sd_{31}+f_{113}P_s^2,\\ \pi_{13}^E &= \pi_{13}^0+2g_{13}P_sd_{33}+f_{133}P_s^2,\\ \pi_{31}^E &= \pi_{13}^0+2g_{33}P_sd_{31}+f_{313}P_s^2,\\ \pi_{33}^E &= \pi_{11}^0+2g_{33}P_sd_{33}+f_{333}P_s^2.\end{aligned}\tag{6}$$

Under the constant electric displacement condition (constant D), the total polarization P_3 equals $P_s+d_{31}T_1/K_3+d_{33}T_3/K_3$, where K_3 is the relative permittivity.[11] So, the piezo-optical coefficient π^D can also be derived as

$$\begin{aligned}\pi_{11}^D &= \pi_{11}^0+2g_{13}P_sd_{31}/K_3+f_{113}P_s^2\approx\pi_{11}^0+f_{113}P_s^2,\\ \pi_{13}^D &= \pi_{13}^0+2g_{13}P_sd_{33}/K_3+f_{133}P_s^2\approx\pi_{13}^0+f_{133}P_s^2,\\ \pi_{31}^D &= \pi_{13}^0+2g_{33}P_sd_{31}/K_3+f_{313}P_s^2\approx\pi_{13}^0+f_{313}P_s^2,\\ \pi_{33}^D &= \pi_{11}^0+2g_{33}P_sd_{33}/K_3+f_{333}P_s^2\approx\pi_{11}^0+f_{333}P_s^2.\end{aligned}\tag{7}$$

Since for material studied here K_3 is around 1000, the approximation in Eq. (7) is reasonable.

In the ferroelectric tetragonal phase the linear electro-optic effect is related to the quadratic PO effect, as $r_{13}=2g_{13}\epsilon_3P_s$ and $r_{33}=2g_{33}\epsilon_3P_s$, where r_{13} and r_{33} are the linear electro-optic coefficients, and ϵ_3 are the dielectric permittivity of the crystal.[5] Therefore, Eq. (6) can be rewritten as

$$\begin{aligned}\pi_{11}^E &= \pi_{11}^0+r_{13}d_{31}/\epsilon_3+f_{113}P_s^2,\\ \pi_{13}^E &= \pi_{13}^0+r_{13}d_{33}/\epsilon_3+f_{133}P_s^2,\\ \pi_{31}^E &= \pi_{13}^0+r_{33}d_{31}/\epsilon_3+f_{313}P_s^2,\\ \pi_{33}^E &= \pi_{11}^0+r_{33}d_{33}/\epsilon_3+f_{333}P_s^2,\end{aligned}\tag{8}$$

and Eq. (7) as,

$$\begin{aligned}\pi_{11}^E &= \pi_{11}^D+r_{13}d_{31}/\epsilon_3,\\ \pi_{13}^E &= \pi_{13}^D+r_{13}d_{33}/\epsilon_3,\\ \pi_{31}^E &= \pi_{31}^D+r_{33}d_{31}/\epsilon_3,\\ \pi_{33}^E &= \pi_{33}^D+r_{33}d_{33}/\epsilon_3.\end{aligned}\tag{9}$$

Equation (9) shows that the difference between the π^E and π^D is caused by the combination of both piezoelectric and electro-optic effects. If either the piezoelectric or electro-optic effects are equal to zero, then π^E should be equal to π^D. By knowing the relevant coefficients, this difference can also be directly calculated from Eq. (9). Making use of the electro-optic coefficients measured in Ref. 5, the piezoelectric coefficients and dielectric constants measured here that are listed in Table II,[5,6] the differences $\pi_{ij}^E-\pi_{ij}^D$ are evaluated. As shown in Table III, the calculated differences match quite well with the measured ones.

From the measured results, some of the coefficients in Eq. (2) can be estimated. The quadratic PO coefficients g_{ijmn} have been discussed in Ref. 5 and from Eq. (7), one can get,

$$\begin{aligned}\pi_{33}^D-\pi_{11}^D &\approx (f_{333}-f_{113})P_s^2,\\ \pi_{13}^D-\pi_{31}^D &\approx (f_{133}-f_{313})P_s^2.\end{aligned}\tag{10}$$

Using the values in Table I from 0.9PZN–0.1PT and $P_s=0.4\,\mathrm{C/m^2}$, $f_{333}-f_{113}=24\times10^{-12}\,\mathrm{m^6/NC^2}$ and $f_{133}-f_{313}=13\times10^{-12}\,\mathrm{m^6/NC^2}$ are obtained.

It should also be pointed out that the coefficients in Eq. (2) should remain nearly constant as the PZN–PT crystal composition changes from 0.9PZN–0.1PT to 0.88PZN–0.12PT. As a result, Eq. (7) reveals that the piezo-optical coefficients π^D should not change with composition for the two compositions investigated. Indeed, π_{33}^D measured from the two compositions are nearly the same. The observed difference in other π^D is caused by the experiment error, where except π_{33}, the correction term due to the stress induced sample dimension change is the same as or even larger than the term from the stress induced refractive change. The

TABLE III. Difference of A–O coefficients between constant E and constant D conditions ($\times10^{-12}\,\mathrm{m^2/N}$).

0.9PZN–0.1PT	$\pi_{33}^E-\pi_{33}^D$	$\pi_{13}^E-\pi_{13}^D$	$\pi_{11}^E-\pi_{11}^D$	$\pi_{31}^E-\pi_{31}^D$
Calculated	15.4	0	0	−4.9
Measured	13.6	0.9	−0.1	−5.8
0.88PZN–0.12PT	$\pi_{33}^E-\pi_{33}^D$	$\pi_{13}^E-\pi_{13}^D$	$\pi_{11}^E-\pi_{11}^D$	$\pi_{31}^E-\pi_{31}^D$
Calculated	11.5	0.6	−0.2	−4.0
Measured	12.2	−1.1	−0.5	−5.4

larger value of π_{33}^E for 0.9PZN–0.1PT in comparison with 0.88PZN–0.12PT is the MPB effect as discussed in the Introduction.

It is also interesting to compare the piezo-optical coefficients for PZN–PT crystals investigated here with the currently widely used acousto-optic material TeO_2, which has $\pi_{11} = -19.19 \times 10^{-12}\,m^2/N$ and $\pi_{12} = 19.85 \times 10^{-12}\,m^2/N$.[12] Apparently, 0.9PZN–0.1PT single crystal has a comparable photoelastic effect. In addition, this material has relatively large elastic compliance which results in a lower sound velocity (~2400 m/s).[13] Therefore, the figure of merit for an acousto-optic device will also be large.[2]

IV. CONCLUSIONS

The photoelastic effect of 0.9PZN–0.1PT single crystals was characterized under uniaxial stress using an interferometer method. The piezo-optical coefficients π_{33}, π_{31}, π_{11}, and π_{13} under both constant electric field and constant electric displacement conditions were measured. It was found that the piezo-optical coefficient π_{33}^E is $19.8 \times 10^{-12}\,m^2/N$, which is very large in comparison with currently known photoelastic materials. Therefore, the crystal is a very good candidate for stress sensors and other acousto-optic devices. In particular, since this material also possesses a very large electro-optic effect[5,6] and piezoelectric effect,[3,4,7] the combination of these three effects make it very attractive and more flexible in producing high performance multifunctional devices.

ACKNOWLEDGMENTS

The authors wish to thank Drs. S.-E. Park, T. Shrout, and S.-F. Liu for supplying the PZN–PT single crystals used in this study. This work was supported by the Office of Naval Research.

[1] J. A. Bucaro, H. D. Dardy, and E. F. Carome, Appl. Opt. **16**, 1761 (1977).
[2] T. S. Narasimhamurty, *Photoelastic and Electro-Optic Properties of Crystals* (Plenum, New York, 1981).
[3] S.-E. Park and T. R. Shrout, J. Appl. Phys. **82**, 1804 (1997).
[4] S.-F. Liu, S.-E. Park, T. R. Shrout, and L. E. Cross, J. Appl. Phys. **85**, 2810 (1999).
[5] Y. Lu, Z.-Y. Cheng, S.-E. Park, S.-F. Liu, and Q. M. Zhang, Jpn. J. Appl. Phys., Part 1 **39**, 141 (2000).
[6] Y. Barad, Y. Lu, Z.-Y. Cheng, S.-E. Park, and Q. M. Zhang, Appl. Phys. Lett. **77**, 1247 (2000).
[7] J. Kuwata, K. Uchino, and S. Nomura, Ferroelectrics **37**, 579 (1981).
[8] O. Noblanc, P. Gaucher, and G. Calvarin, J. Appl. Phys. **79**, 4291 (1996).
[9] Q. M. Zhang, S. J. Jang, and L. E. Cross, J. Appl. Phys. **65**, 2807 (1989).
[10] P. Bernasconi, M. Zgonik, and P. Günter, J. Appl. Phys. **78**, 2651 (1995).
[11] J. F. Nye, *Physical Properties of Crystals: Their Representation by Tensors and Matrices* (Oxford University Press, New York, 1985).
[12] N. Uchida and Y. Ohmachi, J. Appl. Phys. **40**, 4692 (1969).
[13] S. Saitoh, T. Kobayashi, K. Harada, S. Shimanuki, and Y. Yamashita, IEEE Trans. Ultrason. Ferroelectr. Freq. Control **45**, 1071 (1998).

Appendix 22

Y. Lu, Z.–Y. Cheng, and Q.M. Zhang, "Optic Detection of Ultrasound based on Time Domain Quadrature Detection," submitted to IEEE (2001).

Optic Detection of Ultrasound based on Time Domain Quadrature Detection

Y. Lu*, Z.-Y. Cheng, and Q. M. Zhang

Department of Electrical Engineering and Materials Research Institute

The Pennsylvania State University, University Park, PA 16802

Abstract:

We report on an optic detection of ultrasound based on a time domain quadrature detection approach. This approach eliminates the need to actively feedback control of the optic detector to an operation point. Making use of $Pb(Zn_{1/3}Nb_{2/3})O_3$-$PbTiO_3$ single crystal, this new approach is demonstrated. In addition, the high piezoelectric response of $Pb(Zn_{1/3}Nb_{2/3})O_3$-$PbTiO_3$ also makes it possible to use the optic detector as an ultrasonic transmitter, which is distinctively advantageous compared with other optic detectors (passive detectors) reported.

*Current address: Lucent Technologies, Norcross, GA 30071.

PACS No. 78.20.Hp, 42.79.Jq, 77.84.-s, 43.38. Zp

Sub. IEEE 2001

Optic detection of ultrasound has attracted a great deal of attention in the past two decades.[1-7] Compared with the piezoelectric detection of the ultrasonic waves, optic detection offers the advantages of a small active device size, simplicity of construction, and no electromagnetic interference (EMI) noise. The operation principle of most optic detectors is based on the interference signal of the reflections from the two surfaces of the detector, as schematically shown in figure 1(a). In this detection scheme, the interferometer transfer function (ITF), which measures the change in the optic intensity caused by the acoustic wave, usually has a functional form as schematically shown in figure 1(b), where ϕ is the directly proportional to the optic path length difference between the two reflected beams. The incident acoustic wave induces change in ϕ which is detected by the interference signal. Under the assumption that this change in ϕ is very small (as schematically shown in figure 1(b)), the etalon is biased in an operation point (the middle point between the interference maxima and minima) to create a linear region between the input stress signal and the optic intensity change and also to maximize the ITF. The optic bias point is normally achieved via a feedback control such as tuning the laser frequency.[6,7] Such an approach introduces extra complication in the optic detector and could be a problem when used in an array transducer where the active tuning of each array element may be very difficult concerning a large number of array elements.

This letter describes a new approach for the optic detection of ultrasonic signals, which eliminates the need for the feedback control of the operation point. As will be seen in the following, such an approach is made feasible by the recent development on $Pb(Zn_{1/3}Nb_{2/3})O_3$-$PbTiO_3$ (PZN-PT) single crystals, which have been shown to possess a very high piezoelectric response and high acousto-optic responses.[8-10]

For a Fabry-Perot etalon with the surface reflectivity R, the incident acoustic stress wave causes change in the optic path length difference between the two beams ($2n\ell$, where n is the refractive index and ℓ is the etalon thickness) due to the elastic effect and acousto-optic effect. The resulting interference signal I_R can be derived as,

$$\frac{I_R}{I_0} = \frac{4R\sin^2(\phi/2)}{(1-R)^2 + 4R\sin^2(\phi/2)} \qquad (1)$$

where the phase factor $\phi = \frac{4\pi n\ell}{\lambda}$ and λ is laser wavelength, and I_0 is the incident laser intensity.

For a low finesse F-P etalon (R<<1) or for an etalon with one surface reflectivity near 1 and the other R<<1 (such as the one schematically shown in figure 1(a)), equation (1) can be reduced to

$$\frac{I_R}{I_0} \approx 2R(1-\cos(\phi)) \qquad (2)$$

As we have pointed out, in most of the current detection scheme, a small change in ϕ is assumed which leads to a linear relationship between the change in the optic pathlength and the interference signal

$$\delta I_R = I_0 \frac{8\pi R}{\lambda}\sin(\phi)\delta(n\ell) \qquad (3)$$

When a feedback loop is used to bias the interferometer at $\phi=(m+1/2)\pi$, a maximum sensitivity is achieved. Clearly, for such a detector to function properly, a feedback control of the operation point is required.

Now, if instead of a single interference signal, a two interference signal detection scheme is used. Further, if the phase in the two interference signals is $\pi/2$ with respect to each other (quadrature detection), the one signal will be from equation (2) and omit the DC component and "-" sign,

$$I_{R1} = 2RI_0 \sin(\phi)$$

and the second will be

$$I_{R2} = 2RI_0 \cos(\phi).$$

For these two signals, through a signal processing as outlined in figure 2 where for simplicity we assume the coefficient before the sine and cosine functions as 1, one can directly obtain the whole information of ϕ. In such a measurement scheme, there is no need to bias the detector in an operation point and no limitation on the small signal assumption, which would also significantly improve the dynamic range of the detection.

In the following, we present a device realization of this quadrature detection scheme which is made feasible by the high piezoelectric activity in the PZN-PT single crystals. The schematic of the set-up is shown in figure 3 where a standard ultrasonic transducer is used to generate an acoustic signal and a PZN-PT single crystal is used for the detection of acoustic signal. The distance between the transducer and optic detector is chosen such that the detector is located at the far field.[11] For high optic quality, the single crystal is chosen at the tetragonal composition and poled along <001> direction (the z-axis in figure 1(a)).[8,9] Because of the relatively high elastic compliance (s_{33}^E=95x10^{-12} m^2/N) and high piezo-optic coefficient (large refractive index change),[10] PZN-PT single crystals offer high sensitivity in the change of the optic path length $2nl$ from the acoustic signal. Moreover, the high piezoelectric response makes it possible to use a

low voltage signal to induce the thickness change for the quadrature signals as will be discussed in the following.[9]

For the demonstration purposes of this quadrature detection scheme we use an unltrasonic transducer with the center frequency at 5 MHz and the thickness of the PZN-PT single crystal is also chosen to match 5 MHz resonance condition to maximize the sensitivity. One surface (the detection surface) of the crystal faces the water and the other is backed in air. For the experiments presented here, the optic detector is not optimized in its ultrasonic performance (for example, no matching or backing are used) except the thickness of the crystal to match the resonance frequency of 5 MHz.[11] To realize a low finesse F-P etalon, ITO (Indium Tin Oxide) electrode (1500 A thickness) is used for the partial reflection surface as well as served as the electrode. Evaporated Aluminum is served as the other high reflection surface and also the electrode. A test on the interference intensity versus the optic pathlength indicates that the optic detector indeed behaves as a low finesse F-P etalon.

To produce the two interference signals, we use two consecutive identical pulses separated by 11 μs time interval (this time interval is needed to avoid the ringing in the transducer and optic detector from the first pulse overlapping with the second pulse, longer time interval is also used and there is no change in the result) from the transducer. For the optic detector, after receiving the first pulse in an 11 μs time period, a bias voltage is applied to the crystal to cause change in the thickness in the etalon to produce the phase change in ϕ of $\pi/2$ and the detector catches the second pulse. This bias voltage is determined by the piezoelectric coefficient of the crystal used in the optic detector and for the PZN-PT single crystal used here, d_{33}=770 pm/V which is quite

high compared with common piezoceramics. The field applied to produce the $\pi/2$ phase change is 2 kV/cm. Presented in figure 4 is the resulting optic signal by combining the two interference signals. The signal processing is performed by MATLAB at a sampling rate of 100 MHz. For the comparison, we also measured the interference signal in single channel detection when the F-P etalon is biased at the operation point as shown in figure 1(b) and the result is also presented in figure 4. It is obvious that the two results match each other quite well. The small difference is caused by the small deviation in the etalon of the phase change ϕ from $\pi/2$.

From this detection principle, it is clear that this time domain duatrature detection requires the objects to be probed to be stationary in the time duration of the two consecutive pulses. For most of the ultrasonic imaging and non-destructive evaluation, this requirement can be satisfied since the operation frequency of the ultrasound is in the range above 1 MHz and the time duration for the two pulses is at most 30 to 40 μs.

It should also be pointed out that although in the experiment reported in this letter, an external ultrasonic transducer was used to generate the ultrasound signal. The PZN-PT single crystal itself is an excellent acoustic transmitter material as has been demonstrated in many other experiments.[12,13] Therefore, the optic etalon here can itself be used as a transmitter which is distinctively different from almost all the other optic detectors reported in the literature where the detector is merely a passive element and another transducer or ultrasonic generation mechanism is required to produce the probing pulses to be detected.[1-7]

This work was supported by the Office of Naval Research.

References:

1. A. J. Ducaro, H. D. Dardy, and E. F. Carome, Appl. Optics, **16**, 1761 (1977).
2. J. Stausfield and W. Eisenmenger, Ultrasonics, **31**, 267 (1993).
3. P. Nash, IEEE Proc.—Radar, Sonar Navig., **143**, 204 (1996).
4. C. B. Scruby and L. E. Drain, *Laser Ultrasonics* (Adam Higher, Bristol, Philadelphia, and New York 1990).
5. C. Koch, Ultrasonics, **34**, 687 (1996).
6. J. Hamilton, C. Brooks, G. Vossler, and M. O'Donnell, IEEE Trans. Ultras. Ferro. and Freq. Contr. **45**, 719 (1998).
7. P. Beard, F. Perennes, and T. Mills, IEEE Trans. Ultras. Ferro. and Freq. Contr. **46**, 1575 (1999).
8. J. Kuwata, K. Uchino, and S. Nomura, Ferro. **37**, 579 (1981).
9. S.-E. Park and T. R. Shrout, J. Appl. Phys. **82**, 1804 (1997).
10. Y. Lu, Z.-Y. Cheng, Y. Barad, and Q. M. Zhang, Appl. Phys. Lett. **89**, 5075 (2001).
11. G. Kino, *Acoustic Waves: Devices, Imaging, and Analog Signal Processing* (Prentice-Hall, Inc. NJ 1986).
12. S. Saitoh, T. Takeuchi, T. Kobayashi, K. Harada, S. Shimanuki, and Y. Yamashita, IEEE Trans. Ultrason. Ferroelect. & Freq. Contr. 41, 152 (1999).
13. T. Ritter, K. K. Shung, X. Geng, P. D. Lopath, S.-E. Park, and T. Shrout, , IEEE Trans. Ultrason. Ferroelect. & Freq. Contr., 47, 792 (2000).

Figure captions:

Figure 1. (a) Schematic of the Fabry-Parot etalon for detecting of ultrasound pulses used here. The voltage pulse can be used to change the optic pathlength of the detector for the quadrature detection. (b) Schematic of the relationship between the interference intensity and phase difference between the two beams. In conventional optic detection, an active feedback control is used to stabilize the detector at the operation point.

Figure 2. Schematic of the signal processing for the two signals from the quadrature detection where digital signal processing is used.

Figure 3. Schematic of the test set-up for the optic detector based on time domain quadrature detection. An ultrasonic analyzer and transducer are used to generate the two consecutive ultrasonic pulses to be detected by the optic detector. In the figure, PBS is a polarized beam splitter.

Figure 4. Comparison between the signal detected based on time domain quadrature detection (solid curve) and the signal from the single phase detection (dashed curve) in which the detector is controlled to be at the operation point as shown in figure 1(b).

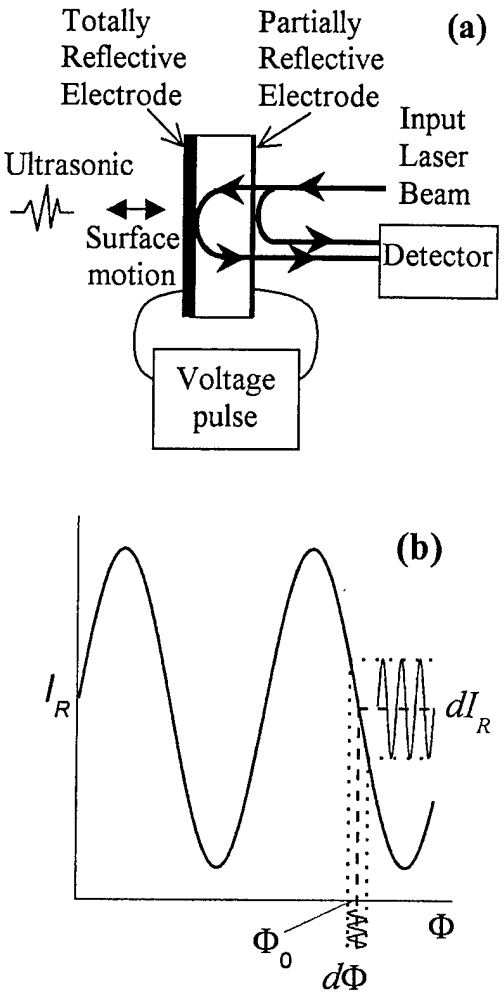

Figure 1 Yu LU, *et al.*

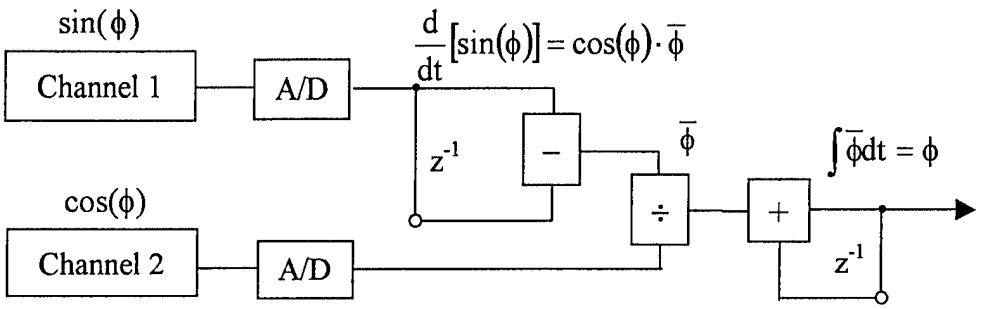

Figure 2 Yu LU, *et al.*

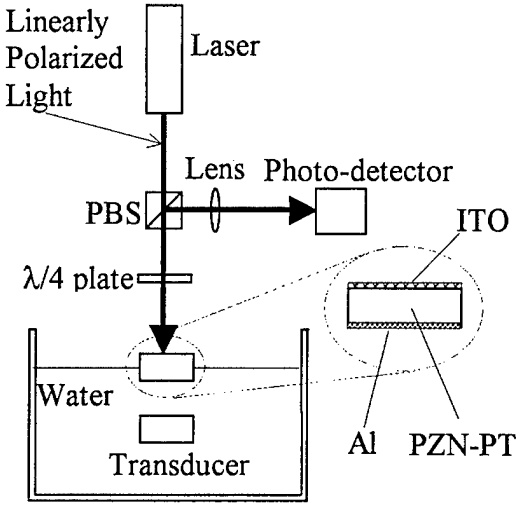

Figure 3 Yu LU, *et al.*

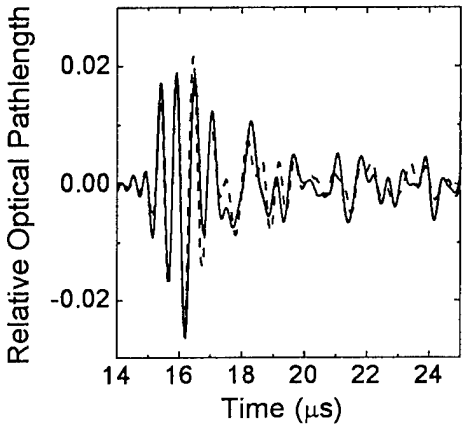

Figure 4 Yu LU, *et al.*

Appendix 23

Yu Lu, Zhong-Yang Cheng, Seung-Eek Park, Shi-Fang Liu, and Qiming Zhang, "Linear Electro-optic Effect of $0.88Pb(Zn_{1/3}Nb_{2/3})O_3$–$PbTiO_3$ Single Crystal," Japanese Journal of Applied Physics, 39, 141–145 (January 2000).

Jpn. J. Appl. Phys. Vol. 39 (2000) pp. 141–145
Part 1, No. 1, January 2000

Linear Electro-optic Effect of $0.88Pb(Zn_{1/3}Nb_{2/3})O_3$–$0.12PbTiO_3$ Single Crystal

Yu LU, Zhong-Yang CHENG, Seung-Eek PARK, Shi-Fang LIU and Qiming ZHANG*

Materials Research Laboratory and Department of Electrical Engineering, The Pennsylvania State University, University Park, PA 16802, USA

(Received August 23, 1999; accepted for publication October 14, 1999)

The linear electro-optic (E-O) coefficients of poled $0.88Pb(Zn_{1/3}Nb_{2/3})O_3$–$0.12PbTiO_3$ single crystal were characterized using an automated scanning Mach-Zehnder interferometer and the senarmont compensator method at room temperature. They were obtained at a wavelength of 632.8 nm: $r_{33} = 134$ pm/V, $r_{13} = 7$ pm/V, $r_{51} = 462$ pm/V, and $r_c = 131$ pm/V respectively and the refractive indices: $n_e = 2.57$ and $n_o = 2.46$. The large r_{51} coefficient compared with r_{33} is caused by the high dielectric constant at perpendicular to the polar-axis compared with the dielectric constant along the c-axis. Comparison with the quadratic E-O coefficients measured at near and above the Curie temperature suggests that the values of the quadratic E-O coefficients measured earlier may be smaller than the intrinsic ones due to the influence of micro-polar regions. The development of an automated scanning Mach-Zehnder interferometer, which is less susceptible to the errors caused by the laser intensity fluctuation and drafting in the optical path length in the system, is also described.

KEYWORDS: ferroelectric, electro-optic, refractive index, interferometer

1. Introduction

Ferroelectric crystals, such as $LiNbO_3$ and KH_2PO_4 (KDP), are widely used in electro-optic (E-O) devices such as electro-optic modulators, electro-optic switches, and light valves.[1,2] More recently, there is an increased interest in the relaxor ferroelectric crystal $Pb(Zn_{1/3}Nb_{2/3})O_3$–$PbTiO_3$ (PZN–PT), which over a broad composition range possesses a very high electromechanical coupling factor, piezoelectric coefficients, and field induced strain response.[3–7] A uniqueness of this crystal system is that relatively high quality single crystals can be grown at compositions near the tetragonal-rhombohedral morphotropic phase boundary (MPB). It is well known that many of the material responses exhibit increased activity near a MPB.[8,9] In this paper, we report the result of the linear E-O coefficients in 0.88PZN–0.12PT single crystal, which is near the MPB on the tetragonal side.[3,5]

The E-O effect describes the change of refractive index Δn_{ij} due to the applied field:

$$\Delta n_{ij} = -\frac{1}{2} n_{ij}^3 \left(\sum_{j=1}^{3} r_{ijk} E_k + \sum_{j,k=1}^{3} R_{ijkl} E_k E_l \right) \quad (1)$$

where r_{ijk} and R_{ijkl} are linear and quadratic E-O coefficients, respectively. The quadratic coefficients for PZN–PT crystals at temperatures near and above the dielectric constant maximum have been characterized earlier, and in this paper all three non-zero linear E-O coefficients ($r_{33} = r_{333}$, $r_{13} = r_{113}$, and $r_{51} = r_{311}$) were measured for 0.88PZN–0.12PT in the ferroelectric tetragonal phase (room temperature).[10] The comparison of the two results, indicates that the coefficients measured at the high temperature phase may be affected by the relaxor ferroelectric nature of the PZN–PT system, and will be discussed in the paper. In addition, we will also report briefly a modified interferometric method for the characterization of these coefficients, which is based on the dynamic scanning concept.

*To whom correspondence should be addressed. E-mail: qxz1@psu.edu

2. Experimental

2.1 *0.88PZN–0.12PT single crystal and related E-O coefficients*

The 0.88PZN–0.12PT crystal used in this study was grown using the high temperature flux method.[5,6,11] It is known that 0.88PZN–0.12PT has a tetragonal structure at room temperature and that the spontaneous polarization is along ⟨001⟩ (c-axis) direction.[3–5] The single crystal sample was oriented along the ⟨001⟩ direction using a Laue camera, then the ⟨100⟩ faces were polished to optical quality. The sample was poled at a temperature of 230°C, which is much higher than the paraelectric to ferroelectric phase transition temperature, with an electric field of 5 kV/cm for 30 min. Then, the sample was slowly cooled down to room temperature under the electric field. It was found that poling at room temperature resulted in fractures in the sample since the domain switch induces very large strain, expansion along the poling direction. The dimension of the sample is $1.85 \times 3.85 \times 4.83$ mm^3 and the poling field was applied across the 3.85 mm thickness.

For the tetragonal symmetry, there are three non-zero E-O coefficients, i.e., r_{33}, r_{13}, and r_{51}. In this study, r_{33} and r_{13} were measured using a interferometric method, where the applied field E_3 is along the c-axis and the light passes through the sample along the ⟨100⟩ axis (a-axis),

$$\Delta n_e = -n_e^3 r_{33} E_3/2 \quad (2a)$$

$$\Delta n_o = -n_o^3 r_{13} E_3/2 \quad (2b)$$

where n_o and n_e denote the refractive index perpendicular and parallel to the c-axis, respectively. In the r_{33} measurement, the polarization direction of the laser beam is along the c-axis and in measuring r_{13}, the polarization direction is perpendicular to the c-axis.

For the PZN–PT crystal studied, the E_3 field will also induce a change in the sample thickness along the path of the laser beam due to the piezoelectric effect,[12]

$$\Delta l_1 = d_{31} E_3 l_1$$

where l_1 is the thickness of the crystal along the beam path and d_{31} is the piezoelectric coefficient. Hence, the total measured optical path length change in the interferometric method

is $\Delta n_i \cdot l_1 + (n_i - 1) \cdot \Delta l_1$.

The E-O coefficient $r_{51}(\Delta(1/n_{31}^2) = \Delta(1/n_5^2) = r_{51}E_1)$ was measured by the Senarmont compensator method, where the applied field E_1 is along the $\langle 010 \rangle$ axis perpendicular to both the c-axis and the light propagation direction.[13] The polarization direction of the laser beam is canted 45° with respect to the c-axis. In the r_{51} measurement, there is no correction due to the piezoelectric effect.

Using the Senarmont compensator method, the E-O coefficient r_c, which is defined as $r_c = r_{33} - n_o^3 r_{13}/n_e^3$ and determines the half-wave voltage of the material, was also measured.[13,14]

2.2 *Operation principle of scanning Mach-Zehnder interferometer for E-O coefficient measurement*

Shown in Fig. 1 is a typical Mach-Zehnder interferometer.[15] The interference pattern at the detection point depends on the optic path length difference ($\Phi = 2\pi(n_R l_R - n_S l_S)/\lambda$, where n and l are the refractive indices and the path lengths respectively, R and S in subscript expresses the reference and signal arms, respectively) between the signal and reference beams,

$$I = I_1 + I_2 + 2\sqrt{I_1 I_2}\cos(\Phi) = \frac{1}{2}(I_{max} + I_{min}) + \frac{1}{2}(I_{max} - I_{min})\cos(\Phi) \quad (3)$$

where $I_{max} = (\sqrt{I_1} + \sqrt{I_2})^2$ and $I_{min} = (\sqrt{I_1} - \sqrt{I_2})^2$ are the maximum and minimum intensities of interference fringes, respectively, and I_1 and I_2 are the light intensities of signal beam and reference beam, respectively. From eq. (3), one can find that when Φ has a small change ($\Delta\Phi$) around $\Phi_0 = (m + 1/2)\pi$, $m = 0, \pm 1, \ldots$, $\cos(\Phi_0 + \Delta\Phi) \approx \pm\Delta\Phi$, and the $\pm$ signs depend on the value of m, and

$$\Delta I = I - \frac{1}{2}(I_{max} + I_{min}) = \pm\frac{1}{2}(I_{max} - I_{min})\Delta\Phi. \quad (4)$$

Hence, by stabilizing the system at Φ_0 (working point), the change of interference intensity will depend linearly on the change of the optic path length. When this change is measured by a photo-detector, eq. (4) can be converted into the voltage form as:

$$\Delta\Phi = \frac{v_{out}}{(V_{max} - V_{min})/2} = \frac{v_{out}}{V_{p\text{-}p}/2}. \quad (5)$$

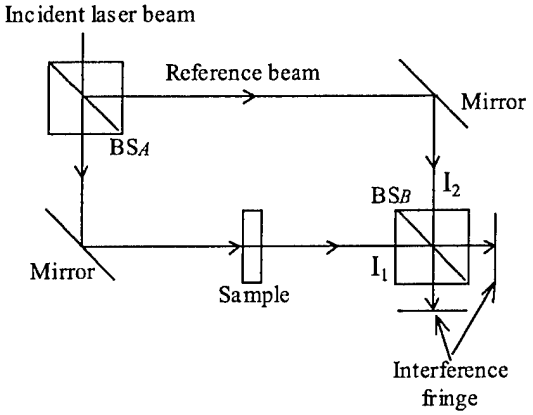

Fig. 1. Schematic drawing of a typical Mach-Zehnder interferometer.

Where v_{out} corresponds to ΔI, V_{max} and V_{min} correspond to I_{max} and I_{min} respectively and $\Delta\Phi = 2\pi\Delta(nl)/\lambda$. For E-O or piezoelectric coefficient measurement under an ac electric field of frequency (f_0), a lock-in amplifier can be used to measure v_{out} which yields a high sensitivity of the system in resolving the change in $\Delta\Phi$.

However, in developing a computer controlled experimental set-up to measure the change in the optic path length (and hence $\Delta\Phi$), we found that the approach of stabilizing the system near the working point (by using a feedback loop to control the path length of the reference arm) is not convenient. The change in the incident light intensity and other factors such as air turbulence in the system and the variation of the light absorption in the sample due to thermal and electric field can cause shift in the working point light intensity.[16] As a result, the stabilized experimental point will be no longer at Φ_0. Further more, those changes will also result in changes in I_{max} and I_{min}, causing errors in the experimental results on $\Delta(nl)$.

If instead of stabilizing the system at any specific point, an optic translation stage is used to drive a slow change in the path length l_R of the reference arm, Φ will be changed continuously. As a result, the interference intensity will change with time, from which I_{max} and I_{min} can be measured readily. If an AC electric field with a frequency f_0 is applied to a sample which causes a small change (much smaller than the wave length) in the optic path length in the signal arm, the change in the phase Φ will be $\Phi_{ref} + \Delta\Phi$. The resulting signal will be:

$$I = \frac{1}{2}(I_{max} + I_{min}) + \frac{1}{2}(I_{max} - I_{min})\cos(\Phi_{ref} + \Delta\Phi) \quad (6)$$

where Φ_{ref} describes the drifting in the phase caused by the optic path length change of the reference arm and also in the signal arm due to slow drifting, and $\Delta\Phi$ is the phase change caused by the sample due to the applied AC electric field. Since $\Delta\Phi$ is very small, one can get

$$I = \left(\frac{1}{2}(I_{max} + I_{min}) + \frac{1}{2}(I_{max} - I_{min})\cos\Phi_{ref}\right) - \left(\frac{1}{2}(I_{max} - I_{min})\sin\Phi_{ref}\right)\Delta\Phi. \quad (7)$$

Therefore, when $\Phi_{ref} = (m + 1/2)\pi$, eq. (7) is reduced to eq. (4). When $\Phi_{ref} = m\pi$, the second term on the right hand side of the equation is zero and the first term yields I_{max} and I_{min}. Thus, $V_{p\text{-}p}/2$ can be obtained. Hence, in one scanning period of the reference beam, all the quantities in eq. (5) can be determined and yield $\Delta\Phi$. Clearly, even if v_{out}, V_{max} and V_{min} may vary due to various noise sources, the corresponding variation in $\Delta\Phi$ which is the ratio between them [eq. (5)] will be much smaller. This has been verified experimentally. In addition, the data accuracy can be improved further by averaging $\Delta\Phi$ thus obtained over long time period.

Based on these considerations, a Mach-Zehnder interferometer with the reference arm scanned was developed to measure E-O or piezoelectric coefficients (as schematically shown in Fig. 2). In this scanning Mach-Zehnder interferometer, the reference mirror is driven by a servo-transducer made of piezoelectric material. In experiments for E-O or piezoelectric measurement, f_0 typically runs from 100 Hz to 100 kHz, and the corresponding scan frequency may be varied from 0.003 Hz to 3 Hz to satisfy the condition that the scanning fre-

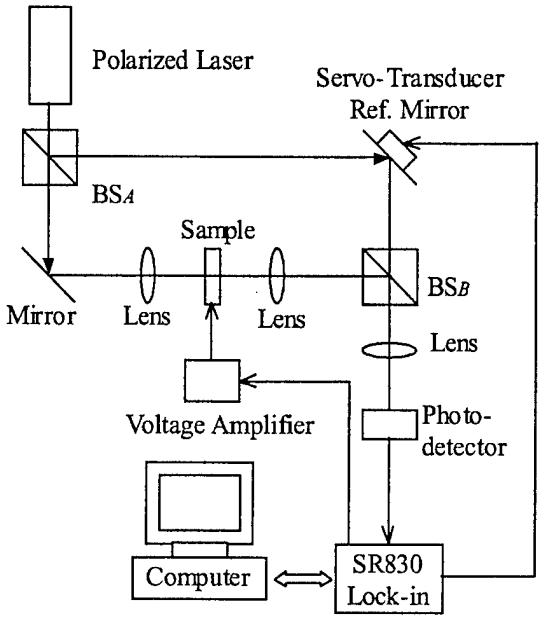

Fig. 2. Schematic drawing of the setup of the automated scanning Mach-Zehnder interferometer developed for E-O measurement.

quency is much lower than the signal frequency. Both the AC and DC components of the photo-detector output are transmitted to a digital lock-in amplifier (SRS SR830). A computer is used to control the system and acquire the data from the SR830 through a GPIB cable. The system can be controlled easily by the computer over a long time period. The computer software was programmed using LabView 4.1.

3. Experiment Results and Discussion

3.1 Experimental results

For the 0.88PZN–0.12PT single crystal used in this experiment, no data of the refractive index at room temperature were available. Hence, the first step is to measure these indices. Although the refractive index can be measured by the minimum deviation method, the sample needs to be made into a wedge shape.[14,15] In order to measure the E-O coefficients, the sample has to be reshaped to a rectangular parallelepiped. Because of the relatively small size sample, instead, Brewster's angle method was used in which only one reflection surface is required.[14,15] Hence the sample used in the refractive index measurement can also be used directly in E-O measurement.

Brewster's angle (θ_B) is the incident angle at which the reflection intensity is zero for polarized light with the polarization direction parallel to the incident plane. The relationship between the refractive index and θ_B is: $n = \tan\theta_B$. By changing the orientation of the crystal with respect to the linearly polarized incident laser beam, both n_o and n_e can be determined. The obtained θ_B for the PZN–PT crystal are 68.75° and 67.84°, yielding $n_o = 2.57 \pm 0.01$ and $n_e = 2.46 \pm 0.01$ at 632.8 nm wavelength for the sample at room temperature.

To facilitate the discussion, apparent E-O coefficients r_{13}^* and r_{33}^* are introduced here to denote the coefficients obtained directly from $\Delta\Phi$ without the correction of the piezoelectric effect,

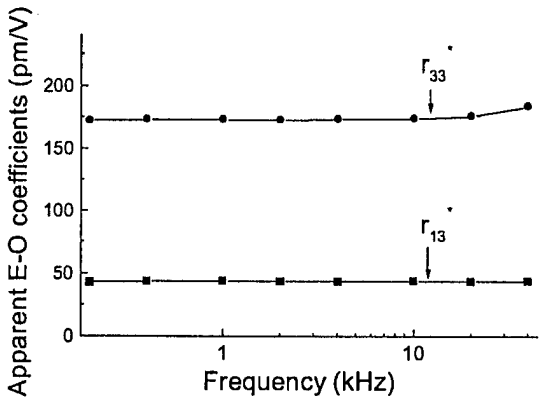

Fig. 3. Apparent E-O coefficients (r_{33}^* and r_{13}^*) measured at different frequencies for 0.88PZN–0.12PT single crystal at room temperature.

$$\Delta(n_e l) = \frac{\lambda}{2\pi}\Delta\Phi = r_{33}^* n_e^3 l E_3/2$$

or

$$\Delta(n_o l) = \frac{\lambda}{2\pi}\Delta\Phi = -r_{13}^* n_o^3 l E_3/2$$

The apparent E-O coefficients r_{13}^* and r_{33}^* are measured separately for the sample under a stress free condition. For a piezoelectric material, it is well known that there are serious resonance frequencies at which the electric field induced strain can no longer be described by the linear piezoelectric equation.[12] This certainly imposes frequency windows in which the E-O coefficient can be measured reliably. In addition, any mechanical resonance in the sample holding system can also cause error in the measurement. In this study, the frequency window used is from 200 Hz to 40 kHz, well below the first (lowest) resonance frequency (f_r) which is at several hundreds kHz. To ensure the weak field condition in the measurement, the applied field is about 15 V/cm which is also well below the room temperature coercive field of about 5 kV/cm.

The results for r_{13}^* and r_{33}^* are shown in Fig. 3. In the frequency range measured, there is no large change of the E-O coefficients with frequency and the average values of r_{13}^* and r_{33}^* are 44±1 pm/V and 173±4 pm/V, respectively. A mechanical resonance due to the sample holding system was observed at frequencies above 40 kHz, which affects the data acquired near 40 kHz.

To subtract the piezoelectric effect, the piezoelectric d_{31} coefficient was measured using a single beam laser interferometer: $d_{31} = -210 \pm 10$ pm/V. From $r_{33} = r_{33}^* + 2(n_e - 1)d_{31}/n_e^3$ and $r_{13} = r_{13}^* + 2(n_o - 1)d_{31}/n_o^3$, the E-O coefficients r_{33} and r_{13} are obtained: $r_{33} = 134 \pm 5$ pm/V and $r_{13} = 7 \pm 2$ pm/V at 632.8 nm wavelength for 0.88PZN–0.12PT at room temperature.

One of the concerns in the single crystal PZN–PT is the imperfect poling which results in residual domains in the sample. This will affect the measured E-O coefficients. In order to check this, the E-O coefficients under high DC bias field were measured. In the experiment, an oil chamber was built so that the sample can be immersed in an insulation oil which prevents electric breakdown through air when the sample is subject to a high DC voltage. Shown in Fig. 4 are the apparent E-O coefficients r_{13}^* and r_{33}^* measured at 1 kHz as a func-

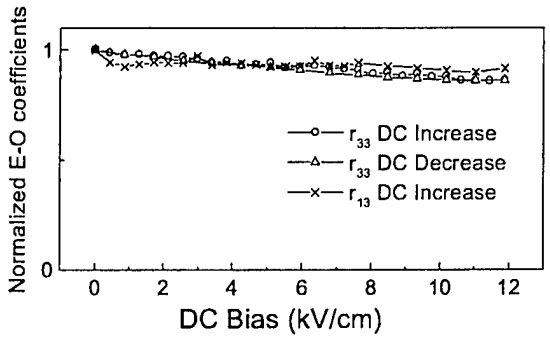

Fig. 4. The E-O coefficients as a function of the DC electric bias field for 0.88PZN–0.12PT single crystal at room temperature.

tion of a DC bias field which is applied parallel to the original poling direction up to 15 kV/cm, much higher than the room temperature coercive field. Apparently, the measured coefficients do not show much change with a DC bias field (except a small decrease which is expected) and as the bias field is reduced to zero, the E-O coefficients return to their original values. The results indicate that the sample used in this study was properly poled.

The r_{51} coefficient measured by the senarmont compensator method is $r_{51} = 462$ pm/V which is much larger than r_{33} and in the frequency range measured, (below 40 kHz), r_{51} does not show much change with frequency.

Using the senarmont compensator method, the E-O coefficient r_c was also characterized. The coefficient measured direct from the experiment data is the apparent coefficient r_c^* which is

$$r_c^* = r_{33}^* - \frac{n_o^3}{n_e^3} r_{13}^* = r_c + \frac{2(n_e - n_o)}{n_e^3} d_{31}. \tag{8}$$

Because the difference between n_e and n_o is very small, the piezoelectric effect [the second term on the right hand side of eq. (8)] has much less effect on r_c compared with r_{13} and r_{33}. The measured value of r_c^* for the sample under stress free condition used above is 128 pm/V. The corresponding coefficient after the correction of the piezoelectric effect is $r_c = 131$ pm/V.

From measured values of n_e, n_o, r_{13} and r_{33}, the E-O coefficient r_c can also be deduced from $r_c = r_{33} - n_o^3 r_{13}/n_e^3$. From the measured results of n_e, n_o, r_{13}^* and r_{33}^*, the calculated r_c^* is 124 pm/V, which is very close to 128 pm/V measured directly using the Senarmont compensator method.

A qualitative aging experiment was also performed on the E-O coefficients and it was found that even the poled sample was used for various other measurements, the E-O coefficients were nearly the same when measured after 3 months. Therefore the optical coefficients reported here are the stable material properties of 0.88PZN–0.12PT single crystal.

3.2 *Discussion*

At this point, it is interesting to compare the results obtained here with those reported earlier. For example, the quadratic E-O coefficients $g_{11} - g_{12}$ and g_{44} were measured by Nomura *et al.* [$\Delta n_{ij} = -(1/2) n_{ij}^3 \sum_{k,l=1}^{3} g_{ijkl} P_k P_l$, where P_k is the polarization component along the k-direction].[10] Since in ferroelectric single crystals, the linear E-O effect can be regarded as a polarization biased quadratic E-O effect,[17] the relationships between the linear E-O coefficients and the quadratic E-O coefficients are:

$$r_{33} - r_{13} = 2K_{33}\varepsilon_0 P_s (g_{11} - g_{12}) \tag{9a}$$

$$r_{51} = K_{11}\varepsilon_0 P_s g_{44} \tag{9b}$$

where $g_{11} = g_{1111}$, $g_{12} = g_{1122}$, and $g_{44} = 2g_{2323}$, K_{33} and K_{11} are the dielectric constant along the c-axis and a-axis, respectively, P_s is the spontaneous polarization, and $\varepsilon_0 = 8.85 \times 10^{-12}$ F/m is the vacuum permittivity.

For the crystal investigated here, at room temperature the dielectric constant was measured to be: $K_{33} = 710$ and $K_{11} = 7630$. From the data of ref. 10, $g_{11} - g_{12} = 0.013\,\mathrm{m^4/C^2}$ and $g_{44} = 0.009\,\mathrm{m^4/C^2}$. Hence, the ratio of $(r_{33} - r_{13})/r_{51}$ is equal to $2K_{33}(g_{11} - g_{12})/K_{11}g_{44} = 0.269$ using the dielectric constant measured here and the g coefficients of ref. 10. Using the value of the r coefficients measured here yields the ratio of $(r_{33} - r_{13})/r_{51} = 0.275$. The agreement between the values obtained using two sets of data is surprisingly good.

The results from the two sets of data can also be compared directly if the spontaneous polarization P_s is known. From the room temperature polarization hysteresis loop, P_s is extrapolated: $P_s = 40\,\mu\mathrm{C/cm^2}$. Substituting P_s and other data to the right hand sides of eq. (9) yields $r_{33} - r_{13} = 65.3$ pm/V and $r_{51} = 243$ pm/V. The results show that the linear E-O coefficients deduced from the quadratic E-O coefficients measured at temperatures near and above the dielectric constant maximum are about half of the values of the corresponding coefficients measured directly at poled samples (127 pm/V and 462 pm/V, respectively). In other words, either P_s and/or the g coefficients used in eq. (9) are smaller than the intrinsic values. Although one cannot rule out that the intrinsic P_s value for the crystal studied may be higher than $40\,\mu\mathrm{C/cm^2}$, the difference will not be large enough to account for the discrepancy observed here.

In studies of the relaxor ferroelectric $Pb(Mg_{1/3}Nb_{2/3})O_3$–$PbTiO_3$ system, it was found that the electrostrictive coefficients measured at near and above the dielectric constant maximum are much smaller than the intrinsic values.[18,19] This is caused by the fact that in a relaxor ferroelectric system, the response of the local polar regions under external electric field includes the orientation of the polar regions and the motion of the interface between the non-polar area and the polar region.[20] All these responses contribute to the polarization, but do not totally contribute to the strain responses.[19] PZN–PT is also a typical relaxor ferroelectric system when the PT content is less than 10% and the evolution from a relaxor ferroelectric to a normal ferroelectric is a gradual process covering a broad composition range.[4,21] For the composition studied here, it is still quite close to the MPB and hence will possesses many features resembling a relaxor ferroelectric. For example, if there is a 180° local polar region reorientation, it will not cause a large change in the quadratic E-O coefficient in spite of the fact that there is a large polarization change. On the other hand, this response will influence $g_{11} - g_{12}$ and g_{44} in a similar way which will not affect the ratio between them as observed here. (The ratio of $(r_{33} - r_{13})/r_{51}$ measured here is the same as the ratio of $2K_{33}(g_{11} - g_{12})/K_{11}g_{44}$ deduced from the g-coefficients). Thus, the observed discrepancy be-

Table I. Properties characterized in this study for 0.88PZN–0.12PT single crystal.

$n_o = 2.57$, $n_e = 2.46$, $r_{33} = 134$ pm/V, $r_{13} = 7$ pm/V, $r_c = 131$ pm/V, $r_{51} = 462$ pm/V (all measured at 633 nm wavelength), $d_{31} = -210$ pm/V, $K_{33} = 710$, $K_{11} = 7630$, $P_s = 40\,\mu$C/cm^2

tween the measured linear E-O coefficients and the calculated ones from the quadratic E-O coefficients is reasonable. That is, when the measurement is performed at near the dielectric constant maximum where there is a strong contribution of the polarization responses from the local polar regions, the response of the local polar regions in relaxor systems will make the measured quadratic E-O coefficients deviating from their intrinsic values. By applying a high external field to remove this mesoscopic polarization inhomogeneity in the material, one may be able to obtain the intrinsic coefficients as observed in PMN–PT system.[19,22]

In Table I, the material properties characterized in this study are summarized.

4. Summary and Acknowledgement

Using the newly developed automated scanning Mach-Zehnder interferometer and the Senarmont compensator method, the linear E-O coefficients of 0.88PZN–0.12PT single crystal were measured at room temperature. It is found that the coefficients measured using the interferometer method and the Senarmont compensator method are in excellent accord. It is also found that the ratio of $(r_{33} - r_{13})/r_{51}$ measured here is also in very good accord with that deduced from the quadratic E-O coefficients measured earlier. However, in comparing the absolute values of the linear E-O coefficients measured here with that deduced from the quadratic E-O coefficients, it was found that the quadratic coefficients measured earlier at temperatures near the dielectric constant maximum may be substantially smaller than the intrinsic values of these coefficients due to the existence of mesoscopic polar regions and their different contributions to the polarization response and E-O response.

This work was supported by the Office of Naval Research under Contract No: N00014-98-1-0527.

1) M. E. Lines and A. M. Glass: *Principles and Applications of Ferroelectrics and Related Materials* (Clarendon Press, Oxford 1977).
2) L. J. Pinson: *Electro-optics* (John Wiley & Sons, New York, 1985).
3) J. Kuwata, K. Uchino and S. Nomura: Jpn. J. Appl. Phys. **21** (1982) 1298.
4) J. Kuwata, K. Uchino and S. Nomura: Ferroelectrics **37** (1981) 579.
5) S.-E. Park and T. Shrout: J. Appl. Phys. **82** (1997) 1804.
6) S.-F. Liu, S.-E. Park, T. R. Shrout and L. E. Cross: J. Appl. Phys. **85** (1999) 2810.
7) S.-E. Park and T. R. Shrout: Mater. Res. Innov. **1** (1997) 20.
8) B. Jaffe, W. R. Cook and H. Jaffe: *Piezoelectric Ceramics* (Academic Press, New York, 1971).
9) T. Mitsui and S. Nomura: *Ferroelectric and Related Materials* (Springer-Verlag, Berlin, 1981).
10) S. Nomura, H. Arima and F. Kojima: Jpn. J. Appl. Phys. **12** (1973) 531.
11) S.-F. Liu: unpublished.
12) IEEE Standard Board: An American National Standard, IEEE Standard on Piezoelectricity, ANSI/IEEE Std. **176** (1987).
13) A. R. Johnson and J. M. Weingart: J. Opt. Soc. Am. **55** (1965) 828.
14) D. McHenry: Dr. Thesis, Solid State Science, The Pennsylvania State University (1992).
15) F. W. Sears: *Optics* (Addison-Wesley, Cambridge, 1956).
16) T. Kwaaitaal, B. J. Luymes and G. A. Pijll: J. Phys. D **13** (1980) 1005.
17) F. Jona and G. Shirane: *Ferroelectric Crystals* (Dover, New York 1993).
18) J. Zhao, A. Glazonove, Q. M. Zhang and B. Toby: Appl. Phys. Lett. **72** (1998) 1048.
19) Q. M. Zhang and J. Zhao: Appl. Phys. Lett. **71** (1997) 1649.
20) Z.-Y. Cheng, R. S. Katiyar, X. Yao and A. S. Bhalla: Phys. Rev. B **57** (1998) 8166.
21) A. Halliyal, U. Kumar, R. E. Newnham and L. E. Cross: J. Am. Ceram. Soc. **70** (1987) 119.
22) J. Zhao: Dr. Thesis, Solid State Science, The Pennsylvania State University (1998).

Appendix 24

Y. Barad, Yu Lu, Z.–Y. Cheng, S.–E. Park, and Q.M. Zhang, "Composition, temperature, and crystal orientation dependence of the linear electro-optic properties of $Pb(Zn_{1/3}Nb_{2/3})O_3$–$PbTiO_3$ single crystals," Applied Physics Letters, 77[9], 1247–1249 (August 2000).

Composition, temperature, and crystal orientation dependence of the linear electro-optic properties of $Pb(Zn_{1/3}Nb_{2/3})O_3-PbTiO_3$ single crystals

Y. Barad, Yu Lu, Z.-Y. Cheng,[a] S.-E. Park, and Q. M. Zhang
Materials Research Laboratory, The Pennsylvania State University, University Park, Pennsylvania 16802

(Received 1 May 2000; accepted for publication 3 July 2000)

The linear electro-optic (EO) coefficients of $Pb(Zn_{1/3}Nb_{2/3})O_3-PbTiO_3$ single crystals over a broad composition range were investigated at temperatures from −20 to 80 °C. The orientation effect on the EO coefficients was also examined. For crystals poled in the ⟨001⟩ direction, a large r_{33} was observed near the morphotropic phase boundary (MPB). More importantly, r_{33} was found to be independent of temperature for the crystals on the tetragonal side of the MPB. In contrast, r_{13} was nearly zero for all compositions examined at all the temperatures. The large r_{33} near the MPB and the observed crystal orientation effect of the EO coefficients were also analyzed. © *2000 American Institute of Physics.* [S0003-6951(00)02735-2]

Ferroelectric crystals with high electro-optical (EO) coefficients are highly desirable for use in devices for optical communications and other commercial applications.[1,2] The search for a class of materials with high EO coefficients will allow for smaller size devices and lower operating voltage. A good candidate as such a substance is $Pb(Zn_{1/3}Nb_{2/3})O_3-PbTiO_3$ (PZN–PT) single crystals, which were found recently to possess both very high piezoelectric coefficients and electric-field-induced strains by working with different crystal orientations.[3–6] A unique feature to this crystal system is that relatively high-quality single crystals can be grown at compositions close to the tetragonal–rhombohedral morphotropic phase boundary (MPB) and a high EO response is expected at near the MPB.[7] In the following, we report on the results of a recent investigation of the linear EO coefficients of PZN–PT single crystals over a broad composition range (i.e., PZN–PT with 0%, 4.5%, 8%, 10%, and 12% PT), especially near the MPB, and in a temperature range of −20 to 80 °C [below the ferroelectric–paraelectric (FE–PE) transition temperature].

The crystals used in this work were grown by means of a high-temperature flux technique using high-purity (>99.9%) powders of Pb_3O_4, ZnO, Nb_2O_5, and TiO_2.[4,5] The single-crystal samples were orientated along the spontaneous polarization direction using a Laué camera. The crystals were then poled to ensure a single-domain configuration. The poling process was performed at a temperature about 50 °C higher than the FE–PE phase transition and then slowly cooled down to room temperature under the field. The poled samples were carefully polished to an optical grade, without affecting the crystal polarization. The poling direction was ⟨111⟩ for crystals on the rhombohedral side of the MPB (PZN–PT with 0%, 4.5%, and 8% PT) and ⟨001⟩ for crystals on the tetragonal side of the MPB (PZN–PT with 10% and 12% PT), respectively. To study the crystal orientation effect, the EO coefficients were also characterized for 0.92PZN–0.08PT poled in the ⟨001⟩ direction.

The EO effect describes the change (Δn_{ij}) in the refractive index due to an applied electric field (E_k). For poled ferroelectric crystals, we have[1,7]

$$\Delta n_{ij} = -\frac{1}{2} n_{ij}^3 \sum_{k=1}^{3} r_{ijk} E_k, \tag{1}$$

where r_{ijk} and n_{ij} are the linear EO coefficient and refractive index, respectively. In this work, the EO coefficients, r_{13} ($=r_{113}$) and r_{33}($=r_{333}$), were measured at a wavelength of 623.8 nm using a computer-controlled scanning Mach–Zender interferometer similar to the one reported in Ref. 7. For the work described here, the optical setup was upgraded to allow for varying temperature among the crystals measured. A precise feedback-controlled temperature stage was designed and built to fit into the optical setup. This apparatus can operate in a temperature range of −20–80 °C at a precision of less than 0.1 °C.

For the PZN–PT single crystals, applying an electric field contributes in two ways to the change in the optical path length (the principal parameter directly measured by the interferometer). The first is the change in optical index due to the EO effect; second is the change (Δl) in sample thickness along the optical path due to the piezoelectric effect ($\Delta l/l = d_{31}E_3$, where d_{31} and l are the transverse piezoelectric coefficient and the sample thickness along the optical path direction). In order to determine the real values of the EO coefficients, the contribution of the piezoelectric effect to the apparent EO coefficient r_{ij}^* was measured. The correction was made using the relation.[7]

$$r_{ij} = r_{ij}^* + \frac{2(n_i - 1)}{n_i^3} d_{31}, \tag{2}$$

where $ij = 33$ and 13, n_i is n_e when correcting for the value of r_{33}, and n_0 when the correction is made for the value of r_{13}.[7]

A summary of the EO coefficients measured at room temperature for the five investigated compositions is presented in Table I. Both the apparent and corrected EO coefficients are listed, along with the measured piezoelectric coefficient d_{31}. The results in Table I reveal several interesting features. First, compared with r_{33}, r_{13} is nearly zero. This is

[a]Electronic mail: zxc7@psu.edu

TABLE I. EO coefficients (r_{33} and r_{13}) of PZN–PT single crystal at room temperature. Here, r_{33}^* and r_{13}^* are the apparent values, d_{31} is the piezoelectric coefficient, and r_{33} and r_{13} are the real values.

Composition	Poling direction	r_{33}^* (pm/V)	r_{13}^* (pm/V)	$-d_{31}$ (pC/N)	r_{33} (pm/V)	r_{13} (pm/V)
PZN	⟨111⟩	77	8	10	75	6
0.955PZN–0.045PT	⟨111⟩	81	9	15	78	6
0.92PZN–0.08PT	⟨111⟩	105	24	42	97	16
0.92PZT–0.08PT	⟨001⟩	655	220	1070	450	15
0.9PZN–0.1PT	⟨001⟩	224	42	247	177	~0
0.88PZN–0.12PT	⟨001⟩	173	44	210	134	7

true for crystals in both the rhombohedral and tetragonal phases. Second, large r_{33} is observed for compositions near the MPB (see, also, Fig. 1). Third, for the same composition (e.g., 0.92PZN–0.08PT), the r_{33} coefficient of the crystal poled in the ⟨001⟩ direction is much higher than that of the crystal poled in the ⟨111⟩ direction.

For crystals in the tetragonal phase, the measured linear EO coefficients can be related to the polarization-related quadratic EO coefficients g_{11} and g_{12}, which can be determined at the prototype cubic phase at temperatures above the FE–PE transition temperature [$\Delta n_{ij} = -(1/2) n_{ij}^3 \times \Sigma_{k,l=1}^3 g_{ijkl} P_k P_l$, where P_k is the polarization component in the k direction], as follows:[8,9]

$$r_{33} = 2K_{33}\epsilon_0 P_s g_{11} \quad \text{and} \quad r_{13} = 2K_{33}\epsilon_0 P_s g_{12}, \tag{3}$$

where $g_{11} = g_{1111}$ and $g_{12} = g_{1122}$, and P_s and K_{33} are the spontaneous polarization and dielectric constant, respectively, in the ⟨001⟩ direction. ϵ_0 is the vacuum permittivity ($=8.85\times10^{-12}$ F/m). Therefore, the observation of a near-zero r_{13} in comparison to r_{33} implies a near-zero g_{12} in comparison to g_{11} or $g_{11} - g_{12} \approx g_{11}$.

For crystals in the rhombohedral phase, the measured r_{33} and r_{13} can be also linked to g_{ij} in the prototype cubic phase:[8,9]

$$\begin{aligned} r_{33} &= (2/3)K_{33}\epsilon_0 P_s(g_{11} + 2g_{12} + 2g_{44}), \\ r_{13} &= (2/3)K_{33}\epsilon_0 P_s(g_{11} + 2g_{12} - 2g_{44}). \end{aligned} \tag{4}$$

Using $g_{11} - g_{12} = 0.013\ \text{m}^4/\text{C}^2$ and $g_{44} = 0.009\ \text{m}^4/\text{C}^2$ as acquired by Nomura, Arima, and Kojima for PZN–PT at compositions near the MPB, and the fact that g_{12} is near zero,[10] Eq. (4) shows that the r_{13} is very small, which is consistent with experimental results. A large r_{33} and a near-zero r_{13} indicate that the applied electric field in the spontaneous polarization direction does not affect the overall electronic polarization of the unit cell in the directions perpendicular to it. Furthermore, the near-zero g_{12} implies that the refractive index in these directions will not change with P_s as the temperature is varied, even when it passes the FE–PE transition.

It should be noted that in Eq. (4), P_s and K_{33} are the spontaneous polarization and dielectric constant, respectively, in ⟨111⟩ direction, which differs from those used in Eq. (3). Using Eqs. (3) and (4), one can directly compare the EO coefficients for the crystals in the rhombohedral and tetragonal phases since the g_{ij} value changes little at the two

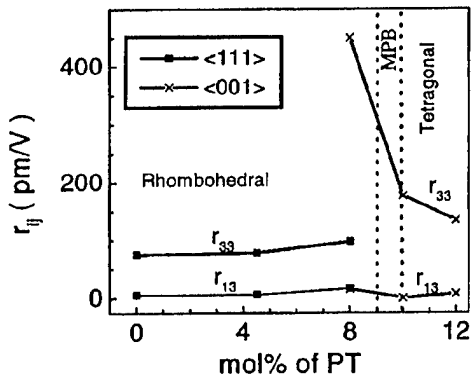

FIG. 1. EO coefficients at room temperature vs compositions for PZN–PT single crystals.

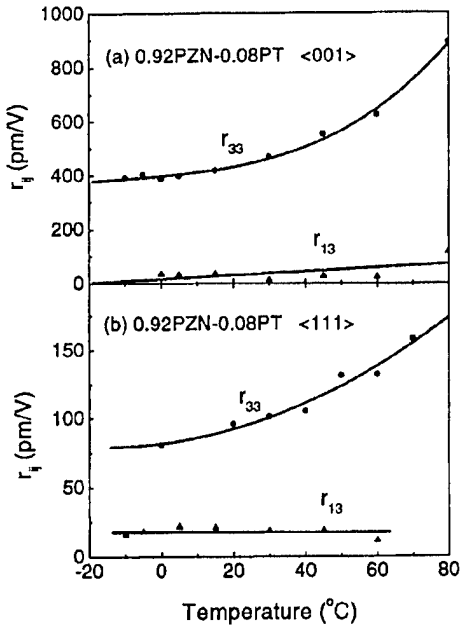

FIG. 2. Temperature dependence of EO coefficients for 0.92PZN–0.08PT single crystal poled in different directions: (a) ⟨001⟩ and (b) ⟨111⟩.

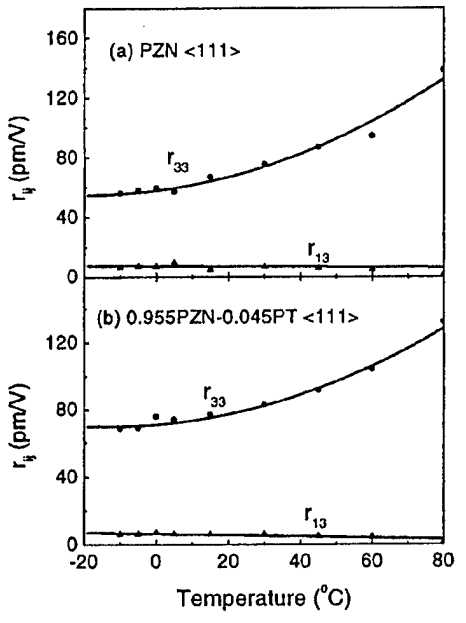

FIG. 3. Temperature dependence of EO coefficients for PZN and 0.955PZN–0.045PT single crystals poled in the ⟨111⟩ direction.

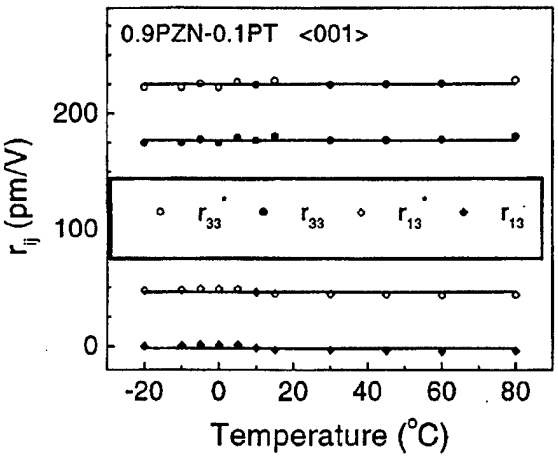

FIG. 4. Temperature dependence of EO coefficients for 0.9PZN–0.1PT single crystal poled in the ⟨001⟩ direction.

sides of the MPB. For 0.92PZN–0.08PT, the EO coefficients were measured for crystals poled along both the ⟨111⟩ and the ⟨001⟩ directions. Both the dielectric constant and P_s were also acquired for the corresponding crystals. For the crystal poled in the ⟨111⟩ direction, P_s and K_{33} in ⟨111⟩ are 0.45 C/m^2 and 807, respectively, while for the crystal poled in ⟨001⟩ direction, P_s and K_{33} are 0.32 C/m^2 and 3800, respectively. Using these values and Eqs. (3) and (4), the ratio of r_{33} between the tetragonal crystal and the rhombohedral crystal is about 4.2, while the experimentally measured ratio is 4.6. The two ratios are quite close to each other, indicating that the EO coefficients were from the responses of single-domain crystals in both cases. Also, the result suggests that K_{33} for both ⟨001⟩ and ⟨111⟩ poled 0.92PZN–0.08PT should stem mostly from the single-domain crystal. In that the quadratic EO coefficient g_{ij} exhibits no anomalous changes in compositions across the MPB, Eqs. (3) and (4) suggest that the large linear EO response observed here near the MPB is due to the large dielectric constant of the material at that region.

It should be also mentioned that direct comparison of the measured r_{33} with that from either Eq. (3) or (4) shows that the measured value is much larger than that deduced from the equations. For example, for 0.92PZN–0.08PT crystal poled in the ⟨001⟩ and ⟨111⟩ directions, the calculated r_{33} using Eqs. (3) and (4) is about 280 and 66 pm/V, respectively, while the measured r_{33} is 450 and 97 pm/V, respectively. As discussed in an early publication,[7] the discrepancy could stem from the fact that the measured g_{ij} using the EO effect at temperatures above the FE–PE transition may be smaller than the real single-crystal value. This is due to the relaxor nature of the material, in which resides local polarization regions even at temperatures higher than the FE–PE transition temperature.[11–13] Both the orientation and breathing of the polar regions contribute to the dielectric behavior (polarization) of the materials,[14,15] but do not contribute totally to the refractive-index change.[7] For example, a 180° local polar region reorientation, which leads to a large polarization change, will not cause a large change in the optic index.

We now discuss the temperature dependence of these EO coefficients. Figure 2 shows the EO coefficient r_{ij} as a function of temperature for 0.92PZN–0.08PT poled in the ⟨001⟩ and ⟨111⟩ directions, respectively, which reveals that r_{ij} changes with temperature. This temperature-dependence behavior was also observed for other compositions on the rhombohedral side of the MPB (see Fig. 3). In contrast, for the two compositions on the tetragonal side of the MPB, the EO coefficient is nearly independent of temperature, as shown in Fig. 4, where both the apparent and real EO coefficients are displayed. Since g_{11} should be nearly temperature independent, Eq. (3) implies that the value of the dielectric constant times spontaneous polarization ($K_{33}P_s$) should be nearly independent of temperature. Indeed, the directly measured P_s and K_{33} of the crystal with temperature confirm this effect.

In summary, a large r_{33} coefficient was observed for PZN–PT single crystals near the MPB. In addition, the coefficient is independent of temperature for the tetragonal phase crystal in the experimental temperature range of −20–80 °C. In comparison to r_{33}, r_{13} is nearly zero for all compositions investigated. These features are very attractive for device applications. It was also found that r_{33} for the tetragonal phase is much higher than that for the rhombohedral phase. Detailed analysis indicates that this increase is caused largely by the high dielectric constant.

This work was supported by ONR under Grant No. N00014-98-1-0527.

[1] M. E. Lines and A. M. Glass, *Principles and Applications of Ferroelectrics and Related Materials* (Oxford University Press, New York, 1977), Chap. 16.4.
[2] F. T. S. Yu and S. Jutamulia, *Optical Signal Processing, Computer, and Neural Network* (Wiley, New York, 1992).
[3] J. Kuwata, K. Uchino, and S. Nomura, Ferroelectrics **37**, 579 (1981).
[4] S.-E. Park and T. Shrout, J. Appl. Phys. **82**, 1804 (1997).
[5] S.-F. Liu, S.-E. Park, T. Shrout, and L. E. Cross, J. Appl. Phys. **85**, 2810 (1999).
[6] S. Nomura, T. Takahashi, and Y. Yokomizo, J. Phys. Soc. Jpn. **27**, 262 (1969).
[7] Y. Lu, Z.-Y. Cheng, S.-E. Park, S.-F. Liu, and Q. Zhang, Jpn. J. Appl. Phys., Part 1 **39**, 141 (2000).
[8] M. DiDomenico and S. H. Wemple, J. Appl. Phys. **40**, 720 (1969).
[9] S. H. Wemple, M. DiDomenico, and I. Camlibeel, Appl. Phys. Lett. **12**, 209 (1968).
[10] S. Nomura, H. Arima, and F. Kojima, Jpn. J. Appl. Phys. **12**, 531 (1973).
[11] G. Burns and B. A. Scott, Solid State Commun. **13**, 423 (1973).
[12] G. Burn and F. H. Dacol, Phys. Rev. B **30**, 4012 (1980).
[13] G. Burn and F. H. Dacol, Ferroelectrics **104**, 25 (1990).
[14] Z.-Y. Cheng, R. S. Katiyar, X. Yao, and A. S. Bhalla, Phys. Rev. B **57**, 8166 (1998).
[15] Q. M. Zhang and J. Zhao, Appl. Phys. Lett. **71**, 1649 (1997).